

International Journal of Photoenergy

Photovoltaic Materials and Devices 2014

Guest Editors: Bhushan Sopori, Peter Rupnowski, Sudhakar Shet,
and Prakash Basnyat





Photovoltaic Materials and Devices 2014

International Journal of Photoenergy

Photovoltaic Materials and Devices 2014

Guest Editors: Bhushan Sopori, Peter Rupnowski,
Sudhakar Shet, and Prakash Basnyat



Copyright © 2014 Hindawi Publishing Corporation. All rights reserved.

This is a special issue published in "International Journal of Photoenergy." All articles are open access articles distributed under the Creative Commons Attribution License, which permits unrestricted use, distribution, and reproduction in any medium, provided the original work is properly cited.

Editorial Board

- M. S. A. Abdel-Mottaleb, Egypt
Xavier Allonas, France
Nicolas Alonso-Vante, France
Wayne A. Anderson, USA
Yanhui Ao, China
Raja S. Ashraf, UK
V. Augugliaro, Italy
Detlef W. Bahnemann, Germany
I. R. Bellobono, Italy
Raghu N. Bhattacharya, USA
Pramod H. Borse, India
Alessio Bosio, Italy
Stephan Buecheler, Switzerland
Gion Calzaferri, Switzerland
C. Chen, China
Sung Oh Cho, Republic of Korea
V. Cimrová, Czech Republic
Juan M. Coronado, Spain
Ying Dai, China
D. D. Dionysiou, USA
Pingwu Du, China
M. M. El-Nahass, Egypt
Polycarpos Falaras, Greece
Chris Ferekides, USA
Paolo Fornasiero, Italy
Hermenegildo García, Spain
Germà Garcia-Belmonte, Spain
E. I. Garcia-Lopez, Italy
Beverley Glass, Australia
M. A. Gondal, Saudi Arabia
Jr-Hau He, Taiwan
Shinya Higashimoto, Japan
Cheuk-Lam Ho, Hong Kong
Wing-Kei Ho, Hong Kong
Fuqiang Huang, China
Adel A. Ismail, Egypt
Chun-Sheng Jiang, USA
Misook Kang, Republic of Korea
Shahed Khan, USA
Sun-Jae Kim, Republic of Korea
Jong Hak Kim, Republic of Korea
Sungjee Kim, Republic of Korea
Cooper H. Langford, Canada
Tae-Woo Lee, Republic of Korea
Lecheng Lei, China
Xinjun Li, China
Zhaosheng Li, China
Yuexiang Li, China
Stefan Lis, Poland
Vittorio Loddo, Italy
Gongxuan Lu, China
Dongge Ma, China
N. M. Mahmoodi, Iran
Nai Ki Mak, Hong Kong
Rajaram S. Mane, India
D. Mantzavinos, Greece
Ugo Mazzucato, Italy
Sheng Meng, China
Jacek Miller, Poland
Claudio Minero, Italy
Antoni Morawski, Poland
Franca Morazzoni, Italy
F. Morlet-Savary, France
M. Muneer, India
Kun Na, Republic of Korea
Ebinazar B. Namdas, Australia
Maria Neves, Portugal
Tebello Nyokong, South Africa
Kei Ohkubo, Japan
Haridas Pal, India
Leonidas Palilis, Greece
Leonardo Palmisano, Italy
Ravindra K. Pandey, USA
H. Park, Republic of Korea
Pierre Pichat, France
Gianluca Li Puma, UK
Tijana Rajh, USA
Peter Robertson, UK
Avigdor Scherz, Israel
Elena Selli, Italy
Ganesh D. Sharma, India
Jinn Kong Sheu, Taiwan
Panagiotis Smirniotis, USA
Zofia Stasicka, Poland
Elias Stathatos, Greece
J. Subbiah, Australia
M. Swaminathan, India
Kazuhiro Takanabe, Saudi Arabia
Mohamad-Ali Tehfe, Canada
K. R. Justin Thomas, India
Yang Tian, China
Nikolai V. Tkachenko, Finland
Ahmad Umar, Saudi Arabia
Thomas Unold, Germany
Veronica Vaida, USA
Roel van De Krol, Germany
Mark van Der Auweraer, Belgium
Rienk Van Grondelle, The Netherlands
Wilfried Van Sark, The Netherlands
Sheng Wang, China
Xuxu Wang, China
Mingkui Wang, China
Ezequiel Wolcan, Argentina
Man Shing Wong, Hong Kong
David Worrall, UK
Jeffrey C. S. Wu, Taiwan
Yanfa Yan, USA
Jiannian Yao, China
Minjoong Yoon, Republic of Korea
Jiangbo Yu, USA
Hongtao Yu, USA
Ying Yu, China
Klaas Zachariasse, Germany
Juan Antonio Zapien, Hong Kong
Tianyou Zhai, China
Lizhi Zhang, China
Guijiang Zhou, China
Yong Zhou, China
Rui Zhu, China

Contents

Photovoltaic Materials and Devices 2014, Bhushan Sopori, Peter Rupnowski, Sudhakar Shet, and Prakash Basnyat
Volume 2014, Article ID 534312, 1 pages

Enhanced Efficiencies for High-Concentration, Multijunction PV Systems by Optimizing Grid Spacing under Nonuniform Illumination, Pratibha Sharma, Alex W. Walker, Jeffrey F. Wheeldon, Karin Hinzer, and Henry Schriemer
Volume 2014, Article ID 582083, 7 pages

Synthesis and Characterization of CZTS Thin Films by Sol-Gel Method without Sulfurization, Xiaoqi Yu, Aobo Ren, Fogen Wang, Ci Wang, Jingquan Zhang, Wenwu Wang, Lili Wu, Wei Li, Guanggen Zeng, and Lianghuan Feng
Volume 2014, Article ID 861249, 6 pages

Device Modeling of the Performance of Cu(In,Ga)Se₂ Solar Cells with V-Shaped Bandgap Profiles, Shou-Yi Kuo, Ming-Yang Hsieh, Dan-Hua Hsieh, Hao-Chung Kuo, Chyong-Hua Chen, and Fang-I Lai
Volume 2014, Article ID 186579, 6 pages

Novel Terthiophene-Substituted Fullerene Derivatives as Easily Accessible Acceptor Molecules for Bulk-Heterojunction Polymer Solar Cells, Filippo Nisic, Alessia Colombo, Claudia Dragonetti, Alessandra Cominetti, Andrea Pellegrino, Nicola Perin, Riccardo Po, and Alessandra Tacca
Volume 2014, Article ID 373497, 10 pages

The Structure and Stability of Molybdenum Ditelluride Thin Films, Zhouling Wang, Wenwu Wang, Ya Yang, Wei Li, Lianghuan Feng, Jingquan Zhang, Lili Wu, and Guanggen Zeng
Volume 2014, Article ID 956083, 6 pages

Analysis and Monitoring Results of a Building Integrated Photovoltaic Façade Using PV Ceramic Tiles in Taiwan, Yen-Chieh Huang, Chi-Chang Chan, Szu-Chi Kuan, Shui-Jinn Wang, and Shin-Ku Lee
Volume 2014, Article ID 615860, 12 pages

Characterizations of Cuprous Oxide Thin Films Prepared by Sol-Gel Spin Coating Technique with Different Additives for the Photoelectrochemical Solar Cell, D. S. C. Halin, I. A. Talib, A. R. Daud, and M. A. A. Hamid
Volume 2014, Article ID 352156, 6 pages

TiCl₄ Pretreatment and Electrodeposition Time Investigations of ZnO Photoelectrodes Preparation for Dye Sensitized Solar Cells, Xiaoping Zou, Yan Liu, Cuiliu Wei, Zongbo Huang, and Xiangmin Meng
Volume 2014, Article ID 890563, 6 pages

Cooperative Optimal Control Strategy for Microgrid under Grid-Connected and Islanded Modes, Xuemei Zheng, Qiuming Li, Peng Li, and Danmei Ding
Volume 2014, Article ID 361519, 11 pages

Characterization of Cu_{1.4}Te Thin Films for CdTe Solar Cells, Guangcan Luo, Bin Lv, Wei Li, Lianghuan Feng, Jingquan Zhang, Lili Wu, and Guanggen Zeng
Volume 2014, Article ID 762576, 5 pages



Performance Improvement of Microcrystalline p-SiC/i-Si/n-Si Thin Film Solar Cells by Using Laser-Assisted Plasma Enhanced Chemical Vapor Deposition, Hsin-Ying Lee, Ting-Chun Wang, and Chun-Yen Tseng

Volume 2014, Article ID 795152, 5 pages

Thermal Field Analysis and Simulation of an Infrared Belt Furnace Used for Solar Cells, Bai Lu, Liang Zongcun, and Shen Hui

Volume 2014, Article ID 391270, 7 pages

Characterization of a-Si:H/c-Si Heterojunctions by Time Resolved Microwave Conductivity Technique, Amornrat Limmanee, Joaquim Nassar, Igor P. Sobkowicz, Jaran Sritharathikhun, Kobsak Sriprapha, Guillaume Courtois, Francois Moreau, and Pere Roca I Cabarrocas

Volume 2014, Article ID 304580, 4 pages

Editorial

Photovoltaic Materials and Devices 2014

Bhushan Sopori,¹ Peter Rupnowski,¹ Sudhakar Shet,² and Prakash Basnyat¹

¹National Renewable Energy Laboratory, National Center for Photovoltaics, 15013 Denver West Parkway, Golden, CO 80401, USA

²New Jersey Institute of Technology, Department of Materials Science and Engineering, 138 Warren Street, University Heights, Newark, NJ 07102, USA

Correspondence should be addressed to Bhushan Sopori; bhushan.sopori@nrel.gov

Received 14 October 2014; Accepted 14 October 2014; Published 22 December 2014

Copyright © 2014 Bhushan Sopori et al. This is an open access article distributed under the Creative Commons Attribution License, which permits unrestricted use, distribution, and reproduction in any medium, provided the original work is properly cited.

Ever increasing demand on the energy has fostered many new generation technologies, which include photovoltaics. In recent years, photovoltaic industry has grown very rapidly. The installed capacity of PV for 2013 was about 37 GW and 2014 sales are expected to be around 45 GW. However, there has been excess production for last several years, which is responsible in part for the low prices (about 60 ¢/W). To lower the PV energy costs further, a major strategy appears to be going to high efficiency solar cells. This approach is favored (over lower cost/lower efficiency) because cell efficiency has a very large influence on the acceptable manufacturing cost of a PV module. Hence, the PV industry is moving toward developing processes and equipment to manufacture solar cells that can yield efficiencies >20%. Thus, further research is needed within existing technologies to accomplish these objectives. Likewise, research will continue to seek new materials and devices.

This is the third special issue of International Journal of Photoenergy on Photovoltaic Materials and Devices and is aimed at selection of papers on recent advances in materials and PV systems. This issue contains thirteen papers on various aspects of photovoltaics. These fall into four broad categories:

- (1) advances in conventional solar cells and materials based on microcrystalline Si, modeling of bandgap-tailored CIGS, and characterization and process modeling of new materials and device designs;
- (2) design and applications of grid connected arrays and applications to building integration: of particular importance in concentrator application is the effect of nonuniform illumination;

- (3) novel materials: fullerene-based OPV and improvements in preparation of dye sensitized solar cells;
- (4) investigations on cuprous oxide, MoTe₂, Cu_{1.4}Te, and CZTS by sol-gel method.

We hope that readers enjoy this issue.

Acknowledgment

Special thanks are due to Dr. Takwa Maged for his continued help in coordinating this issue.

*Bhushan Sopori
Peter Rupnowski
Sudhakar Shet
Prakash Basnyat*

Research Article

Enhanced Efficiencies for High-Concentration, Multijunction PV Systems by Optimizing Grid Spacing under Nonuniform Illumination

**Pratibha Sharma, Alex W. Walker, Jeffrey F. Wheeldon,
Karin Hinzer, and Henry Schriemer**

SUNLAB, University of Ottawa, Ottawa, ON, Canada K1N 6N5

Correspondence should be addressed to Pratibha Sharma; psharm2@uottawa.ca

Received 7 December 2013; Accepted 1 June 2014; Published 7 August 2014

Academic Editor: Przemyslaw Rupnowski

Copyright © 2014 Pratibha Sharma et al. This is an open access article distributed under the Creative Commons Attribution License, which permits unrestricted use, distribution, and reproduction in any medium, provided the original work is properly cited.

The design of a triple junction solar cell's front contact grid can significantly affect cell conversion efficiency under high concentration. We consider one aspect of grid design, choosing a linear grid within a distributed resistance cell model to optimize finger spacings at concentrations between 500 and 2500 suns under uniform and nonuniform illumination. Optimization for maximum efficiency under Gaussian irradiance profiles is done by SPICE analysis. Relative to the optimized uniform illumination designs, we find enhancements of 0.5% to 2% in absolute efficiencies for uniform spacing. Efficiency enhancement with nonuniform spacing under nonuniform illumination is also evaluated. Our model suggests that, at lower concentrations (<1000 suns), the penalty for using uniformly spaced fingers instead of nonuniformly spaced fingers is <0.1%. However, at a concentration of 2500 suns the penalty increases to 0.3%. Thus, relative to a uniform irradiance optimization, an absolute efficiency increase of 2.3% can be attained for an optimized nonuniform spacing given the Gaussian irradiance profile under consideration.

1. Introduction

Multijunction solar cells based on III-V semiconductors are the most efficient of all photovoltaic technologies, with a record efficiency of 44.7% under concentration recently reported [1]. Not only does concentration permit the balance of concentrator photovoltaic system costs to offset the expensive material costs of multijunction solar cells, but it also enhances cell efficiency through the logarithmic increase in open circuit voltage [2]. The effects of concentration lead to a nonuniform profile that is not effectively flattened by secondary optic solutions [3]. Concentrator PV system optics often generate profiles that peak sharply at the center of the cell (Figure 1(a)) and follow a Gaussian distribution [4]. Peak-to-average irradiance ratios (PAR) typically range between 2 and 10 [2], but greater PARs are not unknown [5]. The nonuniformity in irradiance leads to a nonuniformity in current production that can decrease cell efficiency [6, 7].

The decrease in cell performance becomes increasingly evident at higher concentrations, where increasing current densities drive higher series resistance (I^2R) losses. The impact of these I^2R losses is a reduction in fill factor and therefore a reduction in conversion efficiency [8]. For uniform irradiance, a linear grid with even finger spacing, as shown in Figure 1(b), achieves maximum extraction efficiency regardless of such losses. This is not the case for nonuniform irradiance, where the consequent nonuniform current production within each subcell also leads to lateral currents that exacerbate carrier recombination. Continued reliance on uniform irradiance grid designs is therefore a cause for concern [6], motivating analyses of more realistic scenarios.

Simulation tools such as TCAD *Sentaurus* allow for valuable understanding of how solar cell performance depends on material properties and device structure [9]. However, as their complexity drives long computational times, usage of such tools is limited to simulating a small symmetrical

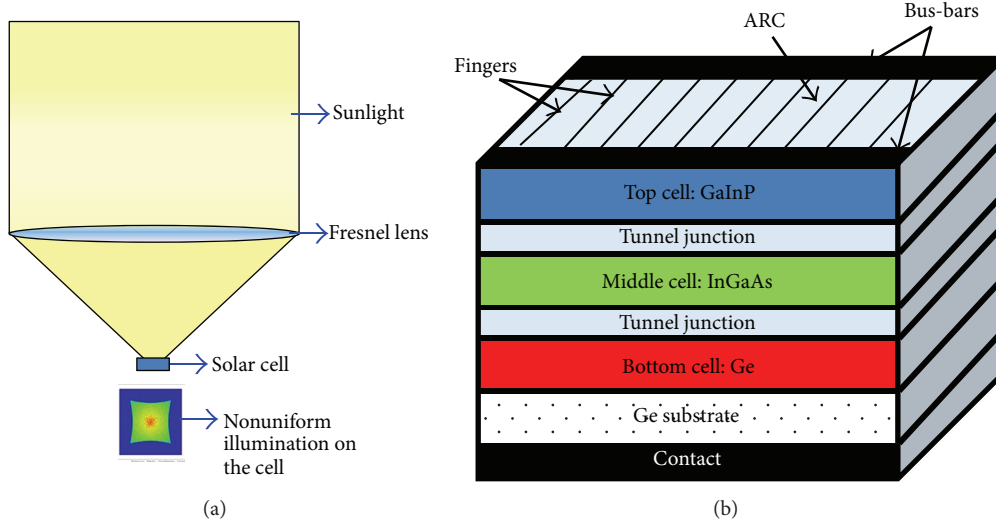


FIGURE 1: (a) A Fresnel-lens based CPV system showing nonuniform illumination on the solar cell. (b) Triple junction solar cell structure with a linear grid design; the bus-bars are outside the illumination area.

element of the device. Therefore, electrical models designed in SPICE (simulation program with integrated circuit emphasis) have been used to characterize the spatial dependence of solar cell performance. Due to their inability to simulate the effects of distributed resistance with varying irradiance profiles, classical lumped SPICE models do not permit realistic simulation. Hence, distributed resistance models, capable of simulating actual cell areas, are required for evaluating the effects of nonuniform illumination.

In this paper, we use a two-diode equivalent circuit for each subcell in a two-dimensional (2-D) distributed resistance model to address non-uniform current production under various Gaussian irradiance profiles. We report on the efficiency enhancements obtained by grid spacing optimization using realistic irradiance profiles at concentrations of 500, 1000, 2000, and 2500 suns with both uniform and nonuniform grid spacing. The results are compared with those obtained from the corresponding uniform irradiance analyses.

2. Numerical Model

2.1. Device Structure and Parameter Extraction. In order to generate values for equivalent circuit parameters that act as an input to the SPICE model, I - V curves for each subcell are required. These can be obtained either by using experimental data from isotopes or by simulating solar cell structures using TCAD tools [9, 10]. In this work, we have designed a triple-junction solar cell (TJSC) structure using TCAD *Sentaurus* by Synopsys. The simulation has been performed on a symmetrical element of a lattice-matched TJSC with 5% shading due to an ohmic contact on a highly doped GaAs cap layer. The structure consists of three subcells composed of GaInP, InGaAs, and Ge layers on a Ge substrate [9] connected in series using low-resistance tunnel junctions [11]. Previous variants of the model have been validated with experimental

TABLE 1: Triple junction solar cell parameters as obtained by curve-fitting simulated subcell I - V curves at 1 sun.

Parameter	Top subcell	Middle subcell	Bottom subcell
I_{01} (A)	1.0×10^{-25}	1.6×10^{-19}	1.6×10^{-6}
I_{02} (A)	1.0×10^{-20}	6.5×10^{-12}	1.3×10^{-5}
I_L (mA)	12.9	12.9	21.5
R_{sh} (k Ω)	10	10	3.5

results. Since a two-diode model yields more accurate results than a one-diode model [12], solar cell parameters have been determined for each subcell by curve-fitting the subcell I - V curves to

$$I = I_L - I_{D1} - I_{D2} - \frac{(V + IR_S)}{R_{sh}}, \quad (1)$$

where the individual diode equations are

$$I_{D1} = I_{01} \left[\exp \left(\frac{q(V + IR_S)}{kT} \right) - 1 \right], \quad (2)$$

$$I_{D2} = I_{02} \left[\exp \left(\frac{q(V + IR_S)}{2kT} \right) - 1 \right].$$

I_L is the light-generated current (which is directly proportional to the solar irradiation), I_{01} and I_{02} are reverse saturation currents, q is the electronic charge, k is the Boltzmann constant, R_S is the series resistance, R_{sh} is the shunt resistance, V is the output voltage, and I is the output current of the solar cell.

Since the values of I , V , and R_S are known from the subcell I - V curves and from the sheet resistances of the TJSC structure, the remaining unknowns, I_L , I_{01} , I_{02} , and R_{sh} , can be determined by curve-fitting using the least-squares method [13]. The parameters thus obtained are shown in Table 1 and have errors of less than 2%.

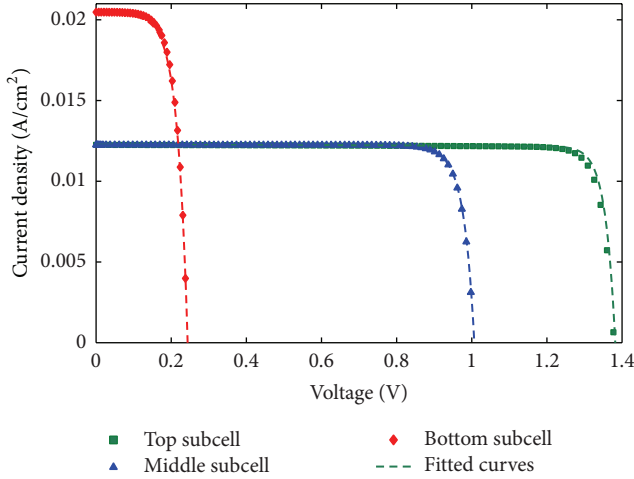


FIGURE 2: Simulated subcell J - V data for the TJSC obtained using TCAD Sentaurus (at 300 K and 1 sun) along with the least-squares, curve-fitted data.

Figure 2 shows the fitted subcell current-density versus voltage (J - V) curves along with the simulated (J - V) curves obtained for this structure using TCAD *Sentaurus*.

2.2. 2-Dimensional Distributed Resistance Model. Equivalent circuit representation of solar cells is useful for CPV system analysis [14–17]. In this work, a 2-D distributed resistance model for a TJSC is used [13]. This model, designed using LTSPICE, is an improvement over the 2-D model described by Nishioka et al. [14] as it includes equivalent circuits for the directly illuminated regions and for the shaded areas underneath the metal contact. The inclusion of equivalent circuits for the shaded areas is essential to analyze the effects of nonuniform illumination on cell efficiency [16].

Figure 3 presents a detailed circuit diagram for the SPICE model depicting illuminated and shaded equivalent circuits that comprise the repeated functional block. Since finger spacing is variable (given constant finger width), the number of functional blocks n varies with spacing for each simulation and is given by

$$n = \frac{A_t}{S_f + W_f}, \quad (3)$$

where A_t is the total cell area, S_f is the finger spacing, and W_f is the finger width. Narrower spacing requires a larger number of functional blocks to represent the physical extent of the TJSC being modeled.

The linear grid means a 2-D model will suffice to describe the TJSC. The model incorporates lateral resistance components connecting the functional blocks across the rows (R_{lat}), tunnel junction resistances (R_T) connecting the subcells in series, and contact resistances (R_{se}) for the electrodes. The number of function blocks for a fixed cell dimension determines the lateral resistance values [13, 18]. Electrode resistances are assumed to be negligible, finger widths are fixed at $5 \mu\text{m}$, and the active cell area is equal to 1 cm^2 . The model therefore accounts for shading losses due to the fingers

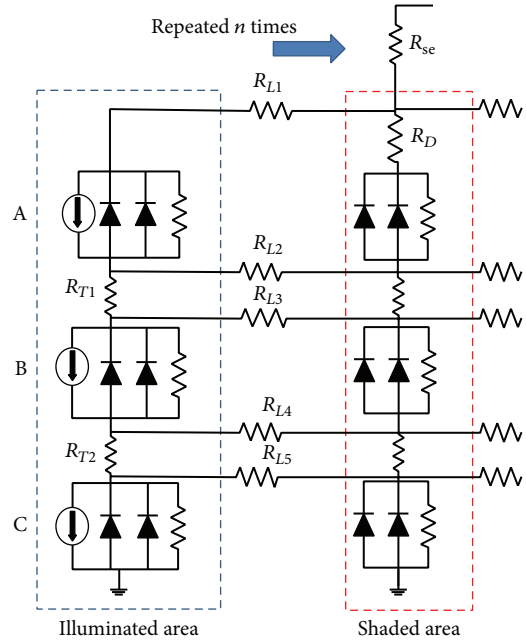


FIGURE 3: 2-D distributed resistance model developed in SPICE showing the two-diode equivalent circuits for each of the subcells where (A) top subcell, (B) middle subcell, and (C) bottom subcell are connected in series using tunnel junctions. An illuminated and a shaded unit form a complete functional block that is repeated n times.

and ohmic losses due to series resistances. Bus bars are assumed to be outside the active cell area and are not included in the model. Shading losses and series resistances due to bus bars are neglected for our simulations.

3. Optimization

In order to optimize finger spacing, the solar cell conversion efficiency is assumed to be a unimodal objective function with one maximum. A derivative-free optimization approach is adopted to maximize cell efficiency. In order to reduce the number of iterations and for a faster convergence, a Golden-section search algorithm is used. Finger spacings range from $50 \mu\text{m}$ to $300 \mu\text{m}$, for a shading range of $\sim 2\%$ to 10% , which is typical for solar cell designs. Convergence of the optimization process is ensured by requiring the absolute change in efficiency to be less than 0.01% ; spacing increments are $3 \mu\text{m}$. Eight to ten iterations are sufficient to achieve convergence. Section 3.1 below describes the optimization process for an ideal uniform irradiance distribution; Section 3.2 describes the process for a nonuniform irradiance distribution.

3.1. Under Uniform Illumination. Figure 4 shows efficiency as a function of finger spacing at concentrations of 500, 1000, 2000, and 2500 suns under a uniform illumination profile ($1 \text{ sun} = 900 \text{ W/m}^2$). The relationship between the short-circuit current and the concentration is assumed to be linear [2]. This implies that the short-circuit current for this cell at 1000 suns is 1000 times that of the short-circuit current under

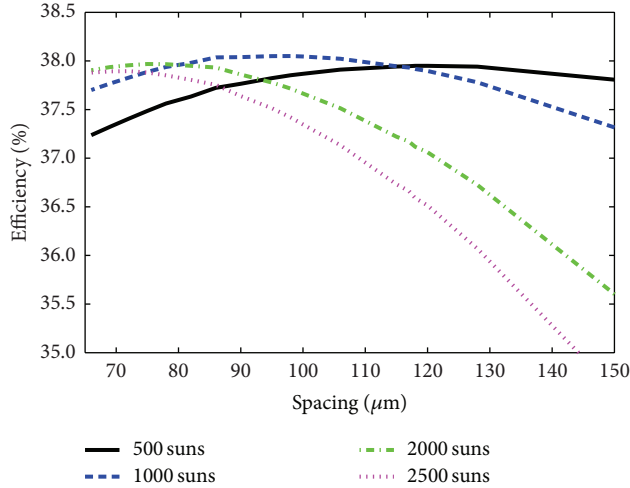


FIGURE 4: Efficiency as a function of spacing at 500, 1000, 2000, and 2500 suns under uniform illumination. An optimal finger spacing is obtained using a Golden section search algorithm after 8–10 iterations.

one sun operation. The figure reveals that the efficiency of the cell reaches a maximum value at each concentration for a specific finger spacing.

The optimal finger spacing at 500 suns is found to be 120 μm . However, at 1000 suns the optimal finger spacing is reduced to 95 μm . It is evident that this cell can perform almost optimally, without much loss in efficiency (<0.2%), at both 500 and 1000 suns if the fingers are spaced from 95 to 120 μm . At 2000 and 2500 suns, however, the cell needs to be designed with more closely spaced fingers (optimal spacing is 75 μm and 72 μm resp.) in order to get the best possible efficiency. A similar trend is reported in an NREL technical report [19]. The highest efficiencies obtained with this cell under uniform illumination are 37.9% at 500 suns, 38.1% at 1000 suns, 38.0% at 2000 suns, and 37.9% at 2500 suns.

An increase in the slope of the efficiency versus spacing curve with concentration indicates that the penalty for using a nonoptimal spacing is greater at higher concentrations (2000 and 2500 suns) than at lower concentrations (500 and 1000 suns). If the cell is designed with a 120 μm spacing and operated under uniform illumination at a concentration of 2500 suns, a 1.3% absolute loss in efficiency is observed as compared to that obtained with the optimal spacing.

3.2. Uniform Spacing under Nonuniform Illumination. To model nonuniform illumination, three Gaussian profiles with different peak to average ratios (PARs) are used to represent various types of concentrating optics. Efficiency optimization is performed for PARs of 1.6, 2.6, and 5.3 at concentrations of 500, 1000, 2000, and 2500 suns across the range of finger spacings. A PAR of 1.6 approximates an ideal concentrating system, while a PAR of 5.3 may represent a system with only a primary Fresnel lens element and no secondary homogenizer. Note that, while the total intensity of each irradiance profile is kept constant, chromatic aberration effects are ignored in the optimization. This implies that current mismatch between

top, middle, and bottom subcells is neglected. Figure 5 shows how the efficiency variation with finger spacing depends on the illumination profile; uniform illumination has also been included, for comparison. The three Gaussian irradiance distributions are shown in the inset. The optimal finger spacing is seen to decrease with both increasing nonuniformity and increasing concentration, and the efficiency is likewise reduced. Figure 5(a), at 500 suns, shows that, for the highest PAR, the efficiency at the optimal uniform spacing of 120 μm is about 0.5% absolute lower than it would be at its optimal 90 μm spacing; for Figure 5(b), at 1000 suns, the efficiency at the optimal uniform spacing of 98 μm is about 0.9% absolute lower than it would be at its optimal 69 μm spacing; and for Figure 5(c), at 2000 suns, the efficiency at the optimal uniform spacing of 75 μm is about 1.5% absolute lower than it would be at its optimal 50 μm . The results clearly illustrate that an increase in concentration and in nonuniformity has an increasingly significant effect on the conversion efficiency of the solar cell.

3.3. Nonuniform Finger Spacing under Nonuniform Illumination. In order to further improve the efficiency of the cell exposed to a nonuniform irradiance profile, a nonuniform grid spacing is investigated to ascertain if unevenly spaced fingers enhance cell efficiency. To reduce computational complexity, the cell is virtually divided into a number of segments of equal area. Spacing is uniform within a segment but differs between segments. For example, consider a solar cell virtually divided into ten segments (say S_1 to S_{10}). Since the segments closest to the center of the cell will receive higher illumination, the fingers should be more narrowly spaced at the center of the cell than at the edges. Also, since Gaussian irradiance profiles have been used to represent nonuniform illumination, a symmetric spacing distribution can be used. For example, the spacing for the two outermost segments, S_1 and S_{10} , is the same.

Simulations show a negligible change in efficiency (<0.01%) when the number of segments is increased beyond ten. Therefore, ten segments are used for our model. Each segment consists of a number of functional blocks given by

$$Y = m * \text{Seg}N + C, \quad (4)$$

where $\text{Seg}N$ is the segment number for the symmetric left half of the cell, m is the slope of the linear profile, and C is a constant.

By varying the values of m and C , the number of functional blocks, and hence the finger spacing, is varied. Changing m varies the spacing between segments more drastically than changing C . In order to implement this in SPICE, recalculation of resistance values for each segment, and for intermediate areas between segment transitions, is required. Maximum slope (Max M) and constant (Max C) values are set to 10 and maximum efficiencies are obtained as the values of m and C are varied between 1 and 10, yielding optimal configurations for all irradiance profiles and concentrations. Figure 6 shows results for a Gaussian irradiance profile of PAR = 5.3 at 1000 suns and 2500 suns. At 1000 suns, a maximum efficiency (η_{max}) of 36.9% is obtained at $m = 2$ and

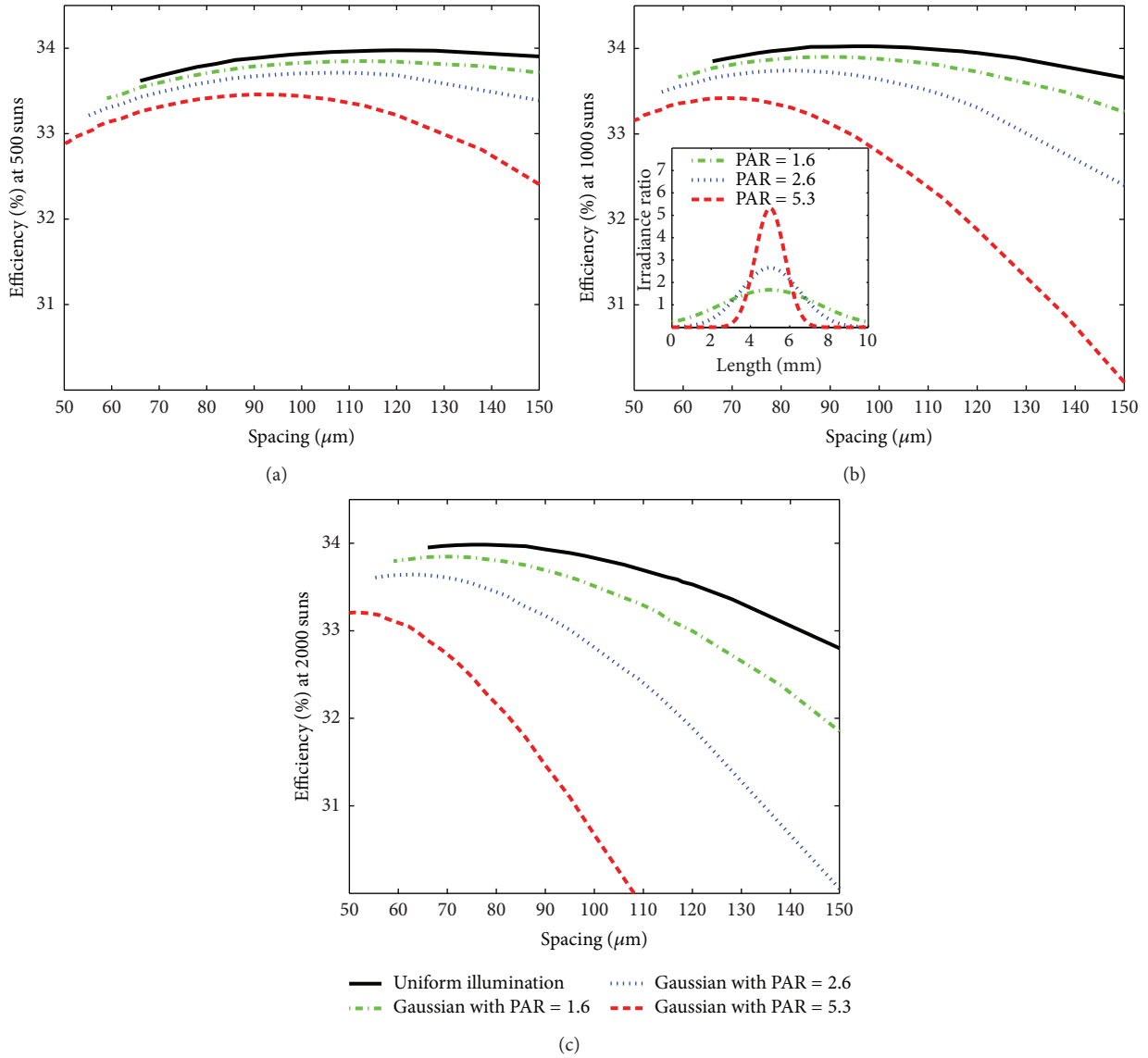


FIGURE 5: Efficiency as a function of finger spacing at a concentration of (a) 500 suns, (b) 1000 suns, and (c) 2000 suns; inset: Gaussian irradiance distributions with different peak to average ratios (PARs).

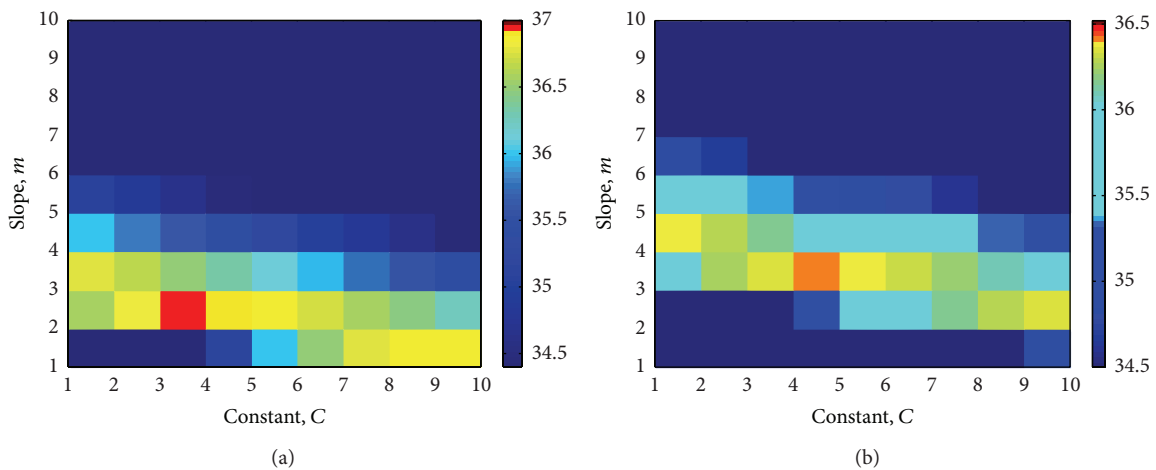


FIGURE 6: Efficiency as a function of slope m and constant C under a Gaussian irradiance distribution (PAR = 5.3) at (a) 1000 and (b) 2500 suns. The color bar indicates the efficiency values (%) obtained with each combination.

TABLE 2: Maximum efficiency (η_{\max}) comparison with uniform and nonuniform spacing under PAR = 5.3 and PAR = 2.6 at various concentrations (X).

X	PAR = 5.3		PAR = 2.6	
	η_{\max} Uniform spacing [%]	η_{\max} Nonuniform spacing [%]	η_{\max} Uniform spacing [%]	η_{\max} Nonuniform spacing [%]
500	36.9	37.0	37.4	37.4
1000	36.8	36.9	37.5	37.5
2000	36.4	36.6	37.3	37.4
2500	36.1	36.4	37.1	37.2

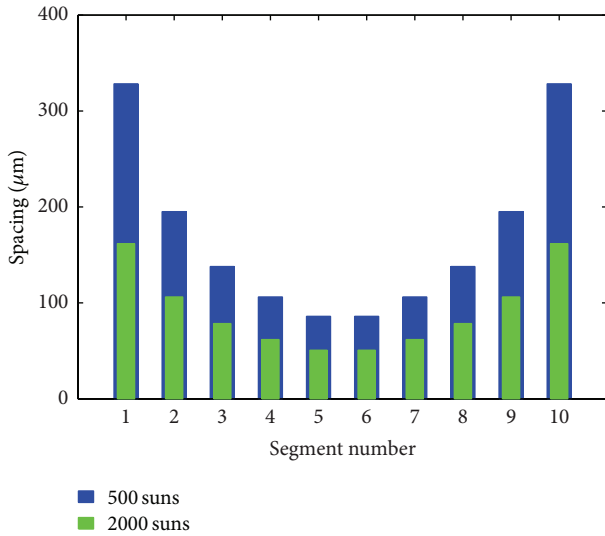


FIGURE 7: Optimal nonuniform spacing profile at (a) 500 suns and (b) 2000 suns under a Gaussian irradiance profile (PAR = 5.3) with the solar cell divided into ten equal segments.

$C = 3$. In this case the spacing varies from $195 \mu\text{m}$ at the cell edges to $72 \mu\text{m}$ at the cell center. At 2500 suns, $\eta_{\max} = 36.4\%$ is obtained at $m = 3$ and $C = 4$. In this case the spacing varies from $137 \mu\text{m}$ at the cell edges to $48 \mu\text{m}$ at the cell center.

Figure 7 shows the optimal spacing profile as a function of segment position under nonuniform irradiance profile with a PAR = 5.3 at concentrations of 500 and 2000 suns. It is evident that the spacings become narrower toward the center of the cell. For 500 suns, the spacing varies from $328 \mu\text{m}$ at the cell edges to $86 \mu\text{m}$ at the cell center; and for 2000 suns, it varies from $162 \mu\text{m}$ at the cell edges to $51 \mu\text{m}$ at the cell center.

Similar simulations have been carried out for illumination profiles with PAR = 1.6 and PAR = 2.6. Negligible change in maximum efficiency was seen for the near-optimal profile (PAR = 1.6). Table 2 shows the maximum efficiency for Gaussian profiles having a PAR of 2.6 and 5.3 at various concentrations.

For lower concentrations and lower PAR values, the penalty for using uniform spacing is minimal. A similar result has been reported in [20] at 1000 suns. However, at higher concentrations, a 0.3% absolute efficiency gain is observed. The effect of using a nonuniform spacing is more pronounced as the irradiance PAR increases.

4. Conclusion

Our results indicate that, under uniform illumination, the finger spacing needs to be optimized for the system concentration. Under nonuniform illumination, the effect of finger spacing on solar cell efficiency can be pronounced. For uniform spacing at 2500 suns, an efficiency enhancement of 2% absolute is obtained when optimizing using a Gaussian profile of PAR = 5.3 rather than a flat profile. For nonuniform spacing an additional enhancement in absolute efficiency of 0.3% was found. At lower concentrations, the penalty for using evenly spaced fingers becomes negligible. The need to optimize grid designs based on nonuniform illumination is thus clearly demonstrated by our optimization of front contact finger spacing on multijunction solar cells using more realistic irradiance profiles across a range of concentrations.

Conflict of Interests

The authors declare that there is no conflict of interests regarding the publication of this paper.

Acknowledgments

The authors would like to thank the National Science and Engineering Research Council of Canada, the Canadian Foundation for Innovation, Canada Research Chair Program, Ontario Research Fund, and Cyrium Technologies Inc. for supporting this work and CMC Microsystems for providing access to Sentaurus software.

References

- [1] F. Dimroth, M. Grave, P. Beutel et al., "Wafer bonded four-junction GaInP/GaAs//GaInAsP/GaInAs concentrator solar cells with 44.7% efficiency," *Progress in Photovoltaics: Research and Applications*, vol. 22, pp. 277–282, 2014.
- [2] C. Algora, "The importance of the very high concentration in third-generation solar cells," in *Next Generation Photovoltaics*, pp. 108–136, Institute of Physics Publishing, London, UK, 2003.
- [3] L. Fu, R. Leutz, and H. P. Annen, "Secondary optics for Fresnel lens solar concentrators," in *7th Nonimaging Optics: Efficient Design for Illumination and Solar Concentration*, vol. 7785 of *Proceedings of SPIE*, San Diego, Calif, USA, August 2010.
- [4] R. Herrero, M. Victoria, C. Domínguez, S. Askins, I. Antón, and G. Sala, "Concentration photovoltaic optical system irradiance distribution measurements and its effect on multi-junction

- solar cells,” *Progress in Photovoltaics: Research and Applications*, vol. 20, no. 4, pp. 423–430, 2012.
- [5] C. Algora and V. Diaz, “Influence of series resistance on guidelines for manufacture of concentrator p-on-n GaAs solar cells,” *Progress in Photovoltaics: Research and Applications*, vol. 8, pp. 211–225, 2000.
- [6] H. Baig, K. C. Heasman, and T. K. Mallick, “Non-uniform illumination in concentrating solar cells,” *Renewable and Sustainable Energy Reviews*, vol. 16, no. 8, pp. 5890–5909, 2012.
- [7] H. Baig, N. Sarmah, K. C. Heasman, and T. K. Mallick, “Numerical modelling and experimental validation of a low concentrating photovoltaic system,” *Solar Energy Materials and Solar Cells*, vol. 113, pp. 201–219, 2013.
- [8] J. Nelson, *The Physics of Solar Cells*, Imperial College Press, London, UK, 2003.
- [9] A. W. Walker, *Bandgap engineering of multi-junction solar cells using nanostructures for enhanced performance under concentration [Ph.D. dissertation]*, Dept. of Physics, University of Ottawa, Ottawa, Canada, 2013.
- [10] A. W. Walker, O. Thériault, M. M. Wilkins, J. F. Wheeldon, and K. Hinzer, “Tunnel-junction-limited multijunction solar cell performance over concentration,” *IEEE Journal of Selected Topics in Quantum Electronics*, vol. 19, no. 5, pp. 1–8, 2013.
- [11] J. F. Wheeldon, C. E. Valdivia, A. W. Walker et al., “Performance comparison of AlGaAs, GaAs and InGaP tunnel junctions for concentrated multijunction solar cells,” *Progress in Photovoltaics: Research and Applications*, vol. 19, no. 4, pp. 442–452, 2011.
- [12] G. Segev, G. Mittelman, and A. Kribus, “Equivalent circuit models for triple-junction concentrator solar cells,” *Solar Energy Materials and Solar Cells*, vol. 98, pp. 57–65, 2012.
- [13] P. Sharma, A. Walker, J. Wheeldon, H. Schriemer, and K. Hinzer, “Optimization of finger spacing for concentrator photovoltaic cells under non-uniform illumination using SPICE,” in *Photonics North Conference*, vol. 8915 of *Proceedings of SPIE*, Ottawa, Canada, June 2013.
- [14] K. Nishioka, T. Takamoto, T. Agui, M. Kaneiwa, Y. Uraoka, and T. Fuyuki, “Evaluation of InGaP/InGaAs/Ge triple-junction solar cell under concentrated light by simulation program with integrated circuit emphasis,” *Japanese Journal of Applied Physics*, vol. 43, no. 3, part 1, pp. 882–889, 2004, 10.1143/JJAP.43.882.
- [15] A. Zekry and A. Y. Al-Mazroo, “A distributed SPICE-model of a solar cell,” *IEEE Transactions on Electron Devices*, vol. 43, no. 5, pp. 691–700, 1996.
- [16] B. Galiana, C. Algora, and I. Rey-Stolle, “Comparison of 1D and 3D analysis of the front contact influence on GaAs concentrator solar cell performance,” *Solar Energy Materials and Solar Cells*, vol. 90, no. 16, pp. 2589–2604, 2006.
- [17] P. Rodrigo, E. F. Fernández, F. Almonacid, and P. J. Pérez-Higueras, “Models for the electrical characterization of high concentration photovoltaic cells and modules: a review,” *Renewable and Sustainable Energy Reviews*, vol. 26, pp. 752–760, 2013.
- [18] K. Nishioka, T. Takamoto, T. Agui, M. Kaneiwa, Y. Uraoka, and T. Fuyuki, “Evaluation of InGaP/InGaAs/Ge triple-junction solar cell and optimization of solar cell’s structure focusing on series resistance for high-efficiency concentrator photovoltaic systems,” *Solar Energy Materials and Solar Cells*, vol. 90, no. 9, pp. 1308–1321, 2006.
- [19] R. King, “Ultra-high efficiency multijunction cell and receiver module, Phase 1B: high performance PV exploring and accelerating ultimate pathways,” Tech. Rep. NREL/SR-520-47602, National Renewable Energy Laboratory, Boulder, Colo, USA, 2010.
- [20] I. Garcia, C. Algora, I. Rey-Stolle, and B. Galiana, “Study of non-uniform light profiles on high concentration III-V solar cells using quasi-3D distributed models,” in *Proceedings of the 33rd IEEE Photovoltaic Specialists Conference (PVSC '08)*, pp. 1–6, San Diego, Calif, USA, May 2008.

Research Article

Synthesis and Characterization of CZTS Thin Films by Sol-Gel Method without Sulfurization

Xiaoqi Yu, Aobo Ren, Fogen Wang, Ci Wang, Jingquan Zhang, Wenwu Wang, Lili Wu, Wei Li, Guanggen Zeng, and Lianghuan Feng

College of Materials Science and Engineering, Sichuan University, Chengdu 610064, China

Correspondence should be addressed to Jingquan Zhang; zjq100@hotmail.com and Wenwu Wang; 93319189@qq.com

Received 10 February 2014; Revised 28 May 2014; Accepted 28 May 2014; Published 22 July 2014

Academic Editor: Sudhakar Shet

Copyright © 2014 Xiaoqi Yu et al. This is an open access article distributed under the Creative Commons Attribution License, which permits unrestricted use, distribution, and reproduction in any medium, provided the original work is properly cited.

One process of layer-by-layer sol-gel deposition without sulfurization was developed. The CZTS films with 1.2 μm and the sulfur ratio of ~48% were prepared and their characteristics were measured. The as-deposited and annealed films are of Kesterite structure. The as-deposited films do not present obvious electric conduction type. However, the annealed 9-LAY-ANN film is p-type conduction and has sheet resistance of 4.08 $\text{k}\Omega/\square$ and resistivity of $4.896 \times 10^{-1} \Omega\cdot\text{cm}$. The optic energy gap is 1.50 eV for as-deposited films and is 1.46 eV after being annealed. The region deposited by using Lo-Con solution is more compact than that by the Hi-Con solution from SEM morphology images.

1. Introduction

Great attention is paid to the earth-abundant and nontoxic CZTS ($\text{Cu}_2\text{ZnSnS}_4$) as a potential candidate for a light absorbing layer in thin film solar cell devices. The theoretical conversion efficiency of single-junction CZTS solar cell is 32.2% [1], because of its high absorption coefficient over 10^4 cm^{-1} and a suitable direct band gap of 1.4–1.5 eV. In general, the methods of fabricating CZTS films consist of the vacuum-based and the liquid-based techniques. The deposition systems are so expensive that they possibly increase the manufacturing cost for the vacuum-based technology, such as thermal evaporation [2] and Magnetron sputtering [3, 4]. However, the low-cost manufacturing system and process can be adopted by liquid-based technology, such as screen printing [5, 6], chemical bath deposition [7], electro-deposition [8], and sol-gel method [9–15].

The optical and electronic properties of CZTS films are dependent on their composition. So the sulfurization process is an indispensable step for vacuum-based techniques in order to obtain the stoichiometric film, because sulfur is apt to be deficient in the vacuum ambiance owing to its high saturation vapor pressure. On the other hand, the toxic H_2S was often used for the liquid-based deposition techniques to avoid S-deficiency during the annealing process [5, 9–13]. So

the liquid-based techniques without intentional sulfurization were developed by some research groups [6–8, 14, 15]. Park et al. reported the CZTS film of 563 nm thickness with the ratio of S being about 50%, which was prepared by using sol-gel technology, by adding excess thiourea into the solution [15]. Yeh et al. reported the CZTS film of 2.9 μm with the ratio of S below 40%, which was prepared by layer-by-layer sol-gel technology in air with the synthesizing temperature of 593 K [14].

Usually, the thickness of CZTS thin film used as solar cell absorbing layer should be more than 1 μm with the purpose of absorbing the light sufficiently and the ratio of sulfur should be about 50%, in order to ensure optical and electronic properties of the film.

In this work, one process of layer-by-layer sol-gel (LBLSG) deposition without sulfurization was developed. The CZTS films with 1.2 μm and the sulfur ratio of ~48% were prepared and their characteristics were measured.

2. Experiment

The sol-gel solutions for CZTS precursors were prepared by dissolving $\text{CuCl}_2\cdot 2\text{H}_2\text{O}$, $\text{Zn}(\text{CH}_3\text{COO})_2\cdot 2\text{H}_2\text{O}$, $\text{SnCl}_2\cdot 2\text{H}_2\text{O}$, and $\text{CH}_4\text{N}_2\text{S}$ into 2-methoxyethanol (2-metho) and

TABLE 1: The amount of starting materials in the two solutions.

Solution	CuCl ₂ ·2H ₂ O (mmol)	Zn(ac) ₂ ·2H ₂ O (mmol)	SnCl ₂ ·2H ₂ O (mmol)	CH ₄ N ₂ S (mmol)	2-metho (mL)	MEA (mL)
Hi-Con	14.4	9.6	8	64	10	1
Lo-Con	3.6	2.4	2	16	10	1

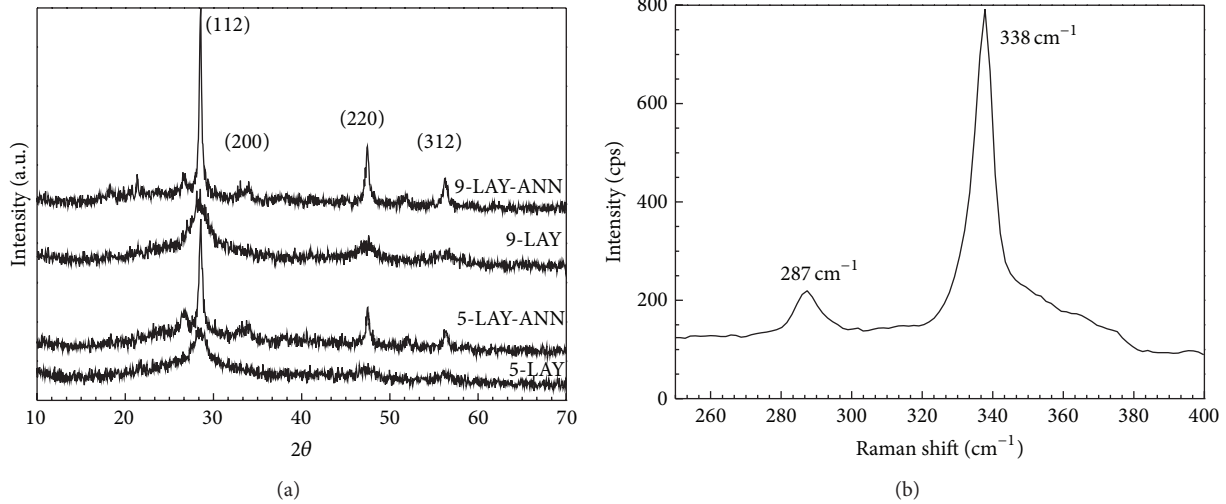


FIGURE 1: (a) XRD patterns of the CZTS films. (b) Raman spectrum of 9-LAY-ANN CZTS thin film.

monoethanolamine (MEA). The 2-metho and MEA were used as the solvent and the stabilizer, respectively. Two types of sol-gel solutions, named as Hi-Con and Lo-Con, were prepared by the recipe shown in Table 1. Each solution was stirred for 20 min at 300 K. The vicious yellow solution Hi-Con was used to make the film thick enough and the pale yellow solution Lo-Con aimed to make the film surface smooth and compact.

CZTS films were deposited on the borosilicate glass. The procedures to deposit each layer in the LBLSG included spin-coating, drying, and baking. Firstly the solution was dropped and rotated for 60 s at 3000 rpm; secondly the spin-coated films were dried at 393 K for 2 h in air on the hot plate; thirdly the dried samples were baked at 523 K for 10 min under nitrogen atmosphere in the quartz tube to prevent O₂ affecting the film. Three samples were prepared. The sample 3-LAY was deposited up to three layers on the borosilicate glass, using solution Lo-Con by LBLSG process. The sample 5-LAY was deposited up to 5 layers, which was deposited with two layers by using solution Hi-Con on the sample 3-LAY. The sample 9-LAY was deposited up to 9 layers, which was deposited with four layers by using solution Lo-Con on the sample 5-LAY. The as-deposited samples of 5-LAY and 9-LAY were annealed at 773 K for 60 min under N₂ atmosphere, named as 5-LAY-ANN and 9-LAY-ANN, respectively.

The structure and phase were characterized by X-ray diffraction (XRD) by using a DX-2500 XRD diffractometer from Dandong Fangyuan Instrument LLC, China. The Raman spectrum was recorded by using a LabRAM-HR Raman Spectrometer from Horiba-Jobin Yvon Ibh Ltd. The film morphologies of surface and cross section were observed by a Hitachi S-4800 scanning electron microscope (SEM),

and the compositions were determined by energy dispersive spectrometer (EDS) attached to SEM. X-ray photoelectron spectroscopy (XPS) was measured in order to analyze the element chemical valence state of films via an X-ray photoelectron spectroscope (KRATOS, AXIS Ultra DLD). The transmittance was measured using a UV-VIS-NIR spectrophotometer PerkinElmer Lambda 950 with 150 mm integrating sphere. The film thickness was determined by a surface profiler (XP-2, Ambios Technology, Inc.). The sheet resistance was measured by RTS-9 four-probe test system from Guangzhou 4Probes Tech. Inc., China. And the conductive type was determined using cold-hot probe method by a PN-12 conductive type measure system from Guangzhou 4Probes Tech. Inc., China.

3. Results and Discussion

The XRD patterns of films are shown in Figure 1(a). The as-deposited thin films, 5-LAY and 9-LAY, were poorly crystalline, while the annealed films, 5-LAY-ANN and 9-LAY-ANN, are well crystalline which match well the Kesterite structure of CZTS (JCPDS card 26-0575). The refined tetragonal lattices parameters for 9-LAY-ANN are $a = b = 5.42 \text{ \AA}$, $c = 10.83 \text{ \AA}$, and $V = 318.24 \text{ \AA}^3$, analyzed by Jade5.0 software; however, for sample 5-LAY-ANN, the refined tetragonal lattices parameters were not figured out because of the major error. The crystallites size of 5-LAY-ANN and 9-LAY-ANN was calculated as 24.9 nm and 31.8 nm, respectively, using Debye-Scherrer formula by Jade5.0 software.

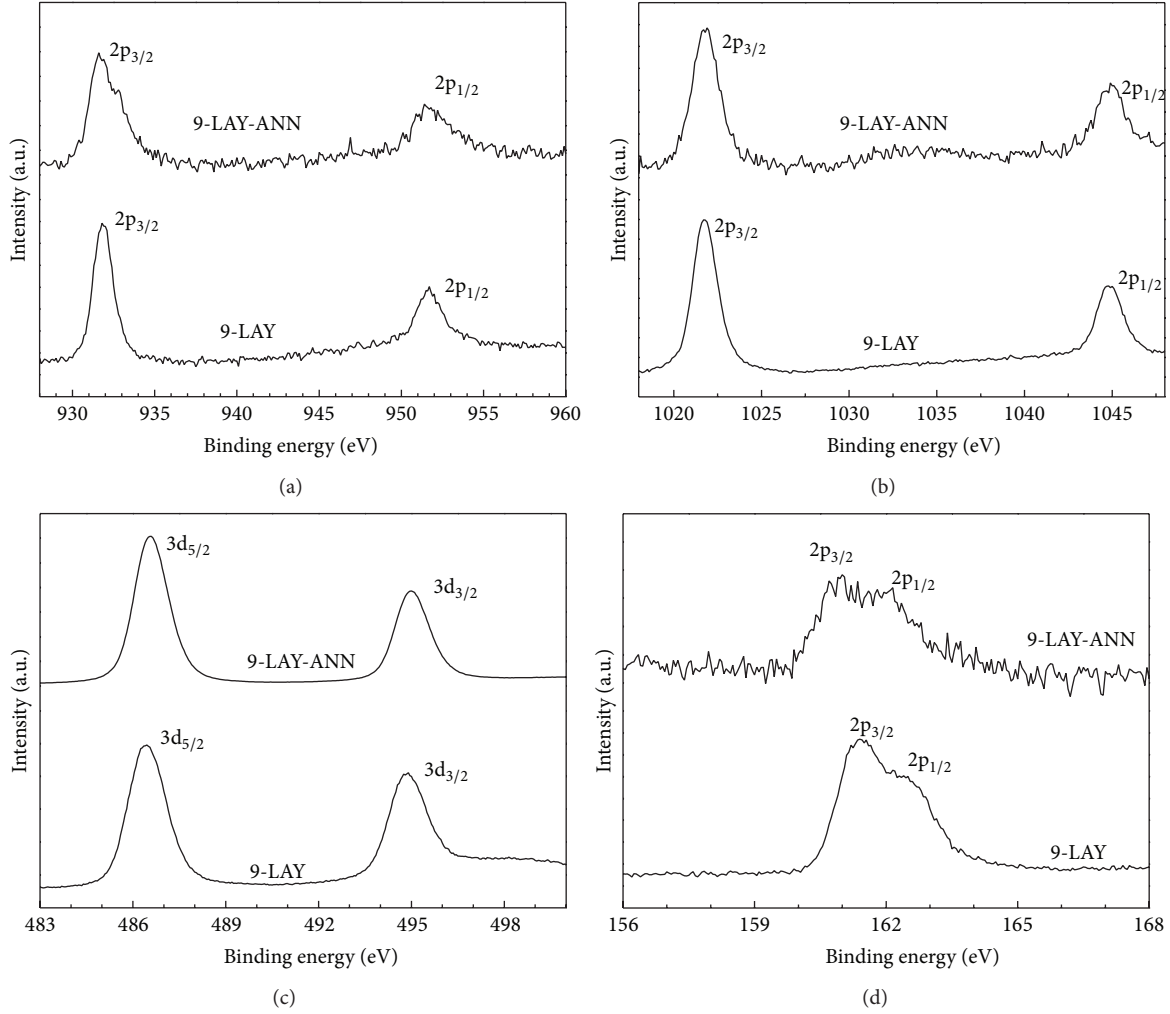


FIGURE 2: XPS spectra of 9-LAY and 9-LAY-ANN CZTS thin films: (a) Cu 2p, (b) Zn 2p, (c) Sn 3d, and (d) S 2p.

TABLE 2: Element binding energy values of CZTS films' XPS spectra.

Sample	Cu 2p _{3/2} (eV)	Cu 2p _{1/2} (eV)	Zn 2p _{3/2} (eV)	Zn 2p _{1/2} (eV)	Sn 3d _{5/2} (eV)	Sn 3d _{3/2} (eV)	S 2p _{3/2} (eV)	S 2p _{1/2} (eV)
9-LAY	932.0	951.4	1021.8	1044.7	486.5	494.9	161.5	163.0
9-LAY-ANN	931.7	951.7	1021.8	1044.9	486.6	495.0	161.0	162.5

Since the (112), (200), (220), and (312) peaks of $\text{Cu}_2\text{ZnSnS}_4$ XRD pattern are very close to the (111), (200), (220), and (311) of ZnS XRD pattern (JCPDS card 65-5476), it is necessary to identify further the phases by Raman spectroscopy [16]. The Raman spectrum of 9-LAY-ANN is presented in Figure 1(b). The $\text{Cu}_2\text{ZnSnS}_4$ Raman peaks are observed at 287 cm^{-1} and 338 cm^{-1} , while the ZnS Raman peak is not observed at 351 cm^{-1} , demonstrating a single-phase Kesterite CZTS.

XPS spectra of 9-LAY and 9-LAY-ANN CZTS thin films are shown in Figure 2. The element binding energy and the spin-orbit splitting values are listed in Tables 2 and 3, respectively, which are consistent with those reported in the literatures [3, 6, 17]. The almost same characteristics of XPS spectra between 9-LAY and 9-LAY-ANN demonstrate that

TABLE 3: Spin-orbit splitting values of CZTS films' XPS spectra.

Sample	Cu 2p (eV)	Zn 2p (eV)	Sn 3d (eV)	S 2p (eV)
9-LAY	19.4	22.9	8.4	1.5
9-LAY-ANN	20.0	23.1	8.4	1.5

the CZTS phase began to grow in the LBLSG process, which is consistent with XRD measurements, in which the broad and weak peaks of (112), (220), and (312) are observed for as-deposited samples.

The transmittance curves of the CZTS thin films are shown in Figure 3(a), and the Tauc curves calculated from the transmittance curves are shown in Figures 3(b)–3(e). The

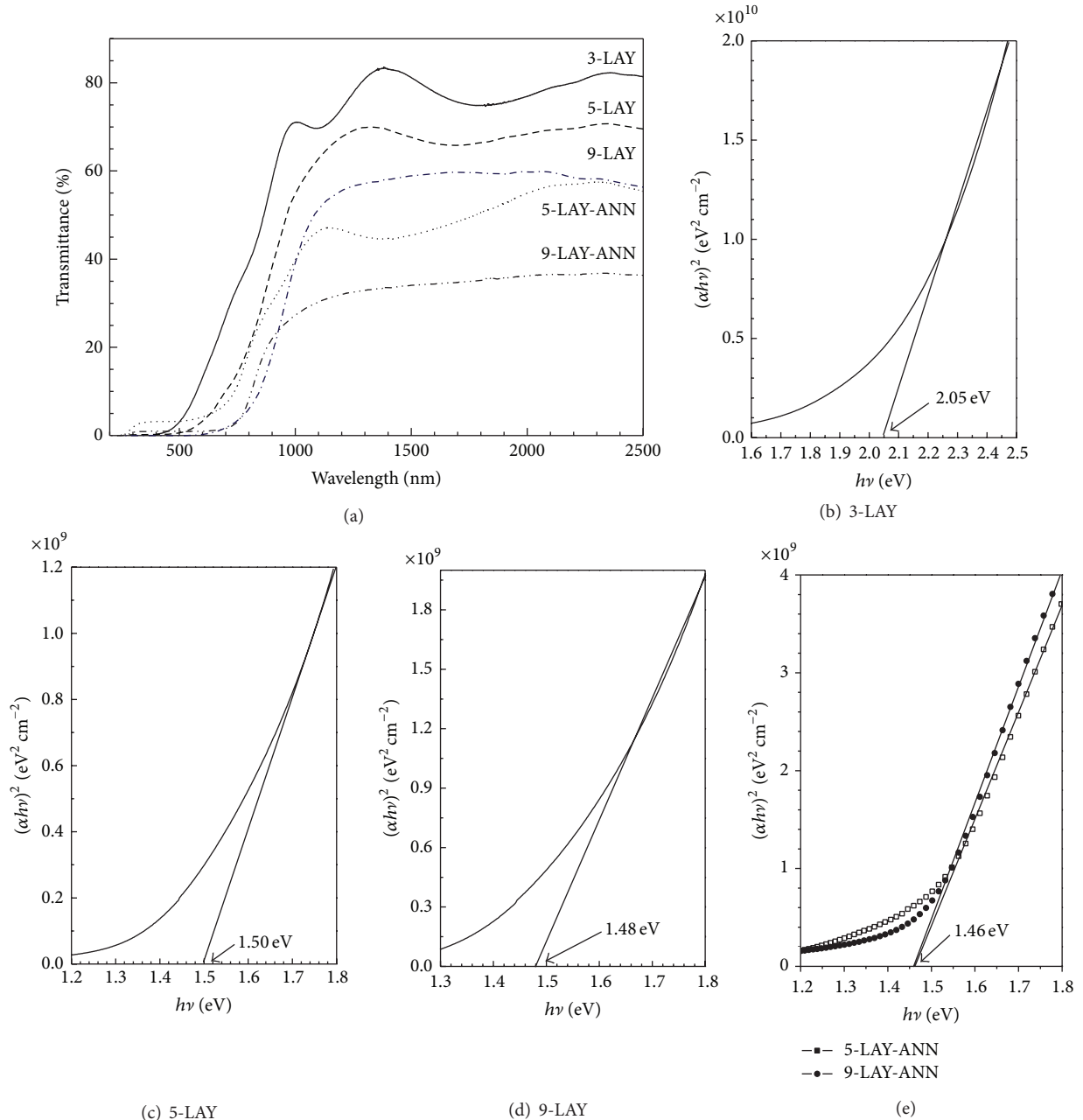


FIGURE 3: (a) Transmittances of CZTS films. (b)–(e) Tauc curves of CZTS films.

absorption band-edge blue shift of sample 3-LAY transmittance is observed compared with 5-LAY. And the absorption band-edge blue shift of sample 5-LAY transmittance is observed compared with 9-LAY. The absorption band-edge is dependent on the material energy band structure, which is determined by the atom arrangement and crystallization degree. So 9-LAY film should have higher crystallinity than 5-LAY and 3-LAY. The optic energy gap from Tauc curves are listed in Table 4. The annealed samples of 5-LAY-ANN and 9-LAY-ANN have lower optic energy band gap compared with the as-deposited samples of 5-LAY and 9-LAY, which

indicates that the annealed films present higher crystallinity. That is consistent with the XRD measurements.

Figure 4 shows SEM photographs concerning surface and cross section morphology of 9-LAY and 9-LAY-ANN CZTS films. There are no obvious grain characteristics for as-deposited 9-LAY film, while about 30 nm grains can be observed for the annealed 9-LAY-ANN film (see Figure 4). Besides, the as-deposited film is compact according to Figure 4(c), while the holes and bigger grains are observed for annealed film as shown in Figures 4(b) and 4(d). The region deposited by using the Lo-Con solution is more compact than

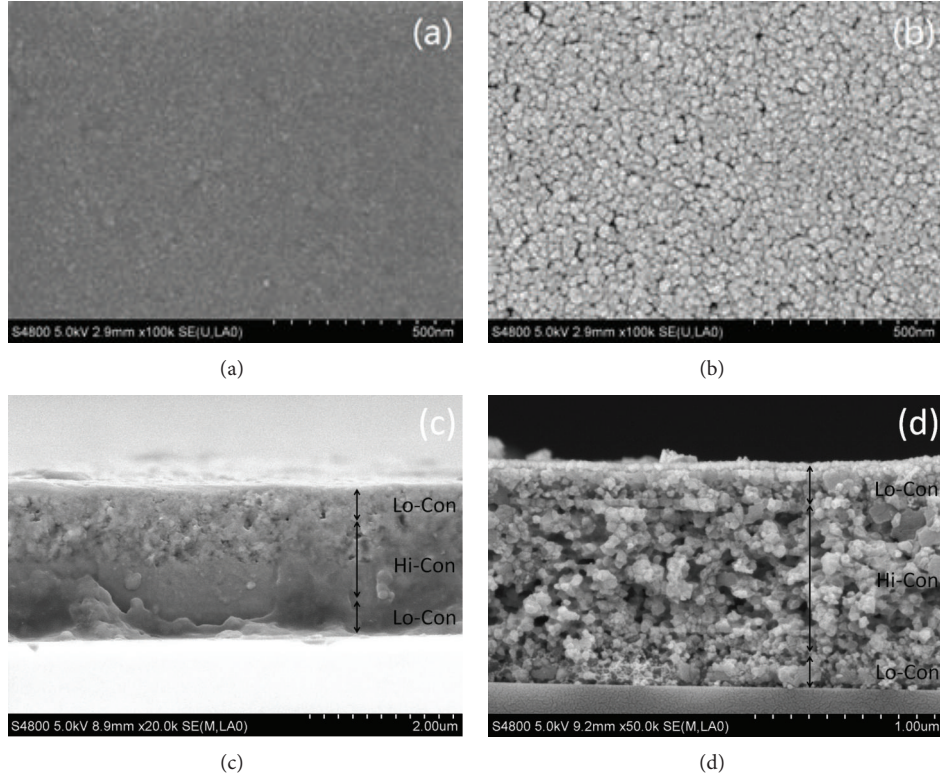


FIGURE 4: SEM photographs of CZTS films. (a) and (c) Surface and cross section of 9-LAY. (b) and (d) Surface and cross section of 9-LAY-ANN.

TABLE 4: Characterizations of the CZTS films.

Sample	Thickness (μm)	Sheet resistance (Ω/\square)	Conduction type	E_g (eV)
3-LAY	0.4	\	\	2.05
5-LAY	1.3	\	\	1.50
5-LAY-ANN	0.9	5.25×10^3	P	1.46
9-LAY	1.7	\	\	1.48
9-LAY-ANN	1.2	4.08×10^3	P	1.46

TABLE 5: The compositions of the CZTS thin films.

Sample	Cu%	Zn%	Sn%	S%	Cl%	Cu/(Zn + Sn)	Zn/Sn
9-LAY	19.44	15.11	10.64	46.44	8.37	0.75	1.41
9-LAY-ANN	23.49	16.04	12.35	48.12	\	0.83	1.30

that deposited by using the Hi-Con solution, as shown in Figures 4(c)-4(d).

Table 5 is the chemical compositions of CZTS films obtained by EDS measurement. There is Cl in the as-deposited sample, 9-LAY, but Cl is not detected from the annealed 9-LAY-ANN film. The ratio of S/(Cu + Zn + Sn) is 1.028 for 9-LAY and decreases to 0.928 after being annealed. The ratio of metal elements, Cu/(Zn + Sn) and Zn/Sn, is 0.83 and 1.30, respectively, for the annealed 9-LAY-ANN, which is Cu-poor and Zn-rich.

The as-deposited films did not demonstrate obvious conduction type and their sheet resistances were too high to be measured by four-probe test system. The sheet resistances of

5-LAY-ANN and 9-LAY-ANN are $5.25 \text{ k}\Omega/\square$ and $4.08 \text{ k}\Omega/\square$, respectively, and their resistivity is $4.725 \times 10^{-1} \Omega\text{-cm}$ and $4.896 \times 10^{-1} \Omega\text{-cm}$, respectively. The film crystallinity change and Cu-poor will promote the formation of copper vacancy in the annealing process, which is the reason that the conduction type and sheet resistance of the annealed films could be detected.

4. Conclusion

CZTS films were prepared by LBLSG technology without specific sulfurization. The CZTS phase began to form in

the LBLSG process. And the grains grew up to ~30 nm after being annealed. The optic energy gap is 1.50 eV for as-deposited film and is 1.46 eV after being annealed. The as-deposited and annealed films are both of Kesterite structure. The as-deposited films do not present obvious electric conduction type. However, the annealed film is p-type conduction and has sheet resistance of 4.08 k Ω / \square and resistivity of 4.896×10^{-1} Ω -cm for 9-LAY-ANN film. The region deposited by using Lo-Con solution was more compact than that by the Hi-Con solution from SEM morphology images.

Conflict of Interests

The authors declare that there is no conflict of interests regarding the publication of this paper.

Acknowledgments

This work was supported by the National High Technology Research and Development Program (no. 2011AA050515) and Sichuan Province Science and Technology Support Program (no. 2013GZX0145).

References

- [1] W. Shockley and H. J. Queisser, "Detailed balance limit of efficiency of p-n junction solar cells," *Journal of Applied Physics*, vol. 32, no. 3, pp. 510–519, 1961.
- [2] B. Shin, O. Gunawan, Y. Zhu, N. A. Bojarczuk, S. J. Chey, and S. Guha, "Thin film solar cell with 8.4% power conversion efficiency using an earth-abundant Cu₂ZnSnS₄ absorber," *Progress in Photovoltaics: Research and Applications*, vol. 21, no. 1, pp. 72–76, 2013.
- [3] F. Jiang, H. Shen, and W. Wang, "Optical and electrical properties of Cu₂ZnSnS₄ film prepared by sulfurization method," *Journal of Electronic Materials*, vol. 41, no. 8, pp. 2204–2209, 2012.
- [4] N. Muhunthan, O. P. Singh, S. Singh, and V. N. Singh, "Growth of CZTS thin films by cosputtering of metal targets and sulfurization in H₂S," *International Journal of Photoenergy*, vol. 2013, Article ID 752012, 7 pages, 2013.
- [5] X. Sheng, L. Wang, Y. Tian, Y. Luo, L. Chang, and D. Yang, "Low-cost fabrication of Cu₂ZnSnS₄ thin films for solar cell absorber layers," *Journal of Materials Science: Materials in Electronics*, vol. 24, no. 2, pp. 548–552, 2013.
- [6] W. Wang, H. Shen, F. Jiang, X. He, and Z. Yue, "Low-cost chemical fabrication of Cu₂ZnSnS₄ microparticles and film," *Journal of Materials Science: Materials in Electronics*, vol. 24, no. 6, pp. 1813–1817, 2013.
- [7] N. M. Shinde, C. D. Lokhande, J. H. Kim, and J. H. Moon, "Low cost and large area novel chemical synthesis of Cu₂ZnSnS₄ (CZTS) thin films," *Journal of Photochemistry and Photobiology A: Chemistry*, vol. 235, pp. 14–20, 2012.
- [8] M. Jeon, T. Shimizu, and S. Shingubara, "Cu₂ZnSnS₄ thin films and nanowires prepared by different single-step electrodeposition method in quaternary electrolyte," *Materials Letters*, vol. 65, no. 15–16, pp. 2364–2367, 2011.
- [9] K. Maeda, K. Tanaka, Y. Nakano, and H. Uchiki, "Annealing temperature dependence of properties of Cu₂ZnSnS₄ thin films prepared by sol-gel sulfurization method," *Japanese Journal of Applied Physics*, vol. 50, no. 5, Article ID 05FB08, 2011.
- [10] K. Tanaka, Y. Fukui, N. Moritake, and H. Uchiki, "Chemical composition dependence of morphological and optical properties of Cu₂ZnSnS₄ thin films deposited by sol-gel sulfurization and Cu₂ZnSnS₄ thin film solar cell efficiency," *Solar Energy Materials and Solar Cells*, vol. 95, no. 3, pp. 838–842, 2011.
- [11] P. K. Sarswat and M. L. Free, "Demonstration of a sol-gel synthesized bifacial CZTS photoelectrochemical cell," *Physica Status Solidi A*, vol. 208, no. 12, pp. 2861–2864, 2011.
- [12] K. Maeda, K. Tanaka, Y. Fukui, and H. Uchiki, "Influence of H₂S concentration on the properties of Cu₂ZnSnS₄ thin films and solar cells prepared by sol-gel sulfurization," *Solar Energy Materials and Solar Cells*, vol. 95, no. 10, pp. 2855–2860, 2011.
- [13] K. Tanaka, N. Moritake, and H. Uchiki, "Preparation of Cu₂ZnSnS₄ thin films by sulfurizing sol-gel deposited precursors," *Solar Energy Materials & Solar Cells*, vol. 91, no. 13, pp. 1199–1201, 2007.
- [14] M. Y. Yeh, C. C. Lee, and D. S. Wu, "Influences of synthesizing temperatures on the properties of Cu₂ZnSnS₄ prepared by sol-gel spin-coated deposition," *Journal of Sol-Gel Science and Technology*, vol. 52, no. 1, pp. 65–68, 2009.
- [15] H. Park, Y. H. Hwang, and B. Bae, "Sol-gel processed Cu₂ZnSnS₄ thin films for a photovoltaic absorber layer without sulfurization," *Journal of Sol-Gel Science and Technology*, vol. 65, no. 1, pp. 23–27, 2013.
- [16] A. Nagaoka, K. Yoshino, H. Taniguchi, T. Taniyama, and H. Miyake, "Preparation of Cu₂ZnSnS₄ single crystals from Sn solutions," *Journal of Crystal Growth*, vol. 341, no. 1, pp. 38–41, 2012.
- [17] W. Liu, B. Guo, C. Mak, A. Li, X. Wu, and F. Zhang, "Facile synthesis of ultrafine Cu₂ZnSnS₄ nanocrystals by hydrothermal method for use in solar cells," *Thin Solid Films*, vol. 535, no. 1, pp. 39–43, 2013.

Research Article

Device Modeling of the Performance of Cu(In,Ga)Se₂ Solar Cells with V-Shaped Bandgap Profiles

Shou-Yi Kuo,¹ Ming-Yang Hsieh,¹ Dan-Hua Hsieh,^{2,3} Hao-Chung Kuo,²
Chyong-Hua Chen,² and Fang-I Lai^{3,4}

¹ Department of Electronic Engineering, Chang Gung University, 259 Wen-Hwa 1st Road, Kwei-Shan, Taoyuan 333, Taiwan

² Department of Photonics and Institute of Electro-Optical Engineering, National Chiao-Tung University, 1001 Ta Hsueh Road, Hsinchu 30013, Taiwan

³ Department of Photonics Engineering, Yuan-Ze University, 135 Yuan-Tung Road, Chung-Li 32003, Taiwan

⁴ Advanced Optoelectronic Technology Center, National Cheng Kung University, No. 1 University Road, Tainan 701, Taiwan

Correspondence should be addressed to Fang-I Lai; filai@saturn.yzu.edu.tw

Received 10 December 2013; Revised 3 May 2014; Accepted 6 May 2014; Published 14 July 2014

Academic Editor: Prakash Basnyat

Copyright © 2014 Shou-Yi Kuo et al. This is an open access article distributed under the Creative Commons Attribution License, which permits unrestricted use, distribution, and reproduction in any medium, provided the original work is properly cited.

The effect of Cu(In,Ga)Se₂ (CIGS) with V-shaped bandgap on device performance is investigated in detail. A series of Ga/(In+Ga) ratio are set to study the influence of V-shaped bandgap profile on the electricity of CIGS thin film solar cells. The modeling of device current density-voltage (J-V) curve and bandgap grading profile corresponded well to measurement results. Detailed characteristic and modeling results show that an increased gradient of bandgap from valley to the buffer layer CdS will result in a barrier and lead to an enhanced recombination in the valley. This phenomenon can be modified by the back electric field resulting from a gradient bandgap from valley (bandgap minimum) to the Mo back contact. These results indicate CIGS-based solar cells can achieve higher performance by optimizing the V-shaped bandgap profile.

1. Introduction

Nowadays, it is an important issue to improve the conversion efficiency of thin-film solar cells. Impressively, the record conversion efficiency of thin-film Cu(In,Ga)Se₂-based solar cells are to date over 20% [1]. The major advantage of the CIGS-based solar cell is that the quaternary material system can attain a variable bandgap energy and lattice parameters by varying the Ga/(In+Ga) ratio [2]. Chalcopyrite CIGS is reported to have an adjustable bandgap from 1.01 eV (CIS) to 1.636 eV (CGS) by changing the gallium content from 0 to 1 [3]. However, only the position of the conduction-band edge will be affected when changing the CIGS bandgap [4, 5]. The latest reported high efficiency CIGS solar cell uses three- or multistage evaporation processes to prepare CIGS absorber layer with a double-graded bandgap profile, a higher gallium content towards the back and the front of the CIGS absorber layer, and a notch of low gallium content in between [6]. From the other earlier research, the influence of the decreasing of

gallium content from the buffer layer towards the notch of the absorber can enhance the electrons generated within the space-charge region [7]. Furthermore, the potential benefit of the Ga content increases from notch towards the back contact induces a back-surface field in the conduction band, which causes electrons to drift away from the rear contact and thereby reduces the recombination at the back contact [8]. As mentioned above, it is an excellent method to provide a variable bandgap of CIGS and obtain higher open circuit voltage and efficiency by using gallium to replace partial of indium.

However, it is hard to understand the benefits and effects of “grading” by studying the actual devices. Therefore, in order to understand how “grading” can improve cell performance, a novel approach is to use numerical modeling [9, 10]. In this paper, we investigate the influence of the Ga content numerically in the CIGS solar cells by modeling and device simulation. The amount of Ga doping is fixed in order to avoid the influence of open-circuit voltage by different

TABLE 1: Base parameters for CIGS numerical model.

	AZO	i-ZnO	CdS	CIGS
Thickness (nm)	500	50	50	2000
ϵ	9	9	10	13.6
μ_n (cm ² /Vs)	50	50	10	300
μ_p (cm ² /Vs)	5	5	1	30
N_A (1/cm ³)	0	0	0	$8.E + 16$
N_D (1/cm ³)	$1.E + 20$	$1.E + 17$	$5.2E + 16$	0
E_g (eV)	3.3	3.3	2.4	grading
χ (eV)	4	4	3.75	3.89

ϵ , dielectric constant; μ_n , electron mobility; μ_p , hole mobility; N_A , effective density of states in conduction band; N_D , effective density of states in valence band; E_g , bandgap energy; χ , electron affinity.

gallium content, and we introduce different distributions in absorber layer to analyze and investigate the effect of different type of gradient bandgap.

2. Simulation

The device characteristics of the CIGS solar cells are studied numerically using the APSYS simulation program, which was developed by Crosslight Software Inc. [11]. The APSYS simulation program can deal with electrical properties by solving several interwoven equations including the basic Poisson's equation, drift-diffusion equations, photon rate equation, and scalar wave equation. To investigate the effect of bandgap grading in a CIGS solar cell, physical parameters of CIGS solar cells needed for electrical modeling are obtained from measurements and earlier literatures to construct the accurate model [12–14]. Table 1 lists the parameters used in the numerical model. In the simulation, the model consists of several layers including 500-nm-thick AZO transparent conductive oxide layer, 50-nm-thick intrinsic ZnO layer, 50-nm-thick CdS buffer layer, and 2- μ m-thick CIGS absorber layer. All simulations have been performed under an AM 1.5G light spectrum.

From the previous reports, the bandgap grading is dependent on the Ga composition, and the variation of the Ga/(In+Ga) ratio, x , will affect the value of bandgap. The relation between Ga/(In+Ga) ratio and bandgap can be described by the following formula:

$$E_g^{\text{CIGS}} = E_g^{\text{CIS}} (1 - X) + X E_g^{\text{CGS}} - bX(1 - X), \quad (1)$$

where $E_g^{\text{CIS}} = 1.01$ eV, $E_g^{\text{CGS}} = 1.636$ eV, $b = 0.167$ eV, and the modeling reference of Ga grading profile was obtained from secondary ion mass spectroscopy (SIMS) data [15, 16].

In order to confirm the validity of our model, the results of numerical analysis are compared with device measurement. Afterward two different types of absorber layer are discussed in detail. In the first type, we fix the Ga doping and vary bandgap notch depth (minimum bandgap). Whereas, the second type keeps bandgap notch depth unchanged but with different front grading (linear variation from notch increase towards the front side). After that, the electrical properties

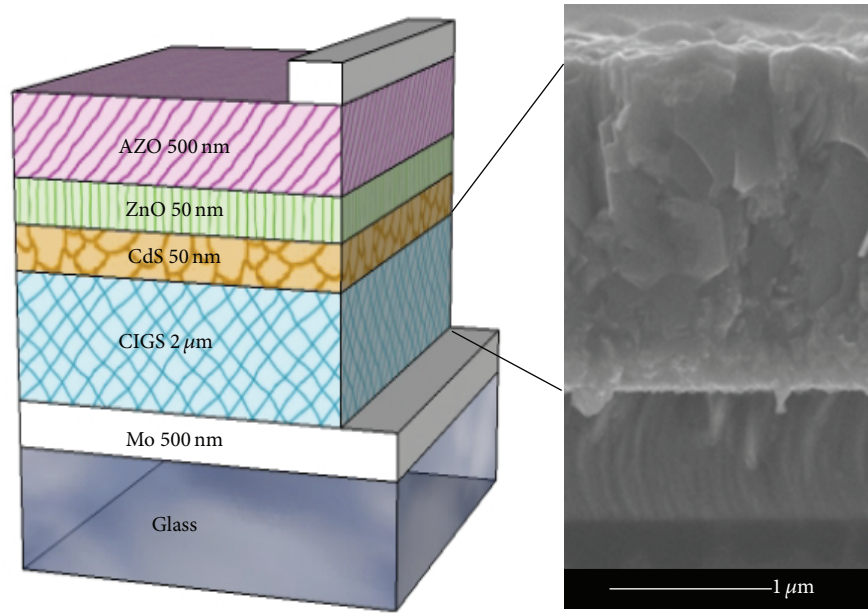
such as current density-voltage (J-V) curves, electric field intensity, and recombination intensity are investigated.

3. Results and Discussion

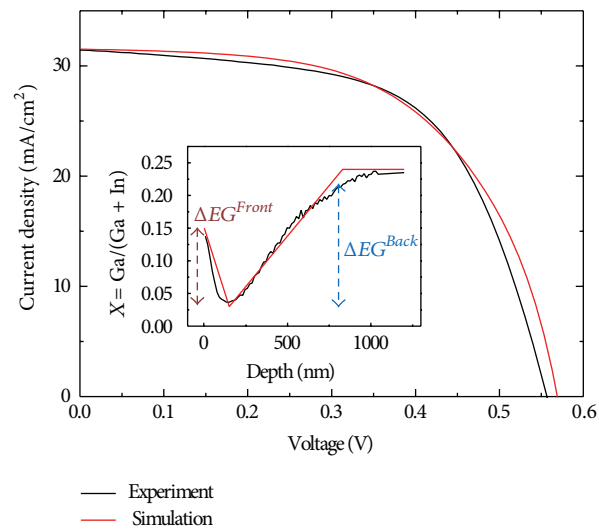
The cell structure and cross-sectional scanning electron microscopy (SEM) photographs of typical CIGS/Mo structure fabricated on Mo-coated soda-lime glass substrate are shown in Figure 1(a). SEM images show a reduction in grain size with increasing Ga content from top to bottom of absorber layer, which agrees well with the results by other groups [17]. In Figure 1(b), the J-V curve from simulation is compared with experimental data, and inset shows the bandgap grading (Ga content) in absorber layer. From SIMS measurement result, one can find that bandgap shows a “V”-shaped grading (see inset in Figure 1(b)) with the minimum gap locating at 150 nm from the CdS/CIGS surface (located at $x = 0$ nm). All measurements and simulations are set under room temperature. At the same time, the simulation of J-V curve with V-shaped grading is corresponding well to measurements. This result indicates that the baseline parameters used in the model are in line with the physical properties of actual device.

It has been well known that Ga doping will not only change the CIGS bandgap but also obtain different open circuit voltage. The parameters are shown in Table 2. Therefore, in the simulation, we compare the samples with same amount of Ga contents in the absorber layer but different minimum bandgap in a distance of 150 nm from the CdS/CIGS surface as shown in inset of Figure 2(a). In addition, we also take the case with no V-shaped grading into consideration. The inset of Figure 1(b) shows the difference between the bandgap minimum and maximum close to the back contact and CdS buffer layer, which is defined as ΔE_g^{Back} and $\Delta E_g^{\text{Front}}$, respectively. From Figure 2(a), the fill factor of photovoltaic device will increase as the depth of valley (minimum gap) in the absorber layer increases. As expected, more recombination might happen in the valley when the valley became deeper. Simultaneously, a stronger electric field is created to provide the carriers more energy to drift out the space charge region (SCR) as the ΔE_g^{Back} becomes larger as shown in Figure 2(b). In this way, the carrier collection will be increased and also the fill factor. From these results we can speculate that the positive ΔE_g^{BF} ($\Delta E_g^{\text{BF}} = \Delta E_g^{\text{Back}} - \Delta E_g^{\text{Front}}$) can reduce the recombination in the valley of absorber layer.

The effect of a $\Delta E_g^{\text{Front}}$ has been studied by many groups. Dullweber et al. [18] have observed that the slight increasing of Ga content in the front of the absorbers can not only enhance the electrons generated but also reduce SCR recombination. However, the Ga content increased strongly in the front of the absorber layer will cause a barrier for electrons. In Figure 3, the recombination intensity corresponding to five kinds of bandgap with different V-shaped grading has been investigated, the inset (a) and (b) show different type profile of the bandgap shape with different depth of bandgap minimum and $\Delta E_g^{\text{Front}}$, respectively. Due to the fact that the



(a)



(b)

FIGURE 1: (a) Cell structure and cross-sectional SEM photographs of a CIGS/Mo solar cell fabricated on Mo-coated soda-lime glass substrate. (b) Simulation result from device modeling with baseline parameters including a grading bandgap compared with experimental J-V curve and SIMS data.

TABLE 2: Photovoltaic parameters of different sample of CIGS solar cells.

Samples	V_{oc} (V)	J_{sc} (mA/cm ²)	F.F.	η (%)	Ga/(Ga + In)	
					$X = 0 \mu\text{m}$	$X = 0.15 \mu\text{m}$
Flat	0.55	28.77	0.45	7.15	0.19	0.19
A	0.56	31.42	0.59	10.43	0.15	0
B	0.56	31.51	0.59	10.33	0.15	0.03
C	0.56	31.57	0.55	9.72	0.15	0.1
D	0.57	31.57	0.49	8.78	0.25	0.03
E	0.57	31.43	0.42	7.46	0.35	0.03

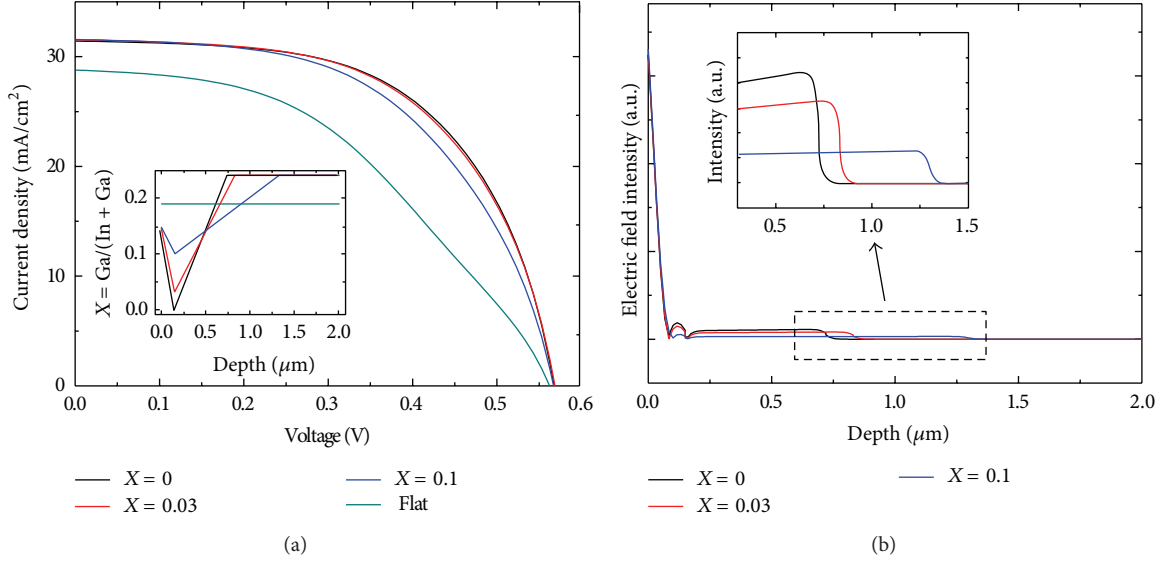


FIGURE 2: (a) Current density-voltage curves and (b) electric field intensity of CIGS cells with different bandgap grading profiles taken under illumination with an intensity of 1 sun at room temperature (300 K).

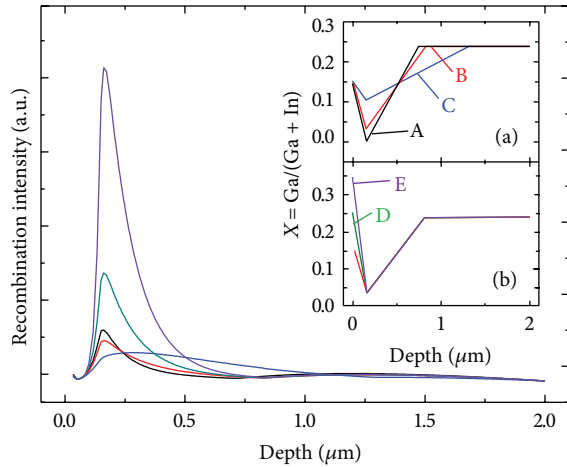


FIGURE 3: Recombination intensity of CIGS cells with different bandgap grading profiles taken under illumination with an intensity of 1 sun at 193 K.

thermal energy in room temperature will cause the electrons to overcome it [19], the environmental temperature is set at 193 K in this simulation.

In the varied-notch depth cases, although the recombination intensity is stronger in the deeper notch situation, the ΔE_g^{Back} is also increased and provides a higher electric field for carriers to overcome the barrier, hence resulting in lower recombination intensity. In the $\Delta E_g^{\text{Front}}$ cases, larger slope will build up a higher barrier and cause the carriers to be localized in the valley to release energy via radiative recombination. In conclusion, there is an inversely proportional relation between the electric field intensity and recombination intensity. The higher electric field intensity

and lower $\Delta E_g^{\text{Front}}$ will cause a lower recombination in the valley. In addition, as the ΔE_g^{BF} is positive, the recombination intensity is larger than that of the negative ΔE_g^{BF} , which agrees with our speculation. In order to illustrate the observed blocking behavior, the band diagrams of grading profiles are shown in Figure 4.

In Figure 4, the diagram describes the influence of ΔE_g^{BF} clearly. In the Figure 4(a), the ΔE_g^{Back} is larger than $\Delta E_g^{\text{Front}}$ (positive ΔE_g^{BF}); ΔE_g^{Back} can produce an inner electric field to repel photo-induced electrons reach the backside, thereby reducing the back-surface recombination velocity. However, as Figure 4(b), the $\Delta E_g^{\text{Front}}$ is larger than ΔE_g^{Back} (negative ΔE_g^{BF}); the inner electric field cannot give enough energy to electrons to reach CdS n-type layer. Therefore, the valley in the conduction band will trap the electrons and lead to an enhanced recombination velocity with the holes in the valence band which reduces the extraction of electricity.

4. Conclusion

In summary, we have developed a well-established model to study the CIGS solar cells with various bandgap absorber layers, and the results are corresponding well to actual device measurements. The simulation results show that a positive ΔE_g^{BF} can bring out an inner electric field to reduce back-surface recombination velocity and overcome the front barrier built up by $\Delta E_g^{\text{Front}}$. On the contrary, the negative ΔE_g^{BF} will generate a barrier between CdS and CIGS layer, and the minority carriers (electrons) will be trapped in the valley easier and lead to low device conversion efficiency. In the future, this model can be adopted to optimize the bandgap grading type and fabricate high conversion efficiency CIGS-based thin film solar cell.

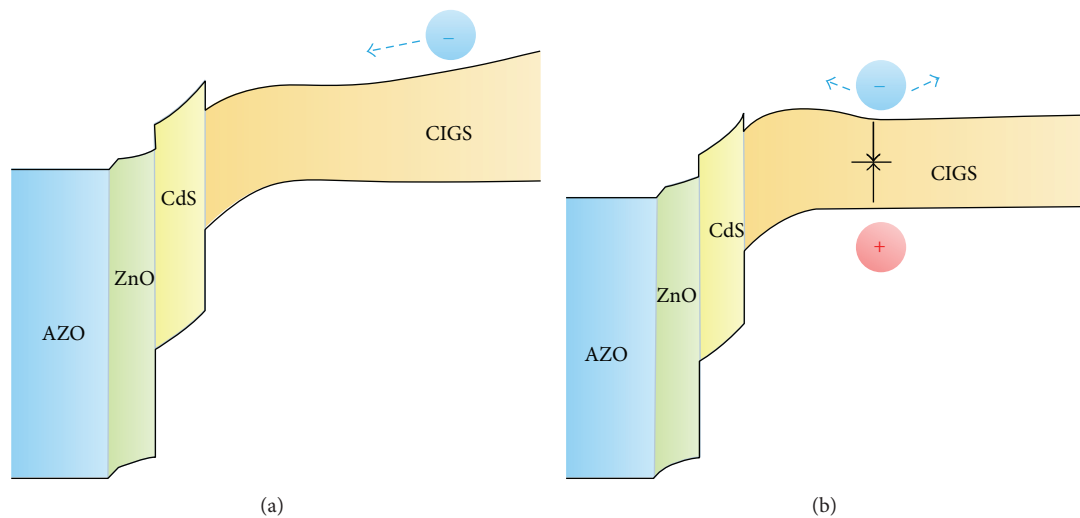


FIGURE 4: The band diagrams of CIGS solar cells with the cases (a) positive ΔE_g^{BF} and (b) negative ΔE_g^{BF} .

Conflict of Interests

The authors declare that there is no conflict of interests regarding the publication of this paper.

Acknowledgments

This work was supported by the Green Technology Research Center of Chang Gung University and the National Science Council (NSC) of Taiwan under contract nos. NSC100-2815-C-155-013-E, NSC100-2112-M-182-004, and NSC101-2112-M-182-003-MY3.

References

- [1] O. Lupan, S. Shishiyanu, V. Ursaki et al., "Synthesis of nanostructured Al-doped zinc oxide films on Si for solar cells applications," *Solar Energy Materials and Solar Cells*, vol. 93, no. 8, pp. 1417–1422, 2009.
- [2] M. Edoff, S. Woldegiorgis, P. Neretnieks, M. Ruth, J. Kessler, and L. Stolt, "CIGS submodules with high performance and high manufacturability," in *Proceedings of the 19th European Photovoltaic Solar Energy Conference*, p. 1690, Paris, France, June 2004.
- [3] B. Dimmler, H. Dittrich, R. Menner, and H. W. Schock, "Performance and optimization of heterojunctions based on $\text{Cu}(\text{Ga},\text{In})\text{Se}_2$," in *Proceedings of the 19th IEEE Photovoltaic Specialists Conference*, IEEE, New Orleans, La, USA, May 1987.
- [4] S. H. Wei, S. B. Zang, and A. Zunger, "Effects of Ga addition to on its electronic, structural, and defect properties," *Applied Physics Letters*, vol. 72, p. 3199, 1998.
- [5] A. Rockett, F. Abou-Elfotouh, D. Albin et al., "Structure and chemistry of CuInSe_2 for solar cell technology: current understanding and recommendations," *Thin Solid Films*, vol. 237, no. 1-2, pp. 1–11, 1994.
- [6] M. Contreras, J. Tuttle, D. Du, Y. Qi, A. Swartzlander, and A. Tennant, "Graded band-gap $\text{Cu}(\text{In},\text{Ga})\text{Se}_2$ thin-film solar cell absorber with enhanced open-circuit voltage," *Applied Physics Letters*, vol. 63, pp. 1824–1826, 1993.
- [7] S. Schleussner, U. Zimmermann, T. Wätjen, K. Leifer, and M. Edoff, "Effect of gallium grading in $\text{Cu}(\text{In},\text{Ga})\text{Se}_2$ solar-cell absorbers produced by multi-stage coevaporation," *Solar Energy Materials and Solar Cells*, vol. 95, pp. 721–726, 2011.
- [8] T. Dullweber, O. Lundberg, J. Malmström et al., "Back surface band gap gradings in $\text{Cu}(\text{In},\text{Ga})\text{Se}_2$ solar cells," *Thin Solid Films*, vol. 387, no. 1-2, pp. 11–13, 2001.
- [9] Y. Hirai, Y. Kurokawa, and A. Yamada, "Numerical study of $\text{Cu}(\text{In},\text{Ga})\text{Se}_2$ solar cell performance toward 23% conversion efficiency," *Japanese Journal of Applied Physics*, vol. 53, Article ID 012301, 2014.
- [10] J. Song, S. S. Li, C. H. Huang, O. D. Crisalle, and T. J. Anderson, "Device modeling and simulation of the performance of $\text{Cu}(\text{In}_{1-x}\text{Ga}_x)\text{Se}_2$ solar cells," *Solid-State Electronics*, vol. 48, no. 1, pp. 73–79, 2004.
- [11] "APSYS by Crosslight Software Inc., Burnaby, Canada," <http://www.crosslight.com>.
- [12] S. Y. Kuo, M. Y. Hsieh, F. I. Lai, Y. K. Liao, M. H. Kao, and H. C. Kuo, "Modeling and optimization of sub-wavelength grating nanostructures on $\text{Cu}(\text{In},\text{Ga})\text{Se}_2$ solar cell," *Japanese Journal of Applied Physics*, vol. 51, Article ID 10NC14, 2012.
- [13] M.-Y. Hsieh, S.-Y. Kuo, H.-V. Han et al., "Enhanced broadband and omnidirectional performance of $\text{Cu}(\text{In},\text{Ga})\text{Se}_2$ solar cells with ZnO functional nanotree arrays," *Nanoscale*, vol. 5, no. 9, pp. 3841–3846, 2013.
- [14] S.-Y. Kuo, M.-Y. Hsieh, H.-V. Han et al., "Dandelion-shaped nanostructures for enhancing omnidirectional photovoltaic performance," *Nanoscale*, vol. 5, no. 10, pp. 4270–4276, 2013.
- [15] M. I. Alonso, M. Garriga, C. A. Durante Rincón, E. Hernández, and M. León, "Optical functions of chalcopyrite $\text{CuGa}_x\text{In}_{1-x}\text{Se}_2$ alloys," *Applied Physics A*, vol. 74, pp. 659–664, 2002.
- [16] W. N. Shafarman and L. Stolt, " $\text{Cu}(\text{In},\text{Ga})\text{Se}_2$ solar cells," in *Handbook of Photovoltaic Science and Engineering*, A. Luque and S. Hegedus, Eds., p. 567, JohnWiley & Sons, Chichester, UK, 2003.
- [17] R. Kaigawa, A. Ohya, T. Wada, and R. Klenk, "Electrical properties of homogeneous $\text{Cu}(\text{In},\text{Ga})\text{S}_2$ films with varied gallium content," *Thin Solid Films*, vol. 515, no. 15, pp. 6260–6264, 2007.

- [18] T. Dullweber, G. Hanna, U. Rau, and H. W. Schock, "A new approach to high-efficiency solar cells by band gap grading in Cu(In, Ga)Se₂ chalcopyrite semiconductors," *Solar Energy Materials and Solar Cells*, vol. 67, no. 1–4, pp. 145–150, 2001.
- [19] U. Rau and H. W. Schock, "Electronic properties of Cu(In,Ga)Se₂ heterojunction solar cells-recent achievements, current understanding, and future challenges," *Applied Physics A*, vol. 69, pp. 131–147, 1999.

Research Article

Novel Terthiophene-Substituted Fullerene Derivatives as Easily Accessible Acceptor Molecules for Bulk-Heterojunction Polymer Solar Cells

Filippo Nisic,¹ Alessia Colombo,¹ Claudia Dragonetti,¹ Alessandra Cominetti,²
Andrea Pellegrino,² Nicola Perin,² Riccardo Po,² and Alessandra Tacca²

¹ Department of Chemistry, University of Milan, UdR dell'INSTM, Via Golgi 19, 20133 Milan, Italy

² Research Center for Non-Conventional Energies, "Istituto Eni Donegani," Eni S.p.A., Via Fauser 4, 28100 Novara, Italy

Correspondence should be addressed to Alessia Colombo; alessia.colombo@unimi.it and
Andrea Pellegrino; andrea.pellegrino@eni.com

Received 26 March 2014; Accepted 8 June 2014; Published 10 July 2014

Academic Editor: Przemyslaw Rupnowski

Copyright © 2014 Filippo Nisic et al. This is an open access article distributed under the Creative Commons Attribution License, which permits unrestricted use, distribution, and reproduction in any medium, provided the original work is properly cited.

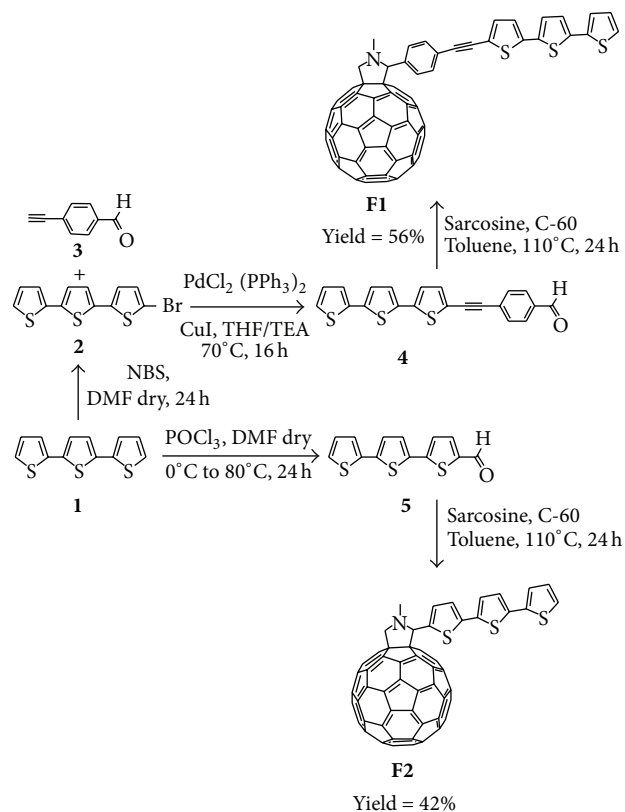
Five fulleropyrrolidines and methanofullerenes, bearing one or two terthiophene moieties, have been prepared in a convenient way and well characterized. These novel fullerene derivatives are characterized by good solubility and by better harvesting of the solar radiation with respect to traditional PCBM. In addition, they have a relatively high LUMO level and a low band gap that can be easily tuned by an adequate design of the link between the fullerene and the terthiophene. Preliminary results show that they are potential acceptors for the creation of efficient bulk-heterojunction solar cells based on donor polymers containing thiophene units.

1. Introduction

The use of renewable energy sources instead of fossil fuel is a necessity for humanity. The Sun is a green and cheap source of energy: 10 minutes of solar irradiation onto the Earth's surface is equal to the total yearly human energy consumption [1, 2]. The world energy challenge can be won harnessing the Sun power with photovoltaic technologies. Organic photovoltaic devices (OPVs) based on conjugated polymers and oligomers have received a lot of attention because of their potential for lightweight, flexible, and low cost photovoltaic energy conversion [3–7]. Among them, the most common devices are bulk-heterojunction (BHJ) polymer solar cells made upon blending an electron donor conjugated polymer with an electron acceptor material such as fullerene derivatives [3–7]. Fullerene-based OPV can be fabricated via vapor deposition; however, considering the expected demand for enhancing cost performance by mass production in the near future, application of roll-to-roll processing (i.e., the solvent casting method) appears highly desirable [8]. Therefore, development of stable fullerene derivatives that show both high

power conversion efficiency and sufficient solubility in organic solvents is strongly desired [3–7]. Various types of fullerene derivatives for use as OPV acceptor materials have thus been developed. [6, 6]-Phenyl-C61-butyric acid methyl ester (PCBM) [9, 10] is known to be the best blending material among these derivatives as an acceptor with polythiophenes such as regioregular poly(3-hexylthiophene) (P3HT), which is a typical donor partner in polymer solar cells [3–7].

Although PCBM is the most popular acceptor material so far for BHJ polymer solar cells, it is important to explore new easily accessible C60 derivatives as acceptor partners for polymer donor materials with a huge diversity of chemical structures. Many efforts have been devoted to the modification of the PCBM skeleton by introducing substituents on the phenyl ring, exchanging methyl groups with long alkyl chains, an ethyleneoxy moiety, or a perfluoroalkyl chain to tune the miscibility, thermal properties, and energy levels, and the resulting methanofullerene derivatives have been used to control the film morphology, raise the open circuit voltage (V_{oc}), and improve the device stability [11–17]. A few years ago, a PCBM analogue containing a thiophene moiety,



SCHEME 1: Synthesis of F1 and F2.

[6, 6]-thienyl-C61-butyric acid methyl ester (TCBM), has been reported to exhibit device performance close to PCBM with P3HT as the donor [11–17]. A series of TCBM analogues with different alkyl chains (methyl, hexyl, and ethylhexyl) at the 5 positions of the thiophene ring was then prepared [18]. Like methanofullerenes, fulleropyrrolidines are efficient acceptors for OPV devices and, recently, it was established that the introduction of a thiophene moiety on the pyrrolidine ring has a favorable effect on the power conversion energy (PCE) of a solar cell [19]. It was reported that 1-(2-(2-methoxyethoxy)ethyl)-2-(2-thiophen-2-yl)fulleropyrrolidine and related derivatives with bithiophene or terthiophene are efficient acceptor partners with P3HT, the compound bearing terthiophene being characterized by the highest V_{oc} but lower fill factor (FF) and short circuit current (J_{sc}) due to reduced solubility when compared to the mono- and bithiophene derivatives [19]. In fact the solubility of a fullerene derivative strongly affects the morphology of its composite with P3HT and therefore the efficiency of the cell [20, 21]. These interesting results prompted us to design novel soluble terthiophene-substituted fullerene derivatives as easily accessible acceptor molecules for BHJ polymer solar cells (Scheme 1). We prepared both terthiophene-substituted fulleropyrrolidines (**F1–F3**) and methanofullerenes (**F4–F5**), with the aim of obtaining soluble acceptor materials with a good affinity for donor polymers based on thiophene units (Figure 1). As our work was in progress, as expected, it was reported by Saravanan et al. that **F2** is a better electron

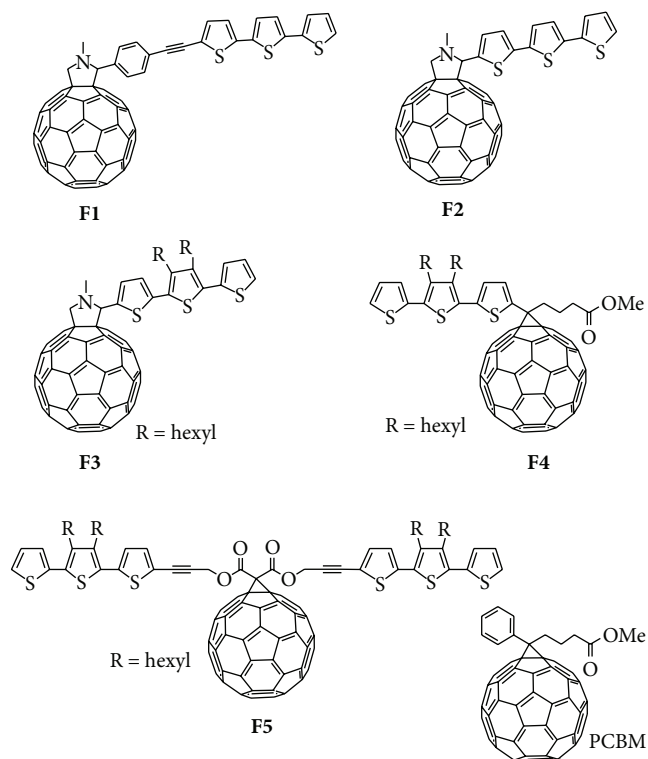


FIGURE 1: Terthiophene-substituted fullerene derivatives studied in the present work.

acceptor than PCBM for the fabrication of P3HT based bulk-heterojunction solar cells [22].

2. Materials and Methods

General Comments. Solvents were dried by standard procedures: tetrahydrofuran (THF) and toluene were freshly distilled from Na/benzophenone under nitrogen atmosphere; *N,N*-dimethylformamide (DMF) was dried over activated molecular sieves; triethylamine (Et_3N) was freshly distilled over KOH. All reagents were purchased from Sigma-Aldrich and were used without further purification (2,2':5',2''-terthiophene 99% purity, fullerene- C_{60} 99.5% purity, and 4-[(trimethylsilyl)ethynyl] benzaldehyde 97% purity). Reactions requiring anhydrous conditions were performed under nitrogen. ^1H and ^{13}C NMR spectra were recorded at 400 MHz on a Bruker AVANCE-400 instrument. Chemical shifts (δ) for ^1H and ^{13}C spectra are expressed in ppm relative to internal Me_4Si as standard. Signals were abbreviated as follows: *s*: singlet; *bs*: broad singlet; *d*: doublet; *t*: triplet; *q*: quartet; *m*: multiplet. Mass spectra were obtained by FT-ICR Mass Spectrometer APEX II & Xmass software (Bruker Daltonics) and 4.7 Magnet and Autospec Fission Spectrometer (FAB ionization). MALDI-TOF mass spectra were obtained using a MICROFLEX LT (Bruker) with dithranol (DHB) or *trans*-2-[3-(4-*tert*-Butylphenyl)-2-methyl-2-propenyldiene]malononitrile (DCTB) as matrix. Absorption spectra were recorded at room temperature with a Perkin-Elmer Lambda 950 spectrophotometer. Samples were

prepared by dissolving the compounds in chlorobenzene solutions in cell with 10 mm optical path length. Thin layer chromatography (TLC) was carried out with precoated Merck F₂₅₄ silica gel plates whereas flash chromatography (FC) was carried out with Macherey-Nagel silica gel 60 (230–400 mesh).

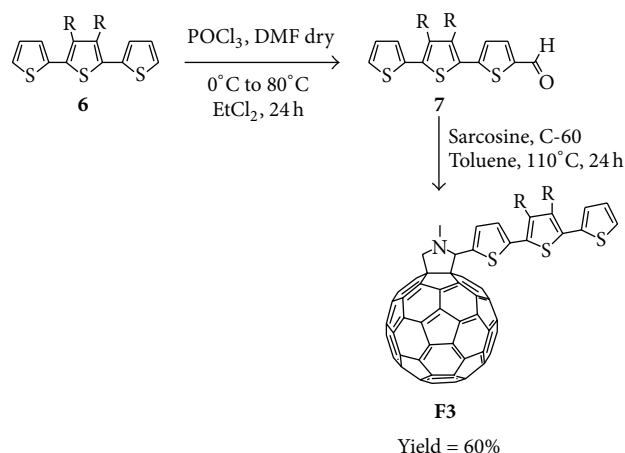
2.1. Preparation of Fullerene Derivatives F1–F3. Fullerenes **F1** and **F2** were prepared according to Scheme 1, by using compounds 1–5 as intermediates, whereas **F3** was prepared according to Scheme 2 with compounds 6 and 7 as intermediates.

2.2. Synthesis of Compound 2. Compound 2 was prepared as reported in the literature [23]. Under a nitrogen atmosphere, *N*-bromosuccinimide (NBS) (176.3 mg, 0.99 mmol, 1 equiv.) was added in small portions to a solution of commercial 2,2':5',2''-terthiophene (**1**) (245.7 mg, 0.99 mmol, 1 equiv.) in *N,N*-dimethylformamide (14.1 mL) and stirred for 24 h at room temperature. The reaction mixture was diluted with CH₂Cl₂ (15 mL) and washed with water (2 × 50 mL): the organic layer was dried over Na₂SO₄ and evaporated to dryness. The product, isolated in quantitative yield (324 mg), was used without further purification. ¹H-NMR (400 MHz, CDCl₃): δ 7.25 (td, 1H, *J* = 1.2 Hz, *J* = 3.6 Hz), 7.20–7.19 (m, 1H), 7.10–7.08 (m, 1H), 7.06–7.02 (m, 2H), 6.99 (d, 1H, *J* = 4 Hz), 6.93 (d, 1H, *J* = 3.6 Hz).

2.3. Synthesis of Compound 4. The novel terthiophene derivative **4** was prepared following a procedure reported for related compounds [24]. To a solution of 4-ethynylbenzaldehyde (**3**) (42.2 mg, 0.32 mmol, 1.2 equiv.), obtained starting from 4-[(trimethylsilyl)ethynyl]benzaldehyde [25], and terthiophene derivative (**2**) (88.5 mg, 0.27 mmol, 1 equiv.) in degassed tetrahydrofuran (6 mL), [PdCl₂(PPh₃)₂] (7.6 mg, 4 mol%), CuI (3.1 mg, 6 mol%), and triethylamine (1.5 mL) were added, under a flow of nitrogen. The reaction mixture was left under stirring at 70°C overnight. The solvent was removed under reduced pressure and the residue was purified by flash chromatography, using dichloromethane/hexane 6/4 as eluant, to give **4** as a dark yellow solid (66.1 mg; yield 65%).

¹H-NMR (400 MHz, CDCl₃): δ 10 (s, 1H), 7.89 (d, 2H, *J* = 8.4 Hz), 7.67 (d, 2H, *J* = 8.4 Hz), 7.27 (d, 2H, *J* = 3.6 Hz), 7.22 (d, 1H, *J* = 3.2 Hz), 7.14 (d, 1H, *J* = 3.6 Hz), 7.11 (t, 2H, *J* = 3.6 Hz), 7.06 (dd, 1H, *J* = 3.6 Hz, *J* = 5.2 Hz).

2.4. Synthesis of Compound 5. The known terthiophene derivative **5** [19] was prepared following a procedure reported for related compounds [26]. To a solution of 2,2':5',2''-terthiophene (**1**) (100.7 mg, 0.40 mmol, 1 equiv.) in *N,N*-dimethylformamide (3 mL), under nitrogen and cooled to 0°C, was added, in small portions, phosphoryl trichloride (75.1 mg, 0.49 mmol, 1.2 equiv.). The cool bath was then removed and the mixture was stirred for 24 h at 80°C. After cooling to room temperature, the reaction mixture was neutralized with NaOH (2 mL, 1.25 M) and then diluted with CH₂Cl₂ and washed with water: the organic layer was dried



SCHEME 2: Synthesis of **F3**.

over Na₂SO₄ and concentrated. The crude product was purified by flash chromatography, using dichloromethane as eluant, to give **5** as a dark solid (77.4 mg; yield 70%). ¹H-NMR (400 MHz, CDCl₃): δ 9.88 (s, 1H), 7.69 (d, 1H, *J* = 3.6 Hz), 7.30 (t, 2H, *J* = 4 Hz, *J* = 2 Hz), 7.25 (t, 2H, *J* = 4 Hz, *J* = 3.2 Hz), 7.15 (d, 1H, *J* = 4 Hz), 7.07 (dd, 1H, *J* = 3.6 Hz, *J* = 5.2 Hz).

2.5. Synthesis of Compound 6. The terthiophene derivative **6** was prepared according to the literature [27]. To a solution of 2,5-dibromo-3,4-dihexylthiophene (523.4 mg, 1.27 mmol, 1 equiv.) and 2-tributylstannylthiophene (1.18 g, 3.17 mmol, 2.5 equiv.) in degassed tetrahydrofuran (8.5 mL), under a flow of nitrogen, [PdCl₂(PPh₃)₂] (71 mg, 8 mol %) and KF (581 mg, 10 mmol, 7.9 equiv.) were added. The reaction mixture was left under stirring at 70°C overnight. The solvent was removed under reduced pressure and the residue was diluted with CH₂Cl₂ and washed with water: the organic layer was dried over Na₂SO₄ and concentrated. The crude product was purified by flash chromatography, using hexane as eluant, to give **6** as a dark green oil (370 mg; yield 70%). ¹H-NMR data are fully consistent with data reported in the literature [27].

2.6. Synthesis of Compound 7. The terthiophene derivative **7** was prepared following a procedure reported for related compounds [26]. To a solution of 3',4'-dihexyl-2,2':5',2''-terthiophene (**6**) (257 mg, 0.62 mmol, 1 equiv.) and *N,N*-dimethylformamide (49.7 mg, 0.68 mmol, 1.1 equiv.) in dichloroethane (6.2 mL), under nitrogen and cooled to 0°C, was added, in small portions, phosphoryl trichloride (104.3 mg, 0.68 mmol, 1.1 equiv.). The cool bath was then removed and the mixture was stirred overnight at 80°C. After cooling to room temperature, the organic solvent was removed and the residue was dissolved in chloroform. A solution of NaOH 1.25 M was added and stirred for 2 h. The organic layer was washed with water, dried over Na₂SO₄, and concentrated. The crude product was purified by flash chromatography, using chloroform as eluant, to give pure **7** (207 mg; yield 75%). ¹H-NMR (400 MHz, CDCl₃): δ 9.91

(s, 1H), 7.72 (d, 1H, $J = 4$ Hz), 7.38 (dd, 1H, $J = 1.2$ Hz, $J = 5.2$ Hz), 7.24 (d, 1H, $J = 4$ Hz), 7.19 (dd, 1H, $J = 0.8$ Hz, $J = 3.6$ Hz), 7.10 (dd, 1H, $J = 3.6$ Hz, $J = 1.6$ Hz), 2.82 (bt, 2H, $J = 8$ Hz, $J = 8.4$ Hz), 2.74 (bt, 2H, $J = 8$ Hz, $J = 8.4$ Hz), 1.63-1.53 (m, 4H), 1.48-1.39 (m, 4H), 1.36-1.33 (m, 8H), 0.91 (bd, 6H). MS (FAB⁺): m/z 376.

2.7. Synthesis of the New Fulleropyrrolidines F1-F3. Fulleropyrrolidines **F1-F3** were prepared by using the Prato cycloaddition procedure [28, 29]. A mixture of the suitable aldehyde (1 equiv.), fullerene C-60 (1 equiv.), and sarcosine (8 equiv.) was refluxed for 24 h in anhydrous toluene under a nitrogen atmosphere. After cooling to room temperature, the solvent was evaporated under vacuum and the residue was purified by flash chromatography, as indicated in each case.

2.8. Synthesis of F1. The crude product was purified by flash chromatography, using hexane/toluene from 4/6 to 3/7 as eluant. Yield is 56%. ¹H-NMR (400 MHz, CDCl₃): δ 7.98 (bs, 2H), 7.63 (d, 2H, $J = 8$ Hz), 7.25 (bd, 1H, $J = 4$ Hz), 7.20-7.17 (m, 2H), 7.10 (q, 2H, $J = 4$ Hz, $J = 7.2$ Hz), 7.06 (d, 1H, $J = 4$ Hz), 7.04 (dd, 1H, $J = 4.8$ Hz, $J = 3.6$ Hz), 5.31 (s, 1H), 5.26 (bs, 1H), 4.46 (d, 1H, $J = 10$ Hz), 3.02 (s, 3H). MALDI-TOF MS: m/z 1122.9 (C₈₃H₁₇NS₃ requires 1123.1, matrix DCTB).

2.9. Synthesis of F2. The crude product was purified by flash chromatography, using hexane/toluene from 1/1 to 3/7 as eluant. Yield is 42%. ¹H-NMR (400 MHz, CDCl₃ + CS₂): δ 7.38 (bs, 1H), 7.23 (d, 1H, $J = 5.2$ Hz), 7.17 (d, 1H, $J = 3.6$ Hz), 7.13 (d, 1H, $J = 3.6$ Hz), 7.11 (d, 1H, $J = 4$ Hz), 7.08 (d, 1H, $J = 3.6$ Hz), 7.03 (dd, 1H, $J = 3.6$ Hz, $J = 4.8$ Hz), 5.29 (s, 1H), 5.05 (d, 1H, $J = 9.6$ Hz), 4.31 (d, 1H, $J = 9.6$ Hz), 2.99 (s, 3H). MALDI-TOF MS: m/z 1022.8 (C₇₅H₁₃NS₃ requires 1023, without matrix).

2.10. Synthesis of F3. The crude product was purified by flash chromatography, using hexane/toluene 1/1 as eluant. Yield is 60%. ¹H-NMR (400 MHz, CDCl₃): δ 7.37 (d, 1H, $J = 3.6$ Hz), 7.32 (bd, 1H, $J = 5.2$ Hz), 7.20-7.18 (m, 1H), 7.14-7.13 (m, 1H), 7.08-7.06 (m, 1H), 5.28 (s, 1H), 5.02 (d, 1H, $J = 9.6$ Hz), 4.28 (d, 1H, $J = 9.6$ Hz), 2.97 (s, 3H), 2.72-2.64 (m, 4H), 1.48-1.44 (m, 2H), 1.40-1.37 (m, 2H), 1.32-1.27 (m, 12H), 0.91-0.85 (m, 6H). MALDI-TOF MS: m/z 1192.6 (C₈₇H₃₇NS₃ requires 1191.2, matrix DHB).

2.11. Preparation of Fullerene F4. Fullerene **F4** was prepared from compounds **8-10** as shown in Scheme 3.

2.12. Synthesis of Compound 9. The novel compound **9** was prepared as follows. To a solution of 3',4'-dihexyl-2,2':5',2''-terthiophene (**6**) (409.6 mg, 0.98 mmol, 1 equiv.) and methyl 5-chloro-5-oxopentanoate (**8**) (161.7 mg, 0.98 mmol, 1 equiv.) in toluene (1.6 mL), under nitrogen and cooled to 0°C, was added, in small portions, tin tetrachloride (255.3 mg, 0.98 mmol, 1 equiv.) and stirred for 2 h. The reaction mixture was diluted with CH₂Cl₂ and washed with water: the organic layer was dried over Na₂SO₄ and concentrated. The crude

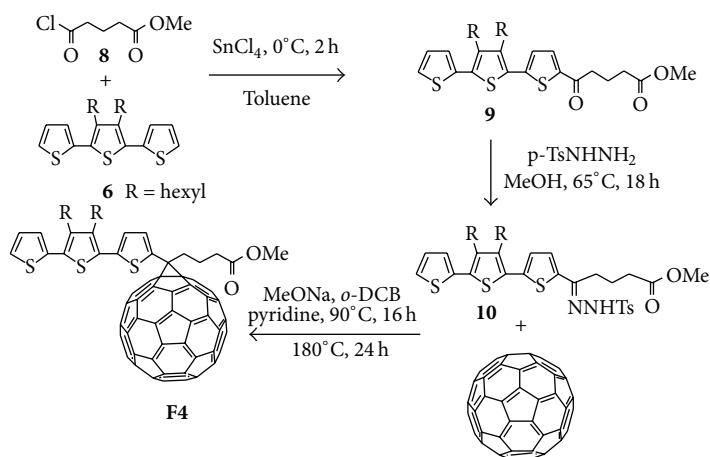
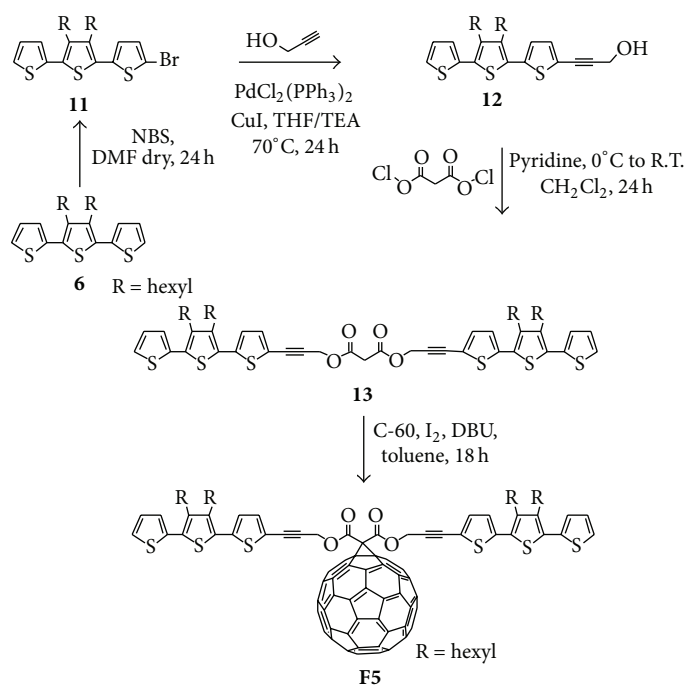
product obtained was purified by flash chromatography, using dichloromethane as eluant, to give **9** as a pure product (347 mg; yield 65%). ¹H-NMR (400 MHz, CDCl₃): δ 7.67 (d, 1H, $J = 4$ Hz), 7.36 (dd, 1H, $J = 0.8$ Hz, $J = 5.2$ Hz), 7.18-7.15 (m, 2H), 7.09 (dd, 1H, $J = 3.6$ Hz, $J = 5.2$ Hz), 3.71 (s, 3H), 2.99 (t, 2H, $J = 7.2$ Hz), 2.81 (bt, 2H), 2.71 (bt, 2H), 2.48 (t, 2H, $J = 7.2$ Hz), 2.15-2.08 (m, 2H), 1.58-1.53 (m, 2H), 1.47-1.39 (m, 4H), 1.36-1.29 (m, 8H), 0.92 (bd, 6H, $J = 6.8$ Hz).

2.13. Synthesis of Compound 10. The novel compound **10** was prepared as follows. A mixture of **9** (165 mg, 0.3 mmol, 1 equiv.) and *p*-toluenesulfonyl hydrazide (68 mg, 0.36 mmol, 1.2 equiv.) was refluxed in MeOH (0.5 mL) for 18 h. After cooling to room temperature, the organic solvent was removed under reduced pressure and the residue was dissolved in dichloromethane and washed with water. The organic layer was dried over Na₂SO₄ and concentrated. The residue was purified by flash chromatography, using hexane/ethyl acetate 7:3 as eluant, to give **10** as a pure product (148 mg; yield 75%). ¹H-NMR (400 MHz, CDCl₃): δ 8.97 (s, 1H), 7.94 (d, 2H, $J = 8$ Hz), 7.35-7.30 (m, 2H), 7.16 (d, 1H, $J = 1.2$ Hz), 7.14 (d, 1H, $J = 4$ Hz), 7.09 (dd, 1H, $J = 3.6$ Hz, $J = 4.8$ Hz), 7.01 (d, 1H, $J = 3.6$ Hz), 3.82 (s, 3H), 2.77-2.69 (m, 4H), 2.62 (t, 2H, $J = 7.6$ Hz, $J = 8$ Hz), 2.45 (s, 3H), 2.35 (t, 2H, $J = 5.2$ Hz, $J = 6.4$ Hz), 1.58-1.54 (m, 4H), 1.45-1.42 (m, 4H), 1.37-1.29 (m, 8H), 0.92 (bd, $J = 6.4$ Hz). MS (FAB⁺): m/z 712.

2.14. Synthesis of F4. The new methanofullerene **F4** was prepared following procedures reported for related compounds [18, 30, 31]. A mixture of **10** (55.3 mg, 0.084 mmol, 1.2 equiv.), sodium methoxide (4.5 mg, 0.084 mmol, 1.2 equiv.), and dry pyridine (0.84 mL) was stirred at room temperature for 30 min. Then a solution of fullerene C-60 (50.3 mg, 0.07 mmol, 1 equiv.) in *o*-dichlorobenzene (4.1 mL) was added, and the homogeneous reaction mixture was stirred at 75°C under nitrogen overnight. Then the mixture was refluxed for 24 h (180°C); after cooling to room temperature the solvent was evaporated at reduced pressure, and the residue was purified by column chromatography on silica gel with toluene/hexane 6:4 as eluent to give **F4** as a pure product (yield 55%). ¹H-NMR (400 MHz, CDCl₃): δ 7.46 (d, 1H, $J = 4$ Hz), 7.33 (dd, 1H, $J = 4.4$ Hz, $J = 0.8$ Hz), 7.18 (dd, 1H, $J = 4.4$ Hz, $J = 0.8$ Hz), 7.15 (d, 1H, $J = 4.4$ Hz), 7.10 (dd, 1H, $J = 3.6$ Hz, $J = 5.2$ Hz), 3.72 (s, 3H), 3.01 (bt, 2H, $J = 8$ Hz), 2.79 (bt, 2H, $J = 8.4$ Hz, $J = 8$ Hz), 2.73 (bt, 2H, $J = 8.4$ Hz, $J = 8$ Hz), 2.63 (t, 2H, $J = 7.2$ Hz), 1.63-1.56 (m, 4H), 1.45-1.40 (m, 4H), 1.35-1.28 (m, 8H), 0.91 (bd, 6H, $J = 6.8$ Hz). MALDI-TOF MS: m/z 1248.9 (C₉₀H₄₀O₂S₃ requires 1248.2, matrix DCTB).

2.15. Preparation of Fullerene F5. Fullerene **F5** was prepared from compounds **11-13** as shown in Scheme 4.

2.16. Synthesis of Compound 11. Under a nitrogen atmosphere, *N*-bromosuccinimide (NBS) (408.6 mg, 0.98 mmol, 1 equiv.) was added in small portions to a solution of 3',4'-dihexyl-2,2':5',2''-terthiophene (**6**) (147.7 mg, 0.98 mmol, 1 equiv.) in *N,N*-dimethylformamide (14 mL, 0.07 M) and

SCHEME 3: Synthesis of **F4**.SCHEME 4: Synthesis of **F5**.

stirred for 24 h at room temperature. The reaction mixture was diluted with CH_2Cl_2 (15 mL) and washed with water (2×50 mL): the organic layer was dried over Na_2SO_4 and concentrated. The product, isolated in quantitative yield (485 mg), was used without further purification. $^1\text{H-NMR}$ (400 MHz, CDCl_3): δ 7.40-7.32 (m, 1H), 7.14 (d, 1H, $J = 2.4$ Hz), 7.08 (dd, 1H, $J = 3.6$ Hz, $J = 5.2$ Hz), 7.04-7.01 (m, 1H), 6.89-6.87 (m, 1H), 2.75-2.64 (m, 4H), 1.63-1.56 (m, 4H), 1.44-1.40 (m, 4H), 1.34-1.28 (m, 8H), 0.90 (bd, 6H, $J = 6.8$ Hz).

2.17. Synthesis of Compound 12. The new terthiophene derivative **12** was prepared according to the following procedure. To a solution of propargyl alcohol (36.5 mg, 0.65 mmol, 1.1 equiv.)

and **11** (247.8 mg, 0.59 mmol, 1 equiv.) in degassed tetrahydrofuran (14.7 mL), under a flow of nitrogen, were added $[\text{PdCl}_2(\text{PPh}_3)_2]$ (16.6 mg, 4 mol %), CuI (6.7 mg, 6 mol%), and triethylamine (3.7 mL). The reaction mixture was left under stirring at 70°C overnight. The solvent was removed under reduced pressure and the residue was purified by flash chromatography, using chloroform as eluant, to give **12** (152 mg; yield 55%). $^1\text{H-NMR}$ (400 MHz, CDCl_3): δ 7.34 (dd, 1H, $J = 4.8$ Hz, $J = 0.8$ Hz), 7.18 (d, 1H, $J = 4.8$ Hz), 7.15 (dd, 1H, $J = 3.6$ Hz, $J = 0.8$ Hz), 7.09 (dd, 1H, $J = 3.6$ Hz, $J = 5.2$ Hz), 7.01 (d, 1H, $J = 3.6$ Hz), 4.55 (s, 2H), 2.74-2.68 (m, 4H), 1.59-1.55 (m, 4H), 1.44-1.41 (m, 4H), 1.36-1.29 (m, 8H), 0.92 (bd, 6H, $J = 6.8$ Hz).

2.18. Synthesis of Compound 13. The new terthiophene derivative **13** was prepared as follows. Malonyl dichloride (1.75 mL, 18 mmol, 1 equiv.) was added to a solution of terthiophene **12** (142 mg, 0.3 mmol, 2 equiv.) and pyridine (23.7 mg, 0.3 mmol, 2 equiv.) in dichloromethane (2.1 mL) at 0°C under nitrogen. After 1 h, the mixture was allowed to warm up to room temperature and then stirred for 18 h, filtered, and evaporated. The residue was purified by flash chromatography, using dichloromethane/hexane 8/2 as eluant, to give **13** (106 mg; yield 70%). ¹H-NMR (400 MHz, CDCl₃): δ 7.34 (d, 2H, *J* = 5.2 Hz), 7.21 (d, 2H, *J* = 4 Hz), 7.14 (dd, 2H, *J* = 3.6 Hz, *J* = 1.2 Hz), 7.08 (dd, 2H, *J* = 3.6 Hz, *J* = 5.2 Hz), 7.01 (d, 2H, *J* = 3.6 Hz), 5.05 (s, 4H), 3.57 (s, 2H), 2.73-2.67 (m, 8H), 1.58-1.54 (m, 8H), 1.46-1.41 (m, 8H), 1.35-1.29 (m, 16H), 0.93 (m, 12H). MS (FAB⁺): *m/z* 1008.

2.19. Synthesis of F5. The new methanofullerene **F5** was prepared following procedures reported for similar compounds [32, 33]. 1,8-diazabicyclo[5.4.0]undec-7-ene (19.3 mg, 0.125 mmol, 2.5 equiv.) was added under nitrogen at room temperature to a stirred solution of fullerene C-60 (39 mg, 0.05 mmol, 1 equiv.), I₂ (19 mg, 0.075 mmol, 1.5 equiv.), and **13** (55 mg, 0.05 mmol, 1 equiv.) in toluene (39 mL) at room temperature. The resulting solution was stirred for 12 h and then filtered through a short plug of silica (CH₂Cl₂) and evaporated. The residue was purified by flash chromatography, using hexane/toluene 6/4 as eluant, to give **F5** (yield 52%). ¹H-NMR (400 MHz, CDCl₃): δ 7.33 (dd, 2H, *J* = 5.2 Hz, *J* = 1.2 Hz), 7.20 (d, 2H, *J* = 4 Hz), 7.13 (dd, 2H, *J* = 3.6 Hz, *J* = 1.2 Hz), 7.07 (dd, 2H, *J* = 3.6 Hz, *J* = 4.8 Hz), 6.98 (d, 2H, *J* = 4 Hz), 5.38 (s, 4H), 2.73-2.68 (m, 8H), 1.56-1.54 (m, 8H), 1.43-1.38 (m, 8H), 1.34-1.28 (m, 16H), 0.92 (m, 12H). MALDI-TOF MS: *m/z* 1729.3 (C₁₁₇H₆₆O₄S₆ requires 1727.3, matrix DCTB).

2.20. Electrochemical Characterization. The cyclic voltammetric (CV) characterization was carried out with an Autolab PGSTAT 128N potentiostat, run by a PC with GPES software. The working cell included a Glassy Carbon (GC) disk embedded in Teflon (Amel, surface 0.071 cm²) as the working electrode, a Platinum counter electrode (Metrohm), and an aqueous saturated calomel electrode (SCE, Amel) as the reference electrode. The sample was dissolved in *o*-dichlorobenzene (≈0.5 mg/mL) and drop coated from a capillary on the GC electrode. The electrolytic solution was acetonitrile (Carlo Erba, HPLC grade) with 0.1 M tetrabutylammonium tetrafluoroborate TBATFB (Fluka, electrochemical grade). The solution was degassed with argon purging. The scan rate was 200 mV s⁻¹. According to IUPAC recommendations the data have been referred to the Fc⁺/Fc redox couple (ferrocenium/ferrocene).

E_{HOMO} and E_{LUMO} values were extrapolated from the onset peaks potential.

2.21. Preparation and Characterization of Solar Cells. Solar cells were fabricated on patterned ITO-coated glass substrates previously cleaned with detergent and water and then ultrasonicated in acetone and isopropyl alcohol for 15 min each.

A PEDOT : PSS (Clevios P VP AI 4083) layer was spin-coated at 3000 rpm onto air plasma cleaner ITO-coated substrates to a thickness of around 40 nm and then baked in an oven at 120°C for 10 min. Fullerenes and P3HT were dissolved separately in chlorobenzene (20 mg/mL) (Carlo Erba, HPLC grade), mixed 1:1 w/w obtaining a total concentration of 10 mg/mL, and then stirred overnight at 70°C. The blend solutions were spin-coated at 600 and 1200 rpm in glove box onto the ITO/PEDOT : PSS substrates. The thickness of the active layers, measured with a Veeco Dektak 150 profilometer, ranged between 50 nm and 130 nm. Then the samples were completed with the thermal evaporation of the Al (80 nm) cathode at a base pressure of 10⁻⁶ mbar. The active device area was 25 mm². The devices were postproduction thermal annealed in glove box (nitrogen filled) at 150°C for 10 min. The device electrical characterization was carried out at room temperature in glove box. Solar cells were illuminated using a solar simulator (Sun 2000, Abet Technologies) and the light power intensity was calibrated at AM1.5 illumination conditions (100 mW cm⁻²) using a certified silicon solar cell. The current-voltage curves were taken with a Keithley 2602 source measure.

3. Results and Discussion

Terthiophene is an interesting π -conjugated electron-releasing substituent group that can influence both the light absorbing behavior and charge separation process of fullerenes. Interestingly, it was reported that 1-(2-(2-methoxyethoxy)ethyl)-2-(terthiophene)fulleropyrrolidine is an efficient acceptor partner with P3HT, being characterized by a higher V_{oc} but lower fill factor and shorter circuit current with respect to related compounds bearing thiophene or bithiophene instead of the terthiophene moiety, attributed to its lower solubility [19]. These interesting results prompted us to design novel soluble terthiophene-substituted fullerene derivatives as easily accessible acceptor molecules for BHJ polymer solar cells (Scheme 1). We prepared both terthiophene-substituted fulleropyrrolidines (**F1-F3**) and methanofullerenes (**F4-F5**), with the aim of obtaining soluble acceptor materials with a good affinity for donor polymers based on thiophene units.

The novel terthiophene-substituted fulleropyrrolidines (**F1**, **F3**) and the known **F2** [22] were prepared following a method similar to that originally developed by Prato and Maggini and coworkers (Schemes 1 and 2) [28, 29]. Sarcosine was treated with [C60]-fullerene in the presence of a suitable terthiophene-substituted aldehyde, in toluene, and the mixture was heated under reflux for 24 h under a nitrogen atmosphere.

The novel terthiophene-substituted methanofullerene **F4** was prepared following the procedure reported for other methanofullerenes [18, 30, 31], by reaction of the *p*-tosylhydrazone **10** with sodium methoxide and fullerene C-60 (Scheme 3), whereas **F5** was synthesized by the Bingel reaction [32, 33] treating the novel bisterthiophenylmalonate **13** with iodine, fullerene, and 1,8-diazabicyclo[5.4.0]undec-7-ene (Scheme 4).

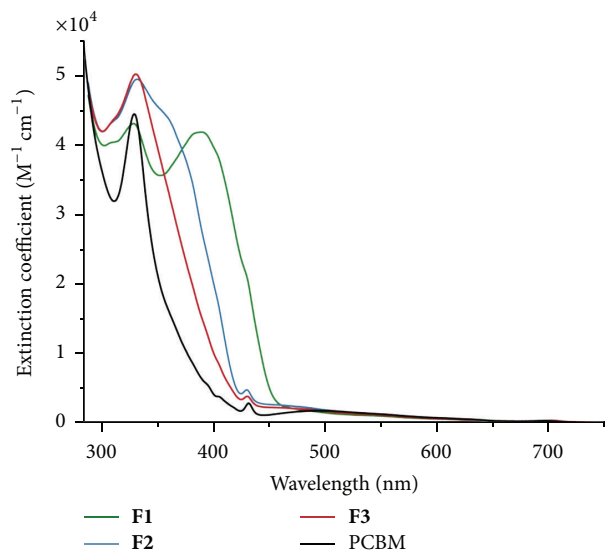


FIGURE 2: UV-visible absorption spectra of **F1–F3** and PCBM in chlorobenzene.

All fulleropyrrolidines and methanofullerenes were purified by silica gel flash chromatography and characterized by elemental analyses, ^1H NMR and UV-visible spectroscopies, mass spectrometry, and cyclovoltammetry (see Section 2).

Figures 2 and 3 show the UV-visible absorption spectra of fullerenes **F1–F5** along with that of PCBM in chlorobenzene solution.

The fulleropyrrolidine **F2** shows a broad absorption band between 350 and 400 nm, as expected for a terthiophene moiety [22]. This band is red shifted in compound **F1**, in agreement with the presence of a π -delocalized bridge between the pyrrolidine and the terthiophene moiety, and blue shifted in compound **F3**, due to the presence of the hexyl chains, responsible of the tilting of the structure and the final reduced conjugation.

Red shifting is observed in the compounds **F4** and **F5** in comparison with PCBM. Interestingly also a large enhancement in the ϵ of the peak at 330 nm (assigned to the fullerene) is obtained. Theoretically this enhancement can benefit the performance of the solar cells being the absorption in this region complementary to P3HT. In fact, it was reported that fullerenes' derivatives with a better light absorption can lead to a better power conversion efficiency since more photons are available to be converted into electricity [34].

The electrochemical properties of the various fullerenes were examined by cyclic voltammetry (CV). Current potential profiles are shown in Figures 4 and 5.

We use the first oxidation and reduction potentials to estimate the HOMO and LUMO energy levels by means of equations $E_{\text{HOMO}}(\text{eV}) = -(E_{\text{OX}} + 4.8)$ and $E_{\text{LUMO}}(\text{eV}) = -(E_{\text{RED}} + 4.8)$, which involve the use of the internal ferrocene standard value of -4.8 eV with respect to the vacuum level [35, 36]. The results are summarized in Table 1. Interestingly, all the novel fullerene derivatives have an enhanced LUMO level with respect to PCBM, possibly improving the V_{oc} . In fact,

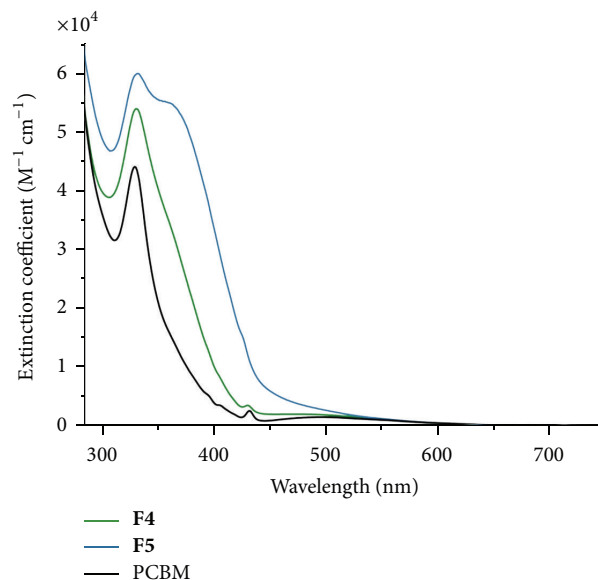


FIGURE 3: UV-visible absorption spectra of **F4**, **F5**, and PCBM in chlorobenzene.

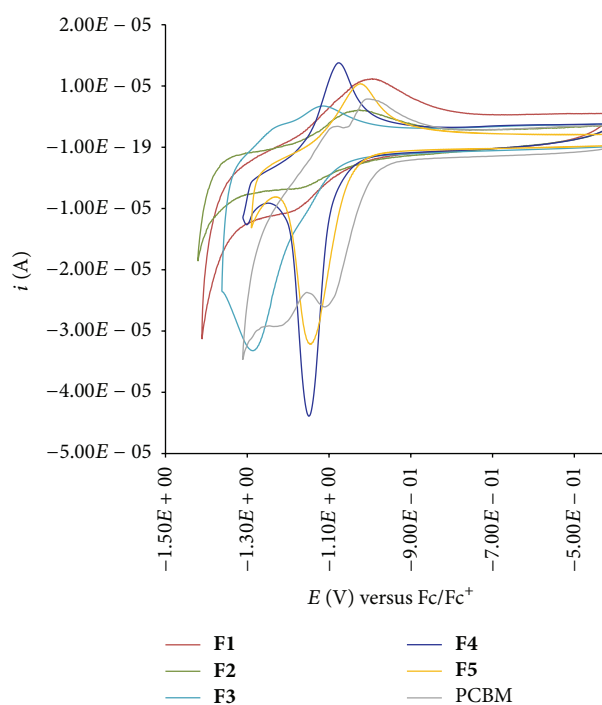


FIGURE 4: Synopsis of cathodic part of cyclovoltammograms for fullerenes **F1–F5** and PCBM.

Kim and coworkers reported that the V_{oc} of an OPV device is determined by the difference between the HOMO level of the p-type semiconductor and the LUMO level of the n-type conductor [37]. Fullerenes **F1–F3** and **F5** are characterized by a remarkably low band gap due to a relatively high HOMO level.

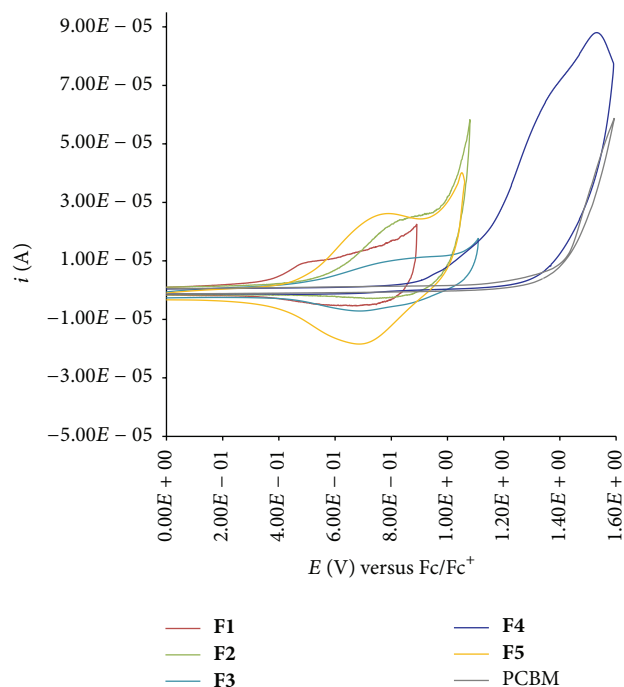


FIGURE 5: Synopsis of anodic part of cyclovoltammograms for fullerenes **F1**–**F5** and PCBM.

TABLE 1

Fullerene derivative	E_{HOMO} (eV)	E_{LUMO} (eV)	Band gap (eV)
F1	-5.15	-3.78	1.37
F2	-5.27	-3.78	1.49
F3	-5.29	-3.74	1.55
F4	-5.67	-3.75	1.92
F5	-5.26	-3.79	1.47
PCBM	-6.01	-3.83	2.18

The use of fullerenes **F1**, **F3**, and **F4** as acceptor molecules for bulk-heterojunction polymer solar cells was investigated in a preliminary way using P3HT as donor polymer. However, up to now the highest power conversion efficiency, reached with **F4**, was 0.46% only, although acceptable FF (0.30) and V_{oc} (0.48 Volt) were obtained. A wider screening of solvents and thickness in order to optimize morphology and performance is in progress in our laboratories.

4. Conclusions

In summary, we have prepared five interesting soluble fulleropyrrolidines and methanofullerenes, bearing one or two terthiophene moieties, as potential acceptors for the creation of efficient bulk-heterojunction solar cells based on donor polymers containing thiophene units. These novel fullerene derivatives are characterized by a better harvesting of the solar radiation with respect to traditional PCBM. In addition, they have a relatively high LUMO level and a low

band gap that can be easily tuned by an adequate design of the link between the fullerene and the terthiophene.

Besides, it is worth pointing out that the new fullerene derivatives prepared in the present work are also of interest as new molecular building blocks for materials with nonlinear optical (NLO) properties [38–43]. In particular, because the methanofullerene **F4** is an excellent candidate as second-order NLO chromophore due to the presence of the highly polarizable electron acceptor C60-fullerene system linked to the donor terthiophene through a cyclopropane group, its quadratic hyperpolarizability is under study in our laboratories.

Conflict of Interests

The authors declare that there is no conflict of interests regarding the publication of this paper.

Acknowledgments

This work was supported by Eni (Contract no. 3500005452). The authors thank Andrea Alessi (Eni S.p.A.) for the UV-visible analysis and the useful discussion.

References

- [1] M. K. Nazeeruddin, E. Baranoff, and M. Grätzel, “Dye-sensitized solar cells: a brief overview,” *Solar Energy*, vol. 85, no. 6, pp. 1172–1178, 2011.
- [2] J.-H. Yum, E. Baranoff, S. Wenger, M. K. Nazeeruddin, and M. Grätzel, “Panchromatic engineering for dye-sensitized solar cells,” *Energy & Environmental Science*, vol. 4, no. 3, pp. 842–857, 2011.
- [3] S. Günes, H. Neugebauer, and N. S. Sariciftci, “Conjugated polymer-based organic solar cells,” *Chemical Reviews*, vol. 107, no. 4, pp. 1324–1338, 2007.
- [4] B. Kippelen and J. Brédas, “Organic photovoltaics,” *Energy and Environmental Science*, vol. 2, no. 3, pp. 251–261, 2009.
- [5] F. G. Brunetti, R. Kumar, and F. Wudl, “Organic electronics from perylene to organic photovoltaics: painting a brief history with a broad brush,” *Journal of Materials Chemistry*, vol. 20, no. 15, pp. 2934–2948, 2010.
- [6] Y. Liang, Z. Xu, J. Xia et al., “For the bright future-bulk heterojunction polymer solar cells with power conversion efficiency of 7.4%,” *Advanced Materials*, vol. 22, no. 20, pp. E135–E138, 2010.
- [7] A. Colombo, C. Dragonetti, D. Roberto et al., “A novel diruthenium acetylide donor complex as an unusual active material for bulk heterojunction solar cells,” *Organometallics*, vol. 30, no. 6, pp. 1279–1282, 2011.
- [8] R. Po, A. Bernardi, A. Calabrese, C. Carbonera, G. Corso, and A. Pellegrino, “From lab to fab: how must the polymer solar cell materials design change?—an industrial perspective,” *Energy & Environmental Science*, vol. 7, pp. 925–943, 2014.
- [9] J. C. Hummelen, B. W. Knight, F. Lepeq, F. Wudl, J. Yao, and C. L. Wilkins, “Preparation and characterization of fulleroid and methanofullerene derivatives,” *Journal of Organic Chemistry*, vol. 60, no. 8, pp. 532–538, 1995.
- [10] G. Yu, J. Gao, J. C. Hummelen, F. Wudl, and A. J. Heeger, “Polymer photovoltaic cells: Enhanced efficiencies via a network of

- internal donor-acceptor heterojunctions," *Science*, vol. 270, no. 5243, pp. 1789–1791, 1995.
- [11] C. Brabec, A. Cravino, D. Meissner et al., "Origin of the open circuit voltage of plastic solar cells," *Advanced Functional Materials*, vol. 11, no. 5, pp. 374–380, 2001.
- [12] C. Yang, J. Y. Kim, S. Cho, J. K. Lee, A. J. Heeger, and F. Wudl, "Functionalized methanofullerenes used as n-type materials in bulk-heterojunction polymer solar cells and in field-effect transistors," *Journal of the American Chemical Society*, vol. 130, no. 20, pp. 6444–6450, 2008.
- [13] Y. Zhang, H. Yip, O. Acton, S. K. Hau, F. Huang, and A. K.-Y. Jen, "A simple and effective way of achieving highly efficient and thermally stable bulk-heterojunction polymer solar cells using amorphous fullerene derivatives as electron acceptor," *Chemistry of Materials*, vol. 21, no. 13, pp. 2598–2600, 2009.
- [14] M. Lenes, S. W. Shelton, A. B. Sieval, D. F. Kronholm, J. C. Hummelen, and P. W. M. Blom, "Electron trapping in higher adduct fullerene-based solar cells," *Advanced Functional Materials*, vol. 19, no. 18, pp. 3002–3007, 2009.
- [15] T. Niinomi, Y. Matsuo, M. Hashiguchi, Y. Sato, and E. Nakamura, "Penta(organo)[60]fullerenes as acceptors for organic photovoltaic cells," *Journal of Materials Chemistry*, vol. 19, no. 32, pp. 5804–5811, 2009.
- [16] S. Y. Nam, H. S. Lee, J. Jung et al., "Ethyleneoxy substituted methanofullerenes for acceptor materials in organic photovoltaic cells," *Journal of Nanoscience and Nanotechnology*, vol. 9, no. 12, pp. 7034–7038, 2009.
- [17] Y. Matsuo, Y. Sato, T. Niinomi, I. Soga, H. Tanaka, and E. Nakamura, "Columnar structure in bulk heterojunction in solution-processable three-layered p-i-n organic photovoltaic devices using tetrabenzoporphyrin precursor and silyl-methyl[60]fullerene," *Journal of the American Chemical Society*, vol. 131, no. 44, pp. 16048–16050, 2009.
- [18] H. Zhao, X. Guo, H. Tian et al., "Alkyl substituted [6,6]-thienyl- C_{61} -butyric acid methyl esters: Easily accessible acceptor materials for bulk-heterojunction polymer solar cells," *Journal of Materials Chemistry*, vol. 20, no. 15, pp. 3092–3097, 2010.
- [19] K. Yoshimura, K. Matsumoto, Y. Uetani et al., "Thiophene-substituted fulleropyrrolidine derivatives as acceptor molecules in a thin film organic solar cell," *Tetrahedron*, vol. 68, no. 18, pp. 3605–3610, 2012.
- [20] L. M. Popescu, P. Van 'T Hof, A. B. Sieval, H. T. Jonkman, and J. C. Hummelen, "Thienyl analog of 1-(3-methoxycarbonyl)propyl-1-phenyl-[6,6]-methanofullerene for bulk heterojunction photovoltaic devices in combination with polythiophenes," *Applied Physics Letters*, vol. 89, no. 21, Article ID 213507, 2006.
- [21] P. A. Troshin, H. Hoppe, J. Renz et al., "Material solubility-photovoltaic performance relationship in the design of novel fullerene derivatives for bulk heterojunction solar cells," *Advanced Functional Materials*, vol. 19, no. 5, pp. 779–788, 2009.
- [22] C. Saravanan, C. Liu, Y. Chang et al., "Fulleropyrrolidines bearing π -conjugated moiety for polymer solar cells: contribution of the chromophoric substituent on C_{60} to the photocurrent," *ACS Applied Materials and Interfaces*, vol. 4, no. 11, pp. 6133–6141, 2012.
- [23] J. J. Kim, H. Choi, J. W. Lee et al., "A polymer gel electrolyte to achieve $\geq 6\%$ power conversion efficiency with a novel organic dye incorporating a low-band-gap chromophore," *Journal of Materials Chemistry*, vol. 18, no. 43, pp. 5223–5229, 2008.
- [24] X. Zhao, C. Piliago, B. Kim et al., "Solution-processable crystalline platinum-acetylide oligomers with broadband absorption for photovoltaic cells," *Chemistry of Materials*, vol. 22, no. 7, pp. 2325–2332, 2010.
- [25] A. Lembo, P. Tagliatesta, and D. M. Guldi, "Synthesis and photophysical investigation of new porphyrin derivatives with β -pyrrole ethynyl linkage and corresponding dyad with [60] fullerene," *The Journal of Physical Chemistry A*, vol. 110, no. 40, pp. 11424–11434, 2006.
- [26] I. Jestin, P. Frère, N. Mercier, E. Levillain, D. Stievenard, and J. Roncali, "Synthesis and characterization of the electronic and electrochemical properties of thienylenevinylene oligomers with multianometer dimensions," *Journal of the American Chemical Society*, vol. 120, no. 32, pp. 8150–8158, 1998.
- [27] P. L. Vidal, B. Divisia-Blohorn, G. Bidan, J. L. Hazemann, J. M. Kern, and J. P. Sauvage, " π -conjugated ligand polymers entwined around copper centres," *Chemistry*, vol. 6, no. 9, pp. 1663–1673, 2000.
- [28] M. Prato, M. Maggini, C. Giacometti, G. Scorrano, G. Sandonà, and G. Farnia, "Synthesis and electrochemical properties of substituted fulleropyrrolidines," *Tetrahedron*, vol. 52, no. 14, pp. 5221–5234, 1996.
- [29] M. Prato and M. Maggini, "Fulleropyrrolidines: a family of full-fledged fullerene derivatives," *Accounts of Chemical Research*, vol. 31, no. 9, pp. 519–526, 1998.
- [30] J. H. Choi, K. Son, T. Kim, K. Kim, K. Ohkubo, and S. Fukuzumi, "Thienyl-substituted methanofullerene derivatives for organic photovoltaic cells," *Journal of Materials Chemistry*, vol. 20, no. 3, pp. 475–482, 2010.
- [31] J. H. Choi, T. Honda, S. Seki, and S. Fukuzumi, "Relationship between crystal packing and high electron mobility in the single crystal of thienyl-substituted methanofullerene," *Chemical Communications*, vol. 47, no. 40, pp. 11213–11215, 2011.
- [32] J. Lehl and J. Nierengarten, "A click-click approach for the preparation of functionalized [5:1]-hexaadducts of C_{60} ," *Chemistry A*, vol. 15, no. 30, pp. 7306–7309, 2009.
- [33] J. Lehl and J. Nierengarten, "Sequential copper catalyzed alkyne-azide and thiol-ene click reactions for the multiple functionalization of fullerene hexaadducts," *Chemical Communications*, vol. 46, no. 23, pp. 4160–4162, 2010.
- [34] Y. Liang, Z. Xu, J. Xia et al., "For the bright future—bulk heterojunction polymer solar cells with power conversion efficiency of 7.4%," *Advanced Materials*, vol. 22, no. 20, pp. E135–E138, 2010.
- [35] W. Y. Wong, X. Z. Wang, Z. He et al., "Metallated conjugated polymers as a new avenue towards high-efficiency polymer solar cells," *Nature Materials*, vol. 6, no. 7, pp. 521–527, 2007.
- [36] R. S. Ashraf, M. Shahid, E. Klemm, M. Al-Ibrahim, and S. Sensfuss, "Thienopyrazine-based low-bandgap poly(heteroaryleneethynylene)s for photovoltaic devices," *Macromolecular Rapid Communications*, vol. 27, no. 17, pp. 1454–1459, 2006.
- [37] J. Y. Kim, S. H. Kim, H.-H. Lee et al., "New architecture for high-efficiency polymer photovoltaic cells using solution-based titanium oxide as an optical spacer," *Advanced Materials*, vol. 18, no. 5, pp. 572–576, 2006.
- [38] F. Langa De La Puente and J.-F. Nierengarten, Eds., *Fullerenes: Principles and Applications*, Royal Society of Chemistry, RSC Nanoscience & Nanotechnology, Cambridge, UK, 2011.

- [39] Y. Zhao, Y. Shirai, A. D. Slepko et al., "Synthesis, spectroscopic and nonlinear optical properties of multiple [60]fullerene-oligo(p-phenylene ethynylene) hybrids," *Chemistry*, vol. 11, no. 12, pp. 3643–3658, 2005.
- [40] S. Muhammad, K. Fukuda, T. Minami, R. Kishi, Y. Shigeta, and M. Nakano, "Interplay between the diradical character and third-order nonlinear optical properties in fullerene systems," *Chemistry*, vol. 19, no. 5, pp. 1677–1685, 2013.
- [41] A. Valore, M. Balordi, A. Colombo et al., "Novel ruthenium(II) complexes with substituted 1,10-phenanthroline or 4,5-diazafluorene linked to a fullerene as highly active second order NLO chromophores," *Dalton Transactions*, vol. 39, no. 42, pp. 10314–10318, 2010.
- [42] C. Dragonetti, A. Valore, A. Colombo et al., "An investigation on the second-order NLO properties of novel cationic cyclometallated Ir(III) complexes of the type $[\text{Ir}(\text{2-phenylpyridine})_2(\text{9-R-4,5-diazafluorene})]^+$ (R = H, fulleridene) and the related neutral complex with the new 9-fulleriden-4-monoazafluorene ligand," *Inorganica Chimica Acta*, vol. 382, no. 1, pp. 72–78, 2012.
- [43] S. Di Bella, C. Dragonetti, M. Pizzotti, D. Roberto, F. Tessore, and R. Ugo, "Coordination and organometallic complexes as second-order nonlinear optical molecular materials," *Topics in Organometallic Chemistry*, vol. 28, pp. 1–55, 2010.

Research Article

The Structure and Stability of Molybdenum Ditelluride Thin Films

Zhouling Wang, Wenwu Wang, Ya Yang, Wei Li, Lianghuan Feng, Jingquan Zhang, Lili Wu, and Guanggen Zeng

College of Materials Science and Engineering, Sichuan University, Chengdu 610064, China

Correspondence should be addressed to Wenwu Wang; www1492@163.com and Wei Li; waylee2000@sohu.com

Received 20 February 2014; Revised 23 May 2014; Accepted 26 May 2014; Published 10 July 2014

Academic Editor: Sudhakar Shet

Copyright © 2014 Zhouling Wang et al. This is an open access article distributed under the Creative Commons Attribution License, which permits unrestricted use, distribution, and reproduction in any medium, provided the original work is properly cited.

Molybdenum-tellurium alloy thin films were fabricated by electron beam evaporation and the films were annealed in different conditions in N_2 ambient. The hexagonal molybdenum ditelluride thin films with well crystallization annealed at 470°C or higher were obtained by solid state reactions. Thermal stability measurements indicate the formation of MoTe_2 took place at about 350°C , and a subtle weight-loss was in the range between 30°C and 500°C . The evolution of the chemistry for Mo-Te thin films was performed to investigate the growth of the MoTe_2 thin films free of any secondary phase. And the effect of other postdeposition treatments on the film characteristics was also investigated.

1. Introduction

Molybdenum ditelluride (MoTe_2) belongs to the large family of layered transition metal dichalcogenides, which is bound by weak van der Waals interactions along the c -axis [1]. The electronic, optical, magnetic, and catalytic properties of the transition metal dichalcogenides have been extensively studied [2–6]. MoTe_2 can act as an efficient absorbing layer in solar cells only if the crystallites of the films are textured with the c -axis perpendicular to the plane of the substrate [7]. Because of the layered structure of MoTe_2 , various metal atoms can be doped between the layers to change its optical and electrical properties [8]. It has been found that H absorption on MoTe_2 monolayers results in large spatial extensions of spin density and weak AFM coupling between local magnetic moments even at the distance of above 12.74 \AA [4]. MoTe_2 has a bandgap of around 1.1 eV and a high work function of $\sim 4.7 \text{ eV}$, and the valence band offset of $\text{CdTe}/\text{MoTe}_2$ is only 0.03 eV [1]; these are advantageous to the hole transport between cadmium telluride and molybdenum ditelluride. Therefore, MoTe_2 is a potential candidate for a stable Cu-free back contact to CdS/CdTe solar cells.

Tellurium pressure or vapor is often indispensable for the preparation of the MoTe_2 thin films [9, 10], and the adhesion or reproducibility of the films is very poor. In this work,

MoTe_2 thin films were synthesized by solid state reactions between Mo and Te thin films followed by an anneal in N_2 ambient. The structural property and stability of Mo-Te thin films were investigated under different postdeposition treatment conditions.

2. Experimental

Molybdenum-tellurium alloy thin films were deposited by electron beam evaporation at room temperature in the pressure of $\sim 10^{-4} \text{ Pa}$. The multilayer Mo/Te films with a stacking sequence Te-Mo-Te-Mo were deposited independently and alternately using high purity molybdenum (99.999% purity, Alfa Aesar) and tellurium (99.999% purity, Alfa Aesar). The deposition rates of molybdenum and tellurium were monitored by a thickness monitor. The total thickness of the molybdenum-tellurium multilayer thin films was $200\sim 450 \text{ nm}$. After deposition, a posttreatment was performed at different temperatures in N_2 ambient. The temperatures reproducible to $\pm 1 \text{ K}$ were obtained from repeated runs on the same sample.

The structure and the surface morphology of the samples were done by X-ray diffraction (XRD) (DX-2600, Dandong, China) and atomic force microscope (AFM) (MFP-3D-BIO,

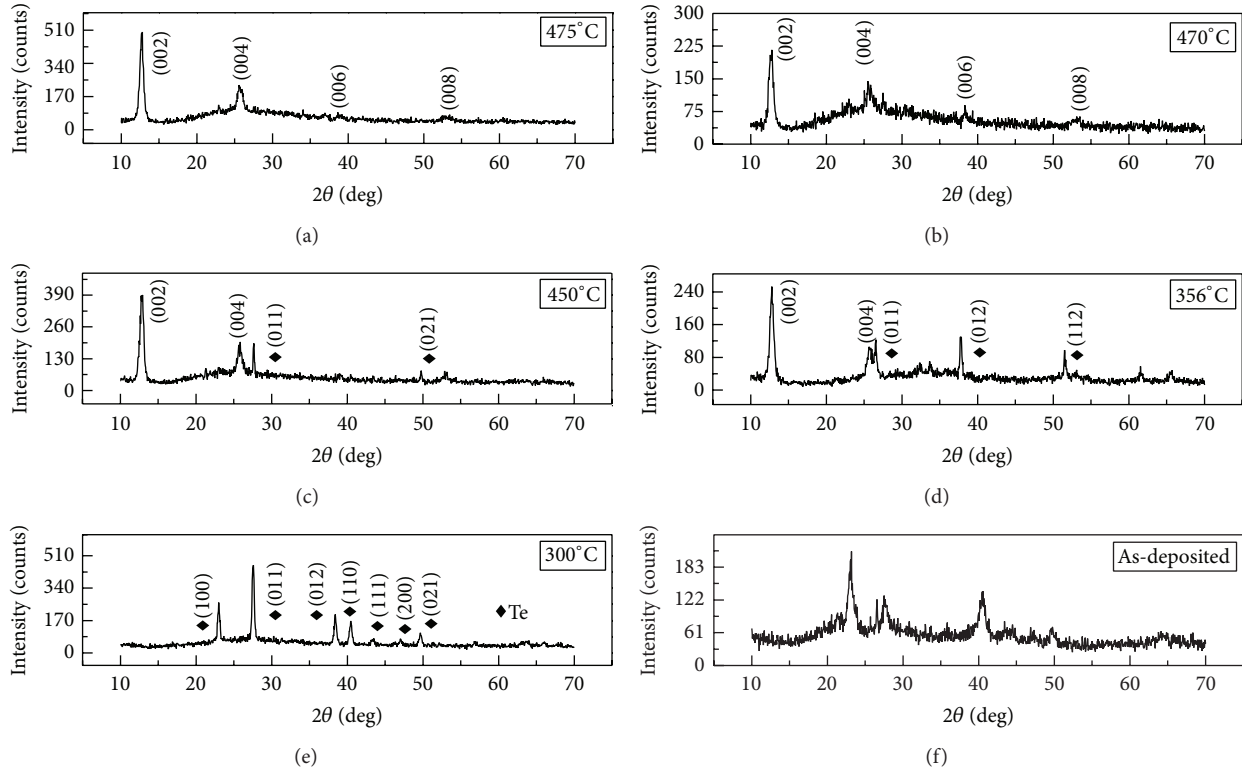


FIGURE 1: XRD patterns of Mo-Te thin films annealed at different temperatures for 15 min in N_2 ambient.

Asylum Research, USA). The film thickness was surveyed using a stylus profiler (XP-2, Ambios Technology Inc., USA). To study the effect of annealing on the $MoTe_2$ thin films, thermogravimetry and differential scanning calorimetry (TG/DSC) (STA 449C, NETZSCH, Germany) analysis were carried out. X-ray photoelectron spectra (XPS) (ESCALAB 250, Thermo Fisher SCIENTIFIC, UK) were performed to determine the atom chemical states.

3. Results and Discussion

Figure 1 shows the XRD patterns of the Mo-Te thin films with 450 nm thickness annealed at different temperatures in N_2 ambient. The peaks marked by rhombus were indexed to the phase of Te (JCPDS NO. 65-3370), and the others were the phase of $MoTe_2$ (JCPDS number 15-0658) (see Figure 1). The reflection positions in the XRD patterns of as-deposited layers were at the angles of 23.029° , 27.560° , 40.454° , and 49.650° , which correspond to Te (100), (011), (110), and (021). In order to form the crystalline compound $MoTe_2$ thin films with a simple hexagonal Bravais lattice, thermal postdeposition treatment was performed. The as-deposited thin films were annealed at $300^\circ C$, $356^\circ C$, $450^\circ C$, $470^\circ C$, and $475^\circ C$ in N_2 ambient, respectively. After annealing at $300^\circ C$ in N_2 ambient, many more diffraction peaks of Te, such as (012), (111), and (200), emerged at 38.263° , 43.353° , and 47.060° . When the annealing temperature reached $356^\circ C$, the patterns of the films were very different from those of

the films annealed at $300^\circ C$; the peaks corresponding to $MoTe_2$ (002) and (004) were revealed by XRD patterns as shown in Figure 1. It was noticed that two diffraction peaks of Te (011) and (112) were also observed in the XRD patterns. The results show that a considerable amount of Te and Mo diffuses into the Mo and the Te films, respectively. The chemical reaction that took place in the thin elemental layers can be described as $2Te + Mo \rightarrow MoTe_2$. The thin films with well crystallization were achieved when annealing was performed at $470^\circ C$ or higher. The peaks of $MoTe_2$ (006) could be observed at 38.905° , and there were no peaks of Te. These results indicate the disappearance of Te but the presence of $MoTe_2$ with increasing the annealing temperature. Therefore, annealing promotes the formation of $MoTe_2$ and annealing at $470^\circ C$ leads to the single phase $MoTe_2$ thin films.

To study the stability of the molybdenum-tellurium alloy thin films, TG and DSC analysis were performed. The thin films as-deposited were cleaved from the substrates; approximately 2.952 mg of sample was used in this work. The gas rate was 30 mL/min, and the heating rate was 10 K/min. Figure 2 shows the TG-DSC curves of as-deposited films. The peaks of as-deposited $MoTe_2$ thin films were extended from $30^\circ C$ to $600^\circ C$. The peaks in DSC values meant endothermic reactions happened while heating. The first endothermic peak was located at $68.5^\circ C$ and it was the endothermic peak of water. Then with the increase of temperature, there were endothermic peaks appearing at about $350^\circ C$ and $448.5^\circ C$ due to the energy consumption, which results from Te atoms and Mo atoms moving into lattice sites so as to form

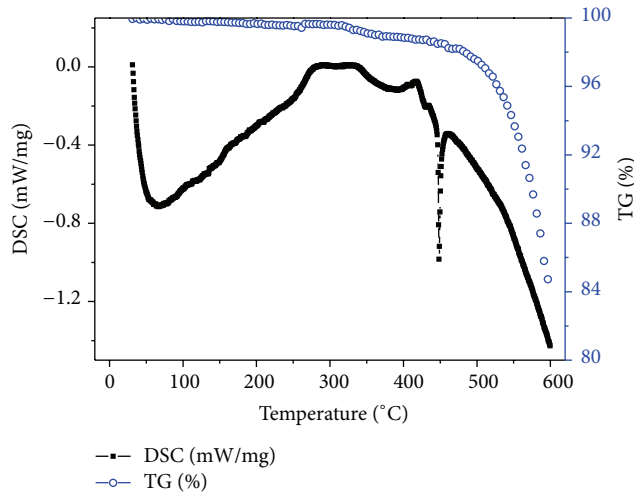


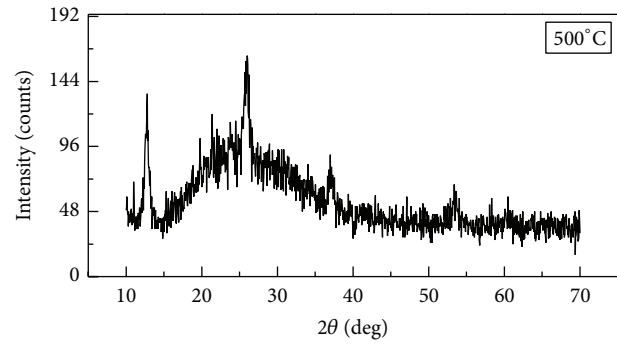
FIGURE 2: TG and DSC analysis of the as-deposited films.

MoTe₂. This behavior is consistent with the results of XRD (Figure 1); that is, polycrystalline MoTe₂ was gradually formed when the annealing temperature increased up to 350°C. From the TG values also shown in Figure 2, one can see that there was almost no weight loss at the temperatures lower than 500°C, whereas the TG curve dropped sharply at the temperatures higher than 500°C. The severe weight-loss might be the reevaporation of tellurium for MoTe₂, the results of which will be discussed later.

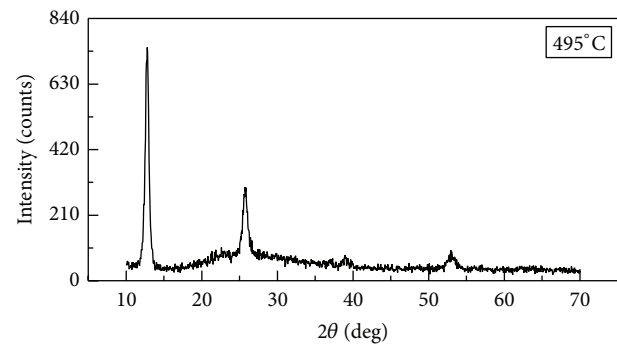
With the increase of the annealing temperature, the intensities of the peaks for the thin films became significantly strong and the positions of the peaks were not changed (Figure 3). These indicate the improved crystallinity and stable structure of MoTe₂ thin films due to the interdiffusion. As the annealing temperature increased up to 500°C, although the weight-loss was about 2% (Figure 2), an amorphous baseline distinctly appeared. We attribute the poor crystallinity of the films to the severe reevaporation of tellurium in the process of the postdeposition treatments. When the annealing temperature was further increased, the adhesion of the films was poor. Grain growth of MoTe₂ thin films may introduce stress at the glass/MoTe₂ interface, resulting in film blistering or peeling.

Based upon the investigations of XRD and TG/DSC analysis, the evolution of the morphology and chemistry for MoTe₂ thin films annealed at temperatures lower than 500°C was studied by AFM and XPS (Figures 4-5). Figure 4 shows the atomic force microscopy of Mo-Te thin films as-deposited and annealed at 475°C in N₂ ambient. The surface of the as-deposited MoTe₂ thin film was smoother than the one annealed at 475°C. The root mean square of the as-deposited film was 1.179 nm while it became 19.803 nm after annealing. That means annealing could promote the growth of the grains. The well-distributed atoms moved to lattice sites so the valleys and peaks on the surface were detected by AFM, and this is consistent with the XRD results.

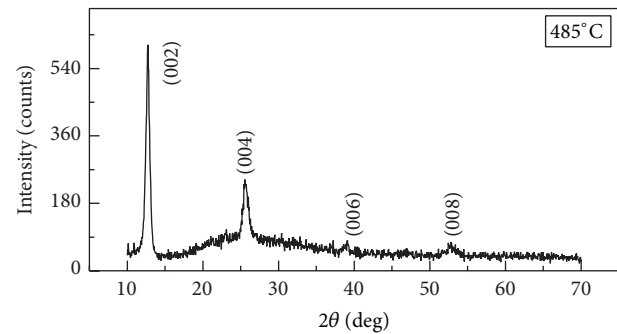
Figure 5 shows XPS spectra of Mo-Te thin films at different temperatures. When the annealing temperature was



(a)



(b)



(c)

FIGURE 3: XRD patterns of Mo-Te thin films with a thickness of 450 nm annealed at 485°C, 495°C, and 500°C for 15 minutes in N₂ ambient.

below 450°C, it was noticed that there was only one emission peak in XPS spectra of Mo 3d_{3/2}, which drew core level lines at about 232.75 eV, and it was a double peak. The emission peak with lower binding energies was determined to be the Mo 3d_{5/2} in MoTe₂ which occurred at 229.2 eV when the annealing temperature reached 450°C or higher. That means MoTe₂ was formed when the annealing temperature rose to 450°C and it has been confirmed by XRD in Figure 1. In Figure 5, the doublet of Te 3d was doubled (the two Te 3d_{5/2} peaks being at about 572.9 eV and 576.5 eV), while the Te 3d_{3/2} position of TeO₂ occurred at 576 eV; maybe there was a small amount of tellurium oxidation at the surface of the films. It was obvious that the ratio of ionized Te/elemental Te increased dramatically after annealing since the peak area was proportional to the chemical composition. The results show

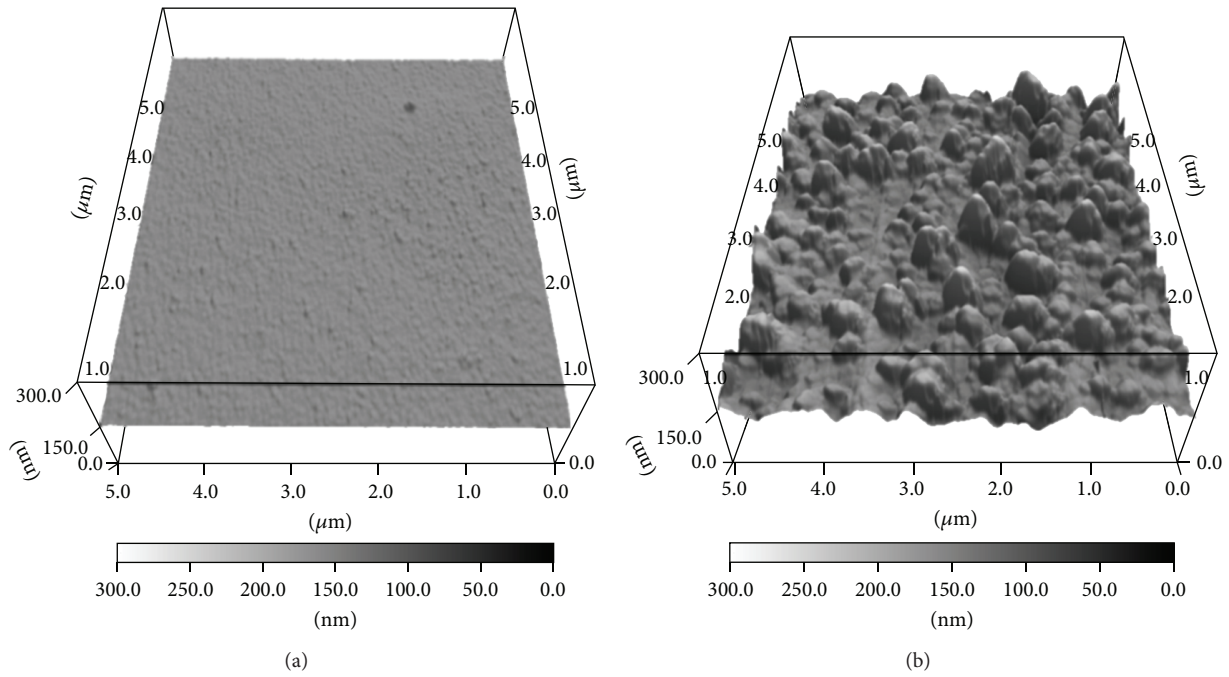


FIGURE 4: AFM images of Mo-Te thin films as-deposited (a) and (b) annealed at 475°C for 15 min in N_2 ambient.

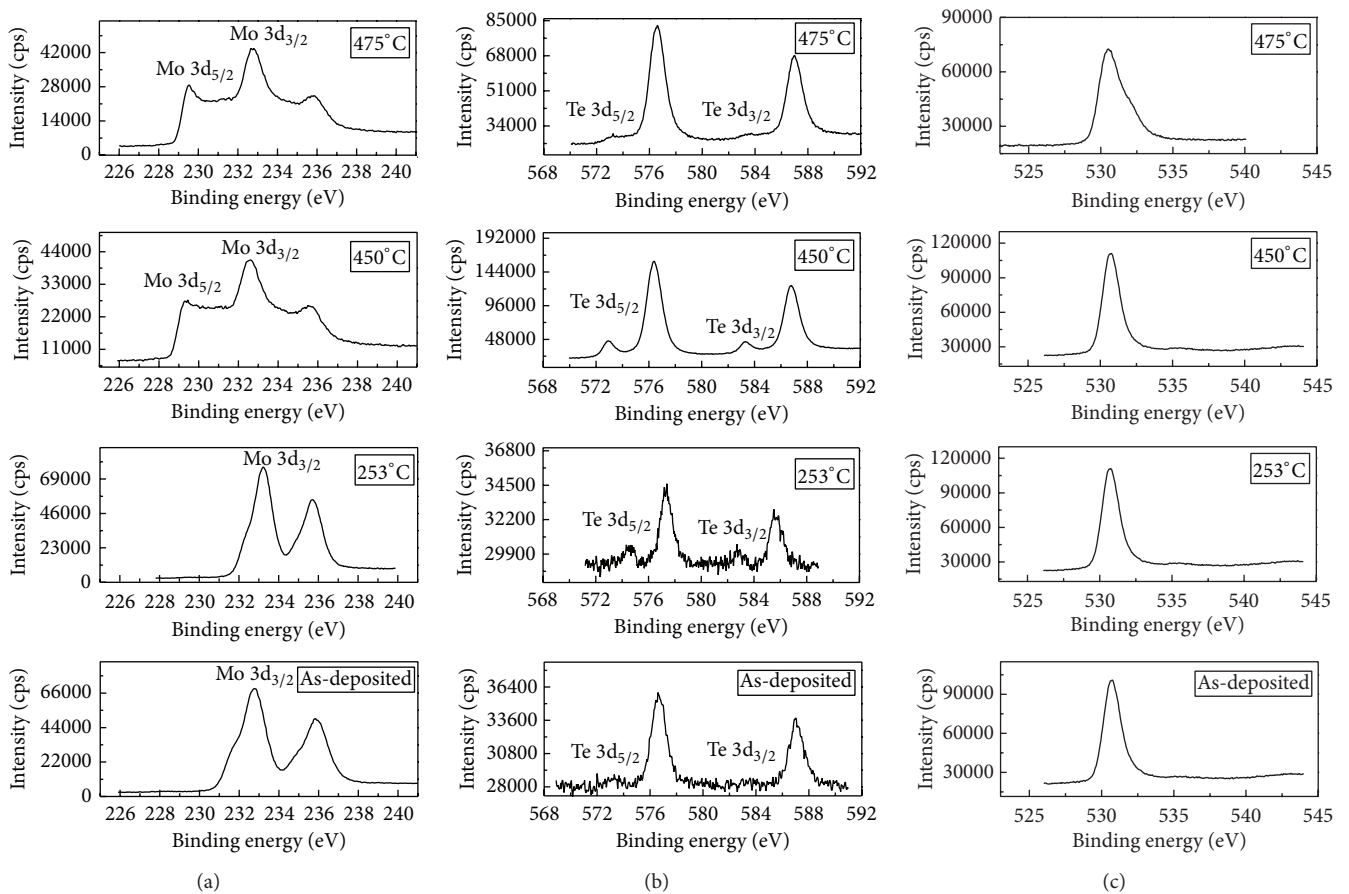


FIGURE 5: XPS spectra of (a) Mo 3d, (b) Te 3d, and (c) O 1s for Mo-Te thin films annealed at different temperatures.

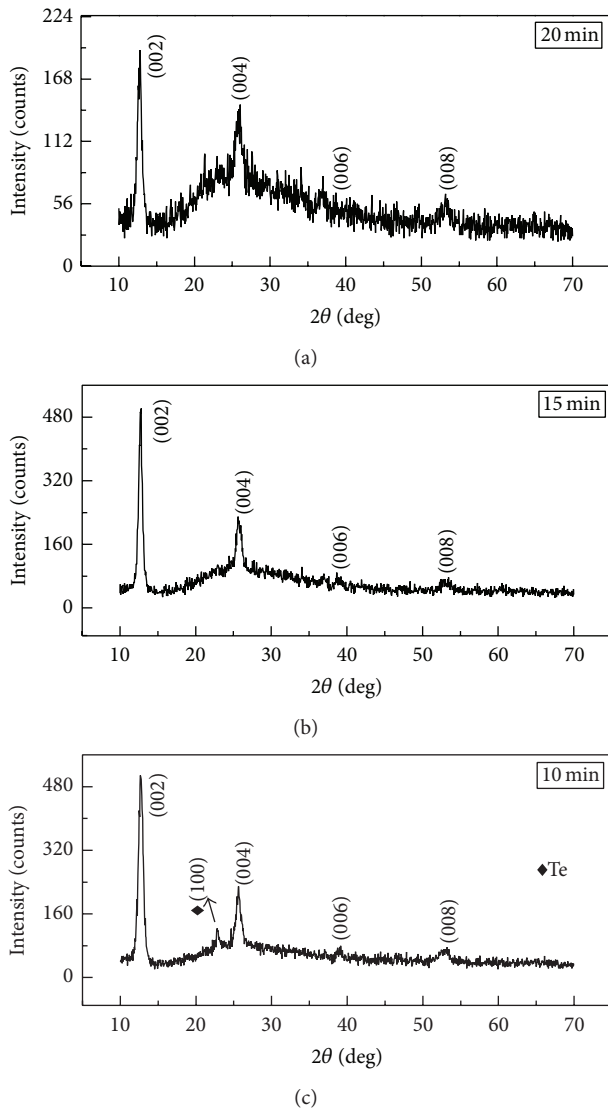


FIGURE 6: XRD patterns of Mo-Te thin films with thickness of 450 nm annealed at 470°C for different times in N_2 ambient.

that a large amount of Te was not alloyed in the as-deposited films. After annealing, most of Te was alloyed with Mo in the form of $MoTe_2$ due to the interdiffusion. This could explain why the peak of Te was firstly detected but disappeared after annealing in XRD patterns (see Figure 1).

To further explore the effect of annealing on the structure of Mo-Te thin films, the other thermal postdeposition treatments such as annealing time and thickness were carried out. Figure 6 shows XRD of Mo-Te thin films with thickness of 450 nm annealed at 470°C for different annealing time. It was noticed that when the annealing time was 10 minutes, peaks of $MoTe_2$ (002), (004), (006), and (008) were revealed with Te (100) at 23.029°, while the annealing time reached 15 minutes and the Te phase disappeared. With the increase of the annealing time (e.g., 20 minutes), the crystallization of the films was not better than that of the films annealed for 15 minutes and the intensities of the peaks became weak.

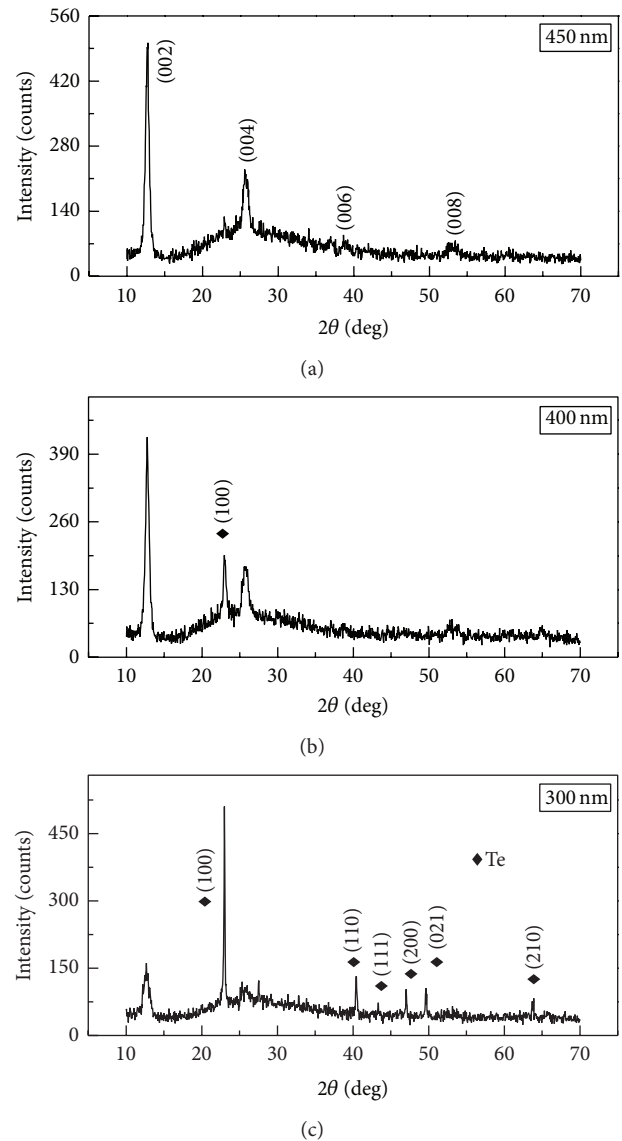


FIGURE 7: XRD patterns of Mo-Te thin films annealed at 470°C in N_2 ambient with different thicknesses.

The poor crystallization can be also attributed in part to the reevaporation of tellurium.

From Figure 7, peaks of Te (100), (110), (111), (200), (021), and (210) for 300 nm thick Mo-Te thin films were detected with $MoTe_2$ (002). As the film thickness increased to 400 nm, the number of diffraction peaks of Te was suppressed and the peak of $MoTe_2$ (004) was firstly observed. With the increase of the thickness for the thin films, more peaks of single phase $MoTe_2$, such as (006) and (008), were detected in the 450 nm thick Mo-Te thin films.

4. Conclusions

Mo-Te thin films were deposited at room temperature by electron beam evaporation, and then the films were annealed in N_2 ambient under different conditions. The formation of

MoTe₂ thin films took place at about 350°C and the structure of the thin films was stable from room temperature to 500°C. As the temperature increased, the growth of the MoTe₂ phase was predominated and the Te secondary phase was suppressed. The thin films were single phase MoTe₂ and well crystallized in the hexagonal structure annealed at 470°C or higher. At a temperature of 500°C or higher, or even for a long annealing time, the thin films were poor due to the reevaporation of tellurium and the adhesion-loss problems.

Conflict of Interests

The authors declare that there is no conflict of interests regarding the publication of this paper.

Acknowledgments

This work was supported by the National Basic Research Program of China (Grant no. 2011CBA007008), National Natural Science Foundation of China (Grant no. 61076058), and the Science and Technology Program of Sichuan Province, China (Grant no. 13ZC2185).

References

- [1] T. Löher, Y. Tomm, C. Pettenkofer, A. Klein, and W. Jaegermann, "Structural dipoles at interfaces between polar II-VI semiconductors CdS and CdTe and non-polar layered transition metal dichalcogenide semiconductors MoTe₂ and WSe₂," *Semiconductor Science and Technology*, vol. 15, no. 6, pp. 514–522, 2000.
- [2] T. Böker, R. Severin, A. Müller et al., "Band structure of MoS₂, MoSe₂, and α -MoTe₂: angle-resolved photoelectron spectroscopy and ab initio calculations," *Physical Review B: Condensed Matter and Materials Physics*, vol. 64, no. 23, Article ID 235305, p. 235305, 2001.
- [3] A. R. Beal, J. C. Knights, and W. Y. Liang, "Transmission spectra of some transition metal dichalcogenides. II. Group VIA: trigonal prismatic coordination," *Journal of Physics C: Solid State Physics*, vol. 5, no. 24, pp. 3540–3551, 1972.
- [4] Y. Ma, Y. Dai, M. Guo, C. Niu, J. Lu, and B. Huang, "Electronic and magnetic properties of perfect, vacancy-doped, and non-metal adsorbed MoSe₂, MoTe₂ and WS₂ monolayers," *Physical Chemistry Chemical Physics*, vol. 13, no. 34, pp. 15546–15553, 2011.
- [5] X. Zong, H. Yan, G. Wu et al., "Enhancement of photocatalytic H₂ evolution on CdS by loading MoS₂ as cocatalyst under visible light irradiation," *The Journal of the American Chemical Society*, vol. 130, no. 23, pp. 7176–7177, 2008.
- [6] J. A. Wilson and A. D. Yoffe, "The transition metal dichalcogenides discussion and interpretation of the observed optical, electrical and structural properties," *Advances in Physics*, vol. 18, pp. 193–335, 1969.
- [7] J. M. Pawlikowski, "Physical limitations of polycrystalline thin film photoelectric devices," *Thin Solid Films*, vol. 190, no. 1, pp. 39–64, 1990.
- [8] A. Conan, A. Bonnet, A. Amrouche, and M. Spiesser, "Semiconducting properties and band structure of MoTe₂ single crystals," *Journal de Physique Paris*, vol. 45, no. 3, pp. 459–465, 1984.
- [9] J. C. Bernede, J. Pouzet, N. Manai, and A. B. Mouais, "Structural characterization of synthesized molybdenum ditelluride thin films," *Materials Research Bulletin*, vol. 25, no. 1, pp. 31–42, 1990.
- [10] A. Ouadah, J. C. Bernede, and J. Pouzet, "MoTe₂ thin films synthesized by solid state reactions between Mo and Te Thin Films," *Physica Status Solidi A*, vol. 134, no. 2, pp. 455–466, 1992.

Research Article

Analysis and Monitoring Results of a Building Integrated Photovoltaic Façade Using PV Ceramic Tiles in Taiwan

Yen-Chieh Huang,¹ Chi-Chang Chan,² Szu-Chi Kuan,²
Shui-Jinn Wang,^{1,3} and Shin-Ku Lee⁴

¹ Institute of Microelectronics, Department of Electrical Engineering, National Cheng Kung University, Tainan 701, Taiwan

² Green Energy & Environment Research Laboratories, Industrial Technology Research Institute, Hsinchu 310, Taiwan

³ Advanced Optoelectronic Technology Center, National Cheng Kung University, Tainan 701, Taiwan

⁴ Research Center for Energy Technology and Strategy, National Cheng Kung University, Tainan 701, Taiwan

Correspondence should be addressed to Shin-Ku Lee; sklee1015@gmail.com

Received 21 February 2014; Accepted 1 May 2014; Published 6 July 2014

Academic Editor: Sudhakar Shet

Copyright © 2014 Yen-Chieh Huang et al. This is an open access article distributed under the Creative Commons Attribution License, which permits unrestricted use, distribution, and reproduction in any medium, provided the original work is properly cited.

Single-crystal silicon-based solar cells laminated with tempered-glass and ceramic tiles for use in a building's façade have been developed. The optical, thermal, and electrical properties of the proposed PV module are first evaluated, and then a wind-resistance test is carried out to evaluate the feasibility of installing it in Taiwan. The electrical and deflection characteristics of the proposed PV module did not change significantly after a 50 thermal cycling test and a 200-hour humidity-freeze test, based on IEC 61215 and a wind-resistance test. Finally, the electrical power generation ability of the proposed BIPV system with 1 kWp electrical power capacity was examined. Building information modeling software tools were used to simulate the BIPV system and carry out the energy analysis. The simulation results show a very consistent trend with regard to the actual monthly electricity production of the BIPV system designed in this work. The BIPV system was able to produce an accumulative electrical power of 185 kWh during the 6-month experimental period. In addition, the exterior temperature of the demonstration house was about 10°C lower than the surface of the BIPV system, which could reduce indoor temperature.

1. Introduction

The world population exceeded seven billion in 2012, presenting problems with regard to shortages of food and conventional energy sources. In addition, emissions of greenhouse gases (GHG), such as carbon dioxide, nitrogen sulfide, and fluorine carbonate, which are related to the burning of fossil fuels, are adversely affecting the environment and leading to a rise in global temperature [1]. Solar energy is a renewable energy resource that can be easily obtained and presents no problems with regard to pollution. However, there are still two main issues that hinder the development of the solar cell industry. One is the cost of generating electrical power per unit cell, which cannot compete with conventional electrical power production based on fossil fuels or nuclear energy. Another is the varied distribution of sun irradiation on

the earth's surface, which makes it difficult to obtain sufficient solar energy at a reasonable cost in many places.

Most current solar cells use Si-based technology and can be divided into single-crystalline, polycrystalline, and amorphous-silicon (α -Si) types. Single-crystal solar cells have the highest efficiency of 16 to 24%, with a maximum modular efficiency of 20%. Polycrystal and α -Si solar cells have efficiencies of 14 to 18% and 4 to 10%, respectively. Although they have a lower photoelectron conversion efficiency compared with single-crystal solar cells, α -Si and non-Si-based solar cells, such as CdTe, CIS, and CIGS, have the advantages of greater flexibility and transparency, as well as lower cost, and these qualities make them suitable for use in thin film technologies [2].

The use of the building incorporated photovoltaic (BIPV) systems is one of the most promising technologies with

regard to the development of the state-of-the-art photovoltaic (PV) systems. Compared to traditional nonintegrated PV systems, BIPV not only requires no extra area to be allocated for the PV systems, brackets, or rails for installation, but also offers instant electrical power for buildings, supporting applications such as air conditioning and illumination. Due to these advantages, BIPV is likely to be one strategy for successful development of PV systems in the future [3]. A BIPV system can replace the traditional envelopes of buildings, like roofs, windows, façades, and shading systems, and thus this technology has attracted the interest of many architects. A BIPV system can also provide shade from the sun, reducing the heat absorbed by the building, thus saving energy and modulating the indoor temperature [4].

While many researchers are working to develop and apply BIPV systems, few studies have evaluated the various benefits associated with the use of integrated PV kits or the effects of such systems on the comfort of those using the related buildings. In order to obtain the maximum benefits with regard to shading effects, indoor temperature, photoelectron conversion efficiency, and indoor light intensity, Kim et al. combined a sensor-embedded motor-controllable louver with solar cells to assess the allocation ability and synergistic advantages of the proposed PV kits [5]. Peng et al. discussed either choosing BIPV or building-attached photovoltaic (BAPV) systems for practical use in China. Their study not only examined how to extend the lifetime of PV systems, but also considered the functionality, price, and fabrication techniques of such systems, as well as how they affected the appearance of buildings. Based on this, they designed a BIPV system whose PV kits can be easily retrofitted and maintained on existing buildings [6].

Yoon et al. integrated transparent α -Si solar cells on a building's envelope in Korea and monitored the performance of the BIPV system for two years, with the results showing that it had electrical power throughputs of 48.4 kWh/kWp/month and 580 kWh/kWp/year. The location of the proposed PV system was inclined by 50° in the southwest and masked by nearby buildings, and the resulting masking effect caused the below-average electrical power output compared to the findings of other studies. The results of a computer simulation, which consider both shading and the solar azimuth angle, showed that the energy generation efficiency could be increased by up to 47% by modifying the location of the BIPV building [7].

Wittkopf et al. constructed a zero-energy office building in Singapore, based on integrated PV modules, and evaluated the performance of the resulting grid-connected BIPV system over 18 months under IEC standard 61724. The results showed a good overall performance ratio and average array yield of 0.81 and 3.86 h/d, respectively. The final yield was 3.12 h/d, averaged over all arrays. The efficiency of the PV system was 11.2%, and the array efficiency was 11.8%, compared to the nameplate PV module efficiency of 13.7%, while the overall inverter efficiency was 94.8%. They also divided the solar irradiation into three levels and discussed the factors that can affect this, such as shading, solar azimuth angle, inclination, and temperature, based on some selected solar cell modules [8].

Santos and Rüther quantified the potential of BIPV and BAPV systems for use with existing single-family detached residential buildings in Florianopolis, Brazil. They compared the output performance of photoelectron conversion efficiency for thin film (α -Si) and single-crystalline solar cells. The proposed PV kits were installed on the roof tops of 496 residential buildings in a mixed residential-commercial area. The roof of a typical single-family, detached home can easily accommodate the proposed PV kits, with 87% of these generators yielding at least 95% of the maximum theoretical generation output. The low-pitched, available roof covers of such residential buildings represent ideal locations for PV integration at low latitudes, and installing BIPV on all of the existing roof areas would be able to transform each and every house into a net energy-positive building [9].

Yoon et al. examined how the increase in temperature on the glass surface of BIPV systems is related to the electrical power output. The results showed that the temperature of windows situated on both the horizontal and inclined planes increased significantly during the summer, with a high solar altitude. With regard to the indoor surface temperature of the windows caused by the thermal insulation effect of BIPV systems, which is closely related to the thermal comfort of the building's occupants, the surface temperature of BIPV windows with low solar heat accumulation was 1°C less than that of normal windows during daytime in summer and was about 2°C higher at night time during winter [10].

This paper examines the case of a BIPV demonstration house composed of PV ceramic tiles that was built at the Industrial Technology Research Institute (ITRI), Hsinchu, Taiwan, at 24°46' north latitude and 121°02' east longitude, with the PV module on the vertical wall of the experimental house facing west. First, the optical, thermal, and electrical properties of the proposed PV module are evaluated. A wind-resistance test based on the ASTM E330 [11] standard is then implemented to evaluate the material performance of the PV module using the architectural dry-suspended method. Finally, the BIPV system is directly hung on the vertical wall of the demonstration house to evaluate the in situ power generation. In addition, a powerful building information modeling (BIM) simulation technology is applied to the modeling and energy analysis of this BIPV system [12].

Since there are some unfavorable factors for widespread installation of BIPV systems. For example, the cost of PV modules is still too high, and a better design approach is needed so that cheaper architectural strategies can be used. In addition, more data needs to be obtained from computer simulations in order to design more energy efficient BIPV buildings.

The current study presents a simulation and energy analysis of a BIPV demonstration house using the BIM modeling software, the results of which can help to evaluate and improve the design of BIPV buildings. More specifically, the electrical power generation performance of the proposed BIPV system was investigated for a period of six months in Taiwan, and the data obtained from this can be used to develop better PV ceramic tiles for use in such systems.

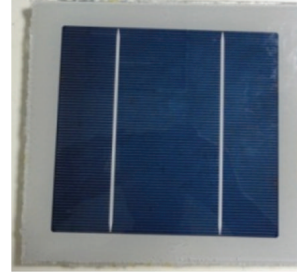
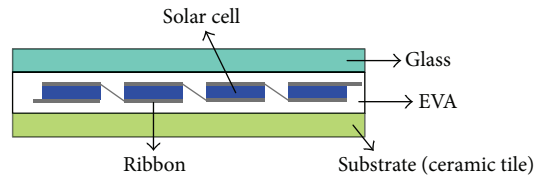


FIGURE 1: Schematic diagram of the proposed PV module.

2. Experimental Setup

2.1. PV Module Structure. A PV module consists of multiple components, including solar cells, mechanical and electrical connections, mountings, and means of regulating and/or modifying the electrical output. All the materials used in the module need to be resistant to water, electricity, and temperature. The structure of the single-crystal solar cells integrated with a ceramic tile is shown in Figure 1. The length, width, and thickness of the PV module are $40\text{ cm} \times 40\text{ cm} \times 12\text{ mm}$, respectively, and this PV module is laminated between tempered-glass and ceramic tile substrate using an ethylene vinyl acetate (EVA) copolymer. The solar cells each are serially connected by copper conducting wires. The proposed PV module is finished when all the interconnecting circuits are completely connected to a connection box on the reverse side of the device.

2.2. Optical Property Measurement. UV-Vis absorption spectra are recorded using a Lambda 900 UV-VIS-NIR spectrophotometer (Perkin-Elmer, UK). Spectral transmittance/reflectance measurements of the samples are carried out to determine the optical properties in the spectral range of solar radiation and thus in the wavelength interval between 300 nm and 2500 nm , based on ISO 9050 [13]. In addition, the emissivity of the samples is determined using an FTIR spectrophotometer (Perkin-Elmer, UK). The FTIR spectra are recorded in the range from 400 cm^{-1} to 4000 cm^{-1} , with a resolution of 4 cm^{-1} , and averaged over 25 scans.

2.3. Thermal Property Measurement. The small-sized hot-box test with a solar simulator lamp, designed in an earlier work [14], is used to evaluate the thermal performance of the PV module. The walls of the chamber are made of 0.05 m thick Styrofoam plates. The inner surfaces of the chamber are painted black to prevent light from being reflected and diffused away from the glass surface. A 1000 W xenon arc lamp is used as a solar simulator lamp to provide the incident radiant energy. The xenon arc lamp is positioned in order to achieve a homogenous distribution of radiant intensity across the whole surface area of the PV module. Six K-type thermocouples are used to measure the surface temperature on both sides of the PV module, and two K-type thermocouples are used to measure the exterior and interior ambient temperatures.

2.4. Maximum Power Determination. The maximum power determination tests are performed under standard test conditions, which correspond to 1000 W/m^2 at a cell temperature of $25 \pm 2^\circ\text{C}$, with an air mass of $AM_{1.5}$ solar spectral irradiance. To assess the performance of the samples under practical conditions, a 50 thermal cycling test and a 200 h humidity-freeze test based on IEC 61215 are carried out [15].

2.5. Wind-Resistance Test Procedure. Figures 2(a) and 2(b) show the solar cell arrays (3×4), with a size of $1,266\text{ mm} \times 1,670\text{ mm} \times 120\text{ mm}$, that are used to evaluate the wind-resistance characteristics of the proposed BIPV system using the architectural dry-suspended method. A wind resistance test based on the ASTM E330 standard is conducted in an approved test chamber at an accredited independent testing laboratory. Applying a test load spectrum allows the structural performance of a BIPV system subjected to an extreme wind event to be assessed. The specified load spectrum should contain a series of varying positive and negative pressure cycles that represent the wind behavior that affects buildings. Based on the mechanical load test in Section 10.16 of the IEC-61215 standard, 2400 Pa ($\pm 800\text{ Pa}$) is used as the standard test condition for the PV module.

The uniform static air pressure differences (P) acting inward and outward are related to the wind velocities (V) and the Beaufort scale (B) by (1) and can be used to confirm to what degree actual wind disaster conditions are achieved:

$$V = 0.836 \times (B^{3/2}), \quad (1)$$

$$P = kV^2,$$

where k is a constant and the value is 0.124 in CGS units. Using wind pressure between 2400 Pa and 6400 Pa , the specified load spectrum is divided into five varying positive and negative progressive pressurized phases. In each phase, the pressure is increased by 1000 Pa , with each increase being one unit on the Beaufort scale. For the deflection measurement, three sets of displacement gauges are mounted at various locations along the longitudinal centerline of the windward and leeward surfaces of the PV module. A visual inspection based on Section 10.1 of the IEC-61215 standard is conducted to detect any cracking, bending, deformation, or damage occurring on the PV module in terms of the solar cell, connecting junction, and the critical looseness of the alumina frames. The critical defects which could significantly affect

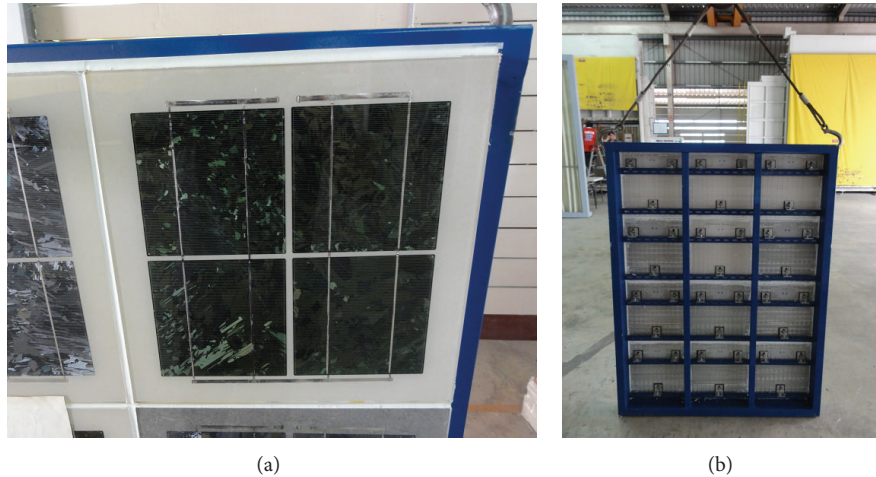


FIGURE 2: (a) Outward and (b) backward sides of the PV module.

the performance of the PV module are determined using a lamp with an illumination of not less than 1,000 lux.

The procedure for the wind-resistance test is as follows.

- (1) Remove any sealing or construction material from the test specimen that will not be used when the assembly is installed in or on a building. Fit the specimen into or against the chamber opening. The outdoor side of the specimen is subjected to positive loads, and the indoor side is subjected to negative loads. Support and secure the specimen by the same number and type of anchors used when installing the unit on a building or, if this is impractical, by the same number of other comparable fasteners, located in the same way as in the intended installations.

Remarks. If the air flow through the test specimen is such that the specimen cannot be secured, then the cracks and joints through which air leaks should be sealed using tape or other means that will effectively stop this, although this should not restrict any of the movements of the specimen components. As an alternative, it is possible to cover the entire specimen and mounting panel using a plastic film with a thickness of 0.05 mm. However, the technique used to apply this is important, in order to ensure that the maximum load is transferred to the specimen and that the plastic film does not prevent the movement or cause the failure of the specimen. The plastic film should be applied loosely, with the folds of the material at each corner and at all offsets and recesses. When the load is applied, there should be no fillets caused by the tightness of the plastic film.

- (2) Check the specimen and adjust it if needed.
- (3) Install any deflection measuring devices at the required locations.
- (4) Apply $1/2$ of the maximum test load and hold for 10 s. Release the pressure difference across the specimen and record the initial reading. The recovery period

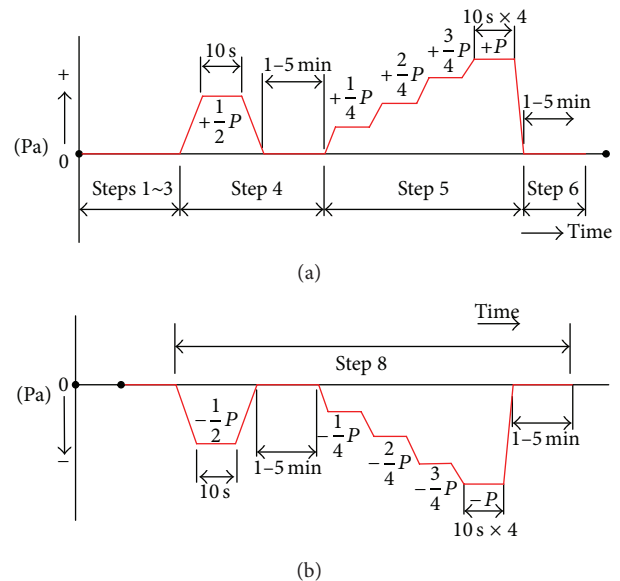


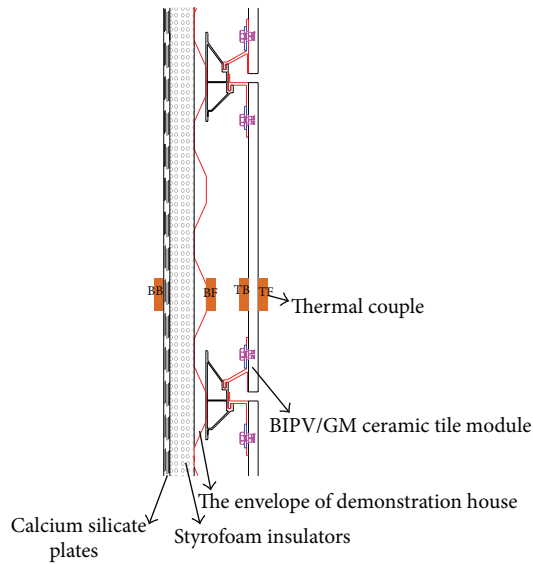
FIGURE 3: (a) Positive wind pressure intervals and (b) negative wind pressure intervals for wind resistance test.

should not be less than 1 min or greater than 5 min at zero loading.

- (5) Apply the load in the number of increments specified by the maximum test load, which should not be less than four approximately equal increments. Apply and maintain the full test load for 10 s unless otherwise specified, and record the related deflection readings (Figure 3(a)).
- (6) Release the pressure difference and, after a recovery period, which allows for stabilization, record the permanent deformation. The recovery period for stabilization should not be less than 1 min or greater than 5 min at zero loading.



(a)



(b)

FIGURE 4: (a) The 1 kWp BIPV system is hung on the vertical wall of the demonstration house, (b) the cross-section structure of the BIPV/GM system.

- (7) If the behavior of the specimen under load indicates that sudden failure may occur, which would damage the measuring specimen, the deflection measuring specimen may be removed, and the load should then be continuously increased until the maximum test load or maximum load that can be sustained is reached. At this point, release the load, and, after a recovery period, record the permanent deformation. The recovery period for stabilization should not be less than 1 min or greater than 5 min at zero load.
- (8) Repeat steps 4~7 in the reverse loading direction (Figure 3(b)).

2.6. Full-Scale Demonstration House and Electrical Plan. Figures 4(a) and 4(b) show the proposed 1 kWp BIPV system composed of 6×14 PV modules, with each containing 2×2 solar cell arrays ($40 \text{ cm} \times 40 \text{ cm} \times 12 \text{ mm}$), which is integrated into the vertical wall of the demonstration house. The length, width, and height of the BIPV system are

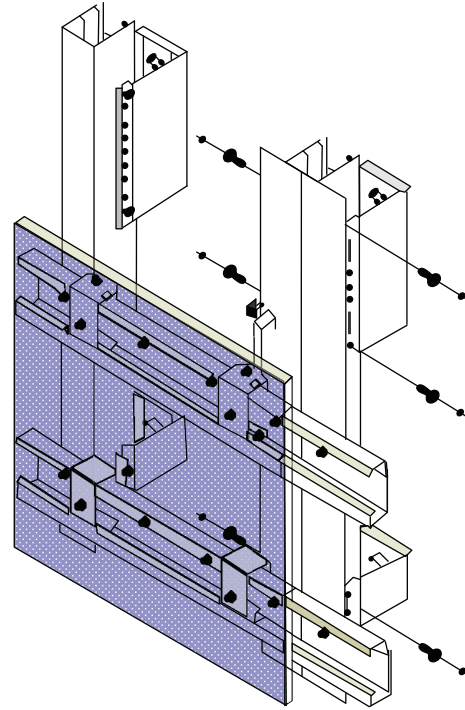


FIGURE 5: Back anchor system.

$604.5 \text{ cm} \times 12 \text{ cm} \times 259 \text{ cm}$, respectively. The demonstration house façade contains a BIPV system, air-gap layer, outer steel frame, 30 mm Styrofoam insulators, and 9 mm calcium silicate plates. Four thermal couples are used to measure the temperature on the front side (TF) and back side (TB) of the BIPV system and exterior surface (BF) and interior surface (BB) of the demonstration house. A pyranometer based on ISO 9060 second class [16] is used to sample the irradiation data every ten seconds and every one minute. The BIPV system adopts the novel architectural dry-suspended method, with the back anchor system shown in Figure 5.

Figure 6 shows the electrical-circuit layout of the 1 kWp BIPV/GM system. Each 21 PV modules by shunt winding are connected to a 10 A no fuse breaker (NFB) switch, which has about 37.8 V of V-MPP. A 250 W charge-discharge controller is used for two sets of serial PV modules and twelve 2 V batteries were charged using the maximum power point tracking (MPPT) solar charge controller. This standalone BIPV system design is used with a 3 kW DC/AC electrical transformer, and this electrical plan can output 24 V DC and 110 V AC voltage to the loads. The total capacity of the batteries is 13,320 Ah (26.6 kWh), which can supply electrical power for up to 20 hours with a 1 kWp AC load.

3. Numerical Simulation

Computer simulations have been shown to be an effective way to evaluate the energy performance of buildings. The computer simulation assessment by the “Autodesk Ecotect Analysis” simulation software carried out in this work analyzes the energy and electrical generation performance of

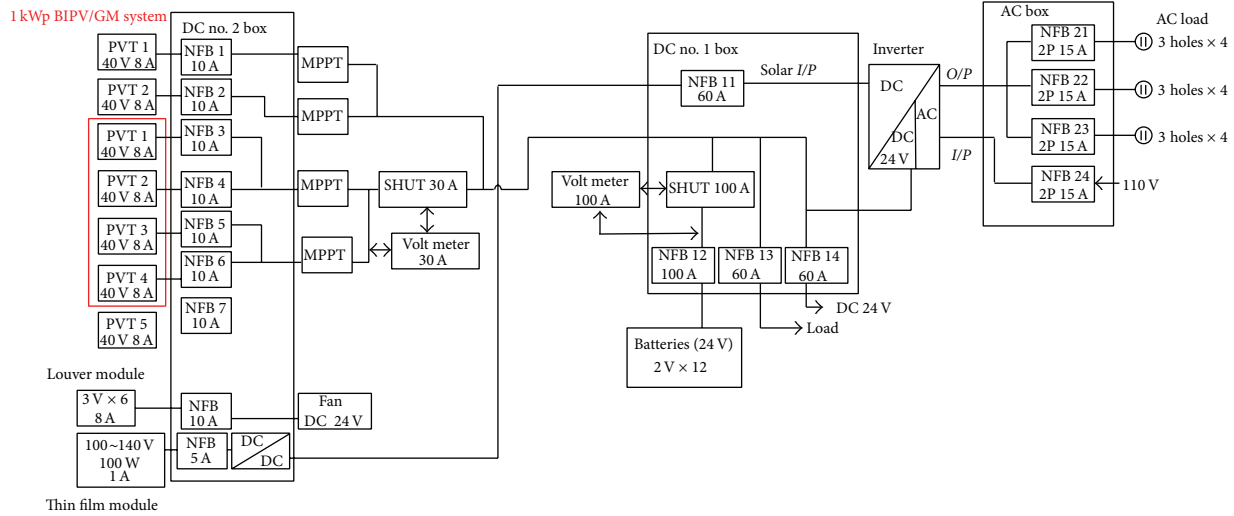


FIGURE 6: The electrical-circuit layout of the 1 kWp BIPV/GM system.

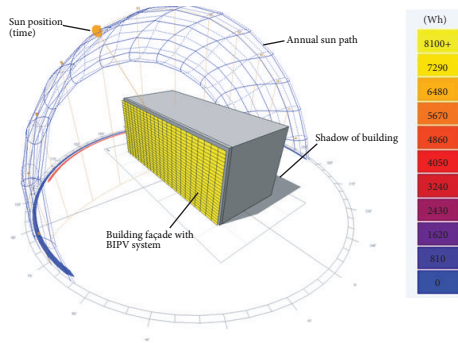


FIGURE 7: The BIM model for the demonstration house.

TABLE 1: Optical properties of the proposed BIPV.

	BIPV module
UV transmittance	0
UV reflectivity	5.40
Visible light transmittance	0
Visible light reflectivity	5.45
Solar irradiation transmittance	0
Solar irradiation reflectivity	8.45
Solar irradiation absorptivity	91.55
Emissivity front side (outdoor)	0.837
Emissivity back side	0.927

whole demonstration house integrated with the BIPV system. In order to find the best design of the BIPV systems used on the building's envelope in all directions and also for four vertical walls of the building in this study, we build both a BIPV demonstration house and a simulation model to simulate the performance of electrical power generation. The simulation model is then used to compile and throughput each electrical power generation condition for the BIPV demonstration house design.

In our experiment, the BIPV demonstration house is located in Hsinchu, Taiwan. The simulation model is based on the average weather data for Hsinchu over the last 10 years (2002–2012; Central Weather Bureau, Taiwan). The computational simulation control factors include the solar azimuth, the building location, the distribution of solar irradiation, the temperature variation, and the shading of the BIPV demonstration house. The BIM model of the BIPV demonstration house is shown in Figure 7.

4. Result and Discussion

Much of the work to integrate PV modules into the design of buildings has focused on the issues of power generation

efficiency and thermal performance, with many examples placing the devices on roofs, since this location has greater solar irradiation intensity and less shade. Most PV modules adopt poly- or α -Si solar cells to make a trade-off between construction cost and electrical generation. In the experiment carried out in the current study, the BIPV system hangs directly on the vertical wall of a demonstration house, and the shading effect and solar azimuth angle will reduce the system's electrical generation capacity. This work thus adopts single-crystal solar cells combined with a ceramic tile for efficient photoelectron conversion and steady electrical power generation. This approach is based on the ideas presented in Iencinella et al., which integrated thin film α -Si solar cells with 10 cm \times 10 cm ceramic tiles [17]. Ceramic tiles are often used as building materials and have the advantages of high porosity and high thermal conductivity. By simultaneously serving as both the building envelope material and a power generation device, the BIPV system presented in the current work can provide savings in both material and electricity costs and add architectural interest to a building.

4.1. Optical Properties. Table 1 shows the optical properties of the proposed PV module. Most solar cells use

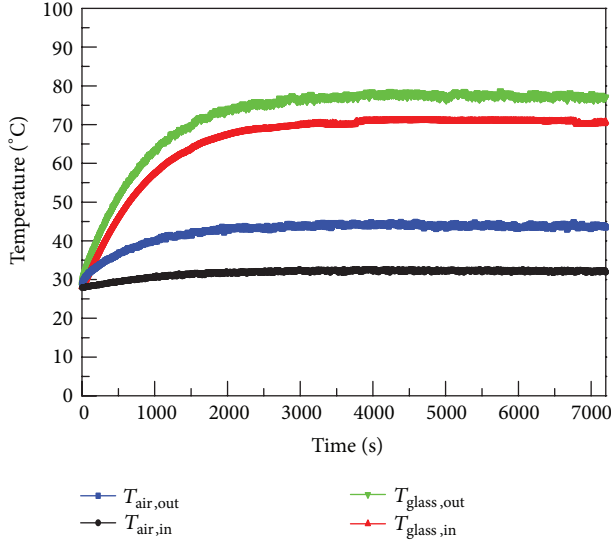


FIGURE 8: Histories of the surface temperature ($T_{glass,out}$ and $T_{glass,in}$) and ambient temperature ($T_{air,out}$ and $T_{air,in}$) for the proposed PV module.

a double-glazed type of packaging, sandwiched between two sheets of tempered-glass. The solar cells are then serially or shuntly connected by copper conducting wires that go into a connection box. Although BIPV systems that use transparent glass have greater visible light transmittance, they also have poor thermal insulating capabilities and are less safe, due to their greater weight and fragility. This study presented a PV module that is integrated with ceramic tiles and directly hangs on a building's façade using the architectural dry-suspended method, and thus a high visible light transmittance is not required. On the other hand, the high solar irradiation absorptivity and surface emissivity of the proposed PV module can help to achieve more efficient photoelectron conversion.

4.2. Thermal Properties. Figure 8 presents the surface temperature of the exterior and interior sides of the proposed PV module. The steady temperature of exterior surface of PV module is 72°C, while that of the other side is 65°C. The temperature on the exterior surface is greater than that on the interior side because of the high heat-absorptive ability and heat accumulation on the rear of the PV ceramic tile. The lower inside temperature of the PV module can reduce the thermal accumulation that otherwise occurs to decrease photoelectron efficiency of solar cells.

4.3. Electrical Characteristics. Table 2 shows the open circuit voltage (V_{oc}), short circuit current (I_{sc}), fill factor (FF), and maximum power determination (P_{max}) for a conventional PV module and the proposed PV module. Although the V_{oc} and I_{sc} of the proposed PV module are a little lower than those of the conventional module, and the P_{max} there is 4.6% lower, the proposed PV module has higher fill factor. Table 3 shows the electrical characteristics of this PV module before and after a 50 thermal cycling test and a 200 h humidity-freeze

TABLE 2: Results of maximum power determination test.

Class: A	STC	$E: 1000 \text{ W/m}^2$	Temp.: 25°C
Items	Unit	Conventional PV module	Proposed PV module
V_{oc}	[V]	0.62	0.61
I_{sc}	[A]	8.27	7.70
P_{max}	[W]	3.59	3.43
FF	[%]	70.33	72.93

TABLE 3: Results of maximum power determination test for PV module.

Class: A	STC	$E: 1000 \text{ W/m}^2$	Temp.: 25°C
Items	Unit	Before test	After test
V_{oc}	[V]	0.60	0.61
I_{sc}	[A]	7.72	7.70
P_{max}	[W]	3.41	3.43
FF	[%]	72.69	72.93

test based on the IEC 61215 standard [15]. The results show that there was no significant decay in terms of the electrical characteristics of the PV module. This indicates that this PV module is suitable for use in the kind of humid weather that is common in Taiwan, which is a subtropical island.

4.4. Wind-Resistance Test. When resistance to severe snow or ice accumulation is required, the IEC-61215 standard states that the front surface pressure of the module should be able to withstand 5400 Pa. The current study thus tested the inward and outward wind resistance up to 6400 Pa, with 2400 Pa used as the benchmark and 6400 Pa as the maximum test conditions. This is of practical interest in Taiwan, as the island is often hit by typhoons. The results shown in Table 4 indicate that the PV module suffered from no significant deflection or damage after wind-resistance test. The proposed PV module is thus able to withstand a level 17 typhoon in Beaufort scale.

4.5. Simulation Results. The BIM modeling and energy analysis software is a powerful tool that can be used to effectively predict and simulate the solar cell irradiation intensity and electrical power generation levels in relation to BIPV buildings. Since solar irradiation on the four directions of building façades (north, south, east, and west) varies with the time of a day, this will also affect the level of electrical power generation. Figures 9(a)~9(h) show the simulation results, based on the annual solar trajectory and solar irradiation intensity, for four façades of the demonstration house at 10 o'clock in the morning and 3 o'clock in the afternoon. And the daily electrical power generation is also shown in Figure 10 for west, east, south, and north cases, and it can be seen that the western facing façade produces the maximum electrical power. In addition, in the western case, the electrical power generation starts at 11 o'clock in the morning and lasts until 4 o'clock in the afternoon, with the maximum at 2 o'clock. The peak of electrical power generation for the west side of the building is the highest, at around 900 Wh at 2

TABLE 4: Results of wind resistance test.

Interval	Wind pressure (Pa)	Maximum deflection	Maximum deflection/span ratio	Visual inspection
01	+2400	0.10 mm	1/15070	No deformation effect
02	-2400	-0.90 mm	1/1674	No deformation effect
03	+3400	1.80 mm	1/837	No deformation effect
04	-3400	-2.00 mm	1/745	No deformation effect
05	+4400	2.30 mm	1/655	No deformation effect
06	-4400	-2.50 mm	1/603	No deformation effect
07	+5400	2.90 mm	1/520	No deformation effect
08	-5400	-3.00 mm	1/502	No deformation effect
09	+6400	3.55 mm	1/425	No deformation effect
10	-6400	-3.80 mm	1/397	No deformation effect

o'clock in the afternoon. The south side of the building has a longer electrical generation time than the east and west sides. However, the peak of electrical power generation for the south side is only about 280 Wh, which means that this side has a lower solar irradiation intensity over a day. Further, the northern facing façade has the lowest electrical power generation, since Taiwan is in the Northern Hemisphere. In summary, the western façade of the building has the greatest electrical power generation of the four cases examined in this work. The results of this simulation can help in the development of an experimental BIPV demonstration house that faces towards the west and thus generates the most electrical power.

Table 5 lists the monthly electrical power generation results for a whole year, with these being 443.1 kWh, 443.5 kWh, 438.6 kWh, and 47.8 kWh for the east, west, south, and north cases, respectively. These results indicate that when the BIPV system faces east, west, or south, it can produce almost the same amount of electrical power. The total annual BIPV power output from the western side of the building is a little higher (0.4 kWh) than that from the eastern and southern sides and almost 10 times greater than that on the northern side. This reveals that the direction that a building façade faces is an important factor with regard to solar irradiation intensity and thus the resulting electricity generation potential.

Figure 11 shows the monthly electrical generation (kWh) of a BIPV system for the building model facing in all four directions. Interestingly, although the east, west, and south cases produce almost the same amount of electrical power, the distribution of electrical power generation over time varies for each direction. For the east and the west cases, the most electrical power is generated in the summer, and for the south it is in the winter period. This information can be used to design more effective BIPV systems that can provide a steady supply of power throughout the year.

4.6. Demonstration House Performance. The BIPV system developed in this work using the architectural dry-suspended method is hung directly on the vertical wall of the demonstration house facing west, with an air gap between the BIPV system and the wall to provide natural ventilation. Good thermal dissipation thus occurs on the back side of the

TABLE 5: Simulation results for monthly electrical power generation.

Month	East (kWh)	West (kWh)	South (kWh)	North (kWh)
January	18.075	16.748	49.297	0.223
February	17.893	15.013	45.315	0
March	22.947	23.085	38.750	0
April	35.784	32.245	27.051	0.400
May	44.128	47.530	9.186	6.415
June	59.503	55.811	1.852	17.459
July	72.133	64.637	4.883	18.269
August	64.150	62.341	24.486	5.011
September	42.896	47.421	47.085	0.093
October	28.200	35.602	60.505	0
November	22.065	26.178	72.440	0
December	15.372	16.919	57.802	0
Annual total	443.146	443.530	438.652	47.870

BIPV system, which can modulate the indoor temperature of the building. Furthermore, the use of the architectural dry-suspended method means that buildings can be easily retrofitted and the BIPV system can be easily maintained.

Figure 12 shows the temperature distribution of the demonstration house and the ambient temperature (T_a), with the daily measurements taken from 8:00 to 17:00. The results indicate that there is no significant variation in temperature between the exterior and the interior surfaces of the demonstration house during 8:00~10:00, because the solar radiation intensity is less than 100 W/m² before 10:00 a.m. This result is the same as that seen in the simulation data, as shown in Figure 10, for the case when the façade faces west. The simulation data show that both electricity generation and solar irradiation intensity increase from 11 o'clock in the morning until 4 o'clock in the afternoon. As the solar irradiation intensity increases over time, the BIPV system starts to generate electrical power, although the temperature on the exterior surface of the demonstration house is still about 10°C lower than that on the front side of the BIPV system. This good insulating effect can ascribe to the high thermal inertia of ceramic tiles and the architectural dry-suspended method adopted for the BIPV system. This BIPV

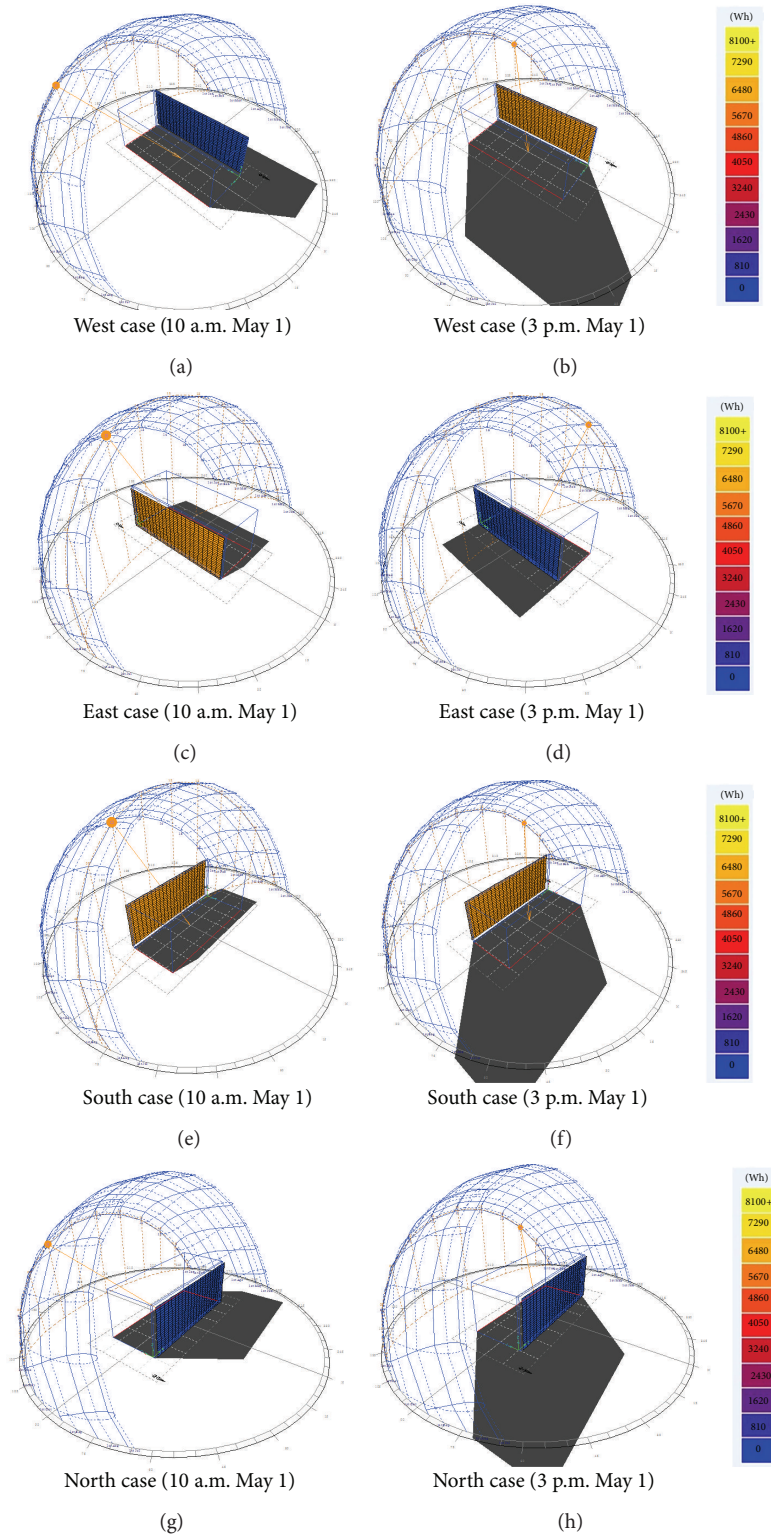


FIGURE 9: Solar trajectory and irradiation intensity of (a), (b) west, (c), (d) east, (e), (f) south, and (g), (h) north cases.

system can thus isolate the heat from solar irradiation and modulate the indoor temperature. In addition, there is also an air gap between the BIPV system and the vertical wall that facilitates natural ventilation, which can also reduce thermal

accumulation and the temperature of the back of the BIPV system. An infrared thermomaging instrument (NEC, TVS-200ES) was used to examine the temperature distribution of the BIPV system. Figure 13 shows the surface temperature

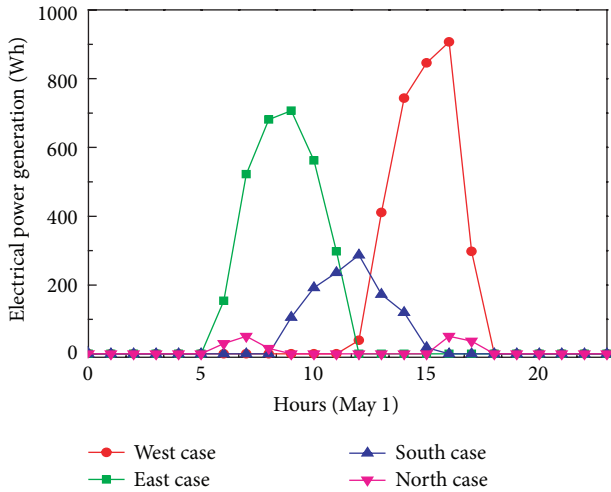


FIGURE 10: Daily electrical power generation of west, east, south, and north cases.

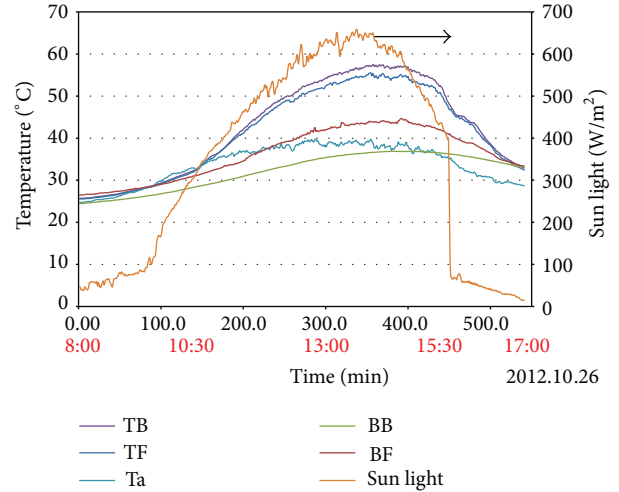


FIGURE 12: Temperature measurement of the BIPV system.

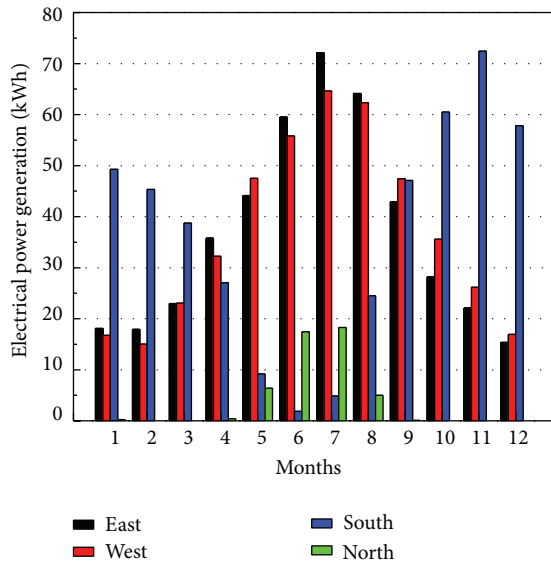


FIGURE 11: The monthly electrical output (kWh) of the BIPV for the building model facing in all four directions.

distribution of the BIPV system at 14:00. The results indicate that the distribution on the perpendicular surface of the BIPV system is almost uniform, and the temperature difference from top to bottom is about 2°C. Since the proposed BIPV system is hung perpendicularly on the vertical wall of the demonstration house, this variation in temperature is caused by different solar azimuth angle and thus changes in the solar irradiation intensity.

Table 6 shows the accumulated electrical power generated by the proposed BIPV demonstration house over six months, with the result being 185 kWh. Figure 14 compares the experimental and simulated electrical power generation data for the period from October, 2012, to March, 2013. The trend of the simulation is consistent with the experimental results, although the former underestimates the latter by

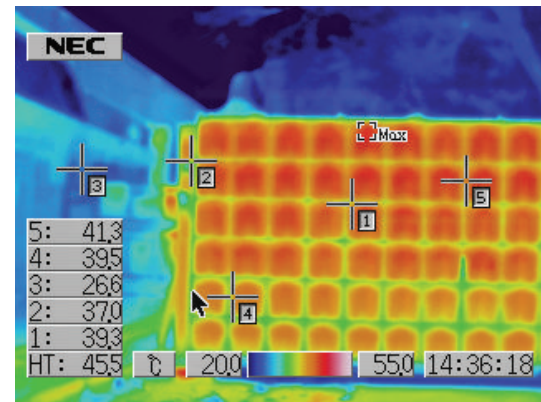


FIGURE 13: Temperature distribution of the BIPV system.

about 27%, which is greater than the difference reported in an earlier study, which underestimated the power generation by about 20% [18]. However, since the data obtained in the current study show a good fit between the trends from the simulated and experimental data, the findings of this work can be used to predict the electrical generation performance of versatile BIPV systems and thus improved the design of this technology.

5. Conclusions

The concepts of net zero energy, zero energy, and passive energy are becoming more important as part of the energy conservation policies adopted by the building construction industry. BIPV systems can be integrated into buildings in order to save energy, reduce installation costs, and modulate the indoor temperature.

This work presented a PV ceramic tile that can prevent thermal accumulation and add aesthetic interest to a building's façade. In addition, the architectural dry-suspended method that is used to install this system can enhance the efficiency of natural ventilation. The results of a 50

TABLE 6: Electrical power accumulation for the six-month experimental monitoring.

Experimental period	Electrical power generation (kWh)
October 1–October 31, 2012	53
November 1–November 30, 2012	26
December 1–December 30, 2012	26
January 1–January 31, 2013	28
February 1–February 28, 2013	22
March 1–March 31, 2013	30
Total	185

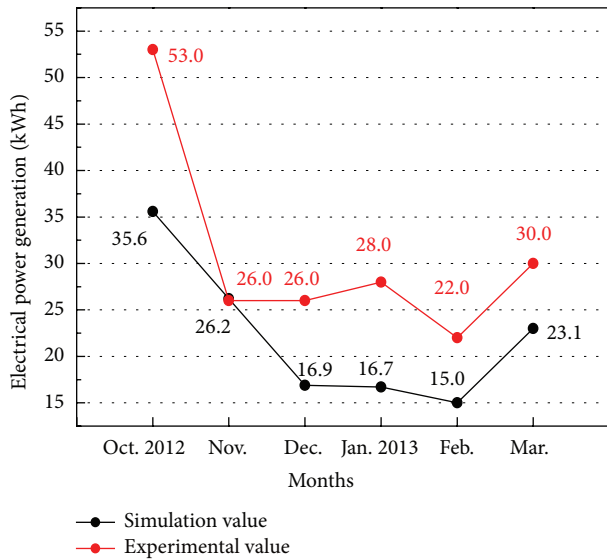


FIGURE 14: Comparison of electrical generation results from the simulation and experiment.

thermal cycling test, a 200 h humidity-freeze test, and a wind-resistance test show that the proposed BIPV system is strong enough to withstand typhoons and a humid climate, both of which are common in Taiwan. In addition, Autodesk software was used to carry out a BIM modeling and energy analysis of the BIPV demonstration house. The results of the simulation have a very similar trend with regard to the level of electrical power generation as the six-month experimental data that was obtained from October, 2012, to March, 2013. This data can be used to improve the design of BIPV systems, making them more efficient and cheaper. The results of the experiments showed that the proposed BIPV system was able to generate an accumulated 185 kWh electricity over a six-month period and thus can replace a significant amount of the electricity that would otherwise be generated by burning fossil fuels. This paper thus provides valuable information for renewable energy planners and architectural designers who are interested in using BIPV systems.

Conflict of Interests

The authors declare that there is no conflict of interests regarding the publication of this paper.

Acknowledgment

The authors would like to thank the financial support from the Bureau of Energy, Taiwan.

References

- [1] McKinsey & Company, *Pathways to a Low-Carbon Economy. Version 2 of the Global Greenhouse Gas Abatement Cost Curve*, McKinsey & Company, 2009.
- [2] M. Raugei and P. Frankl, "Life cycle impacts and costs of photovoltaic systems: current state of the art and future outlooks," *Energy*, vol. 34, no. 3, pp. 392–399, 2009.
- [3] S. Strong, "Building Integrated Photovoltaics (BIPV), Whole Building Design Guide," June 2010, <http://www.wbdg.org/resources/bipv.php>.
- [4] H. J. Chen, C. M. Chiang, C. M. Shu, and S. K. Lee, "Self-power consumption research with the thermal effects and optical properties of the HCRI-BIPV window system," *Journal of Electronic Science and Technology*, vol. 10, no. 1, pp. 29–36, 2012.
- [5] J. J. Kim, S. K. Jung, Y. S. Choi, and J. T. Kim, "Optimization of photovoltaic integrated shading devices," *Indoor and Built Environment*, vol. 19, no. 1, pp. 114–122, 2010.
- [6] C. Peng, Y. Huang, and Z. Wu, "Building-integrated photovoltaics (BIPV) in architectural design in China," *Energy and Buildings*, vol. 43, no. 12, pp. 3592–3598, 2011.
- [7] J. Yoon, J. Song, and S. J. Lee, "Practical application of building integrated photovoltaic (BIPV) system using transparent amorphous silicon thin-film PV module," *Solar Energy*, vol. 85, no. 5, pp. 723–733, 2011.
- [8] S. Wittkopf, S. Valliappan, L. Liu, K. S. Ang, and S. C. J. Cheng, "Analytical performance monitoring of a 142.5 kWp grid-connected rooftop BIPV system in Singapore," *Renewable Energy*, vol. 47, pp. 9–20, 2012.
- [9] Í. P. D. Santos and R. Rüter, "The potential of building-integrated (BIPV) and building-applied photovoltaics (BAPV) in single-family, urban residences at low latitudes in Brazil," *Energy and Buildings*, vol. 50, pp. 290–297, 2012.
- [10] J. Yoon, S. Shim, Y. S. An, and K. H. Lee, "An experimental study on the annual surface temperature characteristics of amorphous silicon BIPV window," *Energy and Buildings*, vol. 62, pp. 166–175, 2013.
- [11] American Society for Testing and Materials, *ASTM E330-02: Standard Test Method for Structural Performance of Exterior Windows, Doors, Skylights and Curtain Walls by Uniform Static Air Pressure Difference*, Philadelphia, Pa, USA, 2002.
- [12] A. Porwal and K. N. Hewage, "Building Information Modeling (BIM) partnering framework for public construction projects," *Automation in Construction*, vol. 31, pp. 204–214, 2013.
- [13] ISO 9050, *Glass in Building—Determination of Light Transmittance, Solar Direct Transmittance, Total Solar Energy Transmittance, Ultraviolet Transmittance and Related Glazing Factors*, International Organization for Standardization, Geneva, Switzerland, 2003.
- [14] G. Alvarez, M. J. Palacios, and J. J. Flores, "A test method to evaluate the thermal performance of window glazings," *Applied Thermal Engineering*, vol. 20, no. 9, pp. 803–812, 2000.
- [15] International Electrotechnical Commission, *CEI/IEC 61215: Crystalline Silicon Terrestrial Photovoltaic (PV) Modules—Design Qualification and Type Approval*, International Electrotechnical Commission, Geneva, Switzerland, 2nd edition.

- [16] ISO 9060, *Solar Energy-Specification and Classification of Instruments for Measuring Hemispherical Solar and Direct Solar Radiation*, International Organization for Standardization, Geneva, Switzerland, 1990.
- [17] D. Iencinella, E. Centurioni, and M. Grazia Busana, “Thin-film solar cells on commercial ceramic tiles,” *Solar Energy Materials & Solar Cells*, vol. 93, no. 2, pp. 206–210, 2009.
- [18] L. Maturi, W. Sparber, B. Kofler, and W. Bresciani, “Analysis and monitoring results of a BIPV system in northern Italy,” in *Proceedings of the 25th European Photovoltaic Solar Energy Conference and Exhibition, and the 5th World Conference on Photovoltaic Energy Conversion*, Valencia, Spain, September 2010.

Research Article

Characterizations of Cuprous Oxide Thin Films Prepared by Sol-Gel Spin Coating Technique with Different Additives for the Photoelectrochemical Solar Cell

D. S. C. Halin,¹ I. A. Talib,² A. R. Daud,² and M. A. A. Hamid²

¹ Center of Excellence Geopolymer & Green Technology (CEGeoGTech), School of Materials Engineering, Universiti Malaysia Perlis (UniMAP), Jalan Kangar-Arau, 02600 Perlis, Malaysia

² School of Applied Physics, Faculty of Science and Technology, Universiti Kebangsaan Malaysia (UKM), 43600 Bangi, Selangor, Malaysia

Correspondence should be addressed to D. S. C. Halin; dewisuriyani@unimap.edu.my

Received 10 December 2013; Revised 16 April 2014; Accepted 14 May 2014; Published 15 June 2014

Academic Editor: Prakash Basnyat

Copyright © 2014 D. S. C. Halin et al. This is an open access article distributed under the Creative Commons Attribution License, which permits unrestricted use, distribution, and reproduction in any medium, provided the original work is properly cited.

Cuprous oxide (Cu_2O) thin films were deposited onto indium tin oxide (ITO) coated glass substrate by sol-gel spin coating technique using different additives, namely, polyethylene glycol and ethylene glycol. It was found that the organic additives added had a significant influence on the formation of Cu_2O films and lead to different microstructures and optical properties. The films were characterized by X-ray diffraction (XRD), field emission scanning electron microscopy (FESEM), and ultraviolet-visible spectroscopy (UV-Vis). Based on the FESEM micrographs, the grain size of film prepared using polyethylene glycol additive has smaller grains of about 83 nm with irregular shapes. The highest optical absorbance film was obtained by the addition of polyethylene glycol. The Cu_2O thin films were used as a working electrode in the application of photoelectrochemical solar cell (PESC).

1. Introduction

Cuprous oxide (Cu_2O) has a cubic crystal structure with a lattice parameter of 4.27 Å and this material is suitable for solar cell applications. As a solar cell material, Cu_2O has the advantages of low cost and great availability [1]. The Cu_2O is very attractive as a photovoltaic material because of its high absorption coefficient in visible regions, nontoxicity, abundantly available starting material (Cu) on earth, low cost to produce, and the theoretical energy conversion efficiency being in the order of 20% [2]. Cu_2O thin films can be prepared by various methods like reactive sputtering [3, 4], vacuum evaporation [5], chemical and thermal oxidation [6, 7], and electrodeposition [8, 9]. In recent times, sol-gel technique has proved to be an attractive method for the preparation of nanoscale grain size of metal and metal oxide materials. Armelao et al. [10] used sol-gel dip coating technique to prepare Cu_2O film with copper acetate and ethanol without any additive. Oral et al. [11] prepared CuO films with copper acetate and isopropyl alcohol and the

additives used were polyethylene glycol 400 and ethylene glycol. In this research, Cu_2O thin film was deposited onto indium tin oxide (ITO) coated glass using sol-gel technique with two different polymer additives such as polyethylene glycol and ethylene glycol because it is a soft bottom-up approach to achieve a good control over film composition and microstructure.

Investigations had shown that some polymer additives, such as polyethylene glycol $((\text{CH}_2-\text{CH}_2-\text{O})_n-\text{H})$, effectively improve the Cu_2O properties under relatively low temperature [12, 13]. To our knowledge, the use of additives is seldom found in Cu_2O preparation. The purpose of this research is to prepare Cu_2O thin film onto indium tin oxide (ITO) coated glass substrate for photoelectrochemical solar cell application (PESC) by means of sol-gel spin coating technique and to investigate the behavior of Cu_2O thin films under different additives. Not many researchers have used polyethylene glycol and ethylene glycol as additives in sol-gel technique. The as-prepared films were annealed at 350°C in 5% H_2 + 95% N_2 atmosphere in order to get single

phase Cu_2O films. The annealing temperature of 350°C is the optimum annealing temperature to prepare the single phase Cu_2O films. If the annealing temperature is increased to 450°C , other phases exist such as Cu or CuO comes into existence. The prepared Cu_2O thin film was used as a working electrode for PESC of ITO/ Cu_2O /PVC- LiClO_4 /aluminum. PESC based on Cu_2O thin films were fabricated and the current-voltage characteristic of PESC of ITO/ Cu_2O /PVC- LiClO_4 /aluminum was studied under light illumination of 100 mW/cm^2 .

2. Experimental

Copper (II) acetate ($\text{Cu}(\text{C}_2\text{H}_3\text{O}_2)_2$, 99.999% purity) was used as starting material for the synthesis of cuprous oxide thin films. Copper (II) acetate was dissolved in isopropyl alcohol and diethanolamine (DEA, $\text{C}_4\text{H}_{11}\text{NO}_2$) solution and mixed continuously. Small amount of glucocon was then added into the solution and continuously stirred for 24 hours using magnetic bar. The solution was then filtered using $0.45\ \mu\text{m}$ filter prior to spinning. Films were prepared by depositing the solution by spin coating technique onto indium tin oxide (ITO) coated glass substrate which was purchased from Sigma-Aldrich. The solution was spread onto the substrate at 3000 rpm for 40 s. The films were dried in the oven at 60°C for 10 min and the process was repeated for three layers of coating in order to get better films which fully covered the substrate. Two different additives were used, that is, polyethylene glycol and ethylene glycol. There were three sets of samples: (a) sample 1 (sample without any additive), (b) sample 2 (sample with polyethylene glycol), and (c) sample 3 (sample with ethylene glycol). Films were annealed at 350°C for 1 h in 5% $\text{H}_2 + 95\% \text{N}_2$ atmosphere. The use of 5% $\text{H}_2 + 95\% \text{N}_2$ atmosphere during annealing because of H_2 strongly affects the phase composition of Cu_2O thin film. Without the atmosphere of 5% $\text{H}_2 + 95\% \text{N}_2$, the phase composition may not be a single phase of Cu_2O thin films because there is more oxygen for copper oxide to form CuO rather than Cu_2O . The microstructure of the films was studied using X-ray diffractometer (XRD) model D-5000 Siemens. The morphology of the film was observed using field emission scanning electron microscope (FESEM) model Supra 55VP and optical properties were measured using ultraviolet-visible (UV-Vis) spectroscopy model 160A Shimadzu in the range of 300–900 nm.

3. Results and Discussion

The XRD patterns of obtained samples with different additives are shown in Figure 1. All diffraction peaks can be indexed to the cubic phase of Cu_2O crystals and match well with standard data (JCPDS 74–1230). No other phases such as CuO or Cu are found in XRD patterns confirming that all the samples exist as main Cu_2O phase. The presence of (110) plane may be due to the mechanism of the thin film which was oxidized to Cu_2O . In the sol-gel technique, the temperature and time are important factors. The single phase of Cu_2O thin films can be prepared at temperature of 350°C and time of annealing of 1 hour. When the temperature is lower or the

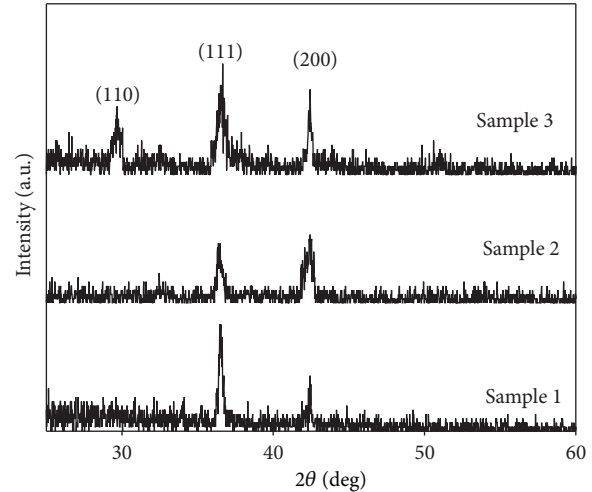


FIGURE 1: The XRD patterns of cuprous oxide thin films with different additives.

TABLE 1: The energy gap, grain size, thickness, and plane (hkl) of the Cu_2O films.

Samples	Energy gap (eV)	Grain size (nm)	Thickness (nm)	Plane (hkl)
1	1.85 ± 0.1	104	102	(111), (200)
2	1.90 ± 0.1	83	395	(111), (200)
3	1.75 ± 0.1	90	59	(110), (111), (200)

time is shorter, it is hard to reduce cupric acetate to cuprous oxide completely, whereas if the temperature is too high or the reaction time is too long, it is easy to get copper rather than cuprous oxide [14].

Figure 2 shows the FESEM micrographs of three set of samples which shows that the films grown on ITO substrate are uniform. The average grain size and thickness of the Cu_2O films for the samples are shown in Table 1. The cross section of thin films was used to measure the thickness of the film while the grain size was measured from the FESEM micrograph. The grain size was reducing from 104 nm to 83 nm, after adding polyethylene glycol. The thickness of thin film increased with the addition of polyethylene glycol. It is shown that the addition of polyethylene glycol will increase the viscosity of solution due to chain length effects [13]. The spin coating rate also can affect the thickness of the thin film; lower spin coating rate produce much thicker film due to less solution spread out from substrate.

The addition of ethylene glycol has been widely used in the polyol synthesis of metal and metal oxide due to its strong reducing ability and relatively high boiling point ($\sim 197^\circ\text{C}$). Polyol synthesis of metal consists in the reduction of metal cation in a polyol medium. Over the past few years, polyols have also been used to elaborate a great variety of oxides [15, 16] and layered hydroxyl-salt [17] by means of hydrolysis and inorganic polymerization. The addition of ethylene glycol (sample 3) with thickness of 59 nm shows that the Cu_2O grains were irregular in shape.

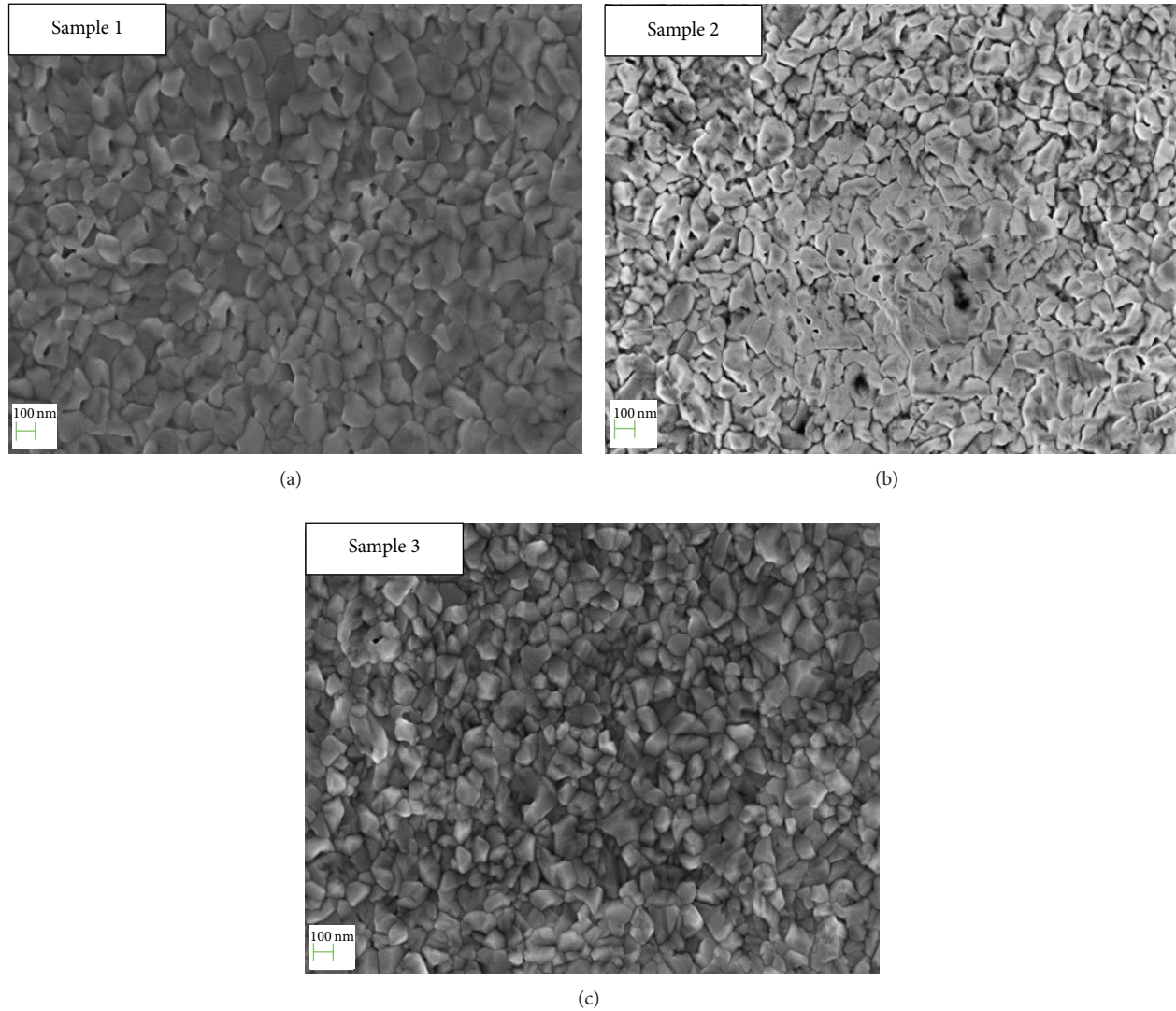


FIGURE 2: FESEM micrographs of cuprous oxide thin films with irregular grain shape.

The UV-Vis spectra of different Cu_2O samples are shown in Figure 3. The absorbance of samples may be influenced by grain size, thickness, shape, and the area of Cu_2O films covered onto ITO coated glass. The films must totally cover the ITO coated glass. The highest absorbance at wavelength of 600–700 nm obtained for sample 2 is due to its maximum thickness and smallest grain size amongst other samples. This behavior agrees well with the earlier results published by Oral et al. [11]. There is a possibility of increasing of absorbance caused by scattering at grain size as reported by Ray [7]. The absorbance of sample 2 and sample 3 shows the same trend and the absorbance can be improved by increasing the thickness of films.

The addition of polyethylene glycol will produce crack free films with high optical absorbance [5]. Since the polyethylene glycol additive can avoid the particle aggregation occurring in the sol-gel solution, sample 2 with polyethylene glycol has fine crystalline grain (83 nm) and thus decreases scattering at crystalline boundary. The absorption

coefficient, α , of the Cu_2O film is related to the photon energy $h\nu$ [7]. Consider

$$(\alpha h\nu) = (h\nu - E_g)^{1/2}, \quad (1)$$

where $h\nu$ is the photon energy and E_g is the energy gap. These energy gaps are calculated from the intercept of straight line on the photon energy ($h\nu$) of $(\alpha h\nu)^2$ versus $(h\nu)$ plot and the values are listed in Table 1. The energy gap for these films was calculated to be in the range of 1.75–2.0 eV and was found to be influenced by film thickness and also the optical absorbance. The addition of polyethylene glycol produced the thickest film with high energy gap and high optical absorbance.

The Cu_2O thin films were used as working electrodes in PESC of ITO/ Cu_2O /PVC- LiClO_4 /aluminum. The layer of PESC of ITO/ Cu_2O /PVC- LiClO_4 /aluminum was shown in Figure 4. Most of PESC reported used an aqueous solution

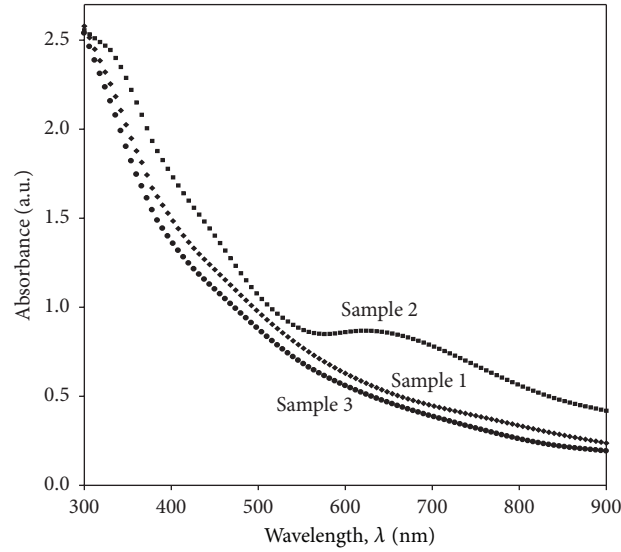


FIGURE 3: The absorbance versus wavelength for three samples with different additives.

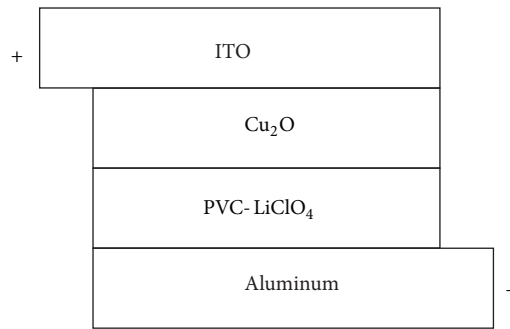


FIGURE 4: Layer of PESC of ITO/Cu₂O/PVC-LiClO₄/aluminum.

of NaOH as an electrolyte. For PESC of ITO/Cu₂O/PVC-LiClO₄/aluminum, the solid polymer electrolyte of PVC-LiClO₄ was used as an electrolyte. The total cell active area was 1.5 cm². Figure 5 shows current-voltage (*I-V*) characteristics of the PESC, under dark and light illumination. The *I-V* characteristic of sample 1 was much different from that of sample 2 and sample 3 due to absence of the additive solutions during its preparation. Sample 2 (sample with polyethylene glycol) and sample 3 (sample with ethylene glycol) have an improvement of *I-V* characteristic because of the additive. This is the first reported demonstration of photoresponse from a deposited Cu₂O thin film of ITO/Cu₂O/PVC-LiClO₄/aluminum. Open circuit voltages (V_{oc}) and short circuit currents density (J_{sc}) of ITO/Cu₂O/PVC-LiClO₄/aluminum PESC were measured under light illumination of 100 mW/cm² and shown in Table 2. The best J_{sc} and V_{oc} obtained at 100 mW cm⁻² were 3.2×10^{-11} mA/cm² and 0.092 V, respectively, for sample 2 which was the thickest film and absorbed more energy from light. From the results shown in Table 2, it was found that J_{sc} obtained from this device is low. The ITO/Cu₂O/PVC-LiClO₄/aluminum current could be improved by depositing an organic dye onto the Cu₂O films [18–20] as light sensitizer.

TABLE 2: Value of J_{sc} and V_{oc} for PESC of ITO/Cu₂O/PVC-LiClO₄/aluminium under light illumination of 100 mW/cm².

Photoelectrochemical solar cell (PESC)	J_{sc} (mA/cm ²)	V_{oc} (V)
Sample 1	1.9×10^{-11}	0.090
Sample 2	3.2×10^{-11}	0.092
Sample 3	1.0×10^{-11}	0.080

This material will absorb a larger quantity of light in the visible region to excite more electrons from its molecule, so that it can be directly sent to the conduction band of Cu₂O film upon illumination. Further studies are needed on ionic conductivity of the solid polymer electrolyte of PVC-LiClO₄, surface morphology of Cu₂O and aluminum films, light intensity, and temperature which influence the performance of the cells.

4. Conclusions

The Cu₂O thin films were successfully grown onto ITO substrates by sol-gel spin coating with different additives and

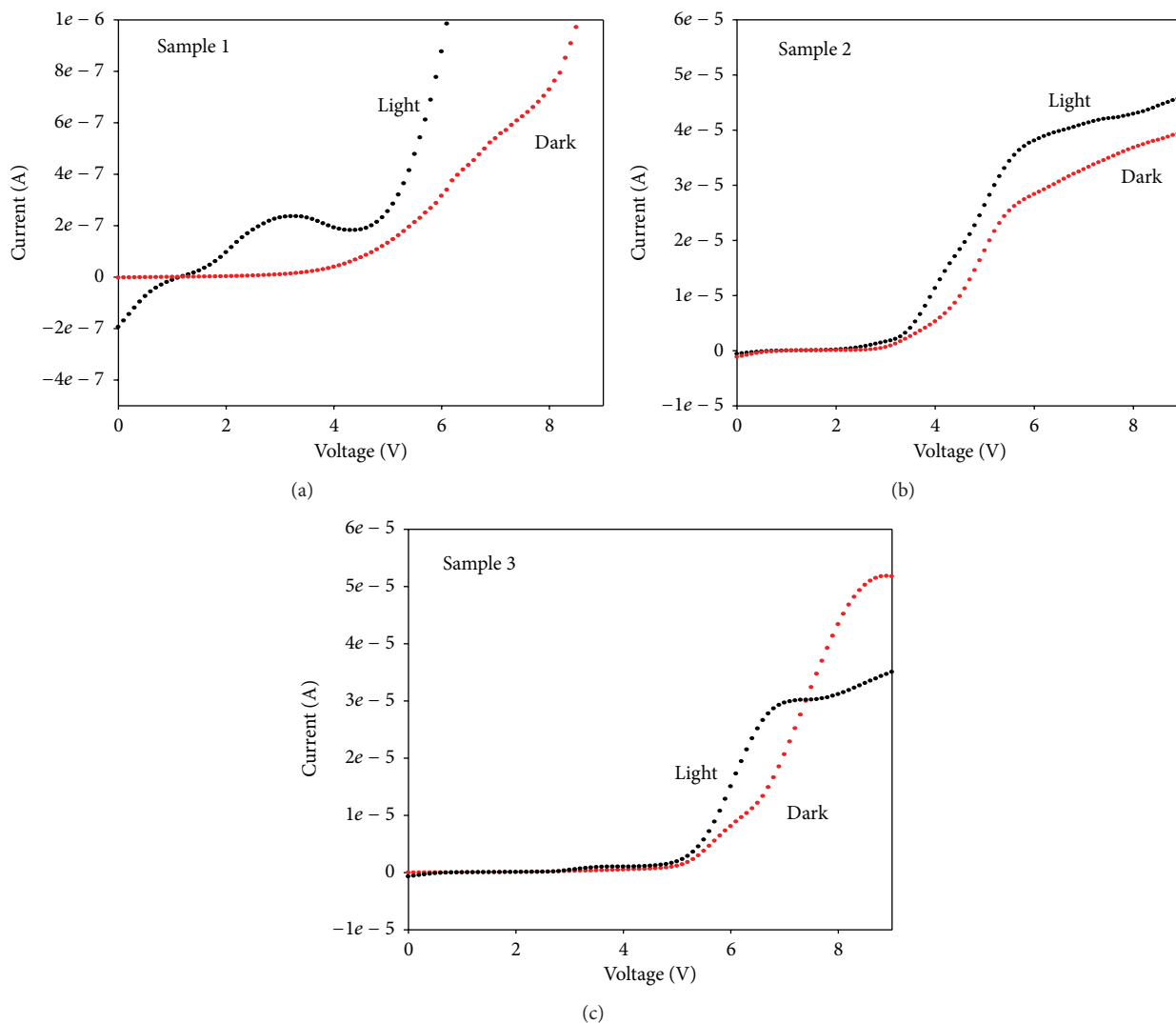


FIGURE 5: Current-voltage (I - V) characteristics of the PESC of ITO/ Cu_2O /PVC- LiClO_4 /aluminum under dark and light illumination.

annealed at 350°C in 5% H_2 + 95% N_2 atmosphere. Various properties of Cu_2O thin films have been characterized. The addition of polyethylene glycol to the parent solution can enhance various properties of the films, such as increasing optical absorbance, energy gap, and the thickness of films. These results indicate that the Cu_2O thin film prepared by sol-gel spin coating technique using polyethylene glycol and ethylene glycol can be used for photoelectrochemical solar cell (PESC).

Conflict of Interests

The authors declare that there is no conflict of interests regarding the publication of this paper.

Acknowledgment

The authors gratefully acknowledge the financial support by MOSTI, through Science Fund Grant no. 03-01-02-SF0211.

References

- [1] V. Georgieva and A. Tanusevski, "Optical band gap energy determination of thin films of cuprous oxide," in *Proceedings of the 5th General Conference of the Balkan Physical Union*, pp. 2311–2315, August 2003.
- [2] H. Tanaka, T. Shimakawa, T. Miyata, H. Sato, and T. Minami, "Effect of AZO film deposition conditions on the photovoltaic properties of AZO- Cu_2O heterojunctions," *Applied Surface Science*, vol. 244, no. 1–4, pp. 568–572, 2005.
- [3] S. Ishizuka, S. Kato, T. Maruyama, and K. Akimoto, "Nitrogen doping into Cu_2O thin films deposited by reactive radio-frequency magnetron sputtering," *Japanese Journal of Applied Physics, Part I: Regular Papers and Short Notes and Review Papers*, vol. 40, no. 4, pp. 2765–2768, 2001.
- [4] S. Ghosh, D. K. Avasthi, P. Shah et al., "Deposition of thin films of different oxides of copper by RF reactive sputtering and their characterization," *Vacuum*, vol. 57, no. 4, pp. 377–385, 2000.
- [5] K. P. Muthe, J. C. Vyas, S. N. Narang et al., "A study of the CuO phase formation during thin film deposition by molecular beam epitaxy," *Thin Solid Films*, vol. 324, no. 1–2, pp. 37–43, 1998.

- [6] M. T. S. Nair, L. Guerrero, O. L. Arenas, and P. K. Nair, "Chemically deposited copper oxide thin films: structural, optical and electrical characteristics," *Applied Surface Science*, vol. 150, no. 1, pp. 143–151, 1999.
- [7] S. C. Ray, "Preparation of copper oxide thin film by the sol-gel-like dip technique and study of their structural and optical properties," *Solar Energy Materials and Solar Cells*, vol. 68, no. 3-4, pp. 307–312, 2001.
- [8] K. Nakaoka and K. Ogura, "Electrochemical preparation of p-type cupric and cuprous oxides on platinum and gold substrates from copper(II) solutions with various amino acids," *Journal of the Electrochemical Society*, vol. 149, no. 11, pp. C579–C585, 2002.
- [9] A. K. Mukhopadhyay, A. K. Chakraborty, A. P. Chatterjee, and S. K. Lahiri, "Galvanostatic deposition and electrical characterization of cuprous oxide thin films," *Thin Solid Films*, vol. 209, no. 1, pp. 92–96, 1992.
- [10] L. Armelao, D. Barreca, M. Bertapelle, G. Bottaro, C. Sada, and E. Tondello, "A sol-gel approach to nanophasic copper oxide thin films," *Thin Solid Films*, vol. 442, no. 1-2, pp. 48–52, 2003.
- [11] A. Y. Oral, E. Menşur, M. H. Aslan, and E. Başaran, "The preparation of copper(II) oxide thin films and the study of their microstructures and optical properties," *Materials Chemistry and Physics*, vol. 83, no. 1, pp. 140–144, 2004.
- [12] K. Kajihara and T. Yao, "Macroporous morphology of the titania films prepared by a sol-gel dip-coating method from the system containing poly(ethylene glycol). IV. General principle of morphology formation and effect of heat treatment," *Journal of Sol-Gel Science and Technology*, vol. 17, no. 2, pp. 173–184, 2000.
- [13] A. Matsuda, T. Kanzaki, K. Tadanaga, M. Tatsumisago, and T. Minami, "Proton conductivities of sol-gel derived phosphosilicate gels in medium temperature range with low humidity," *Solid State Ionics*, vol. 154-155, pp. 687–692, 2002.
- [14] L. Huang, F. Peng, H. Yu, and H. Wang, "Synthesis of Cu₂O nanoboxes, nanocubes and nanospheres by polyol process and their adsorption characteristic," *Materials Research Bulletin*, vol. 43, no. 11, pp. 3047–3053, 2008.
- [15] I. R. Collins and S. E. Taylor, "Non-aqueous thermal decomposition route to colloidal inorganic oxides," *Journal of Materials Chemistry*, vol. 2, pp. 1277–1281, 1992.
- [16] D. Jezequel, J. Guenot, N. Jouini, and F. Fiévet, "Submicrometer zinc oxide particles: elaboration in polyol medium and morphological characteristics," *Journal of Materials Research*, vol. 10, pp. 77–83, 1995.
- [17] L. Poul, N. Jouini, and F. Fievet, "Layered hydroxide metal acetates (metallzinc, cobalt, and nickel): elaboration via hydrolysis in polyol medium and comparative study," *Chemistry of Materials*, vol. 12, pp. 3123–3132, 2000.
- [18] P. M. Sirimanne, T. Shirata, L. Damodare, Y. Hayashi, T. Soga, and T. Jimbo, "An approach for utilization of organic polymer as a sensitizer in solid-state cells," *Solar Energy Materials and Solar Cells*, vol. 77, pp. 15–24, 2003.
- [19] K. Imoto, K. Takahashi, T. Yamaguchi et al., "High-performance carbon counter electrode for dye-sensitized solar cells," *Solar Energy Materials and Solar Cells*, vol. 79, pp. 459–469, 2003.
- [20] S. Ito, T. Kitamura, Y. Wada, and S. Yanagida, "Facile fabrication of mesoporous TiO₂ electrodes for dye solar cells: chemical modification and repetitive coating," *Solar Energy Materials and Solar Cells*, vol. 76, pp. 3–13, 2003.

Research Article

TiCl₄ Pretreatment and Electrodeposition Time Investigations of ZnO Photoelectrodes Preparation for Dye Sensitized Solar Cells

Xiaoping Zou, Yan Liu, Cuiliu Wei, Zongbo Huang, and Xiangmin Meng

Research Center for Sensor Technology, Beijing Key Laboratory for Sensor,
Ministry-of-Education Key Laboratory for Modern Measurement and Control Technology, School of Applied Sciences,
Beijing Information Science and Technology University, Jianxiangqiao Campus, Beijing 100101, China

Correspondence should be addressed to Xiaoping Zou; xpzou2005@gmail.com

Received 19 February 2014; Accepted 1 May 2014; Published 15 June 2014

Academic Editor: Sudhakar Shet

Copyright © 2014 Xiaoping Zou et al. This is an open access article distributed under the Creative Commons Attribution License, which permits unrestricted use, distribution, and reproduction in any medium, provided the original work is properly cited.

TiCl₄ pretreatment is used in the fabrication of high performance photoanodes for dyes-sensitized solar cells (DSSCs). In this paper, TiCl₄ pretreatment was used on fluorine doped tin oxide (FTO) before fabricating ZnO films by electrochemical method. The effects of TiCl₄ pretreatment on some important parameters of solar cells, such as short-circuit current (J_{sc}) and filling factor, were investigated. The morphology of ZnO films was changed after TiCl₄ pretreatment, which can offer large surface area to absorb much more dyes. When the time of electrodeposition was 3 min, the dyes-sensitized solar cells (DSSCs) based on TiCl₄ pretreatment ZnO films showed more superior photoelectrochemical performance. The parameters of DSSCs are greatly improved. The DSSC based on ZnO films after TiCl₄ pretreatment has a very promising value for fabricating high performance solar cells.

1. Introduction

As a promising solar-to-electric energy converter, DSSCs have attracted much of attention due to their high efficiency and low cost [1]. With regard to photovoltaic devices, the conventional silicon-based solar cells are usually too bulky and heavy for flexible applications. Fortunately, new generation photovoltaic devices, such as dye-sensitized solar cells (DSSCs) and organic solar cells, make it possible to utilize solar energy more efficiently. As a result, invented new methods have recently attracted much attention to mesoporous film in the photoelectrodes of dye-sensitized solar cells (DSSCs) and quantum dots-sensitized solar cells (QDSCs) [2–6]. However, insufficient internal surface area limits conversion efficiency at a relatively low level owing to deficient dyes loading and light harvesting.

ZnO is one of the most important semiconductor materials as the photoelectrodes of DSSCs and QDSCs due to its suitable energy-band structure and excellent physical properties. Up to now, to get high performance, many methods have been explored to prepare ZnO porous films to offer large specific surface area for high device performance, such as doctor-blade (DB) method, chemical bath deposition, and

electrodeposition (ED) [7–11]. In this paper, we expected to fabricate high performance photoanodes for dyes-sensitized solar cells (DSSCs). TiCl₄ pretreatment was used on FTO before fabricating ZnO films by electrochemical method. The morphology of ZnO films was changed after TiCl₄ pretreatment, which can offer large surface area to absorb much more dyes. We tried different electrodeposition times. When the time of electrodeposition was 3 min, the quantum dyes-sensitized solar cells (DSSCs) based on TiCl₄ pretreatment ZnO films showed more superior photoelectrochemical performance.

2. Experimental

2.1. Preparation of ZnO Electrode. The base electrolyte used for the electrodeposition of ZnO films contained 0.1 M Zn(NO₃)₂ and 0.1 M KCl. Bath temperature was controlled at 65°C and the electrolyte was stirred vigorously before electrodeposition using a magnetic stirrer (Figure 1). The cathode substrate and graphite anode were dipped into the electrolyte solution about 1 cm deep below solution level controllably. Adjustment distance between electrode and

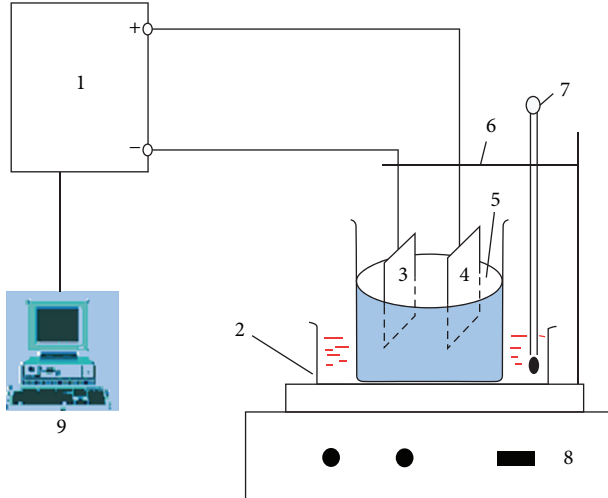


FIGURE 1: Schematic diagram of DC electrochemical deposition device. (1) Electrochemical workstation, (2) constant temperature water bath, (3) the cathode substrate, (4) graphite anode, (5) electrolyte solution, (6) bracket, (7) node thermometer, (8) thermostat magnetic stirrer, and (9) computer.

counter electrode is 2 cm. The electrodeposition was carried out under the potentiostatic condition. After the reaction, the reaction products ZnO/FTO was dipped into deionized water, soaking and cleaning. Then, after annealing for 30 min, ZnO/FTO was taken out from furnace when temperature decreased to 80°C through natural cooling and dipped into the dye (N719, 0.03) for 12 h. Finally they were washed with de-ionized water.

In order to make a performance comparison between TiCl_4 pretreatment and no TiCl_4 pretreatment on ZnO films and photoelectric performance influence, we fabricated another ZnO electrode. To be different, FTO was treated with TiCl_4 solution before making ZnO electrode and annealing 30 min at temperature 450°C.

2.2. TiCl_4 Pretreatment of FTO. The FTO was treated with TiCl_4 solution before fabricating TiO_2 films by method which can be found in the literatures elsewhere. With the pretreatment process, not only adsorption was stronger between TiO_2 films and FTO but also impede carriers recombination between I^{3-} and FTO. The conversion efficiency increased as J_{sc} increased. In this paper, TiCl_4 pretreatment was used on FTO before fabricating ZnO films by electrochemical method and at work current (30 mA) growth 4 min, then annealing 30 min at temperature 450°C.

3. Results and Discussion

Figure 2 shows the comparison after fabricating ZnO films, whether if there has been TiCl_4 pretreatment used on FTO or not, before fabricating ZnO films. It can be readily seen that the fabricated ZnO films are porous flakes, no matter they have TiCl_4 pretreatment or not. Compared with no TiCl_4 pretreatment, fabricated ZnO flake is smaller with TiCl_4

TABLE 1: The performance parameters of DSSCs with TiCl_4 pretreatment and without TiCl_4 pretreatment.

Samples	V_{oc} (V)	J_{sc} (mA/cm ²)	FF	η (%)
Without TiCl_4	0.3977	1.07	0.2820	0.12
TiCl_4	0.4759	2.86	0.3967	0.54

pretreatment. In addition, a large number of ZnO nanorods were produced which can offer large surface area to absorb much more dyes.

Figure 3(a) shows that the UV-Vis absorption spectra of ZnO films used TiCl_4 pretreatment or not after dye sensitized (N719) for 12 h. It can easily be seen that under the same conditions, relative to without TiCl_4 pretreatment, the absorbance of ZnO films increased after TiCl_4 pretreatment and light absorption cutoff wavelength presented a remarkable red shift, effectively broadening the range of ZnO on the absorption of sunlight.

The prepared ZnO films were immersed into dyes (N719) for 12 h; then with Pt electrodes they assembled into dye-sensitized solar cells (DSSCs) and performance was tested. J - V curves obtained from DSSCs are presented in Figure 3(b). Table 1 presents the parameters of DSSCs. It can be seen by the J - V curve that the performance of DSSCs with TiCl_4 pretreatment is much better than the DSSCs without TiCl_4 pretreatment. This experimental result is consistent with the test results of U-V absorption spectrum. As shown in Table 1, the short-circuit current (J_{sc}), open-circuit voltage, conversion efficiency, and filling factor of DSSCs with TiCl_4 pretreatment are greatly improved. The main reason for the results is that ZnO absorbed more dyes with the surface area increasing from ZnO films. Meanwhile, after TiCl_4 pretreatment, a layer of dense TiO_2 on FTO is formed and impede carriers recombination between I^{3-} and FTO effectively, thus, the short-circuit photocurrent density is improved, so the conversion efficiency was increased; this is consistent with literature reported.

Keeping the same experimental conditions, the electrodeposition times of the preparation of ZnO samples were 2 min, 3 min, 4 min, and 5 min, respectively, at the constant current of electrodeposition of 30 mA. Figure 4 shows the SEM of ZnO films under different electrodeposition times. From the SEM photos it can be seen that when the electrodeposition time is 2 min, we can get the ZnO sheet structure, which is composed of small particles with size of about 300 nm. Along with the growth of the electrodeposited time, flakes began to accumulate, at the same time, composed of a small piece of particle size that also increases (electrodeposition time of 4 min, the small particle size increased to 500 nm), resulting in decreased ZnO films surface area. With the electrodeposition time of 5 min, from amplifier SEM photos, it can be seen that the dense ZnO films are significantly higher than 4 min. But too dense film is not conducive to the dyes adsorption.

The XRD pattern in Figure 5(a) reveals the ZnO films under different electrodeposition times. We can get from the XRD that 2θ angle of 31.8°, 36.6°, and 56.64° corresponded to the ZnO thin films (100) (101) (110) diffraction crystal

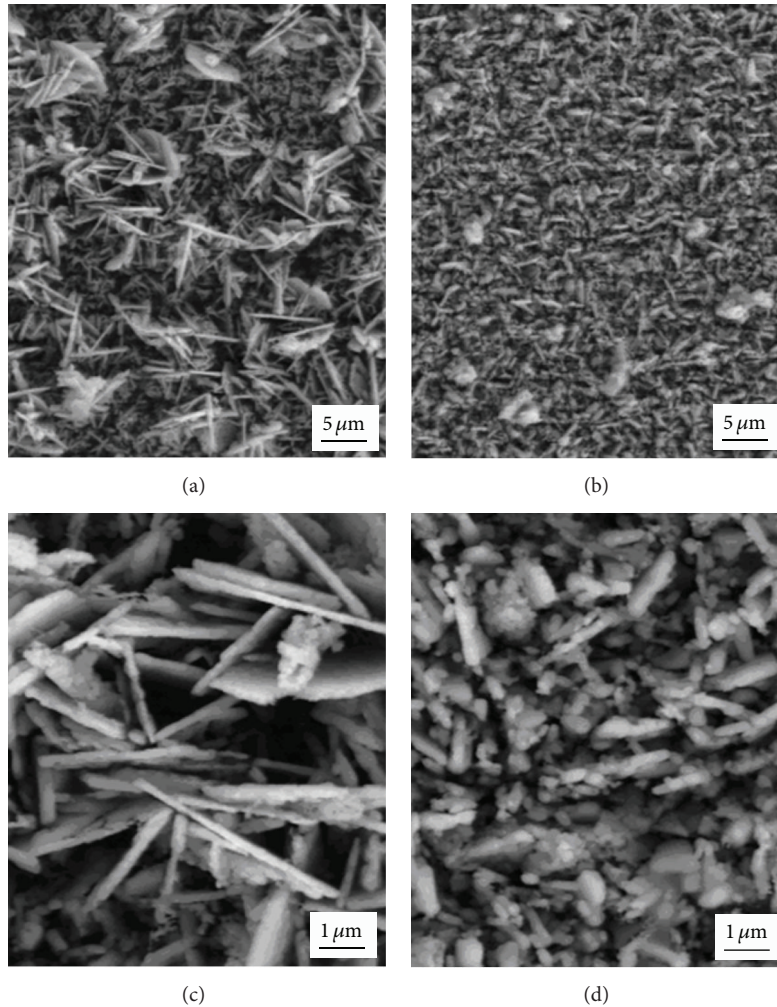


FIGURE 2: SEM images of TiCl_4 pretreatment used on FTO or not. (a) TiCl_4 pretreatment. (b) Without TiCl_4 pretreatment. (c) and (d) The amplification figure of (a) and (b), respectively.

face, respectively, consistent with the standard peak of XRD patterns (JCPDS no. 74-534). In addition, some weak peaks also appeared, (002), (102), (103), (112), and (201). As can be seen by the XRD patterns, ZnO films prepared under different electrodeposition time XRD peak are almost the same with a difference in the peak intensity.

ZnO films prepared under the different deposition times immersed in the N719 dye-sensitized for 12 h, and then, with Pt electrodes, they assembled into DSSC performance testing, J - V characteristic curve shown in Figure 5(b). The performance parameters of DSSCs are listed in Table 2.

As can be seen from Figures 5(a) and 5(b), when other experimental conditions are unchanged, with the growth of the electrodeposition time, the DSSC short-circuit current, filling factor, and the photoelectric conversion efficiency first increase and then decrease. When electrodeposition time is 3 min, the DSSC performance is the best. The main reason is: when the electrodeposition time is short, flake particle size is small and specific surface area is large, but the relatively dense and thin deposition layer is not conducive to the adsorption

TABLE 2: The parameters of DSSCs under different electrodeposition time.

Electrodeposition time (min)	V_{oc} (V)	J_{sc} (mA/cm ²)	FF	η (%)
2	0.6897	2.91	0.3787	0.76
3	0.6922	3.34	0.4758	1.10
4	0.6774	3.38	0.3974	0.91
5	0.6835	3.17	0.3692	0.80

of the dyes, so, short circuit current density of the DSSC is low, the filling factor and conversion efficiency are low too. The small particle size also increases with the growth time. At this point, the thickness of the sediments layer gradually increased and occupied the leading position; combined effect is conducive to dyes adsorption, making the short-circuit current density, filling factor, and efficiency also increase. However, along with the growth time, small flake particle size gradually get big, resulting in specific surface area of ZnO

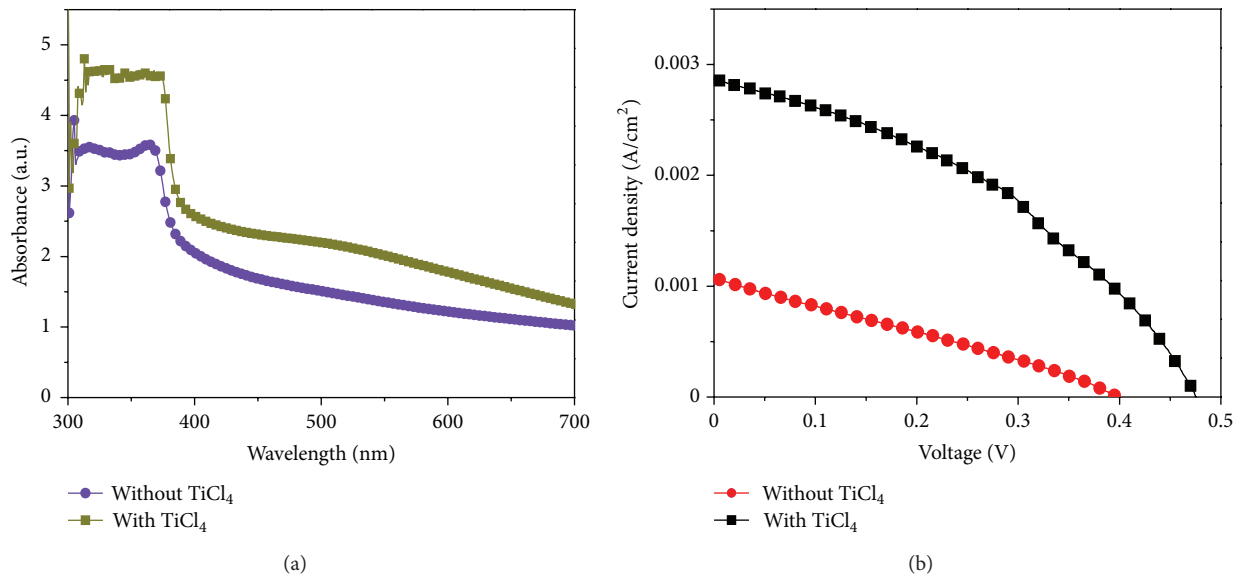


FIGURE 3: (a) UV-Vis absorption spectra of ZnO films. TiCl_4 pretreatment (dark yellow). Without TiCl_4 pretreatment (blue). (b) J - V curves obtained from DSSCs with TiCl_4 pretreatment (black) and DSSCs without TiCl_4 pretreatment (red).

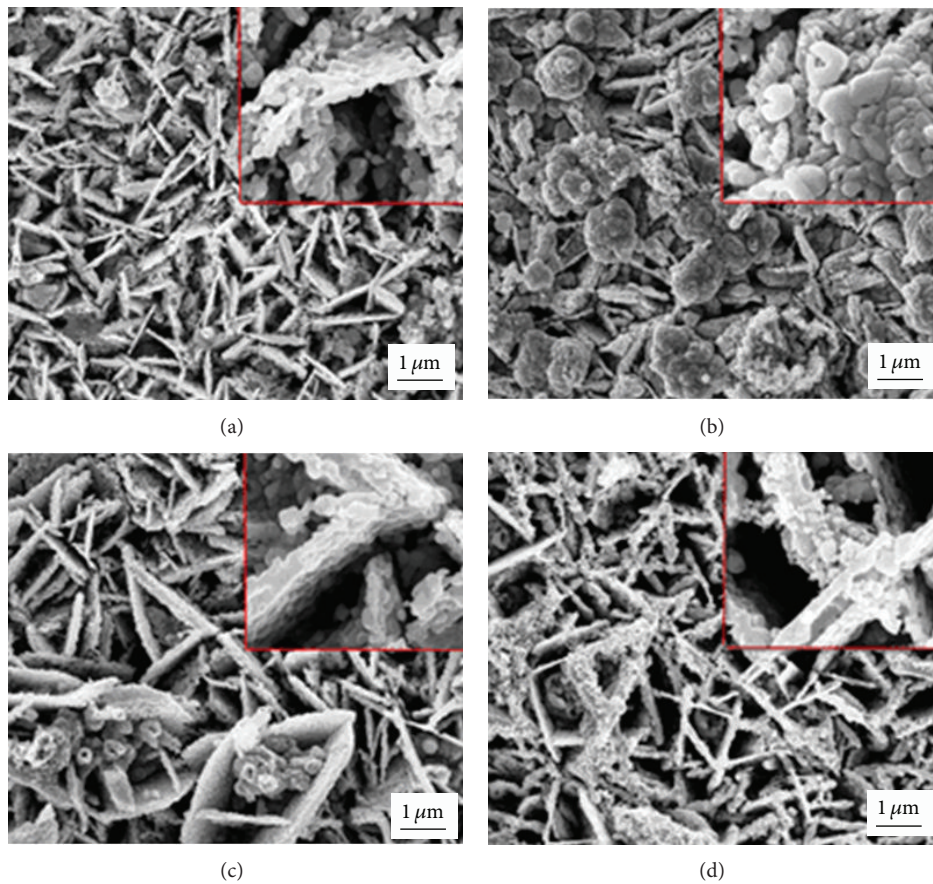


FIGURE 4: SEM images of preparation ZnO under different electrodeposition times: (a) 2 min, (b) 3 min, (c) 4 min, and (d) 5 min. Part of the insert of the red box for enlargement.

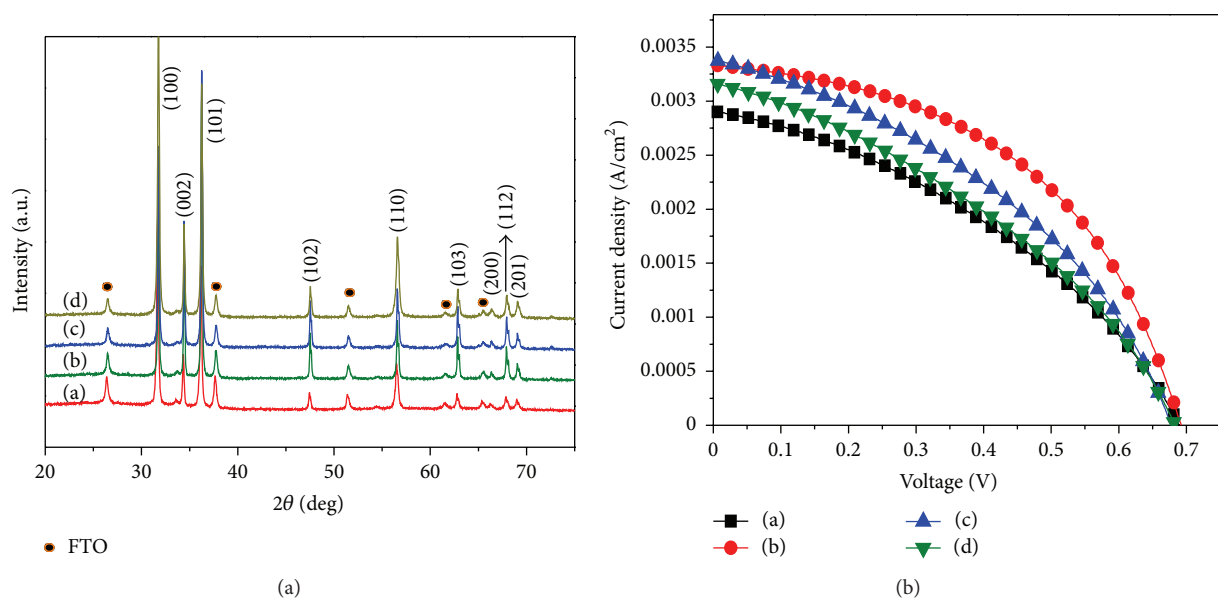


FIGURE 5: (a) XRD pattern of the ZnO films under different electrodeposition times. (b) J - V curves obtained from DSSCs under different electrodeposition times: (a) 2 min, (b) 3 min, (c) 4 min, and (d) 5 min.

films decrease, therefore the performance of the DSSCs get degradation.

4. Conclusions

We have demonstrated an efficient method to prepare high performance ZnO electrode. The ZnO electrode has many porous flakes after TiCl_4 pretreatment. In addition, a large number of ZnO nanorods were produced which can offer large surface area to absorb much more dyes. The absorbance of ZnO electrode is increased after TiCl_4 pretreatment and light absorption cutoff wavelength presents a remarkable red shift, effectively broadening the range of ZnO on the absorption of sunlight. The solar energy-conversion efficiency which is shown by DSSC fabricated following TiCl_4 pretreatment is relatively higher than without TiCl_4 pretreatment, when the time of electrodeposition was 3 min, the DSSC based on TiCl_4 pretreatment ZnO films showed more superior photoelectrochemical performance under the illumination of one sun (AM 1.5, under 100 mW/cm^2). Since the ZnO films fabricated following TiCl_4 pretreatment and deposition of a suitable time, it shows much prospect to be applied in the photoelectrodes of flexible QDSCs or DSSCs.

Conflict of Interests

The authors declare that there is no conflict of interests regarding the publication of this paper.

Acknowledgments

This work was partially supported by Key Project of Beijing Natural Science Foundation (3131001), Key Project of Natural Science Foundation of China (91233201 and 61376057), Key

Project of Beijing Education Committee Science & Technology Plan (KZ201211232040), State 863 Plan of MOST of PR China (2011AA050527), Beijing National Laboratory for Molecular Sciences (BNLMS2012-21), State Key Laboratory of Solid State Microstructures of Nanjing University (M27019), State Key Laboratory for Integrated Optoelectronics of Institute of Semiconductors of CAS (IOSKL2012KF11), State Key Laboratory for New Ceramic and Fine Processing of Tsinghua University (KF1210), Key Laboratory for Renewable Energy and Gas Hydrate of Chinese Academy of Sciences (y207ka1001), Beijing Key Laboratory for Sensors of BISTU (KF20131077208), and Beijing Key Laboratory for photoelectrical measurement of BISTU (GDKF2013005).

References

- [1] B. O'Regan and M. Grätzel, "A low-cost, high-efficiency solar cell based on dye-sensitized colloidal TiO_2 films," *Nature*, vol. 353, pp. 737–740, 1991.
- [2] M. Grätzel, "Photoelectrochemical cells," *Nature*, vol. 414, pp. 338–344, 2001.
- [3] A. Hagfeldt, G. Boschloo, L. Sun, L. Kloo, and H. Pettersson, "Dye-sensitized solar cells," *Chemical Reviews*, vol. 110, no. 11, pp. 6595–6663, 2010.
- [4] P. V. Kamat, "Quantum dot solar cells. Semiconductor nanocrystals as light harvesters," *Journal of Physical Chemistry C*, vol. 112, no. 48, pp. 18737–18753, 2008.
- [5] S. Rühle, M. Shalom, and A. Zaban, "Quantum-dot-sensitized solar cells," *ChemPhysChem*, vol. 11, no. 11, pp. 2290–2304, 2010.
- [6] I. Mora-Seró, S. Giménez, F. Fabregat-Santiago et al., "Recombination in quantum dot sensitized solar cells," *Accounts of Chemical Research*, vol. 42, no. 11, pp. 1848–1857, 2009.
- [7] M. S. Akhtar, M. A. Khan, M. S. Jeon, and O.-B. Yang, "Controlled synthesis of various ZnO nanostructured materials

- by capping agents-assisted hydrothermal method for dye-sensitized solar cells," *Electrochimica Acta*, vol. 53, no. 27, pp. 7869–7874, 2008.
- [8] Z. Gu, M. P. Paranthaman, J. Xu, and Z. W. Pan, "Aligned ZnO nanorod arrays grown directly on zinc foils and zinc spheres by a low-temperature oxidization method," *ACS Nano*, vol. 3, no. 2, pp. 273–278, 2009.
- [9] G. Shen, Y. Bando, and C. -J. Lee, "Synthesis and evolution of novel hollow ZnO urchins by a simple thermal evaporation process," *The Journal of Physical Chemistry B*, vol. 109, no. 21, pp. 10578–10583, 2005.
- [10] H. Chen, L. Zhu, H. Liu, and W. Li, "Growth of ZnO nanowires on fibers for one-dimensional flexible quantum dot-sensitized solar cells," *Nanotechnology*, vol. 23, no. 7, Article ID 075402, 2012.
- [11] H. Chen, W. Li, Q. Hou, H. Liu, and L. Zhu, "Growth of three-dimensional ZnO nanorods by electrochemical method for quantum dots-sensitized solar cells," *Electrochimica Acta*, vol. 56, no. 24, pp. 8358–8364, 2011.

Research Article

Cooperative Optimal Control Strategy for Microgrid under Grid-Connected and Islanded Modes

Xuemei Zheng, Qiuming Li, Peng Li, and Danmei Ding

School of Electrical Engineering and Automation, Harbin Institute of Technology, Harbin 150001, China

Correspondence should be addressed to Xuemei Zheng; xmzheng@hit.edu.cn

Received 19 December 2013; Accepted 6 April 2014; Published 20 May 2014

Academic Editor: Prakash Basnyat

Copyright © 2014 Xuemei Zheng et al. This is an open access article distributed under the Creative Commons Attribution License, which permits unrestricted use, distribution, and reproduction in any medium, provided the original work is properly cited.

This paper investigates the control performance of a physical configuration of a microgrid (MG), integrated with photovoltaic (PV) arrays, battery energy storage systems (BESSs), and variable loads. The main purpose is to achieve cooperative optimal control under both grid-connected and islanded modes for the MG. For the grid-connected mode, a voltage source inverter (VSI) based on sloop control is used to control the MG connection to the grid even if PV arrays are under partially shading conditions (PSC). Then, for the islanded mode, the paper analyzes the model of the PV unit and BESS unit detailed from the small signal point of view and designs the suitable control strategy for them. Finally, the whole MG system combines the droop control and the main/slave control to stabilize the DC bus line voltage and frequency. Both simulation and experimental results confirm that the proposed method can achieve cooperative control of the MG system in both grid-connected and islanded mode.

1. Introduction

To address the challenges of tackling climate change and maintaining energy security, many countries worldwide are committed to decarbonizing their energy systems. As a result, the renewable energy solution becomes an increasingly attractive and important topic, and it contributes to a sustainable development of the society. The development of hybrid power systems incorporating renewable sources represents a big step towards distributed generation (DG). The microgrid (MG) concept [1–4], which represents a cluster of interconnected DGs, loads, and intermediate battery energy storage systems (BESSs), has caught many researchers' interest. The MG flexibility can be achieved by allowing the electricity operation under two different modes [5]: one is the grid-connected mode where the MG is connected to the main grid, being either partially supplied from the grid or injecting power into the grid; the other is the islanded mode, where the MG operates autonomously when it is disconnected from the main grid.

Voltage source inverters (VSI) are often used as a power electronics interface; hence, the control of parallel VSI forming a MG has been intensively investigated in recent years [1–10]. Decentralized and cooperative controllers such as the

droop method have been proposed in the literature. Further, in order to enhance the reliability and performance of the droop control of VSI, virtual impedance control algorithms have been developed, providing the inverters with hot-swap operation, harmonic power sharing, and robustness for large line power impedance variations [11].

However, droop control has several drawbacks such as poor harmonic current sharing and high dependence on the power line impedances. In order to overcome these drawbacks, methods were proposed by combining low-bandwidth communications with average power sharing, droop control, and extra harmonic compensation control loops [12, 13]. Another solution is to combine both master-slave and droop control techniques according to the distance of individual DG unit in an islanded MG [14].

In the case of transferring from the islanded operation mode to the grid-connected mode, it is necessary to first synchronize the MGs to the grid [1]. Once the synchronization is achieved, a static transfer switch is triggered to connect the MG to the grid. After the transition process between islanded and grid-connected mode is completed, it is necessary to control the active and the reactive power flows at the point of common coupling [7].

For the grid-connected mode, the PV source has the advantages of low maintenance cost, no moving/rotating parts, and pollution-free energy conversion. However, a major drawback of the PV source is its ineffectiveness during the nights or low isolation periods or during partially shaded conditions (PSC). A major challenge in using the PV source is posed by its nonlinear current-voltage (I - V) characteristics, which result in a unique maximum power point (MPPT) on its power-voltage (P - V) curve.

Several tracking schemes have been proposed [15–24], among which the popular tracking schemes include the perturb and observe (P&O), hill climbing [17, 18], short-circuit current [17], and open-circuit voltage [20]. The tracking schemes mentioned above have been shown to be effective under uniform solar insolation conditions, where P - V curve of a PV module exhibits only one MPPT for a given temperature and insolation. Under PSC, the entire array, however, does not receive uniform insolation and the P - V characteristic becomes more complex, displaying multiple peaks. The effectiveness of the existing MPPT schemes, which assume a single peak power point on the P - V characteristics, will then become less effective. Therefore, there is a need to develop special MPPT schemes that can track the global peak under PSC.

This paper investigates the control performance of a physical configuration of a MG, which incorporates photovoltaic (PV) arrays, a BESS, and variable loads. In order to improve the conversion efficiency of the PV array and the charger under PSC in MG grid-connected mode, we use a MPPT algorithm under PSC developed by Ji et al. [24] based on the analysis of the P - V and I - V output characteristics. Then, the grid connection requirements of the whole MG system are achieved using a VSI. Then, for the islanded mode, the paper analyzes the model of the PV unit and the BESS unit detailed from the small signal point of view and designs the suitable control strategy for them. Finally, the whole MG system combines the droop control and the main/slave control to stabilize the DC bus line voltage and frequency. Both simulation and experimental results confirm that the proposed method can achieve cooperative control of the MG system in both grid-connected and islanded mode. Both simulation and experimental results confirm that the proposed algorithm can automatically track the global power point under different isolation conditions and coordinated control of the MG is achieved.

This paper is organized as follows. Section 2 describes the physical configuration of the MG under study, Section 3 analyzes the MG system control strategy in grid-connected mode, and Section 4 proposes a coordinated control loop for the MG system in islanded mode. Section 5 details the simulation and experimental results. Finally, Section 6 concludes the paper.

2. Physical Configuration of the Microgrid under Study

The paper considers the following physical configuration of a MG as depicted in Figure 1, which consists of 2 PV units

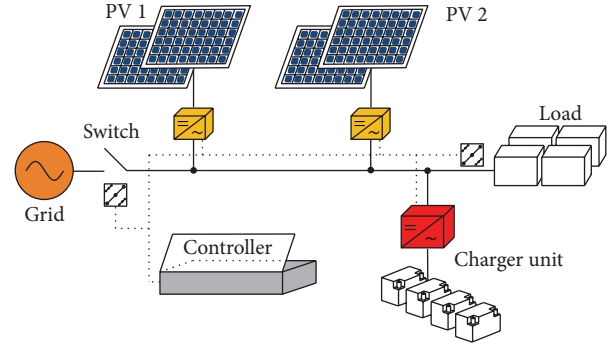


FIGURE 1: The structure of MG under study.

representing renewable power and a BESS, central controller, and the local loads, which are all connected to an AC bus line through static switch. The static switch will connect to the AC grid and realize grid-connected mode and islanded mode through the static switch on and off mode. The PV power systems are subject to the atmosphere condition and thus generate variable power. An inverter consisting of a DC/DC converter, a DC bus, and an H-bridge can realize the interface between the PV panels and the MG. The inverter injects active power and reactive power through the point of common coupling based on different operation conditions.

The battery energy storage system ensures the power balance in the MG, acting as a load or a source according to power unbalance situation. In the ideal condition, the active power balance is given by

$$P_{\text{BESS}} = P_L - P_{\text{PV}}, \quad (1)$$

where P_L is the load power requirement, P_{BESS} is the BESS power (charging or discharging), and P_{PV} is the PV power.

The active power balance must be ensured at any time and the purpose is to maintain the frequency of the system within the required limits. The main sources of uncertainties are from the PV power systems, which inject variable active power according to the actual requirements, and also from the loads that vary quasirandomly.

3. MG Control Strategy under Grid-Connected Mode

When the MG works in grid-connected mode, the frequency and the voltage of the MG are maintained within a tight range by the main grid. In this section, we consider the MG control design under grid-connected mode.

3.1. Normal Model of a PV Array. To control the MG with integration of PV power as shown in Figure 1, modeling the PV array is necessary. A PV array is composed of several PV modules connected in series parallel to produce desired voltage and current. Usually, more PV cells are needed to form the series-parallel PV array. The relationship of the

output voltage and current of one PV cell can be represented as follows:

$$I = I_{ph} - I_s \left\{ \exp \left[\frac{q}{AKT} (U + IR_s) \right] - 1 \right\} - \frac{U + IR_s}{R_{sh}}, \quad (2)$$

where I is the output current of PV cell; U is the output voltage of PV cell; I_{ph} is the photocurrent; I_s is the reverse saturation current of diode; q is the electronic charge (1.6×10^{-19} C); K is Boltzmann's constant (1.38×10^{-23} J/K); T is junction temperature; A is the diode ideality factor; R_s is series resistor; R_{sh} is shunt resistor.

Due to the large value of shunt resistance R_{sh} , the last term in (2) is often omitted, the short-circuit current and photocurrent are considered to be equal ($I_{sc} \approx I_{ph}$), and when the PV cell is on open circuit, the output current is zero, so output current of a PV cell can be approximated as

$$I = I_{sc} \left\{ 1 - \exp \left[\frac{q}{AKT} (U + IR_s - U_{oc}) \right] \right\}. \quad (3)$$

Equation (3) is an implicit function relating the voltage and current. To help with the analysis, it can be shown that

$$U = \frac{AKT}{q} \ln \left(1 + \frac{I}{I_{sc}} \right) - IR_s + U_{oc}. \quad (4)$$

Then, the output power of a PV cell is

$$P = UI = \frac{AKTI}{q} \ln \left(1 + \frac{I}{I_{sc}} \right) - I^2 R_s + IU_{oc}. \quad (5)$$

Equations (4) and (5) can be used to produce output characteristic curve of the PV cell. When these series-parallel PV cells constitute a $N_s \times N_p$ array (N_s is the number of PV cells in series, and N_p is the number in parallel), the corresponding PV array output voltage, current, open-circuit voltage, short-circuit current, and series resistance can be formulated as

$$\begin{aligned} U_A &= N_s U, \\ I_A &= N_p I, \\ U_{ocA} &= N_s U_{oc}, \\ I_{scA} &= N_p I_{sc}, \\ R_{sA} &= \left(\frac{N_s}{N_p} \right) R_s. \end{aligned} \quad (6)$$

Taking an array of $N_s \times N_p = 3 \times 2$ PV as an example, Figure 2 shows the I - V curve and P - V curve, respectively, under the normal condition.

3.2. MG Unit Control under PSC. To control the MG configured in Figure 1, we first aim to achieve the PV MPPT control and improve the efficiency of the PV array power conversion under PSC. Then, we use DC/DC converter to make the output current and the grid voltage following the same phase and frequency to realize the unit power factor control.

An important target in MPPT control is to track the global MPPT under PSC. One of the key issues is to identify the PSC, and, in this paper, we adopt the following PSC judgment criteria which was originally proposed in [24]:

$$\begin{aligned} \Delta U_{pv} &= U_{pv}(n) - U_{pv}(n-1) < \Delta U_{set}, \\ \frac{\Delta I_{pv}}{I_{pv}(n-1)} &= \frac{I_{pv}(n) - I_{pv}(n-1)}{I_{pv}(n-1)} < \Delta I_{set} \approx -\frac{I_{pv}(n-1)}{N_p}, \end{aligned} \quad (7)$$

where ΔU_{pv} is the voltage change of PV array, ΔU_{set} is a preset voltage variation limit of PV array, ΔI_{pv} is the current change of PV array, and ΔI_{set} is a preset current voltage variation limit of PV array.

The overall configuration of the control system for MG under PSC is shown in Figure 3, and it has two separate parts that can be controlled individually. The first part incorporates the global MPPT into the inverter to connect DC power from the PV array to the MG. The back part is the inverter for controlling the integration of MG to the AC line. In this configuration, the key element is the MPPT control of the PV system with a PSC judging mechanism.

In Figure 3, the first converter is the boost converter and adopts voltage loop control, which is used to achieve the MPPT control through adjusting the output voltage of the PV array. The second converter is with a two-phase bridge, and T_1 - T_4 are the control signals of the four switches, and it is connected with the first converter by a large capacitor C_2 , and the output current of the first converter is the control target in the back converter.

DC bus line control is also necessary. Although MPPT control can make the PV array track the MPPT, the different levels of isolation will affect the power output, and the power change will cause the DC bus line to drift. If the PV output energy increases sharply, the power delivery of DC bus line will be increased if there is no converter or load to consume the extra energy. On the contrary, if the PV output energy is decreased and cannot satisfy AC line voltage peak value, the converter cannot work; therefore it is necessary to keep the DC bus line balanced.

The second part has two loops, that is, the outer voltage loop and inner current loop. The function of the voltage loop is to keep the DC bus line balanced; it is controlled by a PI controller by comparing the actual value U_{dc} and the given value U_{dc}^* as the error for driving the PI controller. The output of the outer loop PI controller produces the AC given current value, which is multiplied by the sine output signal of the phase-locked loop (PLL) of the AC voltage u_{ac} to produce the given current i_{ac}^* . The aim of the inner current loop is to realize the AC current control. The given current i_{ac}^* is compared with the actual i_{ac} , producing the error, and is controlled by the inner loop PI controller. The output of the inner loop PI controller is compared with the triangle wave for generating the PWM signal to control T_1 to T_4 and thus produce the AC current output, which has the same frequency and phase with the grid side.

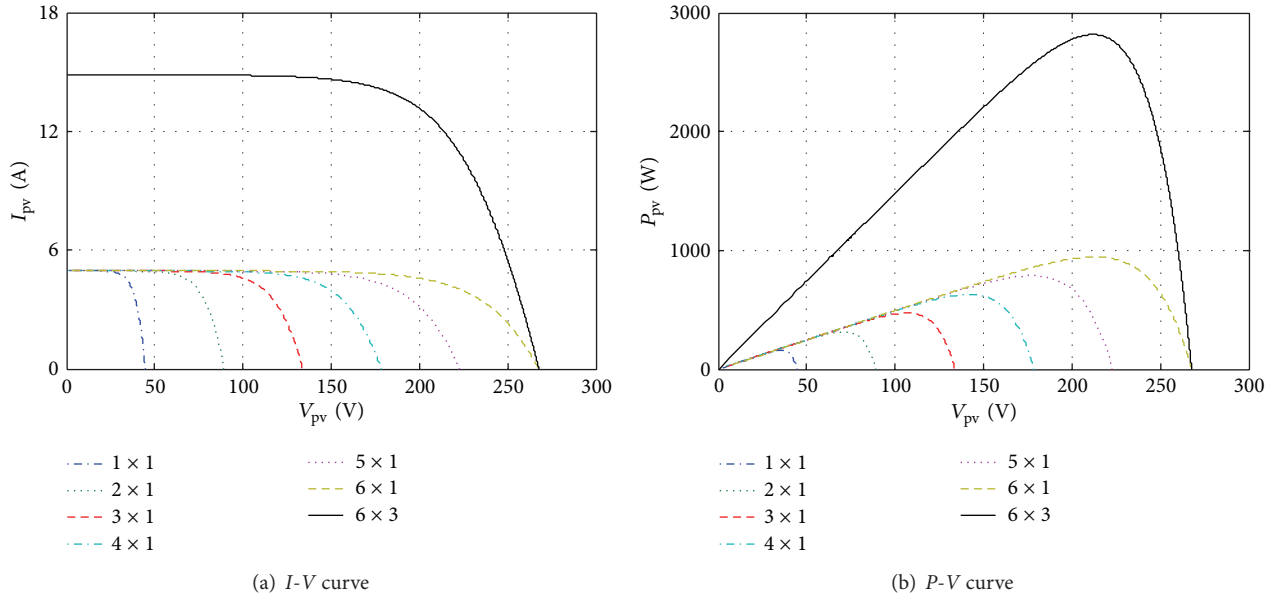


FIGURE 2: I-V and P-V characteristic curve under normal condition.

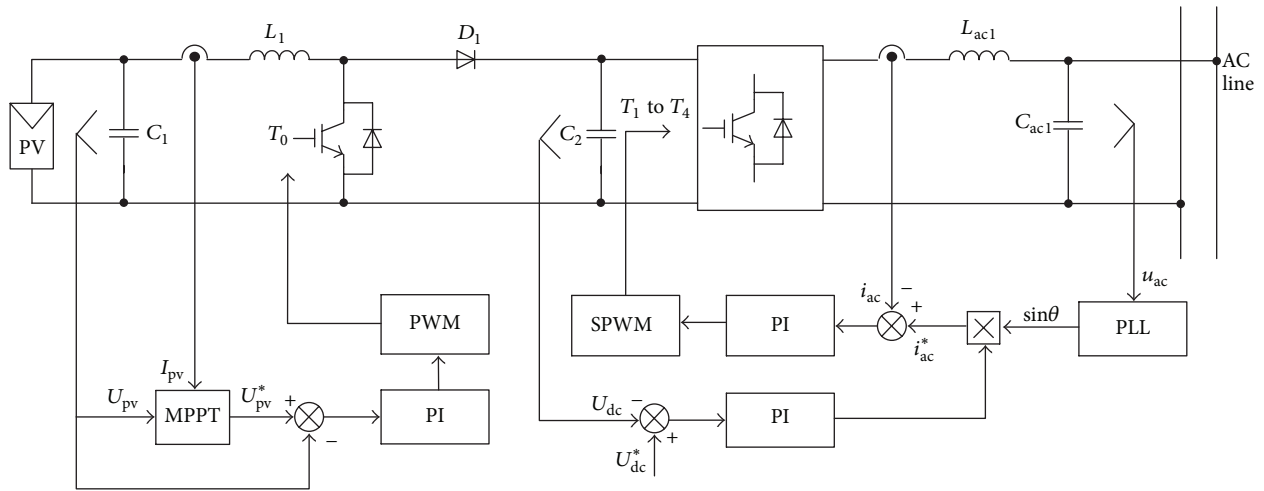


FIGURE 3: The whole control system configuration of MG under grid-connected mode.

4. Control Strategy for Islanded Mode

When the MG is in the islanded mode, the two PV units and one BESS are all in parallel connection with the AC bus line (Figure 1). As the MG system is separated from the grid, and the frequency and voltage will not be provided by the grid, the MG system needs a suitable control strategy to balance the frequency and the volume of the AC line.

The control method proposed in the paper is shown in Figure 4. The MG system adopts two-layered control strategy, where the upper layer is the main controller to realize the energy prediction and balance, while the lower layer controller is connected to the main controller and achieves the output power control, bus line control, and the control of the PV array and the BESS system state. As shown in Figure 4, the PV array adopts droop control in the main controller to achieve stable voltage and frequency regulation. The BESS

inverter is the slave inverter and adopts PLL control and active and reactive power (P/Q) control to ensure that the frequency and phase are synchronized with the MG system. If the solar irradiation is less than the normal value, the PV array will stop generating power and the BESS system adopts voltage/frequency (V/f) control to provide the energy for the load and run the MG system continuously.

4.1. The PV Unit Islanded Control Strategy. Figure 5 is the control system structure of PV unit. The first boost converter can raise the PV voltage to the needed level and the second converter adopts voltage and current loop to improve the response and the property of MG system. When the MG is in the islanded mode, the PV unit will act as the main converter to provide the voltage and the frequency for the other converters.

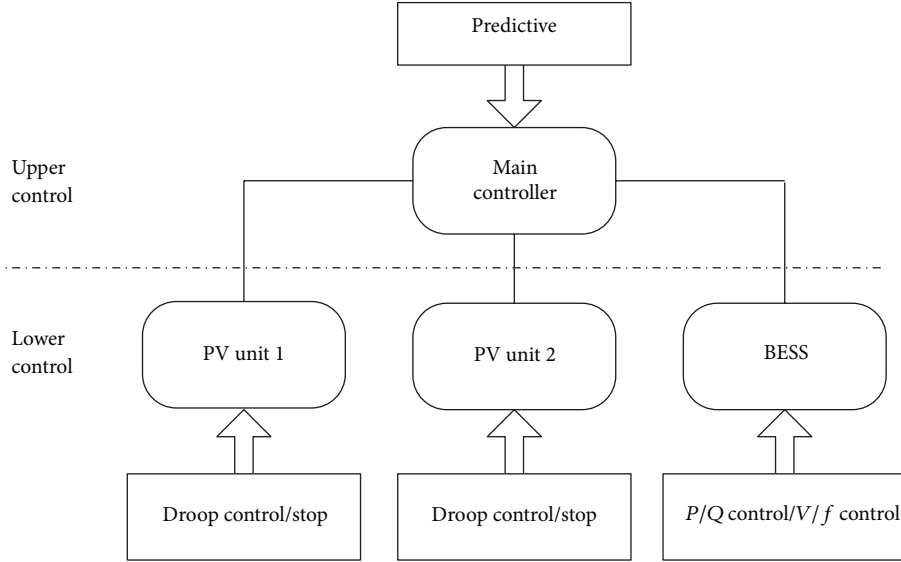


FIGURE 4: MG system control strategy under the islanded mode.

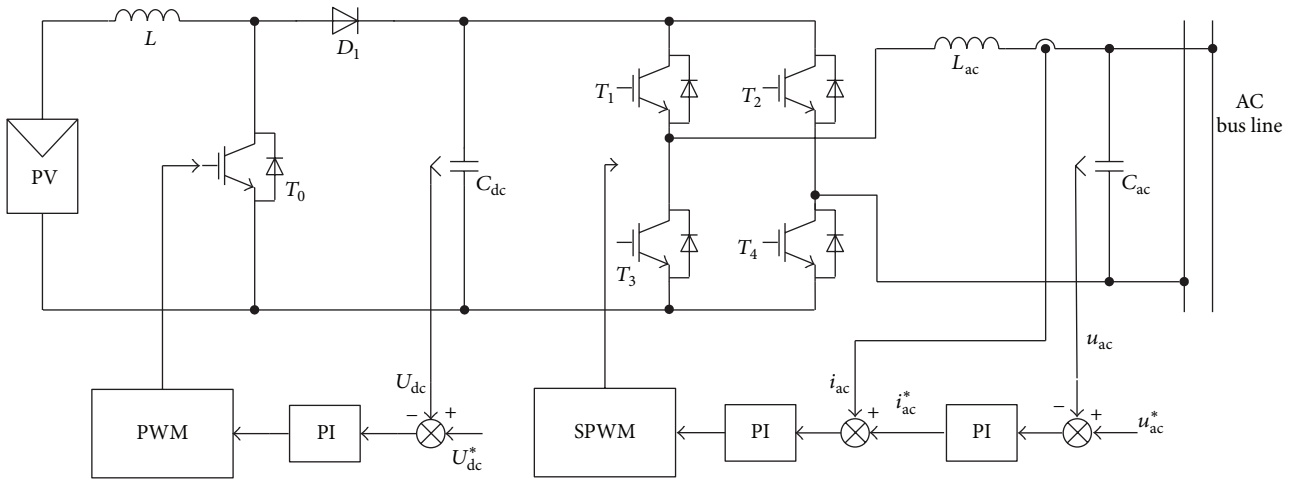


FIGURE 5: The control system structure of PV unit.

4.1.1. Small Signal Model of Boost Converter. In the circuit topology shown in Figure 5, variety of the boost switch duty cycle d affects equivalent impedance of the PV system directly and the PV modules can work at their MPP by adjusting the duty cycle d . So the output of PV modules should respond to the change of d as quickly as possible [15]. By analyzing small signal model of the system, the transfer function of the output voltage and the inductor current versus the boost switch duty cycle d can be shown as

$$\begin{bmatrix} \frac{d\hat{i}_L(t)}{dt} \\ \frac{d\hat{u}_{dc}(t)}{dt} \end{bmatrix} = \begin{bmatrix} 0 & -\frac{1-d}{L} \\ \frac{1-d}{C_{dc}} & -\frac{1}{RC_{dc}} \end{bmatrix} \begin{bmatrix} \hat{i}_L(t) \\ \hat{u}_{dc}(t) \end{bmatrix} + \begin{bmatrix} \frac{U_{dc}}{L} \\ -\frac{1}{L} \end{bmatrix} \hat{d}(t) + \begin{bmatrix} \frac{1}{L} \\ 0 \end{bmatrix} \hat{u}_{pv}(t), \quad (8)$$

where U_{dc} and I_L are the output voltage and inductor current at static point. From (8), we can get the following transfer function:

$$\left. \frac{\hat{u}_{dc}(s)}{\hat{d}(s)} \right|_{\hat{u}_{pv}(s)=0} = \frac{(1-d)U_{dc} \{1 - Ls/[R(1-d)^2]\}}{LC_{dc}s^2 + Ls/R + (1-d)^2}. \quad (9)$$

In order to raise the dynamic characteristic of PV unit, we add a PI controller (shown in (10)) in the original PV unit:

$$G'_{odc}(s) = \frac{k_{pdc}s + k_{idc}}{s} \frac{(1-d)U_{dc} \{1 - Ls/[R(1-d)^2]\}}{LC_{dc}s^2 + Ls/R + (1-d)^2}. \quad (10)$$

Figure 6 showed the frequency characteristic of boost converter before and after PI correction. Comparing them, it can be seen that the phase margin and the gain margin are all raised, and the stability of the MG system is improved.

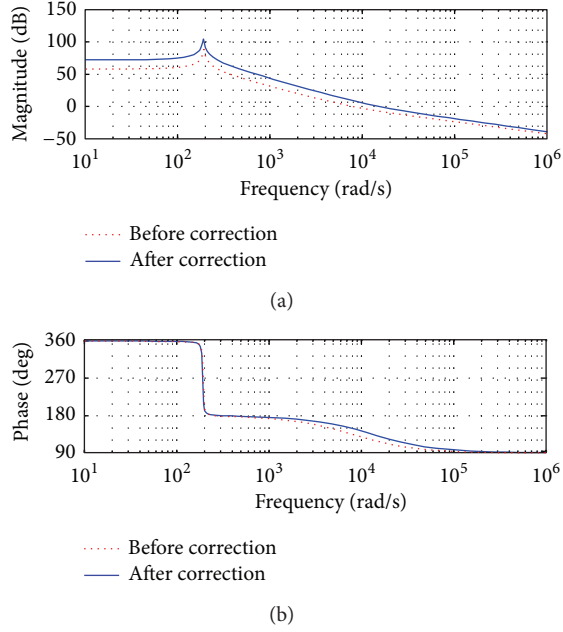


FIGURE 6: The frequency characteristic of voltage loop in inverter after correction.

4.1.2. Small Signal Model of Full-Bridge Converter. When the PV unit is under the islanded mode, it can be considered an AC voltage source. Through analyzing the switch which is on the different states, we can get the small signal model of the system and the transfer function of output voltage and the inductor current are shown in

$$\left. \frac{\widehat{u}_{ac}(s)}{\widehat{d}_{ac}(s)} \right|_{\widehat{u}_{dc}(s)=0} = \frac{2R_{ac}U_{ac}}{R_{ac}LC_{ac}s^2 + s - (2d_{ac} - 1)R_{ac}}, \quad (11)$$

$$\left. \frac{\widehat{i}_{Lac}(s)}{\widehat{d}_{ac}(s)} \right|_{\widehat{u}_{dc}(s)=0} = \frac{2U_{ac}(R_{ac}C_{ac}s + 1)}{R_{ac}L_{ac}C_{ac}s^2 + L_{ac}s - 2d_{ac} + 1}.$$

We add a PI controller as shown in

$$G'_{oiac}(s) = \frac{k_{piac}s + k_{iiac}}{s} \frac{2U_{ac}(R_{ac}C_{ac}s + 1)}{R_{ac}L_{ac}C_{ac}s^2 + L_{ac}s - 2d_{ac} + 1}. \quad (12)$$

Figure 7 is the frequency characteristic of voltage loop after correction. And we can see that, after the correction, the phase margin is 81.6 dB and the angle margin is 48.9°. The MG system dynamic response is improved.

4.2. BESS Unit Control Strategy. BESS unit is the most important part in the MG system, for it will influence the property and the cost of MG. It is necessary to use and control the BESS unit. Normally, the BESS unit can have two states, that is, the charging state and the discharging state. The control aim of the BESS unit is to let the BESS system realize energy balance and stable output in the MG system based on charging and discharging strategy. In this paper, we adopt constant-voltage limit current charging method.

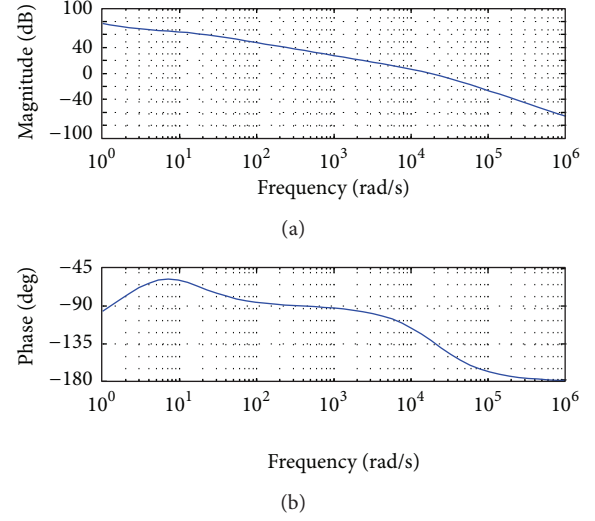


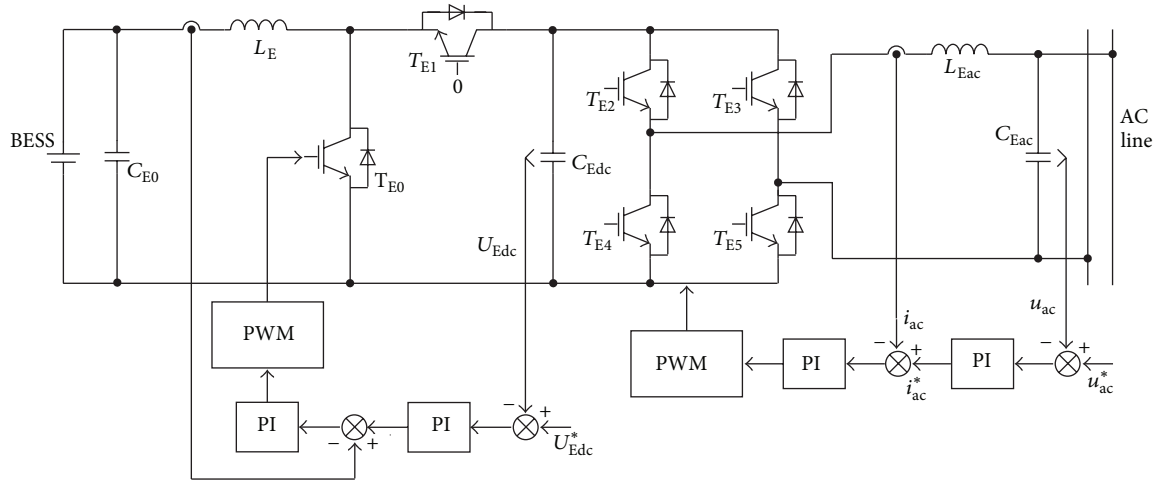
FIGURE 7: The frequency characteristic of boost converter before and after correction.

Figure 8 is the control block of energy storage unit on different modes. The first and the second converter are controlled individually in order to decrease the design difficulty. Figure 8(a) is the figure of BESS unit which acts as a master. The first converter control DC bus line and BESS unit discharged, while the second converter adopts voltage and current loop control and exchange with AC line. Figure 8(b) is the figure of BESS unit that acts as a slave. Under this state, the first converter has the same controller as in Figure 8(a). Bidirectional converter worked as boost converter, BESS unit discharges, and the second converter provides the energy for the loads. Figure 8(c) is the BESS unit that works on charge mode, at which the first converter worked as buck mode, BESS unit is charged, and the second converter is to keep the DC bus line voltage and the AC input current stable.

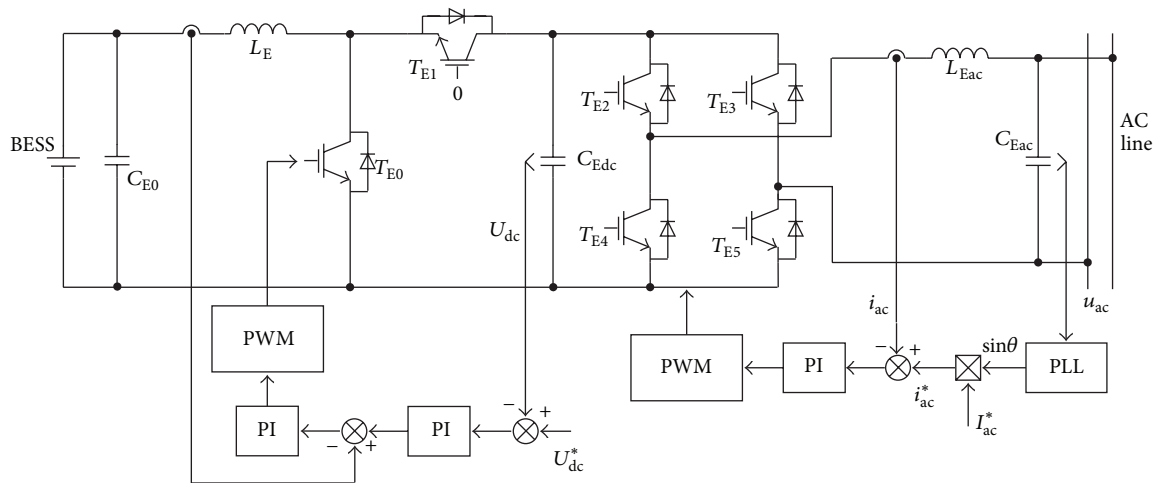
4.3. MG System Islanded Control Strategy. Figure 9 is the whole MG control block under the islanded mode. Every PV unit adopts VSI for connection to the MG, and there is no need for the PV units to adopt MPPT control and they only need to adjust voltage loop to keep DC bus balanced. The inverter adopts droop control strategy with an additional power calculation loop.

5. Simulation and Experimental Results

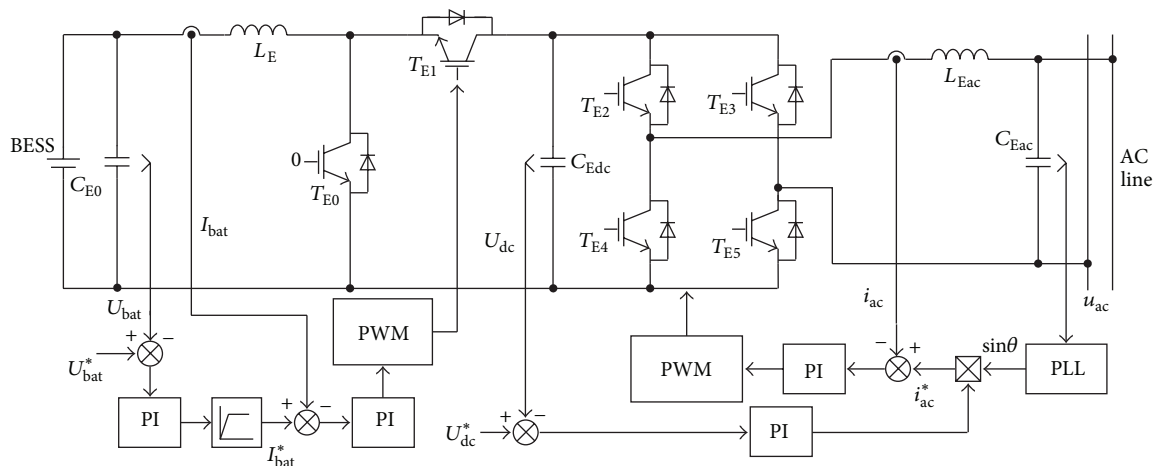
The above described configuration and control methods were first simulated over four different scenarios considering the variations in the produced PV power and the demand in the grid-connected mode. Figure 10 shows the simulation results adopting the control strategy in Figure 4, where u_{grid} , i_{grid} , i_{load} , i_{pv1} , i_{pv2} , P_{pva1} , and P_{pva2} are the grid voltage, grid current, load current, the output current of PV1 and PV2, and the output power of PV1 and PV2, respectively. During 0.1 s~0.2 s, the PV array produced 6000 W power and the total power was greater than the load demand, so excessive



(a) The energy storage unit acts as a master



(b) The energy storage unit acts as a slave



(c) The energy storage unit works on charge mode

FIGURE 8: The control block of energy storage unit on different modes.

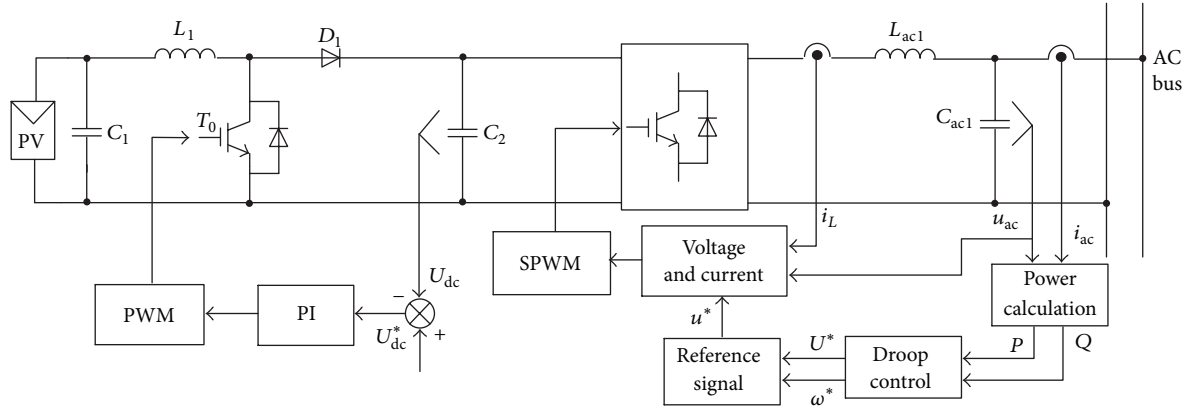


FIGURE 9: The control block of MG under islanded mode.

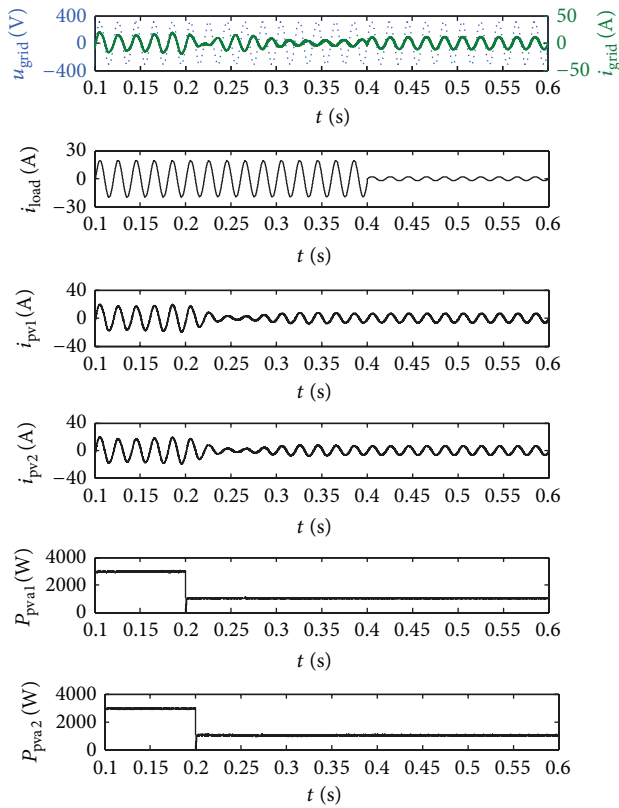


FIGURE 10: The simulation results of PV array connected to the grid.

power was fed back to the grid and the current had the same phase as the grid voltage. During 0.2 s~0.4 s, as light intensity was decreased, the total PV energy was reduced to 2200 W, which could not meet the demands, so the extra power was injected from the grid, and the grid side current and the grid voltage had different phase. Between 0.4 s and 0.6 s, although the PV array produced 2200 W power, the load demand was decreased, and the extra PV power was fed back to the grid again. It is evident from these figures that the quality of the output current of converter was satisfied and the response of MPPT control strategy was swift.

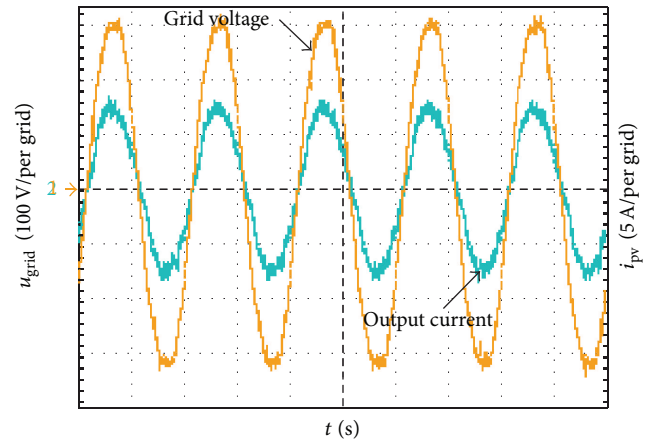


FIGURE 11: The experimental results in grid-connected mode.

The proposed control schemes were then applied to physical setup for the grid-connected mode, and Figure 11 shows the experimental results when the PV was connected to the grid. It can be seen that the output current and the output voltage of converter have the same phase and the unit power factor has been achieved.

Simulation results of the energy storage unit working on different modes are shown in Figure 12.

From the simulation results, it can be seen that, whether the BESS unit is in the master or the slave, the voltage of BESS unit is always kept stable and the output current changed with the AC line and kept the DC bus line voltage stable also. From Figures 12(a) and 12(b), it can be seen that the DC bus line is stable in 400 V quickly. From Figure 12(c), it can be seen that when the BESS unit is in the charging state, the energy will flow into BESS from AC line and the phase angle between the charging state and the discharging state is 180°.

Figure 13 is the simulation and experiment of BESS charging state. U_{bat} and I_{bat} are the voltage and current of battery, respectively. From the results, it can be seen that battery can realize from constant-current charging to constant-voltage charging and there is no current peak.

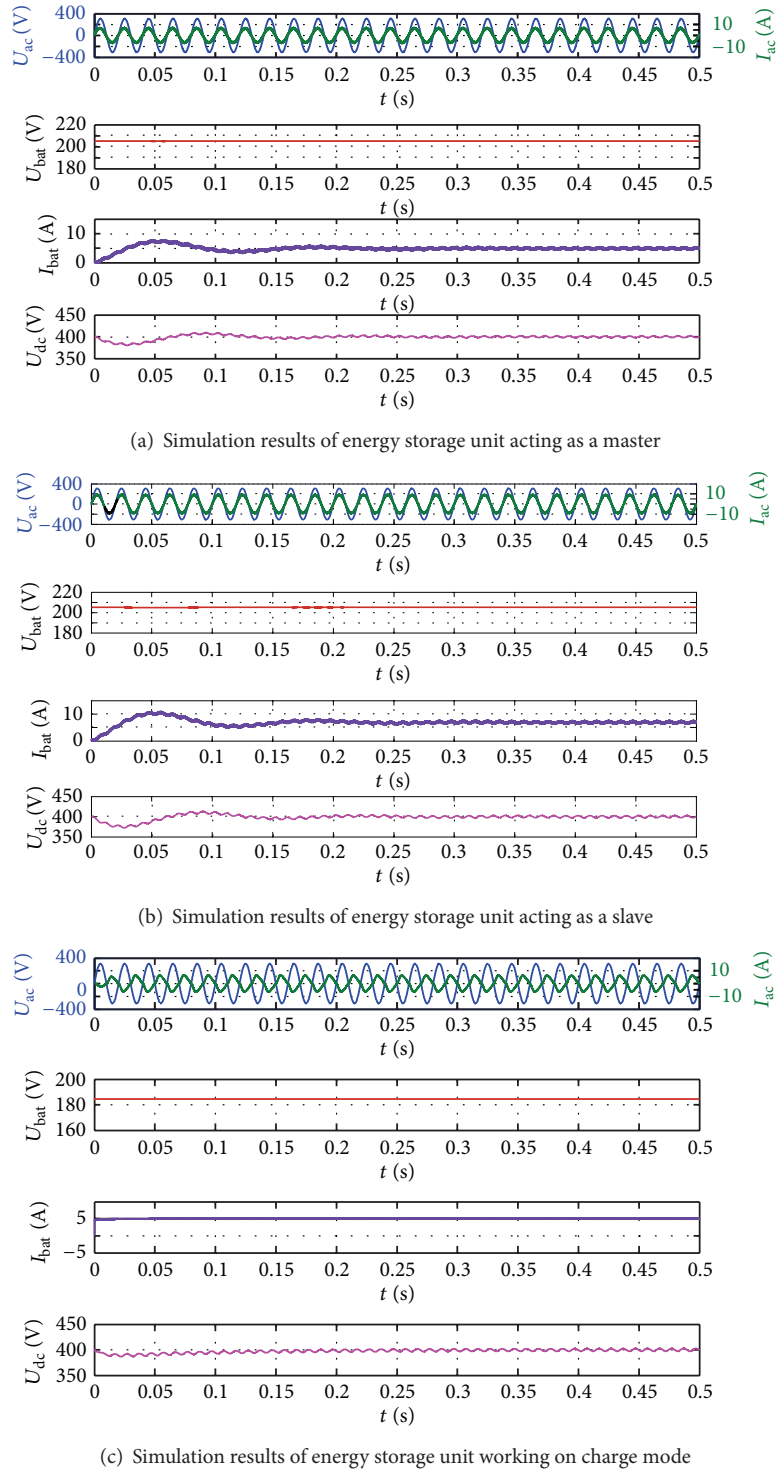


FIGURE 12: Simulation results of the energy storage unit working on different modes.

The proposed control scheme was then simulated under 5 different scenarios for the islanded mode. Figure 14 is the simulation results adopting the control strategy under the islanded mode. u_{load} , i_{load} , u_{pv1} , i_{pv1} , u_{pv2} , i_{pv2} , i_c , P_{pv1} , Q_{pv1} , P_{pv2} , Q_{pv2} , and f are the load voltage and current, the voltage, current, active power and reactive power of PV1 and PV2,

and the frequency, respectively. Between 0 s and 0.1 s, the MG had no load; therefore, the current and the active power and reactive power of PV units were all zero. At 0.1 s, the load of MG became larger and nearly half of the rated load, the voltage and the current had the same phase, and the active power was increased to 1500 W, while the reactive

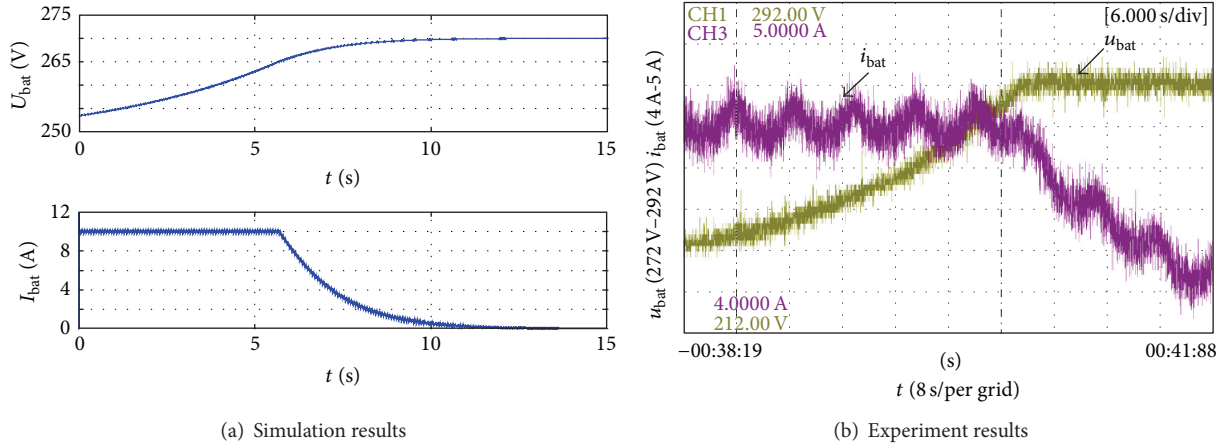


FIGURE 13: Results of constant-voltage current-limiting charge method.

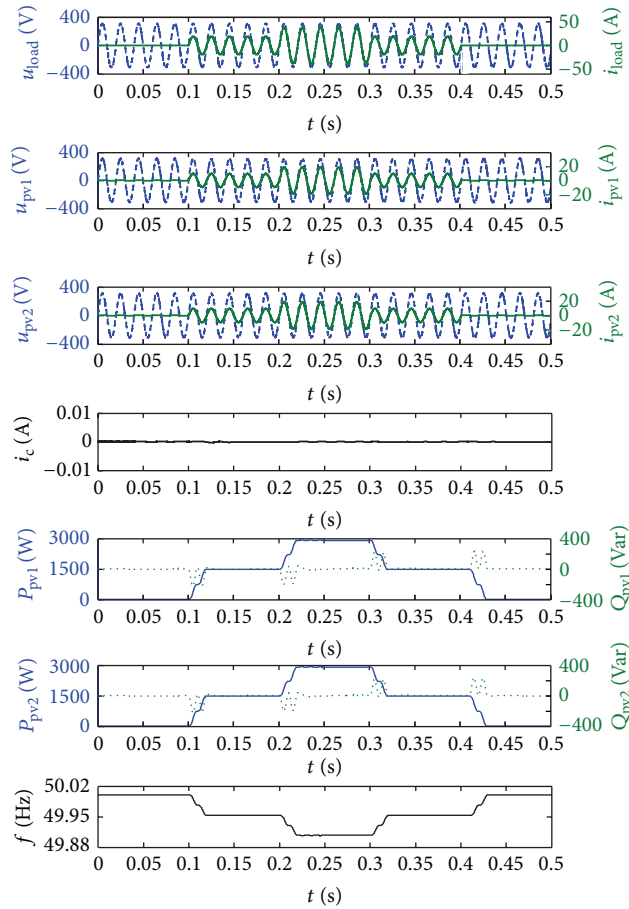


FIGURE 14: Droop control inverter simulation.

power was still 0 W and the frequency was lower than the prior frequency. Between 0.2 s and 0.3 s, the load increased continuously; between 0.3 s and 0.4 s, the load was decreased to half load again, and, during 0.4 s~0.5 s, the MG had no load again. From the simulation results, it can be seen that

the MG system responded exceptionally well and the loop current is small and even the load changes continuously. In the meantime, the results show that the droop control used for the control of the inverter could achieve stability of the whole MG system under different operation scenarios.

6. Conclusion

This paper studied a MG system integrated with PV panels, variable loads, a BESS, and AC line under the grid-connected mode and islanded mode. For the grid-connected mode, the paper adopts the MPPT combined PSC judgment to get the maximum power, while for the islanded mode the paper proposed to combine the droop control and the main/slave control to achieve the demanded voltage and the frequency and analysis of the function of BESS unit. Finally, simulation and experimental results have shown that the proposed method can automatically track the global power point under grid-connected mode and realize collaborative control of the MG system in islanded mode.

Conflict of Interests

The authors declare that there is no conflict of interests regarding the publication of this paper.

References

- [1] J. Vasquez, J. Guerrero, J. Miret, M. Castilla, and L. G. de Vicuna, "Hierarchical control of intelligent microgrids," *IEEE Industrial Electronics Magazine*, vol. 4, no. 4, pp. 23–29, 2010.
- [2] T. C. Green and M. Prodanović, "Control of inverter-based micro-grids," *Electric Power Systems Research*, vol. 77, no. 9, pp. 1204–1213, 2007.
- [3] N. Pogaku, M. Prodanović, and T. C. Green, "Modeling, analysis and testing of autonomous operation of an inverter-based microgrid," *IEEE Transactions on Power Electronics*, vol. 22, no. 2, pp. 613–625, 2007.
- [4] R. Teodorescu, F. Blaabjerg, M. Liserre, and P. C. Loh, "Proportional-resonant controllers and filters for grid-connected voltage-source converters," *IEE Proceedings: Electric Power Applications*, vol. 153, no. 5, pp. 750–762, 2006.
- [5] A. G. Tsikalakis and N. D. Hatziargyriou, "Centralized control for optimizing microgrids operation," *IEEE Transactions on Energy Conversion*, vol. 23, no. 1, pp. 241–248, 2008.
- [6] M. B. Delghavi and A. Yazdani, "An adaptive feedforward compensation for stability enhancement in droop-controlled inverter-based microgrids," *IEEE Transactions on Power Delivery*, vol. 26, no. 3, pp. 1764–1773, 2011.
- [7] C. K. Sao and P. W. Lehn, "Control and power management of converter fed microgrids," *IEEE Transactions on Power Systems*, vol. 23, no. 3, pp. 1088–1098, 2008.
- [8] E. Barklund, N. Pogaku, M. Prodanovic, C. Hernandez-Aramburo, and T. C. Green, "Energy management in autonomous microgrid using stability-constrained droop control of inverters," *IEEE Transactions on Power Electronics*, vol. 23, no. 5, pp. 2346–2352, 2008.
- [9] R. Majumder, A. Ghosh, G. Ledwich, and F. Zare, "Angle droop versus frequency droop in a voltage source converter based autonomous microgrid," in *Proceedings of the IEEE Power and Energy Society General Meeting (PES '09)*, pp. 1–8, Calgary, Canada, July 2009.
- [10] F. Katiraei and M. R. Iravani, "Power management strategies for a microgrid with multiple distributed generation units," *IEEE Transactions on Power Systems*, vol. 21, no. 4, pp. 1821–1831, 2006.
- [11] J. M. Guerrero, J. C. Vásquez, J. Matas, M. Castilla, and L. García de Vicuna, "Control strategy for flexible microgrid based on parallel line-interactive UPS systems," *IEEE Transactions on Industrial Electronics*, vol. 56, no. 3, pp. 726–736, 2009.
- [12] M. N. Marwali and A. Keyhani, "Control of distributed generation systems I: voltages and currents control," *IEEE Transactions on Power Electronics*, vol. 19, no. 6, pp. 1541–1550, 2004.
- [13] M. N. Marwali, J.-W. Jung, and A. Keyhani, "Control of distributed generation systems II: load sharing control," *IEEE Transactions on Power Electronics*, vol. 19, no. 6, pp. 1551–1561, 2004.
- [14] M. Popov, H. Karimi, H. Nikkhajoei, and V. Terzija, "Modeling, control and islanding detection of microgrids with passive loads," in *Proceedings of the 14th International Power Electronics and Motion Control Conference (EPE/PEMC '10)*, pp. T11107–T11112, September 2010.
- [15] K. Kobayashi, I. Takano, and Y. Sawada, "A study on a two stage maximum power point tracking control of a photovoltaic system under partially shaded insolation conditions," in *Proceedings of the IEEE Power Engineering Society General Meeting*, pp. 2612–2617, July 2003.
- [16] A. Al-Diab and C. Sourkounis, "Multi-tracking single-fed PV inverter," in *Proceedings of the 15th IEEE Mediterranean Electrotechnical Conference (MELECON '10)*, pp. 1117–1122, April 2010.
- [17] H. Patel and V. Agarwal, "Maximum power point tracking scheme for PV systems operating under partially shaded conditions," *IEEE Transactions on Industrial Electronics*, vol. 55, no. 4, pp. 1689–1698, 2008.
- [18] Z. Cheng, H. Zhou, and H. Yang, "Research on MPPT control of PV system based on PSO algorithm," in *Proceedings of the Chinese Control and Decision Conference (CCDC '10)*, pp. 887–892, May 2010.
- [19] T. Mishima and T. Ohnishi, "Power compensation system for partially shaded PV array using electric double layer capacitors," in *Proceedings of the 28th Annual Conference of the IEEE Industrial Electronics Society*, pp. 3262–3267, November 2002.
- [20] B.-Y. Liu, C.-H. Liang, and S.-X. Duan, "Research on topology of DC-module-based building integrated photovoltaic system," *Proceedings of the CSEE*, vol. 28, no. 20, pp. 99–104, 2008.
- [21] E. Karatepe, T. Hiyama, and M. Boztepe, "Power controller design for photovoltaic generation system under partially shaded insolation conditions," in *Proceedings of the International Conference on Intelligent Systems Applications to Power Systems (ISAP '07)*, pp. 1–16, IEEE, Toki Messe, Niigata, November 2007.
- [22] D. Nguyen and B. Lehman, "A reconfigurable solar photovoltaic array under shadow conditions," in *Proceedings of the 23rd Annual IEEE Applied Power Electronics Conference and Exposition (APEC '08)*, pp. 980–986, Austin, Tex, USA, February 2008.
- [23] S. A. Khajehoddin, A. Bakhshai, and P. Jain, "A novel topology and control strategy for maximum power point trackers and multi-string grid-connected PV inverters," in *Proceedings of the 23rd Annual IEEE Applied Power Electronics Conference and Exposition (APEC '08)*, pp. 173–178, Austin, Tex, USA, February 2008.
- [24] Y.-H. Ji, D.-Y. Jung, C.-Y. Won, B.-K. Lee, and J.-W. Kim, "Maximum power point tracking method for PV array under partially shaded condition," in *Proceedings of the IEEE Energy Conversion Congress and Exposition (ECCE '09)*, pp. 307–312, San Jose, Calif, USA, September 2009.

Research Article

Characterization of $\text{Cu}_{1.4}\text{Te}$ Thin Films for CdTe Solar Cells

Guangcan Luo, Bin Lv, Wei Li, Lianghuan Feng, Jingquan Zhang,
Lili Wu, and Guanggen Zeng

College of Materials Science and Engineering, Sichuan University, Chengdu 610064, China

Correspondence should be addressed to Wei Li; waylee2000@sohu.com

Received 17 February 2014; Accepted 28 April 2014; Published 15 May 2014

Academic Editor: Prakash Basnyat

Copyright © 2014 Guangcan Luo et al. This is an open access article distributed under the Creative Commons Attribution License, which permits unrestricted use, distribution, and reproduction in any medium, provided the original work is properly cited.

The copper telluride thin films were prepared by a coevaporation technique. The single-phase $\text{Cu}_{1.4}\text{Te}$ thin films could be obtained after annealing, and annealing temperature higher than 220°C could induce the presence of cuprous telluride coexisting phase. $\text{Cu}_{1.4}\text{Te}$ thin films also demonstrate the high carrier concentration and high reflectance for potential photovoltaic applications from the UV-visible-IR transmittance and reflectance spectra, and Hall measurements. With contacts such as $\text{Cu}_{1.4}\text{Te}$ and $\text{Cu}_{1.4}\text{Te}/\text{CuTe}$, cell efficiencies comparable to those with conventional back contacts have been achieved. Temperature cycle tests show that the $\text{Cu}_{1.4}\text{Te}$ contact buffer has also improved cell stability.

1. Introduction

Copper chalcogenides have attracted much interest because of their potential applications in thermoelectric devices [1] and in heterojunction structures [2–7]. Cusano [3] prepared a CdTe solar cell with an efficiency of 7.5% in which cuprous telluride (Cu_2Te) was used as a *p*-type partner to the *n*-type CdTe semiconductor. To further improve device performance of CdTe solar cells, Cu_2Te is commonly used as a *p*-type back contact layer to facilitate low resistance contact formation [4, 5]. However, due to the fast diffusivity of Cu in CdTe and the apparent instability of Cu_2Te ($\text{Cu}_2\text{Te} \rightarrow \text{CuTe} + \text{Cu}$, $\text{Cu}_2\text{Te} \rightarrow 2\text{Cu} + \alpha\text{Te} + 1/2(1-\alpha)\text{Te}_2$ [8, 9]), copper is suspected to be responsible for changes in cell performance and stability with exposure to light [10–12]. Since this particular element plays a key role in cell performance and characteristics, it is important to minimize the Cu supply while maintaining the ohmic characteristics of p^+CdTe contact. Thus, an extensive investigation of the properties of copper tellurides (Cu_xTe) and stability of CdTe-based solar cells with Cu_xTe has been carried out [13]. It has been found that Cu_xTe shows bistability with energy minimum at $x \approx 1.25$ and $x \approx 1.75$ [13]. These results using first-principles calculations are consistent with experimental observations, which find stable Cu_xTe structures at two different Cu concentrations (i.e., $1.30 < x < 1.43$ and $x \approx 2$ [6, 7]). The calculated minimum

energy concentrations are slightly smaller than experimental observations due to the fact that strain and temperature effects are not included in the calculation. Therefore, in our work, Cu_xTe thin films at low x ($x = 1.4$) were prepared by vacuum coevaporation. The properties of Cu_xTe thin films at low x were studied and performance of CdTe solar cells with Cu_xTe was investigated and also monitored with the temperature cycle test.

2. Experimental Details

$\text{Cu}_{1.4}\text{Te}$ thin films were deposited on a simultaneous evaporation system DM-400 to a thickness of ~ 200 nm at room temperature. Cu foil (99.999% purity) and Te powder (99.999% purity) were evaporated on substrates from two independent sources, respectively. The deposition rate and the thickness of thin films were monitored by two-thickness monitors (LHC-2, Huazhao Industrial Ltd., China). After deposition, a posttreatment was performed at different temperatures in N_2 ambient. X-ray diffraction (XRD) (DX-2600, Dandong Fangyuan Instrumental Ltd., China) measurements were used to study the copper telluride structure. The transmittance and reflectance spectra were used to investigate the optical properties of materials. The four-probe Van der Pauw method was used to carry out the Hall measurements to

determine the Hall coefficient, mobility, and carrier concentration.

Solar cells were fabricated in a superstrate configuration typical of CdTe devices, that is, glass/TCO/CdS/CdTe/back contact. CdS thin films were deposited by a chemical bath deposition technique to a thickness of 180 nm onto the glass substrate coated with SnO₂:F. CdTe thin films were subsequently prepared in argon and oxygen ambient by close-spaced sublimation to a thickness of ~5 μm. Following the heat treatment of the samples in CdCl₂, the CdTe surface was etched in a bromine/methanol solution (0.05% vol.). The back contact, Cu_{1.4}Te (~100 nm), was deposited on the etched CdTe surface by coevaporation. And then samples were treated in a pure N₂ ambient in the 180°C~220°C range. Finally, Ni thin films (~300 nm) prepared by electron beam evaporation were used as a back electrode to complete the back contacts processing. The photovoltaic devices were characterized using dark *J-V* measurement (4155C, Agilent, USA) and light *J-V* measurement (XJCM-9, Gsolar, China) under simulated AM1.5 illumination (100 mW/cm²). The device stability was performed using the high- and low-temperature cycle tests. As shown in Figure 1 one cycle was the process of the cycling through two temperature extremes (i.e., 85°C and -40°C).

3. Results and Discussion

3.1. Structural, Optical, and Electronic Properties of Cu_{1.4}Te Thin Films. Copper telluride thin films were deposited by coevaporation at room temperature on glass substrates as shown in Figure 2. The thin films as-deposited were an amorphous structure. There are no changes in the phase for copper telluride thin films with annealing temperature up to 170°C. Then the thin films were annealed at 180°C in N₂ ambient. Copper telluride thin films annealed had some diffraction peaks. The peaks at about 2θ of 11.393°, 14.461°, 23.516°, 26.586°, 26.667°, 29.159°, 44.415°, 55.078°, and 60.501° correspond to the (021), (002), (051), (052), (004), (006), (204), and (176) planes of Cu_{1.4}Te, respectively. The results also indicate that the Cu_{1.4}Te thin films are single-phase hexagonal structure with random orientations when annealed at a higher temperature, that is, 200°C. Figure 2 shows XRD pattern of Cu_{1.4}Te thin films annealed at 220°C. The intensity of these diffraction peaks for the thin films increased with annealing temperature. And there are remarkable differences among these two samples annealed at 200°C and 220°C. The peak at 2θ of 12.9°, corresponding to the lattice spacing of 6.8487 Å, was indexed as the 1st order diffraction of the cupric telluride (CuTe). So, the peak positions of the (002), (003), and (004) planes at 2θ of 25.8°, 40°, and 52.8° were the 2nd, 3rd, and 4th order diffraction of CuTe. The presence of other X-ray diffraction peaks associated with a CuTe phase indicated that the coexisting phase had occurred. It is obvious that annealing to 220°C results in the formation of coexisting phase for copper telluride thin films, which may have a strong influence on the stability of the CdTe-based solar cells. Therefore, the devices for this work were

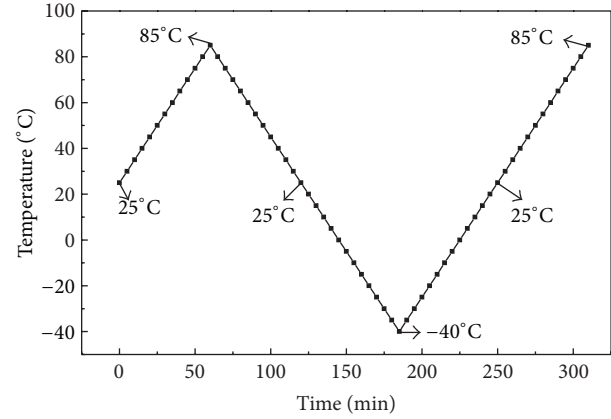


FIGURE 1: The high- and low-temperature cycle testing curve.

postannealed at 180°C~220°C, whose results will be discussed in Section 3.2.

The optical properties of Cu_{1.4}Te thin films with a single-phase hexagonal structure were studied using the UV-Visible-IR transmittance and reflectance spectra as shown in Figure 3. The transmittance of no more than 30% for Cu_{1.4}Te thin films in the range of 300~900 nm was observed. While the reflectance for the thin films increased up to ~50% in the range from 500 to 900 nm, which may reflect the photons in this range to p-n junction. It can be inferred that the thickness of the absorption layer, CdTe, can be reduced in the CdTe solar cells due to the incorporation of the thin films, Cu_{1.4}Te, as the back contact. From the optical properties of Cu_{1.4}Te thin films we suggest that it may be a kind of good photovoltaic materials in CdS/CdTe heterojunction solar cells.

The electronic properties of single-phase Cu_{1.4}Te thin films from the Hall measurements were also investigated. Table 1 shows the parameters for Cu_{1.4}Te thin films such as the mobility, Hall coefficient, and carrier concentration. The results show that Cu_{1.4}Te thin films were *p*-type semiconductor compounds and had high carrier concentration, ~ 10²¹ cm⁻³. The high carrier concentration means high conductivity which can reduce series resistance of the solar cells with a Cu_{1.4}Te layer and thus improve remarkably the device performance. Table 1 also shows that the mobility of Cu_{1.4}Te thin films is very low. The carrier mobility has the following relation:

$$\mu_p = \frac{q\tau_p}{m_p}, \quad (1)$$

where q is the elementary charge, τ_p is the relaxation time, and m_p is the effective mass. Because the carrier effective mass did not alter much, it is deduced that the increase of the mobility is due to the decrease of the relaxation time, which inverses to the scattering probability. Therefore, further improvement in the thin films, such as less defects, small strain, and large grain sizes, for practical use can be made.

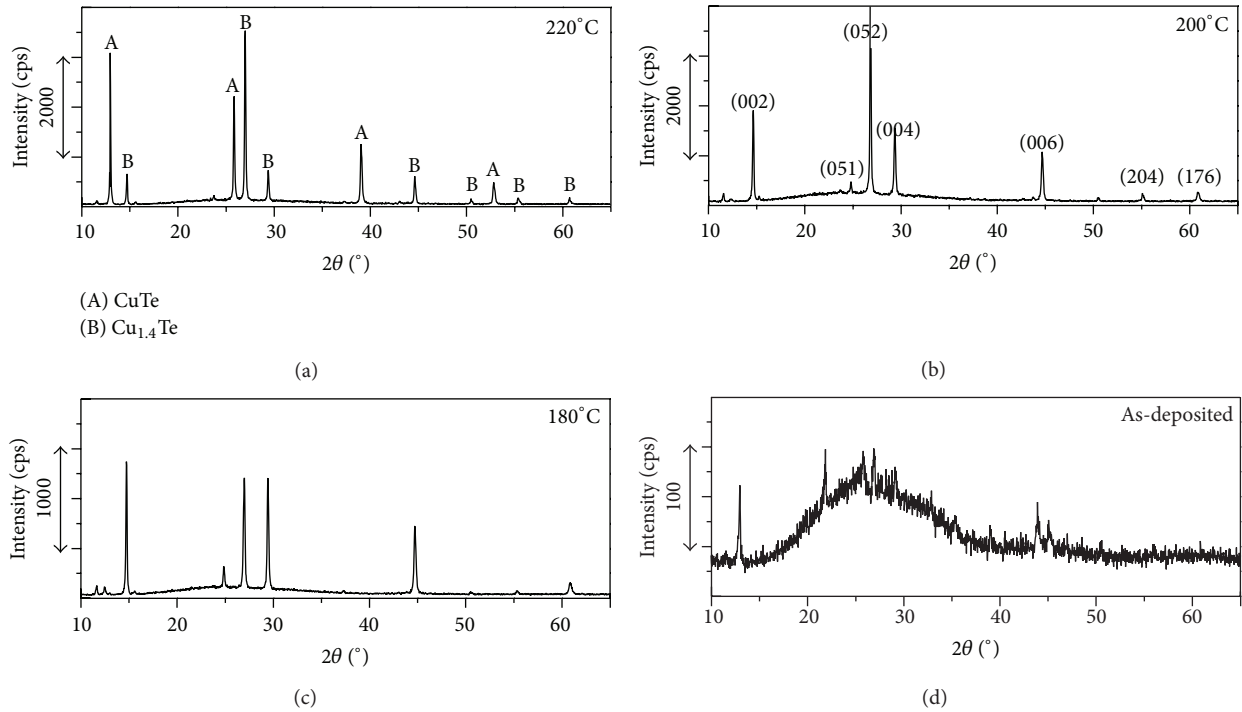


FIGURE 2: XRD patterns of copper telluride thin films as deposited and annealed at different temperatures.

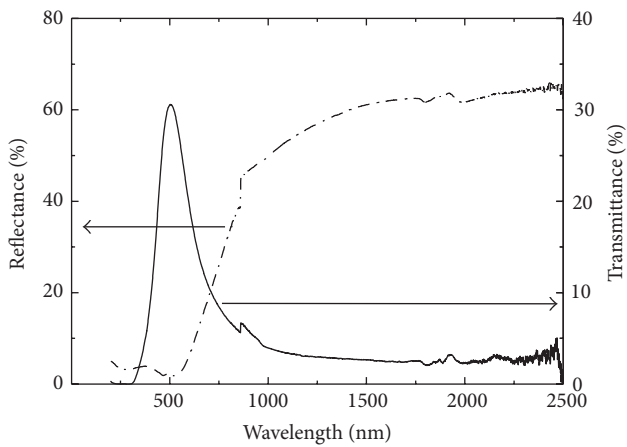


FIGURE 3: Transmittance and reflectance spectra for $\text{Cu}_{1.4}\text{Te}$ thin films.

TABLE 1: Parameters for $\text{Cu}_{1.4}\text{Te}$ thin films.

Sample	Mobility ($\text{cm}^2/\text{V}\cdot\text{s}$)	Hall coefficient (cm^3/Cb)	Carrier concentration (cm^{-3})
$\text{Cu}_{1.4}\text{Te}$	13.82	0.0042	1.48×10^{21}

3.2. *CdTe Solar Cells with $\text{Cu}_{1.4}\text{Te}$ Thin Films.* In this work, the device configuration consisted of a glass/ SnO_2 / CdS / CdTe /back contact/ Ni structure, where back contact was $\text{Cu}_{1.4}\text{Te}$ thin films. After chemical etching, the $\text{Cu}_{1.4}\text{Te}$ thin films were deposited on the CdTe thin films and annealed in N_2 ambient. Figure 4 shows the XRD pattern of CdTe

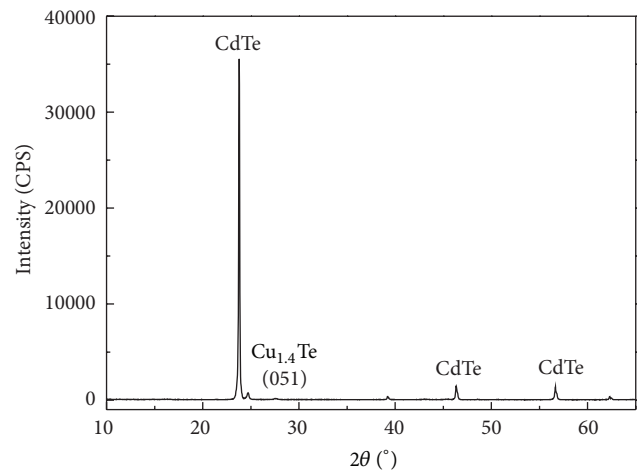


FIGURE 4: XRD pattern of $\text{Cu}_{1.4}\text{Te}$ thin films deposited on the CdTe thin films.

solar cells with a $\text{Cu}_{1.4}\text{Te}$ layer annealed at 200°C before metallization. Besides the diffraction peaks of CdTe , the XRD pattern demonstrates the other phase with weak diffraction intensity, which can be indexed to (051) planes of $\text{Cu}_{1.4}\text{Te}$ thin films.

To investigate the effect of $\text{Cu}_{1.4}\text{Te}$ thin films on back contact formation and device performance, device characterization was performed on CdTe devices. Table 2 shows the device parameters for CdTe solar cells with or without $\text{Cu}_{1.4}\text{Te}$ thin films annealed at different temperatures in N_2 ambient. One can see that CdTe solar cells made with a

TABLE 2: Device parameters for CdTe solar cells with or without Cu_{1.4}Te thin films.

T (°C)	V_{oc} (mV)	J_{sc} (mA/cm ²)	E_{ff} (%)	FF (%)	Area (cm ²)
nb ^c *	667	20.5	7.6	55	0.0707
180	721	22.7	9.7	57	0.19625
200	736	23.6	11.6	67	0.0707
220	788	21.0	9.5	57	0.19625

*nb^c denotes the cells without back contacts.

TABLE 3: Evolution of device parameters for CdTe solar cells with the temperature cycling.

Day and cycle	nb ^c				Cu _{1.4} Te			
	V_{oc} (mV)	FF (%)	J_{sc} (mA/cm ²)	E_{ff} (%)	V_{oc} (mV)	FF (%)	J_{sc} (mA/cm ²)	E_{ff} (%)
Initial	695	55.9	21.45	8.33	732	67.4	23.81	11.75
30d3c*	676	46.4	19.33	6.74	709	58.4	22.95	9.50
90d9c	495	—	17.81	—	712	58.2	23.07	9.56
180d12c					708	57.0	22.56	9.10
420d42c					707	50.5	21.24	7.58

*30d3c denotes 3 cycles after 30 days in the period of testing.

Cu_{1.4}Te layer have better performance than those without Cu_{1.4}Te back-contact. that is, the short circuit current (J_{sc}), open circuit voltage (V_{oc}), fill factor (FF) and conversion efficiency (E_{ff}) increased for CdTe solar cells made with a Cu_{1.4}Te layer. Annealing at high temperatures is commonly used in the back contact formation process for the diffusion and dopant activation [14]. In this work, higher V_{oc} was obtained when the cells were annealed at a higher temperature. This may be attributed to the increase of the acceptors. It can be seen that the device performance of CdTe solar cells with single-phase Cu_{1.4}Te thin films annealed at 200°C is superior to that of the solar cells with coexisting phase copper telluride thin films at 220°C. We suggest that the single-phase Cu_{1.4}Te thin films annealed at 200°C are more suitable for forming *p*-type back contacts between CdTe and the electrodes than coexisting phase thin films.

Dark *J-V* characteristic of solar cells (Figure 5) can be expressed by Shockley diode equation:

$$J = J_0 \left[\exp\left(\frac{qV}{AkT}\right) - 1 \right], \quad (2)$$

where J stands for the diode current, J_0 denotes the dark saturation current, A is the diode ideality factor. From the dark *J-V* characteristic curve (Figure 5), one can obtain a dark saturation current $J_0 = 1.67 \times 10^{-6}$ mA/cm², and a diode quality factor $A = 2.23$, which is consistent with the results reported by Wu et al. [6], for CdTe solar cells with a single-phase Cu_{1.4}Te layer annealed at 200°C. The illuminated *J-V* curve (see also Figure 5) compared to the dark *J-V* curve shows that the crossover is eliminated effectively due to the incorporation of the Cu_{1.4}Te back contact.

The stability of the solar cells with Cu_{1.4}Te back contacts was evaluated with the temperature cycle tests. Table 3 shows the evolution of the photovoltaic parameters for the CdTe solar cells with Cu_{1.4}Te. Under this environmental stress condition, some parameters of the device have quite random values as a function of stress time, which is similar to other

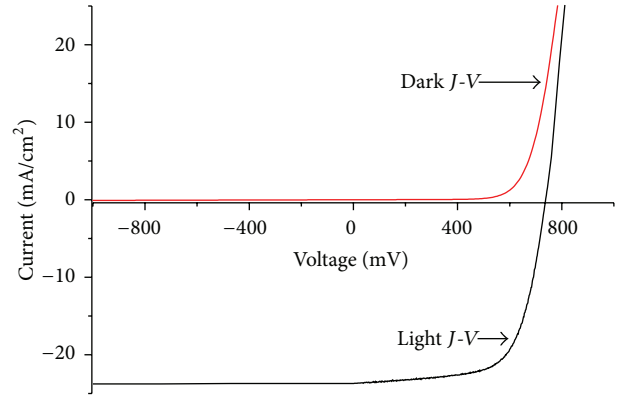


FIGURE 5: Dark and light *J-V* curves for a CdS/CdTe/Cu_{1.4}Te solar cell.

environmental stress tests [12]. This may be evidence of the existence of traps within the absorber CdTe layers. The CdTe cell without Cu_{1.4}Te degraded rapidly in cell efficiency from 8.33% to zero after 90 days and 9 cycles, whereas the CdTe cell with Cu_{1.4}Te showed much improved stability with efficiency loss from 11.75% to 7.58% even after 420 days and 42 cycles. The degradation may be attributed in part to the unencapsulated cells in the laboratory and the back electrodes with exposure to moist air.

4. Conclusions

Copper telluride thin films were prepared by using the vacuum coevaporation method. At low temperature, the copper telluride thin films were an amorphous structure. In the temperatures ranging between 180 and 220°C, the copper telluride thin films indicate the form of the single-phase Cu_{1.4}Te structure, whereas with annealing temperature higher than 220°C, the coexisting phase for the thin films

occurs. With a $\text{Cu}_{1.4}\text{Te}$ as a back contact layer, efficient and stable CdTe solar cells can be obtained.

Conflict of Interests

The authors declare that there is no conflict of interests regarding the publication of this paper.

Acknowledgments

This work was supported by the National Basic Research Program of China (Grant no. 2011CBA007008), National Natural Science Foundation of China (Grant no. 61076058), and the Science and Technology Program of Sichuan Province, China (Grant no. 13ZC2185).

References

- [1] V. V. Gorbatchev, *Semiconducting A_2B^{VI} compounds*, Metallurgia, Moscow, Russia, 1980.
- [2] W. S. Chen, J. M. Stewart, and R. A. Mickelsen, "Polycrystalline thin-film $\text{Cu}_{2-x}\text{Se}/\text{CdS}$ solar cell," *Applied Physics Letters*, vol. 46, no. 11, pp. 1095–1097, 1985.
- [3] D. A. Cusano, "CdTe solar cells and photovoltaic heterojunctions in II-VI compounds," *Solid State Electronics*, vol. 6, no. 3, pp. 217–218, 1963.
- [4] B. Lv, X. Di, W. Li et al., "Preparation of Cu_2Te thin films and back-contact formation of CdTe solar cells," *Japanese Journal of Applied Physics*, vol. 48, no. 8, pp. 0855011–0855014, 2009.
- [5] J. H. Yun, K. H. Kim, D. Y. Lee, and B. T. Ahn, "Back contact formation using Cu_2Te as a Cu-doping source and as an electrode in CdTe solar cells," *Solar Energy Materials and Solar Cells*, vol. 75, no. 1-2, pp. 203–210, 2003.
- [6] X. Wu, J. Zhou, A. Duda et al., "Phase control of Cu_xTe film and its effects on CdS/CdTe solar cell," *Thin Solid Films*, vol. 515, no. 15, pp. 5798–5803, 2007.
- [7] G. Lorenz and C. Wagner, "Investigations on cuprous selenide and copper tellurides," *The Journal of Chemical Physics*, vol. 26, no. 6, pp. 1607–1608, 1957.
- [8] G. Teeter, " Cu_2Te synthesis and in-vacuum thermal decomposition: chemical-kinetics analysis and comparison to equilibrium vapor-pressure measurements," *Thin Solid Films*, vol. 515, no. 20-21, pp. 7886–7891, 2007.
- [9] B. Brunetti, V. Piacente, P. Vassallo, and A. R. Villani, "A torsion-effusion study on the sublimation of Cu_2Te ," *Materials Chemistry and Physics*, vol. 70, no. 3, pp. 263–267, 2001.
- [10] P. R. Kharangarh, D. Misra, G. E. Georgiou, and K. K. Chin, "Characterization of space charge layer deep defects in n+-CdS/p-CdTe solar cells by temperature dependent capacitance spectroscopy," *Journal of Applied Physics*, vol. 113, no. 14, Article ID 144504, pp. 1–6, 2013.
- [11] P. Kharangarh, D. Misra, G. E. Georgiou, and K. K. Chin, "Evaluation of Cu back contact related deep defects in CdTe solar cells," *ECS Journal of Solid State Science and Technology*, vol. 1, no. 5, pp. Q110–Q113, 2012.
- [12] D. L. Bätzner, R. Wendt, A. Romeo, H. Zogg, and A. N. Tiwari, "Study of the back contacts on CdTe/CdS solar cells," *Thin Solid Films*, vol. 361-362, pp. 463–467, 2000.
- [13] J. L. F. da Silva, S.-H. Wei, J. Zhou, and X. Wu, "Stability and electronic structures of Cu_xTe ," *Applied Physics Letters*, vol. 91, no. 9, Article ID 091902, 2007.
- [14] B. Biglari, M. Samimi, M. Hage-Ali, J. M. Koebel, and P. Siffert, "Effects of copper in high resistivity cadmium telluride," *Journal of Crystal Growth*, vol. 89, no. 4, pp. 428–434, 1988.

Research Article

Performance Improvement of Microcrystalline p-SiC/i-Si/n-Si Thin Film Solar Cells by Using Laser-Assisted Plasma Enhanced Chemical Vapor Deposition

Hsin-Ying Lee,¹ Ting-Chun Wang,¹ and Chun-Yen Tseng²

¹ Department of Photonics, Research Center Energy Technology and Strategy, Advanced Optoelectronic Technology Center, National Cheng Kung University, Tainan 701, Taiwan

² Institute of Microelectronics, Department of Electrical Engineering, Advanced Optoelectronic Technology Center, National Cheng Kung University, Tainan 701, Taiwan

Correspondence should be addressed to Hsin-Ying Lee; hylee@ee.ncku.edu.tw

Received 20 February 2014; Accepted 26 April 2014; Published 14 May 2014

Academic Editor: Sudhakar Shet

Copyright © 2014 Hsin-Ying Lee et al. This is an open access article distributed under the Creative Commons Attribution License, which permits unrestricted use, distribution, and reproduction in any medium, provided the original work is properly cited.

The microcrystalline p-SiC/i-Si/n-Si thin film solar cells treated with hydrogen plasma were fabricated at low temperature using a CO₂ laser-assisted plasma enhanced chemical vapor deposition (LAPECVD) system. According to the micro-Raman results, the i-Si films shifted from 482 cm⁻¹ to 512 cm⁻¹ as the assisting laser power increased from 0 W to 80 W, which indicated a gradual transformation from amorphous to crystalline Si. From X-ray diffraction (XRD) results, the microcrystalline i-Si films with (111), (220), and (311) diffraction were obtained. Compared with the Si-based thin film solar cells deposited without laser assistance, the short-circuit current density and the power conversion efficiency of the solar cells with assisting laser power of 80 W were improved from 14.38 mA/cm² to 18.16 mA/cm² and from 6.89% to 8.58%, respectively.

1. Introduction

Recently, the silicon- (Si-) based thin film solar cells with several advantages, such as high absorptivity, easy fabrication, and low cost, have been extensively studied [1, 2]. The hydrogenated amorphous-Si (a-Si:H) films and the microcrystalline-Si (μ c-Si) films have been popularly utilized to fabricate the Si-based thin film solar cells. However, the a-Si:H films deposited using a plasma enhanced chemical vapor deposition (PECVD) system suffer from the light illumination induced degradation (Staebler-Wronski effect) [3]. This degradation phenomenon could be attributed to that when the a-Si:H thin film solar cells were illuminated by sunlight for a period time, a part of Si-H bonds in the a-Si:H films were broken, and the resulting dangling bonds produced carrier quenching centers, which degraded the performances of the solar cells. In contrast, the μ c-Si films did not have this problem and were more suitable to be applied to construct the thin film solar cells. In this work, the laser-assisted plasma enhanced chemical vapor

deposition (LAPECVD) system invented by our research group was used to directly deposit μ c-Si films without further annealing treatment [4–8]. The silane (SiH₄) reacting gas could be easily and efficiently decomposed into Si atoms under the combined action of the plasma and CO₂ laser, due to the high absorption coefficient of SiH₄ reacting gas at a wavelength of CO₂ laser (10.6 μ m). Consequently, the high quality microcrystalline intrinsic Si (μ c-i-Si) films could be deposited by the LAPECVD system at low temperature for the Si-based thin film solar cells. However, compared with the a-Si thin film solar cells, the open circuit voltage (V_{oc}) and fill factor (FF) of the μ c-Si thin film solar cells were lower [9, 10]. To overcome the above problem, the p-SiC film was deposited as the window layer to enhance the V_{oc} and FF. In addition, since the SiC is a wide bandgap material, the carrier recombination in the SiC layer is slower, which is beneficial to the improvement in the efficiency of resulting solar cells.

Since the quality of Si thin films played an important role in the Si-based thin film solar cells, in addition to the film deposition technique, many treatment technologies were

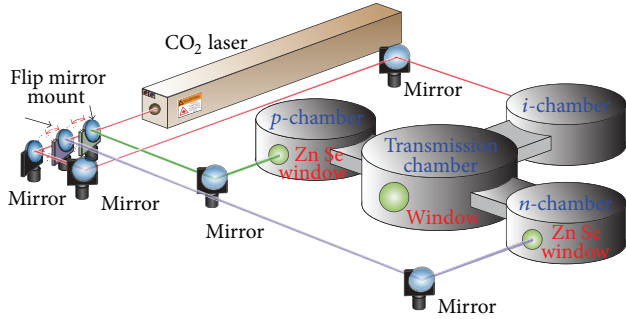


FIGURE 1: Schematic diagram of three-chamber LAPECVD system.

also utilized to passivate the dangling bonds in the Si thin films, such as hydrogen plasma treatment [11–13], HNO_3 treatment [14], chemical HF treatment [15], wet-chemical treatment [16], and Al_2O_3 passivation [17]. In this work, at the deposited processes, to avoid the contamination between the films by the external environment, all the fabricated processes of the microcrystalline p-SiC/i-Si/n-Si solar cells were kept in the vacuum environment. Consequently, among those treatment technologies, the hydrogen treatment technique was used to treat the p-SiC layer surface for decreasing the dangling bonds and improving the performance of the microcrystalline p-SiC/i-Si/n-Si thin film solar cells.

2. Experiments

Figure 1 shows the schematic configuration of the three-chamber LAPECVD system used in the work. The three chambers were designed to prevent the dopants cross contamination during the deposition of the n-type, intrinsic-type (i-type), and p-type Si-based films. To investigate the function of the laser assistance for the improvement in the properties of the deposited i-Si films, 150 nm-thick i-Si films were deposited on glass substrates using a LAPECVD system with various assisting laser powers of 0, 50, 60, 70, and 80 W. Meanwhile, the radio frequency (RF, 13.56 MHz) power, chamber pressure, flow rate of hydrogen-diluted SiH_4 (5%) reacting gas, and substrate temperature were set to be 20 W, 0.6 torr, 60 sccm, and 250°C , respectively. The bonding configuration and crystallization characteristics of the deposited i-Si films were analyzed using Fourier transform infrared (FTIR) spectrometry, micro-Raman scattering spectroscopy, and X-ray diffraction (XRD), respectively.

Figure 2 shows the schematic configuration of the p-SiC/i-Si/n-Si thin films solar cells. A 25 nm-thick p-SiC layer was deposited on the fluorine-doped tin oxide- (FTO-) coated glass substrate with texture structure using the LAPECVD system with assisting laser power of 80 W. The reacting gases, hydrogen-diluted SiH_4 (5%), methane (CH_4), and hydrogen-diluted diborane (B_2H_6) (1%), were utilized as the Si, C, and p-type dopant sources, respectively. The corresponding flow rate was 70 sccm, 25 sccm, and 4 sccm, respectively. The RF power, chamber pressure, and substrate temperature were kept at 20 W, 1.1 torr, and 250°C , respectively. The hole concentration and conductivity of the p-SiC

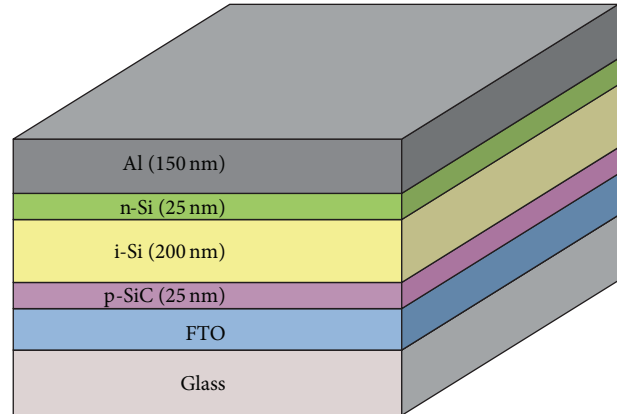


FIGURE 2: Schematic configuration of the p-SiC/i-Si/n-Si thin film solar cells.

layer deposited with assisting laser power of 80 W were $4.06 \times 10^{17} \text{ cm}^{-3}$ and $2.58 \times 10^{-2} \mu\text{S/cm}$, respectively. Prior to the deposition of the i-Si absorption layer, the p-SiC surface was passivated using hydrogen plasma treatment at RF power of 20 W for 25 min. A 200 nm-thick i-Si layer was immediately deposited on the p-SiC layer using the LAPECVD system with assisting laser power of 80 W. The RF power, chamber pressure, flow rate of hydrogen-diluted SiH_4 (5%) reacting gas, and substrate temperature were kept at 20 W, 0.6 torr, 60 sccm, and 250°C , respectively. Subsequently, a 20 nm-thick n-Si layer was deposited, using the same equipment with assisting laser power of 80 W, on the i-Si absorption layer. The hydrogen-diluted SiH_4 (5%) and hydrogen-diluted phosphine (PH_3) (1%) reacting gases were used as the Si and n-type dopant sources, respectively. The corresponding flow rate was 40 sccm and 10 sccm, respectively. The RF power, chamber pressure, and substrate temperature were kept at 60 W, 0.4 torr, and 250°C , respectively. The electron concentration and conductivity of the n-Si layer deposited with assisting laser power of 80 W were $5.74 \times 10^{19} \text{ cm}^{-3}$ and $8.75 \mu\text{S/cm}$, respectively. Finally, a 150 nm-thick Al electrode was deposited on the n-Si layer using the electron beam evaporator. The active area of the solar cell was 0.025 cm^2 . The p-SiC/i-Si/n-Si thin film solar cells deposited without laser assistance were also fabricated for comparison. The hole concentration and conductivity of the p-SiC layer deposited without laser assistance were $2.73 \times 10^{16} \text{ cm}^{-3}$ and $3.45 \times 10^{-3} \mu\text{S/cm}$, respectively. The electron concentration and conductivity of the n-Si layer deposited without laser assistance were $2.61 \times 10^{18} \text{ cm}^{-3}$ and $5.26 \times 10^{-1} \mu\text{S/cm}$, respectively.

3. Experimental Results and Discussion

The bonding configurations of the i-Si films deposited with various assisting laser powers were carried out using a Fourier transformation infrared (FTIR) spectrometry. Figure 3 shows the absorption spectra $\alpha(\omega)$ of the deposited i-Si films, where $\alpha(\omega)$ was the absorption coefficient as a function of wavenumber ω of the light. In particular, the absorption

spectrum $\alpha(\omega)/\omega$ of the i-Si films deposited with assisting laser power of 80 W was shown in the inset of Figure 3. All the measured spectra, after decomposition, exhibited two bands with peak positions of 2000 cm^{-1} and 2100 cm^{-1} , which correspond to the stretching vibrations of SiH and SiH₂, respectively. The microstructure factor R was defined as $R = I_{2100}/(I_{2100} + I_{2000})$, where I_{2000} and I_{2100} were the corresponding intensity of the two decomposed bands. The R of the i-Si films deposited with assisting laser power of 0, 50, 60, 70, and 80 W was 0.382, 0.318, 0.282, 0.237, and 0.221, respectively. The R value decreased with the assisting laser power. In other words, the intensity of the band corresponding to SiH₂ in the deposited i-Si films decreased with the assisting laser power, which implied that the high quality i-Si films could be obtained using the LAPECVD system. The hydrogen concentration (N_{H}) of the i-Si films deposited with assisting laser power of 80 W was estimated by the equation shown below [18]:

$$N_{\text{H}} = A_{2000} \int \frac{\alpha_{2000}(\omega)}{\omega} d\omega + A_{2100} \int \frac{\alpha_{2100}(\omega)}{\omega} d\omega, \quad (1)$$

where A_{2000} and A_{2100} are proportionality constants at wavenumber of 2000 cm^{-1} and 2100 cm^{-1} and equal $9.0 \times 10^{19}\text{ cm}^{-2}$ and $2.2 \times 10^{20}\text{ cm}^{-2}$, respectively, $\alpha_{2000}(\omega)$ and $\alpha_{2100}(\omega)$ are the absorption coefficients of the bands centered at wavenumber of 2000 cm^{-1} and 2100 cm^{-1} , respectively, and ω is the frequency in cm^{-1} . The hydrogen content (C_{H}) of the i-Si films deposited with and without laser assistance could be also estimated by the equation $N_{\text{H}}/N_{\text{Si}} \times 100\%$, where N_{Si} of $5 \times 10^{22}\text{ cm}^{-3}$ is the number density of crystal Si [19]. Figure 4 shows the hydrogen concentration and hydrogen content of the deposited i-Si films as a function of the assisting laser power used in the film deposition. As shown in Figure 4, the N_{H} of $1.10 \times 10^{21}\text{ cm}^{-3}$ and the C_{H} of 2.20% for the i-Si films deposited with assisting laser power of 80 W were smaller than the N_{H} of $5.98 \times 10^{21}\text{ cm}^{-3}$ and the C_{H} of 11.96% for the i-Si films deposited without laser assistance. The N_{H} and C_{H} of the deposited i-Si films decreased with the laser power. It could be attributed to the fact that the SiH₄ reacting gas could be efficiently decomposed into Si atoms by the combined action of plasma and CO₂ laser and less hydrogen atom was left in the obtained microcrystalline i-Si films.

To further clarify the microstructure and the chemical bonding characteristics of the i-Si films deposited with various assisting laser powers, the micro-Raman scattering spectra were measured and the results are shown in Figure 5. As shown in Figure 5, the Raman peak of the i-Si films shifted from 482 cm^{-1} to 512 cm^{-1} as the assisting laser power increased from 0 W to 80 W, indicating a gradual transformation from amorphous to crystalline Si. Therefore, these micro-Raman results verified that the CO₂ laser-assisted deposition led to an enhancement in the crystallinity of the i-Si films and the microcrystalline i-Si films were obtained when deposited with laser assistance of higher power.

The crystallinity of the i-Si films deposited with various assisting laser powers was also examined using X-ray diffraction (XRD) and the results are shown in Figure 6. In the XRD results, no diffraction peak could be found for

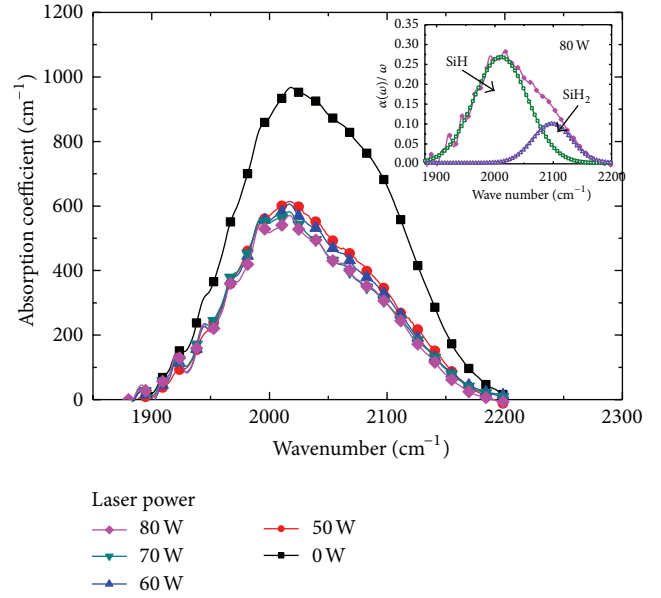


FIGURE 3: Absorption spectra $\alpha(\omega)$ of the i-Si films deposited with various assisting laser powers. The inset shows the absorption spectrum $\alpha(\omega)/\omega$ of the i-Si films with assisting laser power of 80 W.

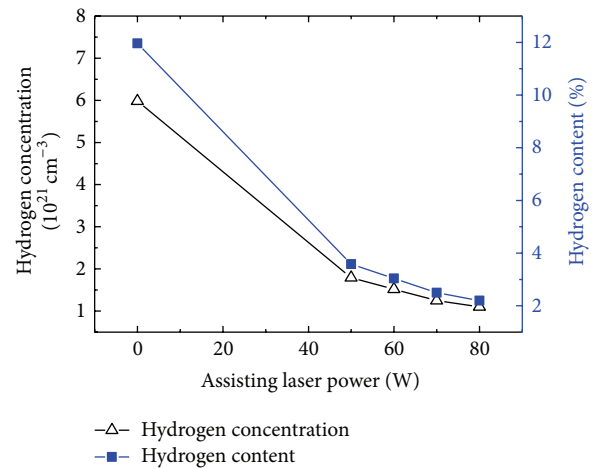


FIGURE 4: Hydrogen concentration N_{H} and hydrogen content C_{H} of the i-Si films deposited with various assisting laser powers.

the i-Si film deposited without laser assistance. On the contrary, for all of the i-Si films deposited with laser assistance, three main diffraction peaks at 2θ positions of 28.47° , 47.34° , and 56.17° were observed clearly, which correspond to the (111), (220), and (311) diffraction of the diamond-cubic Si, respectively. The above XRD results further confirmed that the microcrystalline i-Si films could be directly deposited using LAPECVD system at substrate temperature of 250°C .

Figure 7 shows the current density-voltage (J - V) characteristics of the p-SiC/i-Si/n-Si thin film solar cells deposited without and with 80 W laser assistance. The corresponding short-circuit current density (J_{sc}), open-circuit voltage (V_{oc}), fill factor (FF), and power conversion efficiency (η) were estimated and listed in the inset of Figure 7. The J_{sc} of

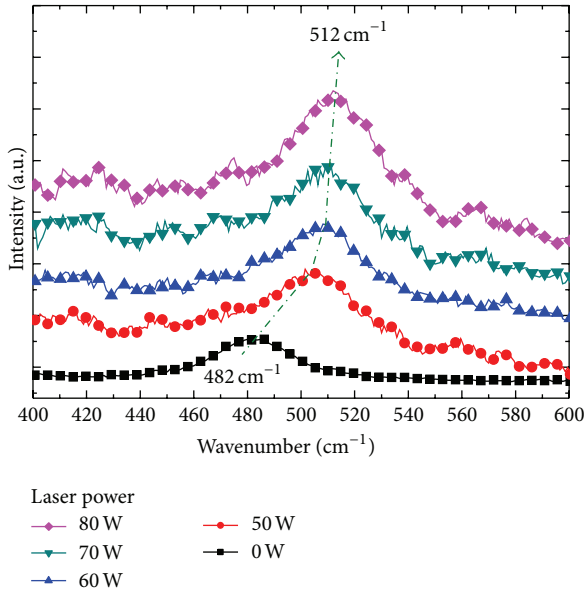


FIGURE 5: Micro-Raman scattering spectra of the i-Si films deposited with various assisting laser powers.

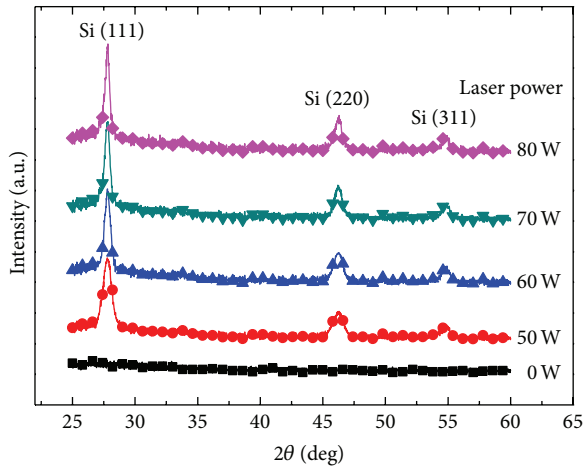


FIGURE 6: XRD spectra of the i-Si films deposited with various assisting laser powers.

the p-SiC/i-Si/n-Si thin film solar cells with 80 W laser assistance was 18.16 mA/cm^2 , much larger than the value of 14.38 mA/cm^2 for the cell without laser assistance. The increase in J_{sc} could be attributed to the enhancement of the crystallinity of the active layer i-Si film deposited with laser assistance. Besides, the electron and hole concentrations in the laser-assisted Si-based solar cells were higher than that in the non-laser-assisted Si-based solar cells. The high build-in electronic field could be increased with the high carrier concentration, which increased the separation velocity of the photo-generated electron-hole pairs in the active layer. Therefore, it could reduce the carrier recombination and increase the J_{sc} of the resulted solar cells with laser assistance. On the contrary, the V_{oc} of the p-SiC/i-Si/n-Si thin film solar cells decreased from 0.80 V to 0.75 V as the assisting laser

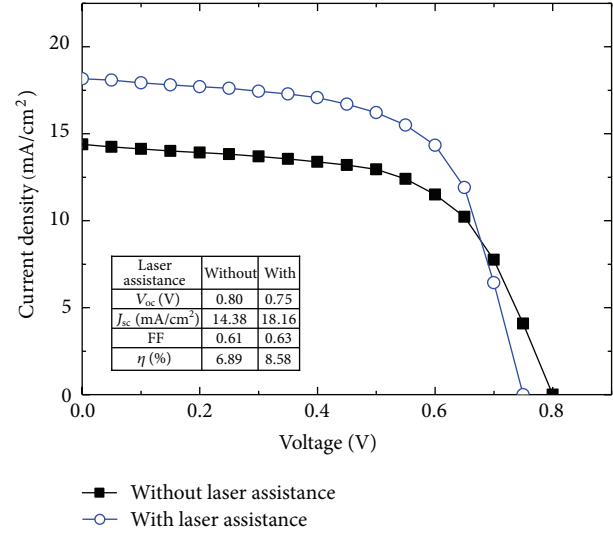


FIGURE 7: Current density-voltage characteristics of the p-SiC/i-Si/n-Si thin film solar cells deposited without and with assisting laser power of 80 W. The inset table shows the V_{oc} , J_{sc} , FF, and η of the p-SiC/i-Si/n-Si thin film solar cells deposited without and with assisting laser power of 80 W.

power used in the film deposition increased from 0 W to 80 W. The reduction of the V_{oc} for the laser-assisted Si-based solar cells was attributed to the crystallization variation of the i-Si absorption layer. The i-Si film deposited without laser assistance was amorphous, while the i-Si film deposited with laser assistance was microcrystalline. It is well known that the energy bandgap of the amorphous Si is larger than that of the microcrystalline Si, which interprets the obtained variation of V_{oc} . Furthermore, the FF of the p-SiC/i-Si/n-Si thin film solar cells decreased when the i-Si layer was deposited under higher assisting laser power. This phenomenon was attributed mainly to the reduction of the V_{oc} . As shown in Figure 7, the power conversion efficiency of the p-SiC/i-Si/n-Si thin film solar cells deposited with and without laser assistance was estimated to be 8.58% and 6.89%, respectively. The significant improvement of the power conversion efficiency for the laser-assisted Si-based solar cells was attributed to the fact that the laser-assisted i-Si absorption layer had lower hydrogen concentration and better crystallinity compared with the non-laser-assisted i-Si absorption layer.

4. Conclusion

In this work, the LAPECVD system was used to prepare the i-Si films as the active layers of solar cells. According to the FTIR measurement, the estimated hydrogen concentration of the deposited i-Si films decreased from $5.98 \times 10^{21} \text{ cm}^{-3}$ to $1.10 \times 10^{21} \text{ cm}^{-3}$ as the assisting laser power used during the film deposition increased from 0 W to 80 W. The micro-Raman and XRD measurements demonstrated that the i-Si films deposited without and with laser assistance were amorphous and microcrystalline, respectively. In particular, deposited with 80 W laser assistance, the high quality i-Si

films with low hydrogen content and microcrystalline structure were obtained.

The p-SiC/i-Si/n-Si thin film solar cells with the active layer i-Si deposited without and with 80 W laser assistance were fabricated and investigated. The short-current density of the laser-assisted Si-based solar cells was larger than that of the cells without laser assistance. The improvement in conversion efficiency of the laser-assisted Si-based thin film solar cells was more than 22.5% compared with the solar cells without laser assistance.

Conflict of Interests

The authors declare that there is no conflict of interests regarding the publication of this paper.

Acknowledgments

The authors gratefully acknowledge the support from the Ministry of Science and Technology of Republic of China under Contract no. MOST 101-2628-E-006-017-MY3, no. MOST 103-3113-E-005-001 and Advanced Optoelectronic Technology Center and Research Center Energy Technology and Strategy of the National Cheng Kung University.

References

- [1] D. Gerlach, R. G. Wilks, D. Wippler et al., "The silicon/zinc oxide interface in amorphous silicon-based thin-film solar cells: understanding an empirically optimized contact," *Applied Physics Letters*, vol. 103, no. 2, Article ID 023903, 2013.
- [2] C. H. Hsu, Y. P. Lin, H. J. Hsu, and C. C. Tsai, "Enhanced spectral response by silicon nitride index matching layer in amorphous silicon thin-film solar cells," *Journal of Non-Crystalline Solids*, vol. 358, no. 17, pp. 2324–2326, 2012.
- [3] D. L. Staebler and C. R. Wronski, "Reversible conductivity changes in discharge-produced amorphous Si," *Applied Physics Letters*, vol. 31, no. 4, pp. 292–294, 1977.
- [4] C. T. Lee and C. H. Lin, "Si nanocrystals embedded in Si suboxide matrix grown by laser-assisted chemical vapor deposition at room temperature," *Japanese Journal of Applied Physics, Part 1: Regular Papers and Short Notes and Review Papers*, vol. 43, no. 5 A, pp. 2793–2794, 2004.
- [5] C. T. Lee, C. H. Lin, T. H. Lee, and T. C. Tsai, "Photoluminescence degradation and passivation mechanisms of Si nanoclusters in silicon oxide matrix," *Japanese Journal of Applied Physics, Part 1: Regular Papers and Short Notes and Review Papers*, vol. 44, no. 6 A, pp. 4240–4244, 2005.
- [6] C. T. Lee, J. H. Cheng, and H. Y. Lee, "Crystalline SiGe films grown on Si substrates using laser-assisted plasma-enhanced chemical vapor deposition at low temperature," *Applied Physics Letters*, vol. 91, no. 9, Article ID 091920, 2007.
- [7] T. C. Tsai, L. Z. Yu, and C. T. Lee, "Electroluminescence emission of crystalline silicon nanoclusters grown at a low temperature," *Nanotechnology*, vol. 18, no. 27, Article ID 275707, 2007.
- [8] C. T. Lee, Y. F. Chen, and C. H. Lin, "Phase-separated Si nanoclusters from Si oxide matrix grown by laser-assisted chemical vapor deposition," *Nanotechnology*, vol. 20, no. 2, Article ID 025702, 2009.
- [9] B. R. Wu, D. S. Wu, M. S. Wan, W. H. Huang, H. Y. Mao, and R. H. Horng, "Fabrication of nc-Si/c-Si solar cells using hot-wire chemical vapor deposition and laser annealing," *Solar Energy Materials and Solar Cells*, vol. 93, no. 6–7, pp. 993–995, 2009.
- [10] A. V. Shah, J. Meier, E. Vallat-Sauvain et al., "Material and solar cell research in microcrystalline silicon," *Solar Energy Materials and Solar Cells*, vol. 78, no. 1–4, pp. 469–491, 2003.
- [11] A. Descoedres, L. Barraud, S. de Wolf et al., "Improved amorphous/crystalline silicon interface passivation by hydrogen plasma treatment," *Applied Physics Letters*, vol. 99, no. 12, Article ID 123506, 2011.
- [12] A. Ulyashin and A. Sytchkova, "Hydrogen related phenomena at the ITO/a-Si:H/Si heterojunction solar cell interfaces," *Physica Status Solidi A*, vol. 210, no. 4, pp. 711–716, 2013.
- [13] F. H. Wang, H. P. Chang, C. C. Tseng, C. C. Huang, and H. W. Liu, "Influence of hydrogen plasma treatment on Al-doped ZnO thin films for amorphous silicon thin film solar cells," *Current Applied Physics*, vol. 11, supplement 1, pp. S12–S16, 2011.
- [14] K. Imamura, M. Takahashi, A. Asuha, Y. Hirayama, S. Imai, and H. Kobayashi, "Nitric acid oxidation of Si method at 120°C: HNO₃ concentration dependence," *Journal of Applied Physics*, vol. 107, no. 5, Article ID 054503, 2010.
- [15] J. H. Choi, S. C. Roh, J. D. Jung, and H. I. Seo, "Chemical HF treatment for rear surface passivation of crystalline silicon solar cells," *Transactions on Electrical and Electronic Materials*, vol. 14, no. 4, pp. 203–207, 2013.
- [16] H. Angermann, J. Rappich, and C. Klimm, "Wet-chemical treatment and electronic interface properties of silicon solar cell substrates," *Central European Journal of Physics*, vol. 7, no. 2, pp. 363–370, 2009.
- [17] M. Bhisare, A. Misra, and A. Kottantharayil, "Aluminum oxide deposited by pulsed-DC reactive sputtering for crystalline silicon surface passivation," *IEEE Journal of Photovoltaics*, vol. 3, no. 3, pp. 930–935, 2013.
- [18] A. A. Langford, M. L. Fleet, B. P. Nelson, W. A. Lanford, and N. Maley, "Infrared absorption strength and hydrogen content of hydrogenated amorphous silicon," *Physical Review B*, vol. 45, no. 23, pp. 13367–13377, 1992.
- [19] M. H. Brodsky, M. Cardona, and J. J. Cuomo, "Infrared and Raman spectra of the silicon-hydrogen bonds in amorphous silicon prepared by glow discharge and sputtering," *Physical Review B*, vol. 16, no. 8, pp. 3556–3571, 1977.

Research Article

Thermal Field Analysis and Simulation of an Infrared Belt Furnace Used for Solar Cells

Bai Lu, Liang Zongcun, and Shen Hui

School of Physics and Engineering, Institute for Solar Energy Systems, State Key Laboratory of Optoelectronic Materials and Technologies, Sun Yat-sen University, Guangzhou 510275, China

Correspondence should be addressed to Liang Zongcun; 2713604996@qq.com and Shen Hui; 2323292429@qq.com

Received 29 January 2014; Accepted 7 April 2014; Published 12 May 2014

Academic Editor: Prakash Basnyat

Copyright © 2014 Bai Lu et al. This is an open access article distributed under the Creative Commons Attribution License, which permits unrestricted use, distribution, and reproduction in any medium, provided the original work is properly cited.

During solar cell firing, volatile organic compounds (VOC) and a small number of metal particles were removed using the gas flow. When the gas flow was disturbed by the thermal field of infrared belt furnace and structure, the metal particles in the discharging gas flow randomly adhered to the surface of solar cell, possibly causing contamination. Meanwhile, the gas flow also affected the thermal uniformity of the solar cell. In this paper, the heating mechanism of the solar cell caused by radiation, convection, and conduction during firing was analyzed. Afterward, four 2-dimensional (2D) models of the furnace were proposed. The transient thermal fields with different gas inlets, outlets, and internal structures were simulated. The thermal fields and the temperature of the solar cell could remain stable and uniform when the gas outlets were installed at the ends and in the middle of the furnace, with the gas inlets being distributed evenly. To verify the results, we produced four types of furnaces according to the four simulated results. The experimental results indicated that the thermal distribution of the furnace and the characteristics of the solar cells were consistent with the simulation. These experiments improved the efficiency of the solar cells while optimizing the solar cell manufacturing equipment.

1. Introduction

Firing is an important step during the fabrication of crystalline silicon solar cell that affects the series-parallel resistance and the fill factor of the solar cells, determining the efficiency of the solar cells [1]. To form the front and back side contacts, metallization paste was printed on the silicon wafers using thick film technology and screen printing. A paste containing aluminum was used for the back side contact; silver was used for the front side contact fingers. Afterward, the pastes were fired in an infrared belt furnace. In the firing zone, the VOC and a few metal particles were removed by the gas flow. When the gas flow was disturbed by the thermal field of the furnace and structure, the metal particles in the discharging gas flow might randomly adhere to the surface of solar cell, causing contamination. Meanwhile, the gas flow also affected the temperature uniformity of the solar cell, causing stress concentration or breakage. Hoornstra et al. showed that the thermal field of the furnace was difficult to measure explicitly [2], making it a key issue.

When comparing the infrared belt furnaces with rapid thermal processing (RTP), they are similar during rapid heating. Cooper et al. [3] simulated RTP to study the physics of solar cell contact formation during mass production using a high-throughput infrared belt furnace. A lower Ag finger contact resistance was observed as the sinter dwell time decreased. Campbell et al. [4] calculated the steady-state temperature distribution and gas flow patterns in a RTP system under various process conditions. The gas flow patterns and temperature distributions were strongly dependent on the pressure and ambient composition. Kakoschke et al. [5] showed a theory of wafer heating during RTP and demonstrated that temperature uniformity was not only limited by radiation loss at the wafer edge in the stationary state, but was also influenced by transient effects during temperature ramping. Gyurcsik et al. [6] used the first-principles approach to model the RTP system for temperature uniformity. No uniform temperatures in the wafers in a RTP system could be counteracted by adjusting the relative power of the individual lamps used to alter the heat flux density at the wafer. However,

the firing furnace is longer, the solar cell is in motion, and the gas flow is heavy, and currently, no comprehensive studies are available.

In this paper, the heating mechanism for solar cells via radiation convection and conduction during firing was analyzed. Furthermore, four 2D models of the furnace were proposed and the transient thermal fields with different gas inlets, outlets, and internal structures were simulated. To verify the result, four types of furnaces were produced according to four simulated structures. The temperature distribution of the furnace firing and the characteristics of solar cell fired will be discussed in this study.

2. Heat Transfer Analysis

The heat transfer mechanism is shown in Figure 1; the near-infrared radiation is emitted from the upper lamps and lower lamps. Most of the radiation is absorbed by the solar cells and the furnace wall, while a small part is reflected and removed by the gas flow. Therefore, heat conduction occurs in the solar cell and the walls of the furnace. Meanwhile, convection occurs among the solar cells, the walls of the furnace and the gas flow. Therefore, the thermal field includes conduction, convection, and radiation.

2.1. Radiant Energy of Solar Cell from the Lamps. Figure 2 shows that a lamp is irradiating a solar cell, where AB denotes a linear light source of the near infrared. I_0 is the radiation intensity along the normal direction of the lamp. L is the radiance [$W/(m^2 \cdot sr)$]. l is the length of the lamp [m]. R is the radius of the lamp [m]. X is a point on the solar cell. h is the vertical distance from point X to the lamp [m], α_1 is the angle between AX and XC [$^\circ$], and α_2 is the angle between BX and XC [$^\circ$].

The maximum radiation intensity of per unit length is

$$I_l = \frac{I_0}{l} = 2LR. \quad (1)$$

The radiation intensity of dx in the DX direction is

$$dI_\alpha = I_l dx \cos \alpha. \quad (2)$$

The irradiance of dx at point X is

$$dE_\alpha = \frac{dI_\alpha}{r^2} \cos \alpha. \quad (3)$$

Figure 2 shows the following:

$$r = \frac{h}{\cos \alpha}, \quad x = h \tan \alpha, \quad dx = \frac{h d\alpha}{(\cos \alpha)^2}. \quad (4)$$

Therefore, the irradiance of dx at point X is as follows:

$$dE_\alpha = I_l \frac{1}{h} (\cos \alpha)^2 d\alpha. \quad (5)$$

The irradiance of AB at point X is as follows:

$$\begin{aligned} E_X &= \int dE_\alpha = I_l \frac{1}{h} \int_{\alpha_2}^{\alpha_1} (\cos \alpha)^2 d\alpha \\ &= I_l \frac{1}{h} \frac{1}{4} [2|\alpha_1 - \alpha_2| + |\sin 2\alpha_1 - \sin 2\alpha_2|]. \end{aligned} \quad (6)$$

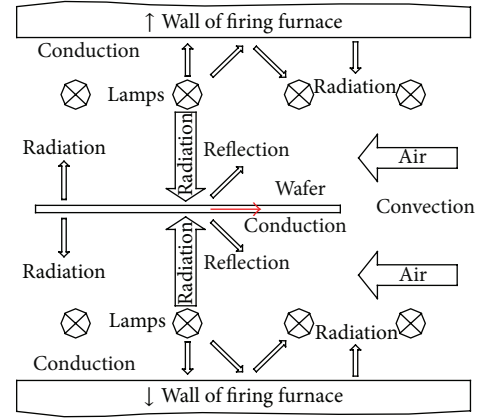


FIGURE 1: Heat transfer mechanism.

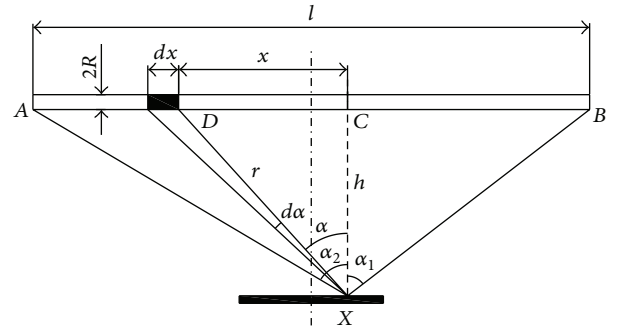


FIGURE 2: Irradiance of solar cell from lamp.

The radiant energy of a solar cell from AB is as follows:

$$Q_l = \iint E_x dA dt. \quad (7)$$

2.2. Radiant Energy of Solar Cell from the Walls. The radiant energy of solar cell from the wall is shown in Figure 3, where ΔA_s is a radiant source on the wall [m^2]. L is the radiance [$W/(m^2 \cdot sr)$]. ΔA is a small area irradiated on the solar cell [m^2]. j is the distance between ΔA_s and ΔA . θ_s and θ are the angles associated with n and j [$^\circ$], respectively.

The radiation intensity of ΔA_s in the j direction is as follows:

$$I = L \cos \theta_s \Delta A_s. \quad (8)$$

The irradiance of ΔA is

$$E_w = \frac{I \cos \theta}{j^2} = L \Delta A_s \frac{\cos \theta \cos \theta_s}{j^2}. \quad (9)$$

The radiant energy of the solar cell from the wall is as follows:

$$Q_w = \iint E_w dA dt. \quad (10)$$

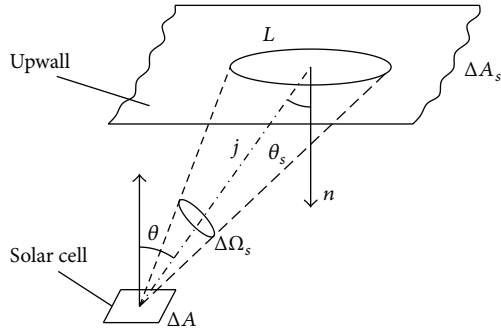


FIGURE 3: Irradiance of a solar cell from the wall.

2.3. *Conduction Heat in the Solar Cell.* The heat transferred via conduction in the solar cell could be expressed by Fourier's law

$$Q_{\lambda} = -\lambda A \frac{\partial T}{\partial n}, \quad (11)$$

where Q_{λ} is the conduction heat per unit time [w], λ is the thermal conductivity coefficient [W/(m·°C)], A is a surface area [m²], and $\partial T/\partial n$ is the temperature gradient of solar cells [°C/m].

2.4. *Convection Heat on the Solar Cell.* Convection was a mixture of conduction and the motion of a fluid. As the gas flowed against the surface of the solar cell, heat was transferred via convection:

$$Q_{\beta} = \beta A (T_w - T_f), \quad (12)$$

where Q_{β} is the convection heat per unit time [w], β is the heat transfer coefficient [W/(m²·°C)], A is a surface area [m²], T_w is the surface temperature of solar cell [°C], and T_f is temperature of the gas [°C].

2.5. *Total Energy.* Based on the solution of (7), (10), and (12), the total energy of a solar cell from a lamp, ΔA_s and the convection is given by

$$Q = Q_l + Q_w + Q_{\beta}. \quad (13)$$

Eighty-four infrared lamps were present in the furnace, the internal surface of the furnace was large, and several ten solar cells were heated at the same time. Therefore, it was quite difficult to calculate the energy of all of the points on each solar cell according to the above formulas, and numerous computations were required. Thus, the numerical method was used to solve this problem in the paper.

3. Numerical Simulations

FLUENT is software for computational fluid dynamics (CFD). It employs a control-volume-based technique to convert the governing equations into algebraic equations that are solved sequentially using the implicit method [7]. In the paper, a first-order upwind scheme was used for the spatial

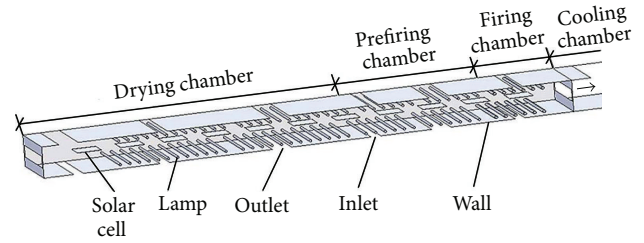


FIGURE 4: Sketch of firing furnace.

dissociation of the convective terms; the SIMPLE algorithm was used to couple the pressure and velocity and solve the pressure-correction implicitly.

3.1. *Physical Assumptions.* When using FLUENT, some physical assumptions and geometric simplifications were employed. The radiant intensity of the lamps was assumed independent of direction, remaining constant across the length of the lamp and uniform at the cell lower surface. The cell was assumed to be infinitely thin. The temperature on the top surface of the cell was identical to the temperature on the lower surface. The chamber was axially symmetrical. The gas was incompressible and could be regarded as an ideal gas. All surfaces were defined as diffuse reflectors and emitters.

3.2. *Geometrical Model.* Figure 4 shows a sketch of the furnace. The furnace is of 6 m long and 0.16 m high, including a drying chamber, a prefiring chamber, a firing chamber, and a cooling chamber. Each chamber contains several walls, infrared lamps, thermocouples, mesh belts, inlets, and outlets. The infrared lamps are arranged on the top and the bottom inside the chambers symmetrically. Because many supports are added to make no contact between the solar cell and the mesh belts, the mesh belts are ignored in the modeling. The inlets and outlets in the chambers wall are used to remove the VOC that came from the paste.

If the 3D solid model of the furnace was used for simulation, the storage and calculation of data during the reconstruction process would be so enormous as to preclude calculation using common computers. Wachter [8] reported that a model of the radioactive heat transfer could occur in an axially symmetric RTP chamber, and a flow included in the RTP process could further improve the temperature uniformity. Therefore, simple and effective 2D models were used.

Based on the work above, four furnaces were proposed for studying the effect of inlets and outlets at different positions on the thermal field and the temperment of the solar cell surface. The four models are shown in Figure 5.

Figure 5(a) shows that all the gas inlets were in the upper portion, while outlets were in the lower portion. The gas flow distance was short, facilitating laminar flow formation and rapid VOC removal.

Figure 5(b) shows that each chamber had one pair of inlets and outlets. The VOC in each chamber were blown out independently.

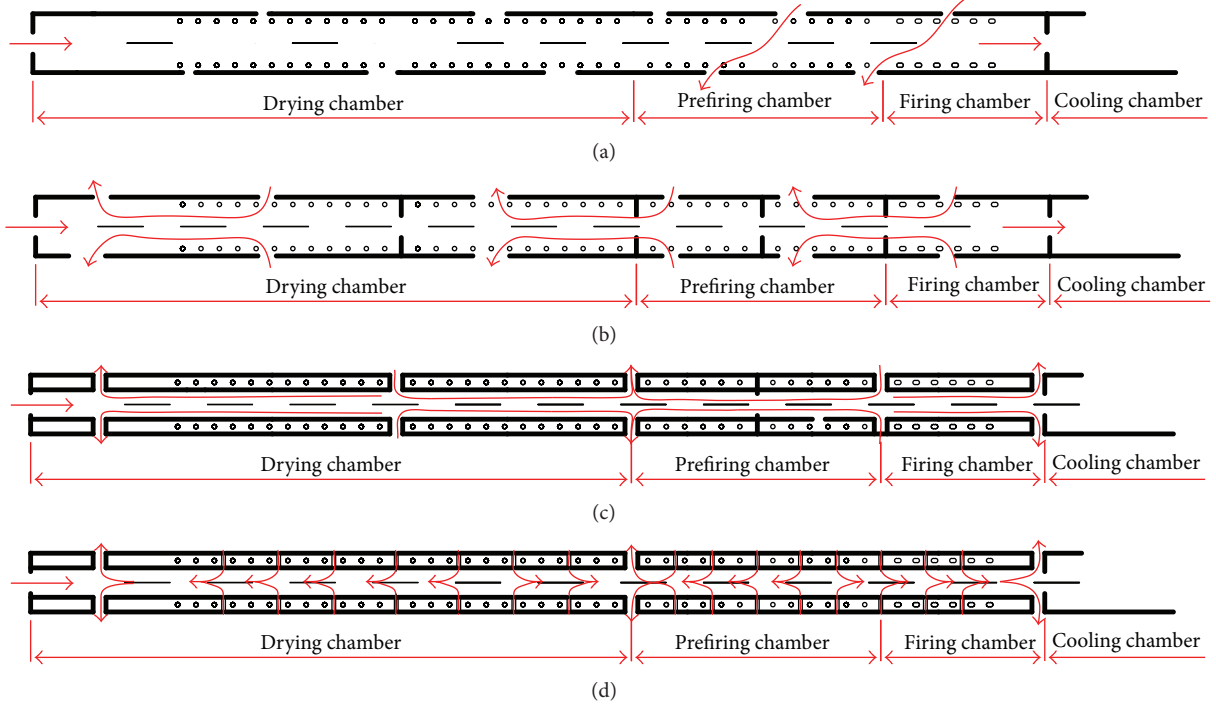


FIGURE 5: The longitudinal section model of the firing furnace.

Wacher [8] found that the smallest chamber height could attain the best temperature uniformity. Therefore, we proposed that the lamps were enclosed by quartz glass, and two pairs of gas inlets and three pairs of gas outlets were installed in the middle and at the ends of the furnace, as shown in Figure 5(c). Furthermore, the chambers of the furnace were smooth and narrow, facilitating laminar flow formation and rapid VOC removal.

Figure 5(d) shows that the lamps were enclosed by quartz glass, the fifteen pairs of inlets were evenly distributed in the furnace, and the three pairs of outlets were installed in the middle and at the ends of the furnace. Here, the chambers of furnace were smooth and narrow, containing more inlets and fewer outlets. Forming laminar flows and quickly removing VOC were enabled.

The longitudinal sections of the furnace were drawn up using traditional engineering computer aided design (CAD) software, as shown in Figure 6. Then, these sections were meshed in the preprocessing software, the integrated computer engineering and manufacturing code for computational fluid dynamics (ICEMCFD) with unstructured grids and triangular elements [9]. Finally, the messed models were exported into FLUENT. FLUENT can use grids comprised of triangular or quadrilateral cells (or a combination of the two) in 2D, and tetrahedral, hexahedral, polyhedral, pyramid, or wedge cells (or a combination of these) in 3D. So we choose the triangular cell of the mesh type to use in the simulation.

3.3. Parameter Setting. The options of pressure-based, transient, laminar, discrete ordinate (DO), dynamic mesh were selected; and the characteristic parameters of the silicon,

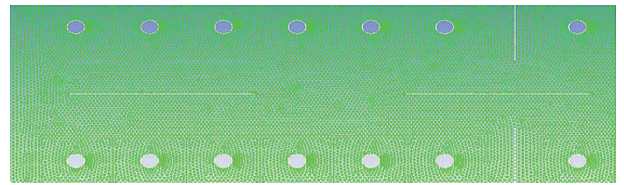


FIGURE 6: The longitudinal section model meshed in ICEMCFD.

quartz glass, and refractory were set in FLUENT. According to the firing process of the PV17, a paste produced by DuPont, the radiant powers of the lamps was set separately. The transport velocity of the solar cell was set to 0.1 m/sec, and the outlet pressure was set to negative 8 Pa. To speed up the calculation process, the initial temperature in the furnace was set to 150°C. The thermal conductivity of the solar cells is 148 W/m·K. The absorption coefficient of the solar cells is 10^5 m^{-1} . The specific heat of the solar cells is 700 J/kg·K. The density of the solar cells is 2329 kg/m³.

The silicon wafers were stationary in RTP but in motion in the furnace. The movement affected the thermal field of the furnace; therefore, a dynamic mesh was used to study it, and the moving mesh boundary function was defined as follows:

$$((\text{move point } 2) (\text{time } 0 \text{ } 200) (v_x \text{ } 0.1 \text{ } 0.1)) \quad (14)$$

(see [10]), where move is the name of the function, point is the type of the function, 2 is number of points, v_x is the symbol of velocity in the x direction, and 0.1 is the velocity of the solar cells at 0 second and 200 seconds, whose unit is m/s.

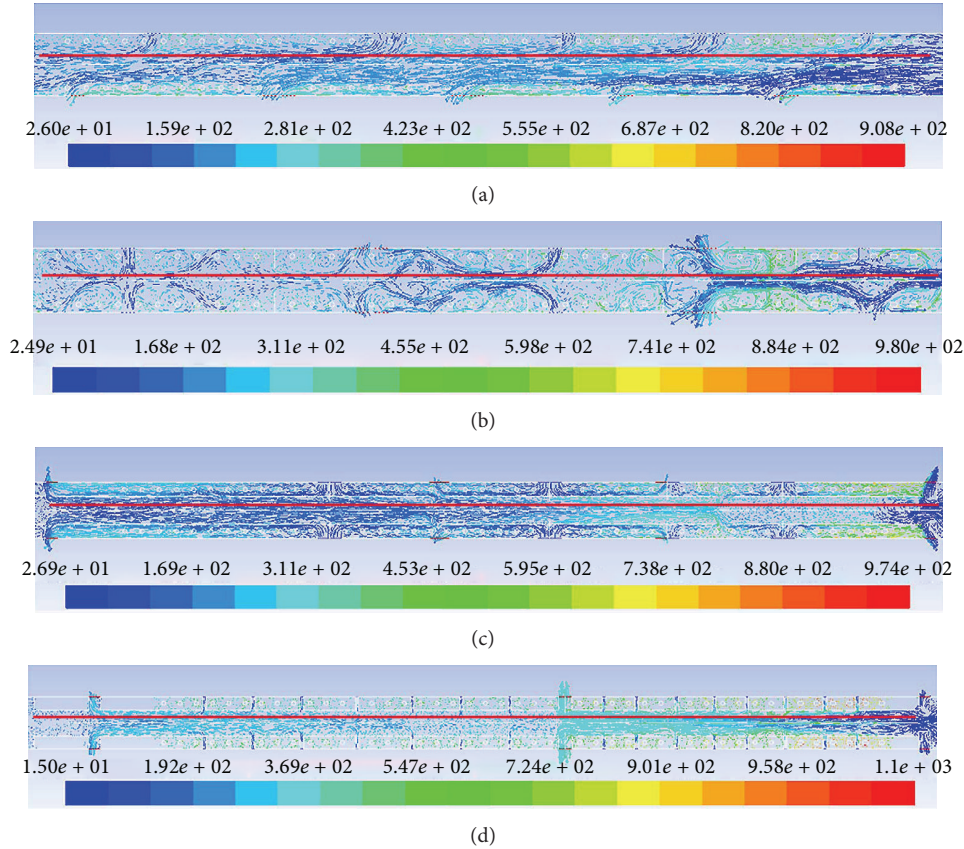


FIGURE 7: Velocity vectors and thermal distribution of the furnace for different settings of gas inlets and outlets.

3.4. Results and Analysis

3.4.1. Thermal Field Distribution. When the number of iterations increased, the transient thermal field gradually stabilized during the simulation, allowing the thermal distribution of the furnace to be obtained.

Figure 7(a) shows the thermal field distribution of Figure 5(a). The gas ran into the furnace from the upper inlets and drained out of the corresponding lower outlets in the direction opposite to the moving solar cells. However, the gas passed through the upper surface of one solar cell and the lower surface of another. Some metal ions evaporated from the upper surface of one solar cell to attach to the lower surface of another, causing contamination.

Figure 7(b) shows the thermal field distribution of Figure 5(b). The gas ran into the furnace from the upper and lower inlets in each chamber and drained out of the corresponding outlets in the opposite direction to the moving cells. Because it is divided into two layers, the gas flow was nonuniform; some of it surrounded the lamps, hindering VOC discharge.

Figure 7(c) shows the thermal field distribution of Figure 5(c). Due to the installment of quartz glass, the furnace chamber became narrow and smooth. The gas ran into the furnace from the upper and lower inlets and drained out of the corresponding outlets in the direction opposite to the moving cells. Because it is divided into two layers,

the gas flow was uniform. However, there was a cutoff in the furnace chamber due to the decrease in the number of inlets, hindering VOC discharge.

Figure 7(d) shows the thermal field distribution of Figure 5(d). Due to the installation of the quartz glass, the furnace chamber became narrow and smooth. The gas ran into the furnace from the upper and lower inlets to drain out of the corresponding outlets in the direction opposite to the moving cells. The gas flow was divided into two uniform and continuous layers, meaning that the VOC discharged cleanly.

After comparing velocity vectors and thermal distribution of the furnace for different settings of gas inlets and outlets, the thermal field of Figure 7(d) is the most reasonable, making the structure of Figure 5(d) optimal.

3.4.2. Surface Temperatures of All Solar Cells. When the thermal field was stable, the solar cells were placed at the points of x -axis in the four models, respectively, and then the temperature of three points on each solar cell surface was obtained from the four simulation results simultaneously as shown in Figure 10. The average temperature of the solar cells' surface is the same as the firing curves of the PV17, a paste. Afterward, the temperature variance of each solar cell was calculated as shown in Figure 8. Curve-d was the lowest, meaning that its surface temperature was the most stable. Consequently, the structure of Figure 5(d) is optimal.

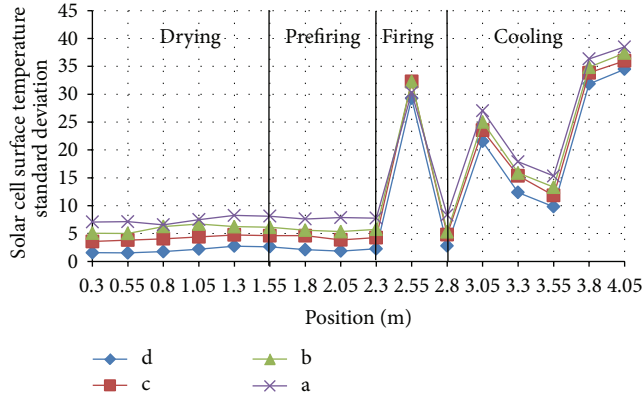


FIGURE 8: Temperature curves for the faces of the solar cells.

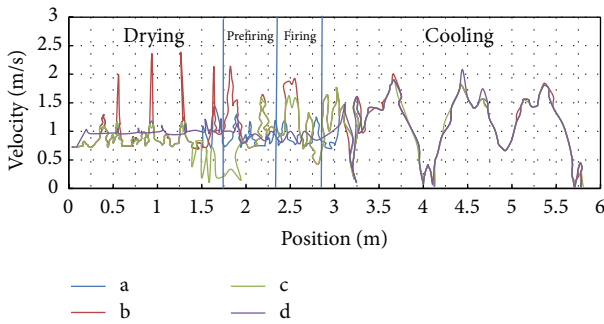


FIGURE 9: Airflow velocity vectors for the solar cell surface.

3.4.3. Gas Flow Velocities of Solar Cell Surface. When the thermal field was stable, the gas flow velocities 20 mm away from the upper surface of each solar cell in the furnace marked with red line in Figure 7 were extracted from the four simulation results simultaneously. Figure 9 shows that the fluctuation of curve-d was the least, meaning that the surface temperature was the most stable. Consequently, the structure of Figure 5(d) is optimal.

4. Model Verification

To verify the simulated result, solar cells that were fabricated on $125 \times 125 \text{ mm}^2$, $2\text{-}\Omega\text{-cm}$ resistivity, $200 \mu\text{m}$ thick, p-type, and Cz-Si wafers were textured using random pyramid formation. And the emitters were formed via POCl_3 diffusion. Furthermore, the wafers were coated with SiN_x via plasma enhanced chemical vapor deposition (PECVD). A front collection grid was created using screen-printed glass-fritted Ag paste. The Al paste was printed on the back with Ag/Al tabbing stripes [3].

4.1. Temperature Measurement of the Solar Cell. When the thermal field was stable, the solar cells were placed at the points of x -axis in the four models, respectively, and then a Q18 produced by Datapaq was used to measure the actual temperature of three points on each solar cell surface

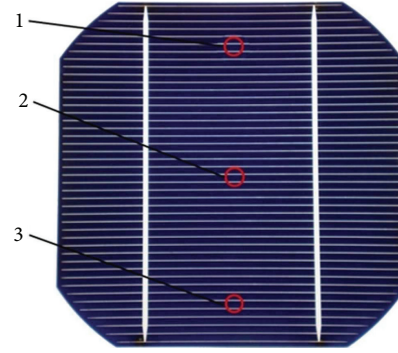


FIGURE 10: Solar cell.

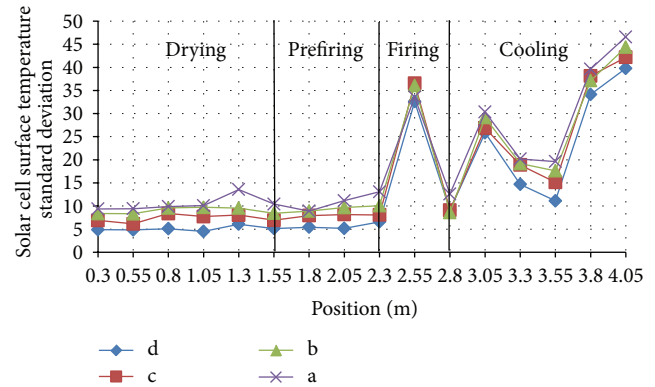


FIGURE 11: Temperature curves on the face of solar cells.

as shown in Figure 10 [2]. Figure 11 shows the surface temperature variations of each solar cell. Curve-d was the lowest, meaning that the temperature is the most uniform. Therefore, the structure of Figure 5(d) is the most reasonable. When comparing the curves in Figure 8, the actual temperature curves were almost the same as those obtained from the simulations.

4.2. Characteristic Measurement of Solar Cell. Four hundred pieces of solar material were made using this process. Afterward, they were divided into four groups and fired in the four experimental furnaces, respectively. Measured by IV-Measurement produced by Halm, Table 1 shows the average characteristic parameters for each group. The Eff (efficiency) and R_{sh} (shunt resistance) are minimized in Table 1-a. Furthermore, according to Figure 7(a), there may be metal contamination in Figure 5(a). The Eff and R_{sh} are maximized in Table 1-d. According to Figure 7(d), we think that the structure of Figure 5(d) is the most reasonable.

5. Conclusions

To investigate the influence of the gas flow on the thermal field of the furnace, the heat-transfer mechanism of the furnace was analyzed; four 2D physical models of the furnace and their corresponding numerical models were proposed.

TABLE 1: Solar cell characteristics.

	F.F. (%)	Eff. (%)	I_{sc} (A)	VOC (V)	R_s (Ω)	R_{sh} (Ω)
a	78.61	17.11	5.321	0.635	0.014312	800.213
b	79.23	17.23	5.361	0.642	0.011806	850.256
c	79.36	17.43	5.375	0.663	0.011612	1010.351
d	81.43	17.74	5.383	0.661	0.011003	1039.231

The following conclusions were obtained using these numerical simulations and experimental studies.

- (1) The thermal field of the furnace was obtained using a simulation that included conduction, convection, and radiation.
- (2) The temperature of a solar cell could be stable and uniform when the gas outlets were installed at the ends and in the middle of the furnace. Furthermore, the gas inlets were distributed evenly on the furnace.
- (3) This work is useful for improving the efficiency of solar cells by optimizing the structure of solar cell manufacturing equipment.

2D models were used to simulate the thermal field of the furnaces, and effect of the mesh net on air flow was simplified, possibly generating differences relative to the practical thermal field in the study.

Conflict of Interests

The authors declare that there is no conflict of interests regarding the publication of this paper.

Acknowledgments

This work was supported by the National Natural Science Foundation (Contract no. 61176055) and a Grant from the Science and Technology Project (2011A080804009) of Guangdong Province, China.

References

- [1] L. A. Dobrzański, M. Muszyfaga, A. Drygała, and P. Panek, "Investigation of the screen printed contacts of silicon solar cells using transmission line model," *Journal of Achievements in Materials and Manufacturing Engineering*, vol. 41, no. 1-2, pp. 57–65, 2010.
- [2] J. Hoornstra, A. van der Heid, J. Bultman, and A. Weeber, "Simple, detailed & fast firing furnace temperature profiling for improved efficiency," in *Proceedings of the Conference PV in Europe—From PV Technology to Energy Solutions*, p. 276, 2002.
- [3] I. B. Cooper, A. Ebong, J. S. Renshaw, R. Reedy, M. Al-Jassim, and A. Rohatgi, "Understanding and use of IR belt furnace for rapid thermal firing of screen-printed contacts to Si solar cells," *IEEE Electron Device Letters*, vol. 31, no. 5, pp. 461–463, 2010.
- [4] S. A. Campbell, K.-H. Ahn, K. L. Knutson, B. Y. H. Liu, and J. D. Leighton, "Steady-state thermal uniformity and gas flow patterns in a rapid thermal processing chamber," *IEEE Transactions on Semiconductor Manufacturing*, vol. 4, no. 1, pp. 14–20, 1991.
- [5] R. Kakoschke, E. Bußmann, and H. Föll, "Modelling of wafer heating during rapid thermal processing," *Applied Physics A*, vol. 50, no. 2, pp. 141–150, 1990.
- [6] R. S. Gyurcsik, T. J. Riley, and F. Y. Sorrell, "A model for rapid thermal processing: achieving uniformity through lamp control," *IEEE Transactions on Semiconductor Manufacturing*, vol. 4, no. 1, pp. 9–13, 1991.
- [7] ANSYS, Inc., *Fluent 12 Theory Guide*, 2009.
- [8] A. Wachter and B. R. Seymour, "A radiation model of a rapid thermal processing system," *Mathematics in Industry Case Studies Journal*, vol. 3, pp. 1–18, 2011.
- [9] ANSYS, Inc., *ICEM 12 Users Guide*, 2009.
- [10] ANSYS, Inc., *Fluent 6.3 User's Guide*, 2006.

Research Article

Characterization of a-Si:H/c-Si Heterojunctions by Time Resolved Microwave Conductivity Technique

Amornrat Limmanee,¹ Joaquim Nassar,² Igor P. Sobkowicz,^{2,3} Jaran Sritharathikhun,¹ Kobsak Sriprapha,¹ Guillaume Courtois,^{2,3} Francois Moreau,² and Pere Roca I Cabarrocas²

¹ Solar Energy Technology Laboratory, National Electronics and Computer Technology Center, 112 Thailand Science Park, Phahonyothin Road, Klong 1, Klong Luang, Pathumthani 12120, Thailand

² LPICM, CNRS-Ecole Polytechnique, Route de Saclay, 91128 Palaiseau, France

³ Total New Energies, 24 Cours Michelet, La Défense 10, 92069 Paris La Défense, France

Correspondence should be addressed to Amornrat Limmanee; amornrat.limmanee@nectec.or.th

Received 17 December 2013; Revised 8 January 2014; Accepted 27 January 2014; Published 3 March 2014

Academic Editor: Peter Rupnowski

Copyright © 2014 Amornrat Limmanee et al. This is an open access article distributed under the Creative Commons Attribution License, which permits unrestricted use, distribution, and reproduction in any medium, provided the original work is properly cited.

In heterojunction solar cells, a-Si:H/c-Si heterointerface is of significant importance, since the heterointerface characteristics directly affect junction properties and thus solar cell efficiency. In this study, we have performed time resolved microwave conductivity (TRMC) measurements on n-type c-Si wafers passivated on both sides with intrinsic and doped a-Si:H layers in order to investigate electrical property and passivation quality of the a-Si:H/c-Si heterojunctions. It was found that the TRMC decay time and decay curve shape varied with the laser wavelength and power intensity and also depended on sample structures. By using 1064 nm laser pulse with high excitation, differences in the decay curve shape between samples with and without p-n junction were observed. The samples containing p-n junction(s) had unique slow decay mode, after the initial fast decay, which we ascribed to the release of carriers from the low-mobility amorphous layer into the high-mobility crystalline wafer as the built-in field of the junction was restored. Experimental results suggest that the TRMC is useful nondestructive technique which is suitable for primary check of the a-Si:H/c-Si heterojunctions during the solar cell fabrication process.

1. Introduction

Heterojunction silicon solar cells, where hydrogenated amorphous silicon (a-Si:H) is deposited onto crystalline silicon (c-Si) wafers to provide both surface passivation and junction formation, receive great attention nowadays owing to known advantages over conventional Si wafer based solar cells, such as low temperature fabrication process, high efficiency, and superior performance at high operating temperature [1–3]. Monitoring of properties of such heterojunctions in the early stages of solar cell production is an essential concern. Microwave photoconductivity decay (μ -PCD) measurement techniques are routinely used to assess the surface passivation in a nondestructive, contactless way [4, 5]. These techniques make use of the fact that photogenerated free carriers induce a change in the microwave reflectivity of a semiconductor material, the magnitude of which is governed by

the mobility and excess density of the free carriers; the latter one is obtained from the photocarrier generation rate and the minority carrier effective lifetime (τ_{eff}). In high-quality crystalline silicon wafers, the τ_{eff} is dominated by surface rather than bulk recombination processes, making surface passivation a key issue.

Time resolved microwave conductivity (TRMC) experiment is a μ -PCD setup, where illumination is achieved through a very short laser pulse that offers the possibility to investigate fast recombination mechanisms, such as those occurring in microcrystalline Si and organic materials [6, 7]. There have been several reports of investigations of hydrogenated amorphous silicon nitride (a-SiN:H)/c-Si and a-Si:H/c-Si heterojunctions by the TRMC technique [8–11]. However, they are mainly mentioned in case of an intrinsic a-Si(N):H/c-Si heterojunctions and single side passivated samples. TRMC measurements on both sides of passivated

samples and characterizations of doped a-Si:H/c-Si heterojunctions have been rarely reported [12]. In this study, we thus have performed TRMC measurements on two-side a-Si:H passivated n-type c-Si substrates, focusing on changes in decay time and decay curve shape of different test structures. Kinetics which caused those variations were also analyzed.

2. Experimental Details

In these experiments, an excess of charge carriers was produced by illumination with 3 ns full width at half maximum (FWHM) pulses of a Nd:YAG laser at 532 and 1064 nm. Optical filters were used to adjust incident light intensity over four orders of magnitude. The microwave probe signal was generated by a Gunn diode and directed via a circulator to the sample. The reflected microwave signal was detected from the sample via a circulator to a detector connected to a transient digitizer. n-doped, (100-) oriented, FZ grown silicon wafers of 280 μm -thickness and resistivity of 1–10 $\Omega\text{ cm}$ were used as substrates. Two-side passivated samples with three different structures are made:

- n a-Si:H/i a-Si:H/n c-Si/i a-Si:H/n a-Si:H* (n-type a-Si:H on both sides),
- p a-Si:H/i a-Si:H/n c-Si/i a-Si:H/p a-Si:H* (p-type a-Si:H on both sides),
- p a-Si:H/i a-Si:H/n c-Si/i a-Si:H/n a-Si:H* (cell structure).

The intrinsic and doped a-Si:H films are prepared by radiofrequency plasma enhanced chemical vapor deposition (13.56 MHz rf-PECVD) technique. The gas sources are silane (SiH_4) and hydrogen (H_2). Phosphine (PH_3) and diborane (B_2H_6) were used as dopant sources for n-type and p-type, respectively. The thickness of the i, n, and p layers was about 8, 28, and 30 nm, respectively. The test samples in this study were also measured with a SINTON lifetime tester (photoconductive decay technique) in the transient mode (short flash) for the comparison of decay time. It should be noted that attention was placed on trends among samples not the absolute value obtained from the measurements since the results varied with the measurement conditions of each technique.

3. Results

3.1. Power and Wavelength Dependent Behavior of TRMC Decay Curve. With increasing laser intensity the microwave reflectivity decay time of all test samples increased. And a significantly longer decay time was observed when the samples were stimulated by long laser wavelength, 1064 nm, as shown in Figure 1. At high excitation an initial fast decay in the first 80–100 μs was observed. By measuring under exactly the same excitation conditions, it was found that TRMC decay time D.T. (sample a) > D.T. (sample c) > D.T. (sample b) (Figure 2). The sample with the n a-Si:H/i a-Si:H passivated on both sides (sample a) indicated the longest decay time while the sample with the p a-Si:H/i a-Si:H on both sides (sample b) showed the shortest decay time.

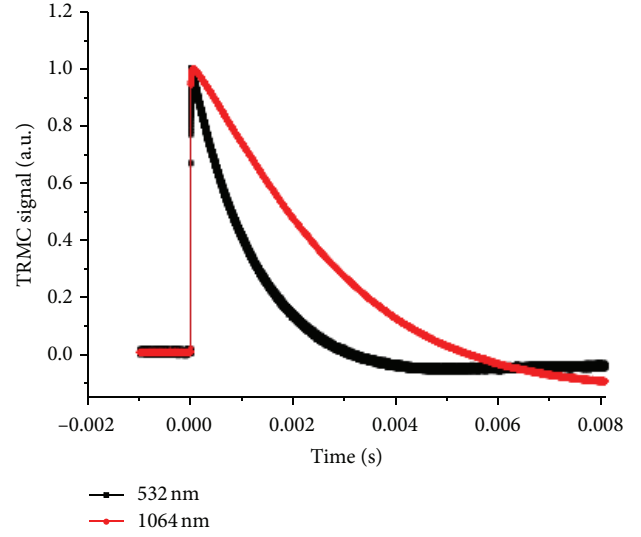


FIGURE 1: TRMC decay curves of sample with n a-Si:H on both sides induced by 532 and 1064 nm.

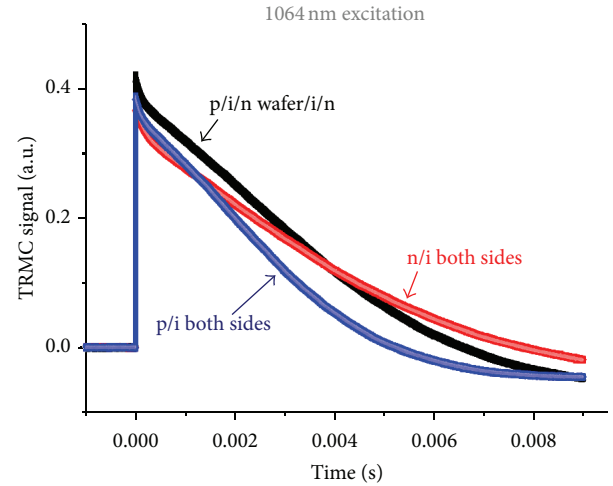


FIGURE 2: TRMC decay curves of samples with different structures; (a) both sides n a-Si:H, (b) both sides p a-Si:H, and (c) cell structure, under the same illuminated conditions.

The τ_{eff} of the samples with different structures estimated by using the SINTON lifetime tester is summarized in Table 1. It can be seen that the τ_{eff} and the decay time from the TRMC measurements of these three structures exhibit the same trend; that is to say, $\tau_{\text{eff}}(\text{a}) > \tau_{\text{eff}}(\text{c}) > \tau_{\text{eff}}(\text{b})$. The effective lifetime of various samples from the TRMC measurements was summarized as a function of photon of laser pulse in Figure 3. Here, the decay curves were deemed to be exponential decay and an exponential fit yielded a $1/e$ lifetime as the τ_{eff} . As the number of photon increased (higher light intensity), the decay time of all samples increased and tended to become saturated at the decay time of about 4 ms, which was likely to be a bulk lifetime of the n-type crystalline wafer used in this study.

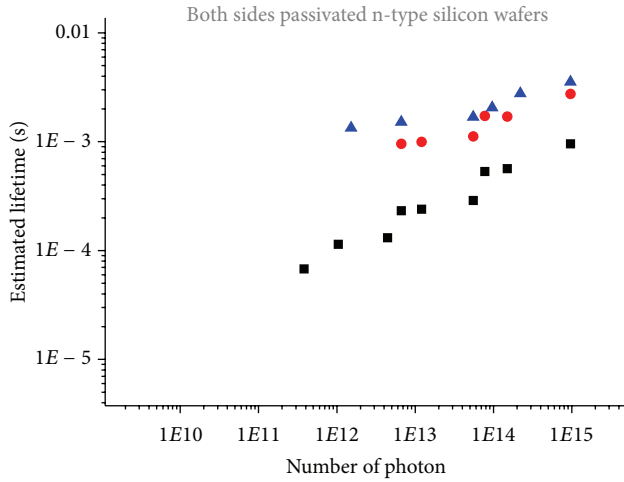


FIGURE 3: Estimated effective lifetime of various samples as a function of number of photon.

3.2. Structure Dependent Behavior of TRMC Decay Curve. By using 1064 nm excitation, differences in the decay curve shape between samples with and without p-n junction were found. The decay curve shape of the samples with p-n junction, samples b and c, can be divided into three portions: (1) initial fast decay mode, (2) slow decay mode, and (3) principal decay mode, as exhibited in Figure 4. The samples without p-n junction seemed to contain only portions (1) and (3).

4. Discussions

The differences in the TRMC signal—both decay time and curve shape—implied the variations in the passivation quality and the junction properties. Analysis of these variations could lead to better understanding of recombination kinetics of the heterojunctions. It is worth noting that two phenomena can contribute to a decrease of the TRMC signal in our heterojunction structures.

(i) *The Electron-Hole Recombination.* It is known that in amorphous region the bulk minority carrier lifetime is less than a few 10^{-8} s, while in high-quality silicon it is in the millisecond range.

(ii) *The Transfer of Carriers from a Crystalline to an Amorphous Region.* Indeed, their mobility in the latter is three orders of magnitude below their mobility in crystalline silicon [11].

This allows us to qualitatively understand the shape of the response curves obtained for the structures with p a-Si:H/n c-Si on one or two sides (Figure 2).

(i) As the built-in electric field keeps the free carrier density to a very low level at the location of the heterojunction, holes generated in the high-mobility n-type silicon crystal diffuse towards the low-mobility p-type amorphous silicon region. Once they enter it, their contribution to the TRMC signal is expected to drop sharply. Yet the resulting charge separation

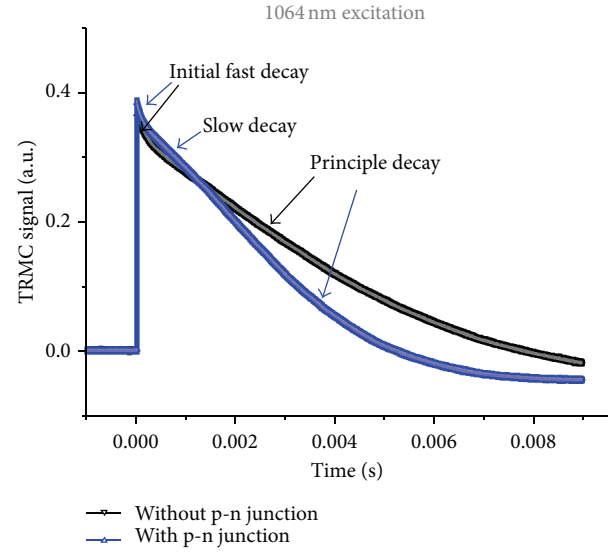


FIGURE 4: Comparison of TRMC decay curves between samples with and without p-n junction.

induces a growing counter electric field that ends up blocking further diffusion. The timescale of the transient diffusion regime can be estimated to be w^2/D_p where w is the thickness of the wafer (about $300 \mu\text{m}$) and D_p is the diffusion constant for minority holes in n-doped crystalline silicon (about $10 \text{ cm}^2 \cdot \text{s}^{-1}$ at room temperature). Accordingly, we obtained a value of $90 \mu\text{s}$, which corresponded to the typical timescale of the observed initial fast decay (Figure 4).

(ii) As recombination goes on in the crystalline silicon region, holes that were stored in the amorphous region are released back into the crystalline region—gradually bringing the electric field back to the built-in equilibrium value of the heterojunction. The decrease of the TRMC response due to recombination is therefore slowed down by the reverse transfer of holes from a low-mobility region back to a high-mobility region, leading to the “slow decay” part of the TRMC response in Figure 4.

(iii) After the electric field recovers its initial value then the “principle mode” sets in. The principle mode, exponential decay portion, can be observed at any illumination intensity.

Among the three structures, the sample with n-type a-Si:H passivated on both sides indicates the longest decay time. The front and rear sides of this structure act as reflecting walls for minority carriers, having excellent passivation property and preventing transfer of holes to the low-mobility layers [11]. Its decay kinetic can be simply expressed in the form of one exponential function. The “slow decay” mode is not observed. Longest lifetime is observed when the excitation wavelength is 1064 nm, corresponding to excess charge carrier generation in the bulk of the c-Si wafer and negligible absorption in the a-Si:H layer, as opposed to an excitation

TABLE 1: Effective lifetime (τ_{eff}) of samples with various structures measured by SINTON lifetime tester in the transient mode at minority carrier density of $2 \times 10^{15} \text{ cm}^{-3}$.

Sample	Structure	Effective lifetime (ms)
a	n a-Si:H/i a-Si:H on both sides	4.2
b	p a-Si:H/i a-Si:H on both sides	1.5
c	Cell structure	2.1

wavelength of 532 nm, which leads to initial excess charge carrier profile generation at the illuminated surface.

It is obvious that the TRMC results can provide information regarding not only the τ_{eff} but also the heterojunction properties, both of which are significantly important properties for the heterojunction silicon solar cell development. These demonstrate that the TRMC technique has high potential as an effective analysis tool for heterojunction silicon solar cells.

5. Conclusions

Based on information from the TRMC decay curves, the electrical property and passivation quality of the a-Si:H/c-Si heterojunctions as well as their changes can be evaluated. The decay curve time and the decay curve shape of samples provided meaningful interpretation of excess charge carrier kinetics in the heterojunctions. The samples with p a-Si:H/n c-Si heterojunction (s) containing a depletion/inversion layer at the interfaces showed the unique slow decay mode at high excitation (after the initial fast decay mode) due to excess charge carrier stored in the amorphous regions. These results agreed well with the change in the τ_{eff} from the SINTON lifetime tester. Experimental results suggest that the TRMC is an useful nondestructive technique which is suitable for primary check of the thin film a-Si:H/c-Si heterojunctions during the solar cell fabrication process.

Conflict of Interests

The authors declare that there is no conflict of interests regarding the publication of this paper.

Acknowledgment

The authors gratefully acknowledge the support of the French Embassy in Thailand through the postdoctoral fellowship program for giving the opportunity to carry out this study.

References

- [1] T. Mikio, K. Kunihiro, T. Sadaji et al., "HIT cells-high-efficiency crystalline Si cells with novel structure," *Progress in Photovoltaics Research and Applications*, vol. 8, pp. 503–513, 2000.
- [2] M. R. Page, E. Iwaniczko, Y.-Q. Xu et al., "Amorphous/crystalline silicon heterojunction solar cells with varying i-layer thickness," *Thin Solid Films*, vol. 519, no. 14, pp. 4527–4530, 2011.
- [3] D. L. Batzner, Y. Andrault, L. Andreetta et al., "Properties of high efficiency silicon heterojunction cells," *Energy Procedia*, vol. 8, pp. 153–159, 2011.
- [4] A. W. Stephens, A. G. Aberle, and M. A. Green, "Surface recombination velocity measurements at the silicon-silicon dioxide interface by microwave-detected photoconductance decay," *Journal of Applied Physics*, vol. 76, no. 1, pp. 363–370, 1994.
- [5] N. Schüller, T. Hahn, K. Dornich, J. R. Niklas, and B. Gründig-Wendrock, "Theoretical and experimental comparison of contactless lifetime measurement methods for thick silicon samples," *Solar Energy Materials and Solar Cells*, vol. 94, no. 6, pp. 1076–1080, 2010.
- [6] S. Kasouit, J. Damon-Lacoste, R. Vanderhaghen, and P. Roca i Cabarrocas, "Contribution of plasma generated nanocrystals to the growth of microcrystalline silicon thin films," *Journal of Non-Crystalline Solids*, vol. 338–340, no. 1, pp. 86–90, 2004.
- [7] S. Kasouit, P. Roca i Cabarrocas, and R. Vanderhaghen, "DTRMC, a probe of transverse transport in microcrystalline silicon," *Thin Solid Films*, vol. 427, no. 1-2, pp. 335–339, 2003.
- [8] M. Kunst, G. Müller, R. Schmidt, and H. Wetzel, "Surface and volume decay processes in semiconductors studied by contactless transient photoconductivity measurements," *Applied Physics A Solids and Surfaces*, vol. 46, no. 2, pp. 77–85, 1988.
- [9] S. von Aichberger, H. Feist, J. Löffler, and M. Kunst, "In situ monitoring of the deposition of a-Si:H/c-Si heterojunctions by transient photoconductivity measurements," *Solar Energy Materials and Solar Cells*, vol. 65, no. 1, pp. 417–422, 2001.
- [10] M. Kunst, O. Abdallah, and F. Wünsch, "Passivation of silicon by silicon nitride films," *Solar Energy Materials and Solar Cells*, vol. 72, no. 1–4, pp. 335–341, 2002.
- [11] M. Kunst, S. von Aichberger, G. Citarella, and F. Wünsch, "Amorphous silicon/crystalline silicon heterojunctions for solar cells," *Journal of Non-Crystalline Solids*, vol. 299–302, no. 2, pp. 1198–1202, 2002.
- [12] F. Wünsch, G. Citarella, O. Abdallah, and M. Kunst, "An inverted a-Si:H/c-Si hetero-junction for solar energy conversion," *Journal of Non-Crystalline Solids*, vol. 352, pp. 1962–1966, 2006.